Micromachined Quantum Circuits

A Dissertation

Presented to the Faculty of the Graduate School

of

Yale University

in Candidacy for the Degree of

Doctor of Philosophy

by

Teresa Brecht

Dissertation Director: Professor Robert J. Schoelkopf

December 2017

Abstract

Micromachined Quantum Circuits

Teresa Brecht

2017

Quantum computers will potentially outperform classical computers for certain applications by employing quantum states to store and process information. However, algorithms using quantum states are prone to errors through continuous decay, posing unique challenges to engineering a quantum system with enough quantum bits and sufficient controls to solve interesting problems. A promising platform for implementing quantum computers is that of circuit quantum electrodynamics (cQED) using superconducting qubits. Here, two energy levels of a resonant circuit endowed with a Josephson junction serve as the qubit, which is coupled to a microwave-frequency electromagnetic resonator. Modern quantum circuits are reaching size and complexity that puts extreme demands on input/output connections as well as selective isolation among internal elements. Continued progress will require adapting sophisticated 3D integration and RF packaging techniques found in today's high-density classical devices to the cQED platform. This novel technology will take the form of multilayer microwave integrated quantum circuits (MMIQCs), combining the superb coherence of three-dimensional structures with the advantages of lithographic integrated circuit fabrication. Several design and fabrication techniques are essential to this new physical architecture, notably micromachining, superconducting wafer bonding, and out-of-plane qubit coupling. This thesis explores these techniques and culminates in the design, fabrication, and measurement of a two-cavity/one-qubit MMIQC featuring qubit coupling to a superconducting micromachined cavity resonator in silicon wafers. Current prototypes are extensible to larger scale MMIQCs for scalable quantum information processing.

Contents

Acknowledgements

Here I take the opportunity to extend sincere gratitude to those what have made my path in graduate school possible. Most of all, I thank my advisor Robert Schoelkopf. He is a leader and scientist as well as motivating visionary. He has an inspiring life and spreads infectious excitement about science among his students and promotes open-mindedness in the field. I believe he has real knack for finding and bolstering solutions that are both creative and uncannily practical. In addition to guiding my path through experimental quantum information, microwave engineering and superconducting circuits, he has taught me how elevate the important aspects of a challenge order to innovate. Michel Devoret is a highly acclaimed scientist, gifted educator and caring mentor. I feel very lucky to have attended his specially-crafted lectures, struggled with his homework problems, and witnessed his unique mind at work as he Socratically questions and hones the direction of his students. Peter Rakich is a relatively recent addition to the department. He is both incredibly positive and sincere, and I enjoy talking with him and appreciate his openness and advice. He has an eye for detail and boundless energy, which seems to be serving him well as he has rapidly built a very cool and productive lab. To these incredible mentors and to all of my teachers: Thanks for challenging me and believing in me.

My success would not have been possible without the advisement of Luigi Frunzio, Michael Powers, and Mike Rooks, each of whom has invested significant time providing me training in fabrication, assistance in problem-solving, and technical as well as professional advice. Their extensive experience and consistent helpfulness are a marvelous resource that is truly appreciated.

I have had the privilege of working alongside dozens of remarkable colleagues in the lab. I am humbled by their intelligence, inspired by their energy, and proud to have been a part of this community. I have been amazed by how much these brilliant people went out of their way to help me learn or accomplish things, and in particular I would like to thank those who have helped me out the most: Michael Hatridge, Shyam Shankar,

List of Publications

This thesis is based in part on the following published articles:

1. M. Reagor, H. Paik, G. Catelani, L. Sun, C. Axline, E. Holland, I. M. Pop, N. A. Masluk, T. Brecht, L. Frunzio, M. H. Devoret, L. Glazman, and R. J. Schoelkopf (2013). "Reaching 10 ms single photon lifetimes for superconducting aluminum cavities". *Appl. Phys. Lett.* **102**, 192604

2. T. Brecht, M. Reagor, Y. Chu, W. Pfaff, C. Wang, L. Frunzio, M. H. Devoret, and R. J. Schoelkopf (2015). "Demonstration of superconducting micromachined cavities". *Appl. Phys. Lett.* **107**, 192603

3. C. Wang, C. Axline, Y. Gao, T. Brecht, Y. Chu, L. Frunzio, M. H. Devoret, and R. J. Schoelkopf (2015). "Surface participation and dielectric loss in superconducting qubits". *Appl. Phys. Lett.* **107**, 162601

4. T. Brecht, W. Pfaff, C. Wang, Y. Chu, L. Frunzio, M. H. Devoret, and R. J. Schoelkopf (2016). "Multilayer microwave integrated quantum circuits for scalable quantum computing". *npj Quantum Information* **2**, 16002 EP–

5. Y. Chu, C. Axline, C. Wang, T. Brecht, Y. Y. Gao, L. Frunzio, and R. J. Schoelkopf (2016). "Suspending superconducting qubits by silicon micromachining". *Appl. Phys. Lett.* **109**, 112601

6. T. Brecht, Y. Chu, C. Axline, W. Pfaff, J. Z. Blumoff, K. Chou, L. Krayzman, L. Frunzio, and R. J. Schoelkopf (2017). "Micromachined Integrated Quantum Circuit Containing a Superconducting Qubit". *Phys. Rev. Applied* **7**, 044018

List of Figures

xiii

List of Tables

List of Abbreviations

AC	**A**lternating **C**urrent
ALD	**A**tomic **L**ayer **D**eposition
AWG	**A**rbitrary **W**aveform **G**enerator
BCS	**B**ardeen-**C**ooper-**S**chrieffer
CMOS	**C**omplementary **M**etal-**O**xide-**S**emiconductor
CPW	**C**o-Planar **W**aveguide
CPWG	**C**o-Planar **W**aveguide with **G**round
cQED	**c**ircuit **Q**uantum **E**lectro-**D**ynamics
DC	**D**irect **C**urrent
DRIE	**D**eep **R**eactive **I**on Etch
HEMT	**H**igh **E**lectron **M**obility **T**ransistor
HFSS	**H**igh **F**requency **S**tructural **S**imulator (HFSS$^{\text{TM}}$ is a product of ANSYS$^{\circledR}$)
IC	**I**ntegrated **C**ircuit
IF	**I**ntermediate **F**requency
IR	**I**nfra-**R**ed
LO	**L**ocal **O**scillator
MMIC	**M**onolithic **M**icrowave **I**ntegrated **C**ircuit
MMIQC	**M**ultilayer **M**icrowave **I**ntegrated **Q**uantum **C**ircuit
PCB	**P**rinted **C**ircuit **B**oard
PECVD	**P**lasma **E**nhanced **C**hemical **V**apor **D**eposition
PR	**P**hoto-**R**esist
QED	**Q**uantum **E**lectro-**D**ynamics

RF	**R**adio **F**requency
RPP	**R**everse **P**ulse **P**lating
RRR	**R**esidual **R**esistance **R**atio
RSFQ	**R**apid **S**ingle **F**lux **Q**uantum
RQL	**R**eciprocal **Q**uantum **L**ogic
RWA	**R**otating **W**ave **A**pproximation
SIS	**S**uperconductor-**I**nsulator-**S**uperconductor
SEM	**S**canning **E**lectron **M**icroscopy
SQUID	**S**uperconducting **Qu**antum **I**nterference **D**evice
TE	**T**ransverse **E**lectric
TLS	**T**wo **L**evel **S**ystem
TM	**T**ransverse **M**agnetic
TSV	**T**hrough **S**ilicon **V**ia
VNA	**V**ector **N**etwork **A**nalyzer

The following are chemical abbreviations that are not composed of the standard elemental symbols or molecular formulae.

BOE	**B**uffered **O**xide **E**tch ($HF + NH_4F$ in water)
HMDS	Hexamethyldisilizane ($[(CH_3)_3 Si]_2 NH$)
IPA	Isopropyl Alcohol, or isopropanol (C_3H_7OH)
MIBK	Methyl Isobutyl Ketone ($(CH_3)_2 CHCH_2CCH_3$)
NMP	N-Methyl-2-Pyrrolidone (C_5H_9NO)
TMAH	Tetramethylammonium hydroxide ($N(CH_3)_4 OH$)

List of Physical Constants

Avogadro constant $\qquad\qquad N_A = 6.022 \times 10^{23}$ mol^{-1}

Boltzmann's constant $\qquad\quad k_B = 1.38 \times 10^{-23}$ m^{2}kg/s^{2}K

Electron charge $\qquad\qquad\quad$ e $= 1.9 \times 10^{-20}$ C

Faraday constant $\qquad\qquad$ F $= 96\,485.33$ C mol^{-1}

Fine structure constant $\qquad\ \boldsymbol{\alpha} = \frac{1}{137}$

Magnetic flux quantum $\qquad \Phi_0 = 2.067\,833\,67\,\mu$V/GHz

Pi $\qquad\qquad\qquad\qquad\qquad \pi = 3.14159$

Plank's constant $\qquad\qquad\quad h = 6.34 \times 10^{-34}$ J s

Plank's constant (reduced) $\quad \hbar = 1.05 \times 10^{-34}$ J s

Speed of Light $\qquad\qquad\qquad c = 2.997\,924\,58 \times 10^8$ m s^{-1}

Vacuum impedance $\qquad\quad Z_0 = \approx 120\pi\ \Omega \approx 376.73\ \Omega$

Vacuum permeability $\qquad\quad \mu_0 = 4\pi \times 10^{-7}$ H m^{-1}

Vacuum permittivity $\qquad\quad \epsilon_0 = 8.854\,187\,8 \times 10^{-12}$ F m^{-1}

List of Symbols

$\hat{a}$	photon creation (raising) operator	
$\hat{a}^{\dagger}$	photon annihilation (lowering) operator	
C	capacitance	F
E	energy	J
$\vec{E}$	electric field	$\mathrm{V\,m^{-1}}$
E_C	charging energy	J
E_J	Josephson energy	J
f	frequency	Hz
g	vacuum Rabi rate	$\mathrm{rad\,s^{-1}}$
G	conductance	Ω^{-1}
g_{seam}	seam conductance per unit length	$(\Omega\mathrm{m})^{-1}$
$H, \hat{H}$	Hamiltonian	J
$\vec{H}$	magnetic field	$\mathrm{A\,m^{-1}}$
I	current	A
I_c	critical current	A
k	wave number	$\mathrm{m^{-1}}$
L	inductance	H
L_J	junction inductance	H
m	mass	kg
$\vec{m}$	magnetic dipole moment	$\mathrm{Am^2}$
$\hat{n}$	Cooper pairs	

$\hat{N}$	photon number operator	
$\bar{n}$	average photon number	
$p, \vec{p}$	momentum	$\mathrm{kg\,m\,s^{-1}}$
$p, \vec{p}$	electric dipole moment	$\mathrm{C\,m}$
P	power	$\mathrm{W\,(J\,s^{-1})}$
p_{cond}	conductor participation ratio	
p_{diel}	dielectric participation ratio	
Q	charge	C
Q_{tot}	total quality factor (of a resonator)	
Q_{int}, Q_i	internal quality factor (of a resonator)	
Q_c	coupling quality factor (of a resonator)	
$\hat{Q}$	charge operator	C
R	resistance	Ω
r, r_i, r_o	radius	m
S_{xy}	element of S-matrix	dB
T_1	energy relaxation time	s
T_2	coherence time	s
T_2^{echo}	coherence time measured with Hahn echo sequence	s
T_ϕ	dephasing time	s
T_C	superconducting critical temperature	K
V	voltage	V
$W_{e,m}$	stored energy (electric, magnetic)	Joule
x	position	m
X	reactance	Ω
Y	admittance	Ω^{-1}
y_{seam}	seam admittance per unit length	$(\Omega\mathrm{m})^{-1}$
Z	impedance	Ω

Greek Symbols

α	anharmonicity	$\mathrm{rad\,s^{-1}}$
β	propagation constant	$\mathrm{m^{-1}}$
Δ	frequency detuning, or energy gap	$\mathrm{rad\,s^{-1}}$
ϵ	dielectric constant (permittivity)	$\mathrm{F\,/m}$
ϵ_r	relative dielectric constant (permittivity)	
γ	qubit decay rate	$\mathrm{rad\,s^{-1}}$
η	wave impedance	Ω
Θ_D	Debye temperature	K
κ	decay rate	$\mathrm{rad\,s^{-1}}$
λ	wavelength	m
λ_0	penetration depth	m
μ	permeability	$\mathrm{H\,/m}$
μ_r	relative permeability	
ξ_0	coherence length	m
σ_-	qubit state lowering operator	
σ_+	qubit state raising operator	
$\hat{\Phi}$	flux operator	$\mathrm{V\,Hz^{-1}}$
ϕ	superconducting phase	
χ	dispersive frequency shift	$\mathrm{rad\,s^{-1}}$
ω	angular frequency	$\mathrm{rad\,s^{-1}}$

Chapter 1

Introduction

In recent decades, experimentalists have begun to harness unique features of quantum mechanics: superposition and entanglement. We have come to treat them as resources that enable processing of information in non-classical ways.

However, compared to quantum information theoretical advancements, and indeed the imaginations of pop-sci magazine readers, the efforts to build quantum information processing systems have resulted in only modest success. This is despite intense public interest, motivated government funding programs, and the world's best research institutions dedicating significant resources to the problem. Why does today's actual quantum information technology lag significantly behind what is theoretically possible? Is there currently some engineering hurdle that, once surmounted, would pave the way for rapid development?

The full extent of what quantum systems may have to offer is not yet fully understood. I find it delightful and inspiring that researchers often do not foresee the crucial ways in which their inventions would one day be used. Similarly, today's advancements in controlling and observing quantum systems may yet reveal unexpected technological applications. Furthermore, they may clarify our description of fundamental physics and thereby improve our understanding of reality.

Surprises and unexpected applications will present themselves as quantum hardware

becomes more routine. Experimentalists strive to attain control over single quantum systems and, in parallel, extend this control to manipulate more complex systems of interacting quantum parts like coherent cogs in a machine. But the first steps in exercising this control are still being made.

1.1 Thesis synopsis

After this brief introductory section, I begin my thesis by motivating the work with a general description of quantum computing in chapter 2. I will define quantum bits, discuss their physical realizations and address how they differ from the classical bits found in ordinary computers. Namely, quantum bits are subject to unique errors characterized with certain coherence times. If these errors can be overcome, large scale quantum computers have various exciting potential applications. I will discuss these, as well as describe several architectural paradigms that are currently being pursued by researchers with the goal of actualizing an advanced quantum computer.

I then dive into one of the physical implementations: superconducting circuit quantum electrodynamics. Chapter 3 lays the physics foundations for the systems discussed in the rest of the thesis. In it, I define and discuss the quantum electromagnetic oscillator and the transmon, which is the specific variant of quantum bit that is experimentally implemented later on. I discuss the interaction of these oscillators and transmons in different regimes, describe the mechanisms of controlling and measuring them with external electronics. In the end, the reader will be convinced that many of these elements aggregated together could serve as a dynamic toolbox for quantum information processing.

Having provided the context and explained the physics underlying cQED systems, in chapter 4, I assess the development of increasingly complex technology in this field. Using comparisons with development of classical computer technology in the past and present, I discuss several critical reasons why scalability for quantum computers will not have the same requirements, or obey the same patterns, as scalability demands for classical

computers. Then, I propose that future cQED-based quantum computers will likely take the shape of multilayer microwave integrated quantum circuits (MMIQCs). These devices will meet the unique demands of isolation and preservation of cohererence by making heavy use of microfabricated 3D structures and superconducing bonds holding together stacks of wafers. This chapter ends with a short literature review of a collection of existing technologies that are relevant to the proposal.

These opening chapters serve to provide context for the experimental work that is now being pursued in the lab. Chapter 5 through chapter 8 concern the initial steps towards actualizing the class of devices proposed in chapter 4. To make this transition, more specific information about microwave resonators is discussed in chapter 5. I cover different types of resonators that have been studied over the years in our lab and others. Then, I list the loss mechanisms that affect resonator coherence times relevant for quantum information storage. This enumeration concludes with an analysis of losses at a seam – a detail to which this thesis devotes special attention. Next, I explain resonator measurement and analysis methods, and finish with measurements of 3D cavity resonators that evidence the importance of seam loss.

In chapter 6, I propose and support the idea that indium is a suitable material for mitigating seam loss in multilayer wafer-based cavity resonators by creating superconducting micromachined cavity resonators. Here, I describe the fabrication, coupling design, and measurements of these first devices of their kind. Chapter 7 continues to explore indium as a material useful for superconducting wafer bonding. I discuss the use of indium bump bonding in developed technologies, and show that I can create and characterize our own indium bumps with an in-house process. I evaluate indium as a superconductor by measuring it's transition temperature and creating and measuring resonators of various types.

The next step is to realize a full cQED system with MMIQC hardware by incorporating a quantum bit with the type of resonator perfected in chapter 6. This is the subject of chapter 8. First, I introduce a unique transmon geometry that is particularly suited for

integration with the micromachined cavity. The bulk of the chapter then covers the design, fabrication, and measurement of a particular two-cavity/one-qubit device that constitutes the first ever MMIQC. Measurements demonstrate the device's performance in the strong dispersive regime of cQED. I end by discussing the important loss mechanisms and plans for improved similar devices.

Chapter 2

Quantum computing

We motivate the rest of the thesis starting with an introduction to quantum information, the possible applications of a quantum computer, and what is needed to build one, in a broad sense. This chapter is introductory – we do not attempt to add to the volumes of material on quantum computation. Instead, we briefly summarize important parts in order to provide motivation and context for the following chapters. More extensive education can be gained starting with other books and lectures (Nielsen and Chuang, 2000; Mermin, 2007; Preskill, 2015; Bennett and Divincenzo, 2000).

2.1   Bits and qubits

A classical bit is a basic unit of binary information. In a quantum computer, the analog of the classical bit is a quantum bit, called a "qubit." It is defined as a pair of levels of any quantum system, and it actually contains more information than a classical bit.

Unlike a classical bit, a quantum bit can exist in a *superposition* of states $|0\rangle$ and $|1\rangle$. More precisely, a qubit state $|\psi\rangle$ is described by a complex linear combination of the computational basis states $|0\rangle$ and $|1\rangle$:

$$|\psi\rangle = \alpha|0\rangle + \beta|1\rangle = \begin{pmatrix} \alpha \\ \beta \end{pmatrix} \tag{2.1}$$

Here, α and β are complex numbers indicating probability *amplitudes*. If this qubit were measured strongly in the computational basis, we would either find $|0\rangle$ with probability $|\alpha|^2$ or $|1\rangle$ with probability $|\beta|^2$. Therefore, $|\alpha|^2 + |\beta|^2 = 1$ for *pure states*. The pure state is represented in two-dimensional complex vector space (or Hilbert space) as a unit vector on what we call the Bloch sphere, as shown in figure 2.1. The arbitrary qubit state can be specified by two angles:

$$|\psi\rangle = \cos\frac{\theta}{2}|0\rangle + e^{i\phi}\sin\frac{\theta}{2}|1\rangle. \tag{2.2}$$

When we *measure* the state of a qubit, we are doing so in a particular measurement basis and we only gain classical information in that measurement basis. For instance, we may choose a computational basis and measure along Z-axis of the Bloch sphere to arrive at an answer of either $|0\rangle$ or $|1\rangle$. The effect of this measurement is to project the actual qubit vector onto the basis of measurement. [1] Note that we could also choose to measure in the basis of the Y-axis, in which case we would project the qubit into either of the states $\frac{1}{\sqrt{2}}(|0\rangle \pm i|1\rangle)$. Such a measurement would then destroy any indication of whether the original qubit state was closer to $|0\rangle$ or $|1\rangle$.

Classical bits are manipulated with gates: either single bit flips (NOT) or operations conditioned on the state of multiple bits (OR, AND, XOR, NAND). Single qubit gates, on the other hand, can be described as manipulations that rotate the qubit state vector in some way on the Bloch sphere. A generalized single-qubit operation is any 2×2 unitary matrix that operates on the qubit state vector. Furthermore, any single-qubit operation can be decomposed into a scaling and a rotation by a combination of one or more of the *Pauli*

---

[1]This description is simplified to *projective* measurements. In fact,it is possible to perform *weak* measurements that only partially project the state onto the measurement axis. The study of quantum measurement backaction is very exciting and is contributing to the fundamental understanding our quantum systems (Hatridge et al., 2013).
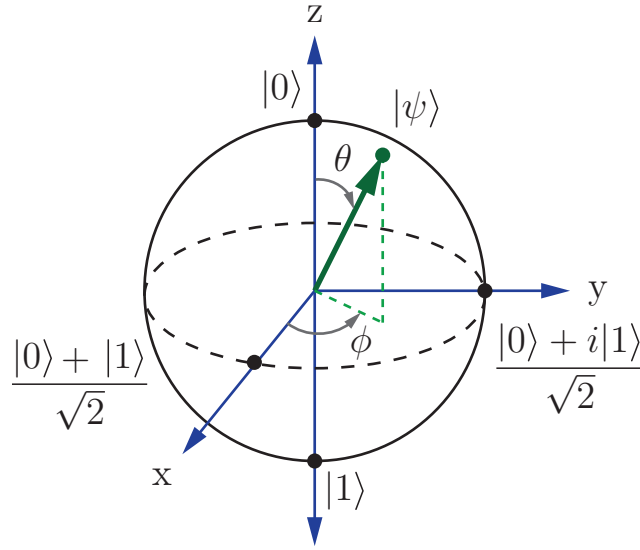
FIGURE 2.1: The green arrow is a qubit state, defined by the two variables θ and ϕ. There are black dots and labels on four of the six cardinal points. The ground state points up and is denoted $|0\rangle$ or $|g\rangle$. The excited state points down and is denoted $|1\rangle$ or $|e\rangle$.

matrices:

$$
\sigma_0 = I = \begin{pmatrix} 1 & 0 \\ 0 & 1 \end{pmatrix} \qquad\qquad \sigma_x = X = \begin{pmatrix} 0 & 1 \\ 1 & 0 \end{pmatrix}
$$
$$
\sigma_y = Y = \begin{pmatrix} 0 & -i \\ i & 0 \end{pmatrix} \qquad\qquad \sigma_z = Z = \begin{pmatrix} 1 & 0 \\ 0 & -1 \end{pmatrix}
$$

(2.3)

In the next chapter, we shall find it useful to define ladder operators by the linear combinations $\hat{\sigma}_\pm = \hat{\sigma}_x \pm i\hat{\sigma}_y$.

When there is more than one qubit, the number of basis states increases rapidly. For instance, a two qubit system has four basis states: $|00\rangle, |10\rangle, |01\rangle, |11\rangle$, and a three qubit system has eight basis states, and an N-qubit system has 2^N basis states. The quantum state of the whole system is described by complex coefficients for each of the basis states, and is written as a vector with 2^N elements.

Multi-qubit gates can be implemented by dynamically controlling the interactions between one or more qubits. Some of these implementations are analogues to classical gates,

and some are more creative. Ideal multi-qubit gates are described by $2^N \times 2^N$ unitary matricies.

In quantum computing algorithms, multi-qubit gates are used to generate *quantum entanglement*. A crucial property of qubits is their ability to establish and sustain this entanglement, in which one bit of information can be shared by two or more different qubits, regardless of their physical separation. For example, the entangled two qubit state $|00\rangle + |11\rangle$ stores information in the correlation between the two qubits. A measurement on one qubit instantly implies knowledge of the other qubit, even if they are physically separate. There are, in fact, two non-local bits contained in this entanglement: one for the information that the two qubits are in the same state, and one for the sign of the entanglement, which here is "+". Entanglement allows for operations on one qubit to affect all qubits with which it shares entanglement, an effect that may be exploited for quantum information processing or communication. Many interesting experiments make use of multi-qubit entanglement as a resource, but they are out of the scope of this thesis.

2.2 Physical realizations

Classically, bits are implemented in various ways. Modern bits are often realized by the two positions of a transistor or other electrical switch, two stable states of a flip-flop circuit, or whether a capacitor carries charge or not. Bits can also be represented by two directions of magnetization or two distinct polarization states. Non-electronically, bits can be stored in the position of a mechanical lever, or the presence or absence of a hole at a specific point of a paper card. In general, a bit of information can be carried by any physical system in which we can consider two distinct states. [2]

---

[2]Though we compare and contrast quantum to classical binary logic here, information in general is of course not limited to binary representations. For example, rather than logic in base 2 using bits, computers might also operate in base 3 using ternary logic on the trit states of -1, 0, and 1. Quantum computing, too, can be achieved with more than two energy states. Regardless, the quantum versus classical distinctions that we make in this chapter are no less poignant. Base 2 is the logic of choice for both bits and qubits for ease of physical implementation.

A qubit is any two-level system with the quantum property of superposition. These two levels may be two excited states of atoms (Briegel et al., 2000) or ions (Cirac and Zoller, 1995; Monroe and Kim, 2013; Blatt and Wineland, 2008). They may also be the spin-up and spin-down of nuclear or electronic spins, for example confined by a crystalline defect (Jelezko and Wrachtrup, 2006). They may be spin states of solid-state quantum dots, e.g. those of a single dot (Loss and DiVincenzo, 1998; Awschalom et al., 2013) or the singlet or triplet total spin states of two dots (DiVincenzo et al., 2000). In this thesis, the qubit is embodied by two energy levels of an anharmonic superconducting circuit. See Clarke and Wilhelm, 2008; Devoret and Schoelkopf, 2013.

Whether classical or quantum, *information is physical*. This statement is not trivial, and while it may seem subtle at first, there are profound implications. However, this is sometimes overlooked because algorithms of information processing are often studied and discussed in the abstract. The fact that physical laws pertain to information has particularly relevant consequences between thermodynamics and quantum information (Landauer, 1996). In particular, irreversible logical operations are accompanied by an increase in entropy of the system or its environment (this principle is true for both classical and quantum computations). The physicality of qubits is also apparent in the sense that their state is inseparable from dissipation of energy in their physical embodiment and/or surroundings, as we discuss in the next section.

2.3   Decoherence of qubits

Computer memory relies on bits keeping their state. Nevertheless, there are 64 billion bits (8 GB) in my laptop's RAM, and they do sometimes have errors. Classical bits can suffer from either hard errors, which are irreparable problems with hardware, or soft errors, which are transient issues caused by events such as random cosmic rays. However, most of the bits are quite robust due to thresholding: A certain amount of voltage fluctuation (either from imperfect components, thermal fluctuations, or cosmic rays) is tolerated and

nothing happens unless this exceeds the threshold value to flip the bit. When errors do happen, they probably do not affect my laptop's performance.

Qubits are not nearly so robust. In fact, they "lose" their state fairly quickly – with an exponential decay on the scale of no more than a millisecond for the types of superconducting qubits on which we will focus. Qubits cannot be protected by thresholding as classical bits can. Furthermore, an initialized quantum state is subject to *decoherence*, which is altogether more frightful than the intermittent bit-flip errors of classical bits.

Coherence is a term that includes several types of information loss. There are two processes that contribute to decoherence of a qubit: The first is energy relaxation, denoted T_1. The second is dephasing, T_ϕ, which is a sign of frequency instability but not energy loss. Combined, the total "coherence time," T_2 is the length of time for which the qubit maintains a particular superposition of states. These timescales are related by

$$\frac{1}{T_2} = \frac{1}{2T_1} + \frac{1}{T_\phi}. \tag{2.4}$$

In any physical quantum system, there may be many channels contributing to energy relaxation and dephasing. These channels can be interactions with the external environment, including (but not limited to) dissipation of energy to the container that surrounds the qubits, or absorption of ambient radiant thermal energy.

A qubit subject to these decoherence effects can be described by a *mixed state*, as opposed to the pure states whose mechanics we have described by unitary operations on the Bloch sphere. On the Bloch sphere, energy relaxation (T_1) causes the state vector to shrink. Dephasing (T_ϕ) causes the state vector to rotate. These types of decohernce are driven by both classical and quantum noise which is statistical in nature. Therefore, to learn any physical observable of the quantum state, it is necessary to ensemble average over the

noise. Both mixed states and pure states can be written as a density matrix defined by

$$\rho = \sum_j p_j |\psi_j\rangle\langle\psi_j|, \tag{2.5}$$

where p_j is the probability that an element of the ensemble is in state $|\psi_j\rangle$. The density matrix must satisfy $\mathrm{Tr}\,\rho = 1$. For pure states, $\mathrm{Tr}\,\rho^2 = 1$, and in fact $\rho^2 = \rho$. For mixed states, $\mathrm{Tr}\,\rho^2 < 1$. The expectation value of an observable $\mathcal{O}$ is given by a trace over its product with the density matrix:

$$\langle\mathcal{O}\rangle = \mathrm{Tr}\,\rho\mathcal{O} = \sum_j p_j \langle\psi_j|\mathcal{O}|\psi_j\rangle. \tag{2.6}$$

2.4 Quantum computation

A quantum computer uses the resources of superposition and entanglement to process quantum information contained in several (or many) qubits. Note that in order to describe the superposition of basis states in a system of N qubits, we need 2^N complex numbers. In some sense, quantum algorithms are performing the classical equivalent operations on many possible classical input states simultaneously (perhaps with classical bit arrangements mapped to the quantum basis states $|00...0\rangle$, $|10...0\rangle$, $|01...0\rangle$ ...,
$|11...1\rangle$). In the end, though, the circuit must arrive at one solution. If set up correctly, all the probability amplitudes of the possible paths have interfered to cancel incorrect solutions and added constructively to the correct solution. This is completely unlike classical computation. The capacity to perform multiple computations simultaneously is known as "quantum parallelism." [3]

---

[3]Quantum parallelism is a term coined by David Deutsch in order to distinguish the computational advantages derived from quantum superpositions from more traditional forms of classical parallel information processing, wherein distinct classical processors work through separated problems in parallel. Deutsch ascribes to the "many worlds interpretation" of quantum mechanics, and so he would describe the parallel computations on the various possible input states as actually happening in other universes. This interpretation, however intriguing, is not necessary to appreciate the power of quantum parallelism.

There are three main categories of algorithms that have gained fame for their promised advantage over classical algorithms. The first class makes use of quantum versions of Fourier transform, and includes the Deutsch-Joza algorithm, which determines if an input function is balance or constant (Deutsch and Jozsa, 1992), and Shor's algorithms for factorization and discrete logarithms (Shor, 1994; Shor, 1997). The classical fast Fourier transform takes about $O\left(N\log N\right) = O\left(N2^N\right)$ steps to Fourier transform a set of N data points. Using a quantum computer, the job could be done using about $O\left(\log^2 N\right) = O\left(N^2\right)$ steps – an exponential improvement. The quantum Fourier transform is a great example of quantum parallelism at work, and it must be cleverly put to use in these algorithms. Shor's integer factorization algorithm is of particular interest to many because the (classical) computational difficulty of integer factorization is the basis of many common encryption schemes, namely public-key RSA (Rivest, Shamir, and Adleman, 1978).

The second class is search algorithms, including Grover's (Grover, 1997). For a search space of size N, classical search algorithms (there are serveral kinds) can complete the search in a time that scales as $O\left(N\right)$, whereas the quantum search algorithm can complete the search in a time that scales as $O\left(\sqrt{N}\right)$.

The third class is quantum simulations. This is the purpose for which quantum computation was first proposed by Richard Feynman in 1982 (Feynman, 1982). Even small quantum systems are difficult for classical computers because the number of complex numbers needed to describe a the system grows exponentially with the size of the system. Fortunately, this is the same scaling property that gives quantum computers their power. Practical matters of quantum simulation and several examples of valuable quantum systems that may be simulated are discussed in Lloyd, 1996.

2.4.1 The DiVincenzo criteria

David DiVincenzo of IBM famously listed five requirements for the implementation of quantum computation (Divincenzo, 1996):

1. *A scalable physical system with well characterized qubits*

    In order to solve any interesting problem (a problem that is intractable to solve using current classical methods), we will need many qubits. They need to preserve quantum properties of superposition and entanglement, regardless of how many more qubits we add. Furthermore, the qubits must be fully understood such that they may be kept within a well defined computational Hilbert space.

2. *The ability to initialize the state of the qubits to a simple fiducial state*

    We must be able to initialize the qubits to a known input state – for instance, the ground state $|000...\rangle$.

3. *Long relevant decoherence times, much longer than the gate operation time*

    The time it takes to perform the quantum logic gates should be faster than the the time that the information being operated upon will be lost due to decoherence. The qubit coherence time need not exceed the total time of the algorithm, however, as long as sufficiently effective quantum error correction is applied (next section).

4. *A "universal" set of quantum gates*

    A set of universal quantum gates is any set of gates upon which any possible quantum computing operation can be reduced. Several possible sets exist. However, it would likely more efficient to have arbitrary rotations of qubits at the operators disposal, in addition to various flexible multi-qubit gates.

5. *A qubit-specific measurement capability*

    We must be able to faithfully retrieve the results of our computation.

    In summary, a quantum computer will require lots of qubits with long lifetimes that we can manipulate and measure. To go further, two additional desirables for quantum communication were later added by DiVincenzo (Divincenzo, 2000). Here, he comments on each the five requirements above and then considers additional properties needed for quantum information processing that is not strictly computing. Examples of quantum

communication include many proposals for quantum key distribution (Bennett and Brassard, 1984), transactions of unforgeable quantum money (Wiesner, 1983), and quantum secret sharing (Hillery, Bužek, and Berthiaume, 1999). The additional requirements are:

6. The ability to interconvert stationary and flying qubits

7. The ability faithfully to transmit flying qubits between specified locations

The "flying qubit" is what moves quantum information through space, and could be of any of the computing qubit implementations. Many proposals take the the flying qubit to be embodied as a photon, with the qubit encoded in either the polarization or spatial wavefuction. Applications in quantum key distribution, for example, require long distance communication of quantum bits. Photons are ideal for this purpose. On the other hand, one may imagine using flying qubits of one kind or another to shuttle quantum information to different locations within a single large quantum computing device. Therefore, the two extra criteria above are worthwhile pursuits for groups interested in quantum computation and quantum communication alike.

2.5 Quantum error correction

Error correction in quantum computers has to be fundamentally different than the error correcting schemes in classical computers. Earlier, we contrasted the discreteness of classical bits with the continuous nature of qubit decoherence. A classical bit can flip accidentally, but only discretely, and my computer's RAM is designed with error correction protocols including redundancy, parity checks, etc. The decoherence of qubits that we have discussed is in fact continuous error accumulation. The single-qubit Bloch vector is constantly subject to spurious environmental noise, however small, that pushes it around continuously in two dimensions. Quantum errors, therefore, are intrinsically continuous. Upon strong measurement, the result may manifest as a qubit flip error, but that is not the

worst of it. A small error in one quit will propagate to affect all of the other qubits with which it must interact in multi-qubit gates throughout the computation.

The nature of measurements of quantum states also presents a challenge to error correction. How can we detect the error without destroying the state? Our means of monitoring the qubit is with projective measurements. Because a qubit state can be anywhere on the Bloch sphere and we must choose to projectively measure with some choice of basis, the result of a measurement is probabilistic. Therefore, different measurement outcomes do not necessarily indicate whether an error has occurred. Not only that, but the unfortunate consequence of the measurement is destruction of the information held in the superposition. Even so-called weak measurements have back-action on the state vector (Hatridge et al., 2013).

We are beginning to see that the same consequences of quantum mechanics that give quantum algorithms their power actually put many classical schemes of error correction off-limits. For instance, the simplest classical error correcting code is a repetition code, in which each bit is written three times, such that a flip of one bit is corrected by being overwritten by majority voting of the three. However, there is a no-cloning theorem for quantum states (Wootters and Zurek, 1982) that prohibits the straightforward application of such redundancy-based classical error correcting codes to the quantum computer. [4]

Some kind of quantum error correction (QEC) is inevitably required because we do not have infinite lifetime qubits, nor can we perform perfect gates, nor can we perform perfect measurements. Furthermore, proving the ability to correct particular errors is not nearly enough to be ready to "scale up" and build a practical quantum computer. The system must function in a *fault tolerant* manner, meaning that it is robust against qubit errors and gate errors that may occur at any point during a calculation. Shor discusses fault-tolerant QEC codes (Shor, 1996), and there are many different strategies for of QEC being investigated (Gottesman, 2010; Bennett et al., 1996; Knill, 2005; Steane, 1996). Many

---

[4]It is, however, possible to implement a 3-qubit repetition code without breaking the no-cloning theorem. See Mermin, 2007.

of these schemes rely on composing logical qubits out of constituent physical qubits, and some of these schemes are specialized to particular architectures, which we discuss next.

Most error correction schemes can be broken into three categories: stabilizer codes, a surface code, and error correction of encoded bosonic states.

The first of these, stabilizer codes (Shor, 1995; Steane, 1996), combine several physical qubits in an error correction scheme to create logical qubits that are more robust than the constituent qubits. For instance, the qubit state to be protected can be mapped with a unitary encoding to an entangled state of several ancillary qubits that is more robust to local perturbations. Depending on the actual error rates, iterated layers of logical qubits may be necessary. The iterated layering of logical qubit levels can be done in a variety of concatenation schemes (Knill and Laflamme, 1996; Knill, Laflamme, and Zurek, 1998).

Second is the surface code, whose operation and advantages are described in Fowler et al., 2012; Dennis et al., 2002. Theoretically, the scheme achieves high error tolerance by employing large numbers of physical qubits to create a network or fabric upon which logical qubits are processed by topological braiding.

A third approach is the encoding of logical qubits in oscillator states (aka bosonic encodings). The state of photons in a quantum harmonic oscillator (chapter 5) can be used as a higher dimensional Hilbert space in which qubits can be encoded in several ways (Gottesman, Kitaev, and Preskill, 2001). Specifically with cQED systems, longer lifetimes can be achieve when the object that is thought of as the qubit in other schemes instead serves to enable readout, control and encoding of a logical qubit state in a microwave resonator (Vlastakis et al., 2013; Leghtas et al., 2013a; Mirrahimi et al., 2014). Superpositions of quantum states can be stored for ~ 1 millisecond without intervention (Reagor et al., 2016). Furthermore, these resonator-based logical qubits can be protected by measurement-based driven dissipative stabilization (Leghtas et al., 2013b), or error corrected by means of active feedback (Ofek et al., 2016).

2.6   Modular architecture for quantum computing

One approach to scalable quantum computing emphasizes modularity of robust components and functions (Monroe, Schoelkopf, and Lukin, 2016; Kimble, 2008; Monroe et al., 2014). This approach is of particular importance to cQED systems because, as we shall see in the next chapter, qubits in cQED systems are capable of strong coupling over large length scales. This is an advantage for experimentalists wishing to manipulate macroscopic quantum systems, but it also presents some challenges. The availability of controllable long-range interactions opens up a variety of ways to implement multi-qubit gates, but it has detrimental effects on single-qubit gates and coherence. Unwanted nearest-neighbor or long-range interactions, which we shall call *"cross-talk"* in chapter 4, tend to propagate errors between qubits in a way that scales unfavorably with the size of the system. Though it is possible to fabricate a device with a large number of qubits, executing a particular complex algorithm including specific single- and multi-qubit gates requires accurately controlling the range of these interactions.

The way to achieve this is to limit the physical connection between qubits, isolating modules consisting of a few qubits and a few cavities that we have learned to operate at high fidelity. Modules may be separated by cables or transmission lines and only interact via intentional measurements. For instance, networking between multiple modules can be achieved by sending a dispersive pulse to interact with both modules before being detected (Cabrillo, 1999; Pfaff et al., 2012). "Heralding" such measurements can generate entanglement between modules, and repeating the entanglement-generating measurements can improve the result by "distillation."

The modular architecture and the three classes of error correction schemes are not altogether exclusive or incompatible. Different approaches could be layered, for example, by developing modules of error corrected logical qubits encoded in oscillator states and then networking those modules into a topology appropriate for surface code computation (Nickerson, Li, and Benjamin, 2013). To some extent, the hardware vision laid out in

chapter 4 appeals to all of these approaches. Additionally, the new experimental material in chapters 5-9 is not necessarily exclusive to any single one of these approaches. In our quantum circuit lab, we are most excited about developing hardware and tools towards a modular approach. One benefit of a modular approach is experimental accessibility. Engineering and development of each module can take place independently, and involves only a small number of qubits at a time.

Chapter 3

Circuit quantum electrodynamics

Experimental quantum information processing is rapidly developing in several physical implementations, and superconducting quantum circuits are a particularly promising candidate for building a practical quantum computer (Devoret and Schoelkopf, 2013; Barends et al., 2014). In these systems, qubits made with Josephson junctions behave like macroscopic atoms with quantized energy levels in the microwave domain. Coupling them to resonators forms a powerful platform known as circuit quantum electrodynamics (cQED) (Blais et al., 2004; Blais et al., 2007; Schoelkopf and Girvin, 2008). The underlying physics of cQED is throughly described in previous theses and papers. For this reason, we make this chapter concise by summarizing important results rather than deriving them here. In addition, we focus only on the particular type of qubit discussed later in this thesis, the transmon, omitting similar systems that explore interesting physics using similar foundations. For a more thorough education on these cQED fundamentals, these notes are highly recommended: Devoret, 1997; Girvin, 2011.

This chapter begins with a short introduction to quantum electrodynamics in general. This is followed by the introduction of quantum electromagnetic oscillators, and then of superconducting qubits. Once the groundwork for these two types of objects is laid, we proceed to study the nature of their interaction with one another in a cQED system. The physics is contained in the Jaynes-Cummings Hamiltonian, which we will manipulate to reveal the mechanisms behind electronic control of qubit states as well as measurements

that are useful for quantum information processing.

3.1 Quantum electrodynamics

The interaction between light (photons, electromagnetic fields) and matter (electrons or atoms) is one of the most pervasive themes of physics, and is known as quantum electrodynamics (QED). The quantum electrodynamics of photons and quantum bits as implemented in superconducting microwave circuits is called circuit QED (cQED). It closely emulates the physics of cavity QED experiments, which were developed beforehand using neutral atoms interacting with trapped light. Before discussing the circuits of cQED, let us appreciate the broader category of QED.

QED was the first successful quantum field theory, for which Richard Feynman, Julian Schwinger and Sin-itero Tomonaga were awarded the 1965 Nobel Prize in physics. The theory concerns all phenomena resulting from the electromagentic fields of charged particles, using photons. It provides the link between quantum mechanics and relativistic theory of electrodynamics. Furthermore, QED incorporates such ideas as particle creation and annihilation, as well as bosonic force-carriers, in a self-consistent framework.

Systems featuring the interaction of light and matter both provide physics insights and enable groundbreaking technology. The operation of lasers, transistors, and magnetic resonance imaging can only be explained with QED physics. This is also the physics that will enable information processing with any of the physical implementations of quantum bits listed in the previous chapter. However, we must draw a distinction between those devices that are quantum in nature (such as lasers and transistors), and the constituents of a quantum computer to be discussed in this chapter, which must be quantum in operation. We require coherent quantum fields with controllable superpositions and entanglement.
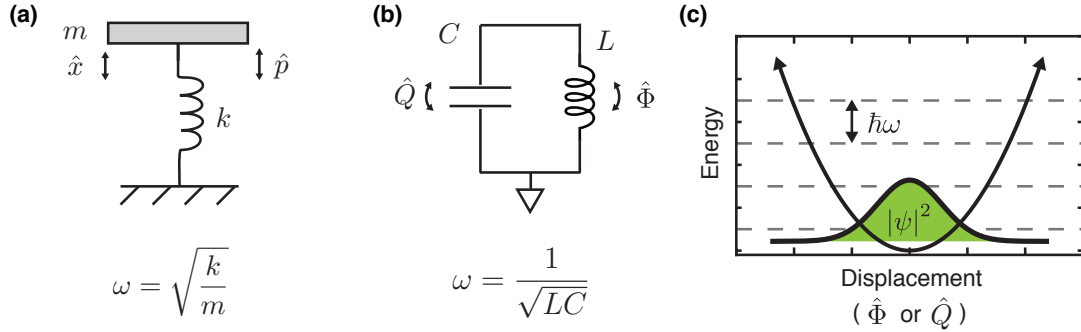
FIGURE 3.1: **Energy levels of the quantum harmonic oscillator embodied by an LC circuit.** Evenly spaced energy eigenstates with $\Delta E = \hbar \omega_c$. The ground state is Gaussian distributed in the conjugate variables of charge $\hat{Q}$ and flux $\hat{\Phi}$. (Figure adapted with permission from Reagor, 2015. See Copyright Permissions.)

3.2 Quantum electromagnetic oscillators

Before getting to superconducting qubits, we will first understand electromagnetic oscillators in a quantized language. To begin, recall that all harmonic oscillators are characterized by their quadratic potential energy relationship. Electromagnetic oscillators follow precisely the same dynamics as a mechanical harmonic oscillator, such as a pendulum or mass on a spring, with a Hamiltonian familiar to students of physics:

$$H = \frac{1}{2m}p^2 + \frac{m\omega^2}{2}x^2, \tag{3.1}$$

where m is the mass, ω is the angular frequency.

We will now write the Hamiltonian for the simple electromagnetic oscillator containing an inductor L and a capacitor C. The momentum and position variables are replaced by quantum operators for flux ($\hat{\Phi}$) and charge ($\hat{Q}$) (Devoret, 1997; Girvin, 2011):

$$\hat{H} = \frac{1}{2L}\hat{\Phi}^2 + \frac{1}{2C}\hat{Q}^2. \tag{3.2}$$

Like momentum and position of a pendulum, the flux and charge are conjugate variables.

The commutation relation is $[\hat{\Phi}, \hat{Q}] = -i\hbar$, analogous to that of the quantum variables of momentum and position. Hamilton's equations of motion provide us with familiar relations for the current through the circuit and the voltage at the LC circuit's node:

$$\dot{Q} = \frac{\partial \hat{H}}{\partial \Phi} = \frac{\Phi}{L} = I \tag{3.3}$$

$$\dot{\Phi} = -\frac{\partial \hat{H}}{\partial Q} = -\frac{Q}{C} = V. \tag{3.4}$$

The ground state energy is

$$\langle 0|H|0\rangle = \frac{1}{2C}\langle 0|\hat{Q}^2|0\rangle + \frac{1}{2L}\langle 0|\hat{\Phi}^2|0\rangle = \frac{\hbar\omega_0}{2}, \tag{3.5}$$

where $\omega_0 = 1/\sqrt{LC}$ is the resonant frequency of the circuit. Next, we can use the equipartition theorem to write the zero-point fluctuations in the charge and flux:

$$Q_{ZPF}^2 = \langle 0|\hat{Q}^2|0\rangle = \frac{\hbar\omega_0 C}{2} = \frac{\hbar}{2Z_c}, \text{and} \tag{3.6}$$

$$\Phi_{ZPF}^2 = \langle 0|\hat{\Phi}^2|0\rangle = \frac{\hbar\omega_0 L}{2} = \frac{\hbar Z_c}{2}, \tag{3.7}$$

where $Z_c = \sqrt{L/C}$ is the characteristic impedance of the circuit.

We can change the variables of equation 3.2 to the raising and lowering operators, $\hat{a}$ and $\hat{a}^\dagger$. We let

$$\hat{Q} = -iQ_{ZPF}(\hat{a} - \hat{a}^\dagger) \tag{3.8}$$

$$\hat{\Phi} = \Phi_{ZPF}(\hat{a} + \hat{a}^\dagger). \tag{3.9}$$

This gives the usual Hamiltonian for a quantum simple harmonic oscillator:

$$\hat{H} = \hbar\omega_0(\hat{a}^\dagger\hat{a} + 1/2) = \hbar\omega_0(\hat{N} + 1/2), \tag{3.10}$$

where $\hat{N} = \hat{a}^\dagger \hat{a}$ is the photon number operator. The raising and lowering operators satisfy commutation relation $[\hat{a}, \hat{a}^\dagger] = 1$. The quadratic potential of the quantum harmonic oscillator is shown in figure 3.1. The ground state has non-zero energy due to the zero-point fluctuations of charge and flux defined above. Successive energy eigenstates are separated by constant ladder spacing $\hbar\omega_0$.

We now have a quantum picture of the electromagnetic oscillator. One can interpret the quantized states as distinct excitation modes of the collective motion of electrons in the wire, or as individual photons present in the entire circuit. In our LC circuit, the electric field oscillations are localized between the capacitor plates and the magnetic field is localized in the inductor, but the reader is encouraged to think of these field oscillations together as single photons. We hold this description regardless of the physical structure of the electromagnetic resonator (several of which are discussed in chapter 5).

3.3 Josephson junction qubits

Inductors and capacitors are the basic linear components in circuit design, and they are implemented by specifying geometry in superconducting circuits no differently than they are in ordinary room temperature circuits. In addition, there is an important additional circuit element that is put to work in superconducting circuits. It is the Josephson junction, which consists of a weak-link between two superconducting electrodes between which quantum tunneling can occur. The special characteristic of this element is that it bestows a nonlinear inductance to the circuit without adding any dissipation (ideally). It will soon be clear why this is useful.

When a tunneling event occurs, it causes phase difference ϕ between the wavefunction on either side of the junction. Furthermore, the junction can sustain a tunneling supercurrent with the relation

$$I = I_c \sin \phi(t), \tag{3.11}$$

where I_c is the junction critical current, which is the maximum current that can flow through the junction. In the presence of a potential difference V across the junction, the phase ϕ evolves in time with the relation

$$\hbar \frac{\partial \phi}{\partial t} = 2eV. \tag{3.12}$$

The time derivative of the current is

$$\frac{\partial I}{\partial t} = \frac{2eV I_c}{\hbar} \cos \phi. \tag{3.13}$$

Note that the relationship is similar to that of an inductor, $V = -L \partial I / \partial t$, but with an inductance that varies with ϕ. We call it the Josephson inductance:

$$L_J = \frac{\Phi_0}{2\pi I_c \cos \phi}, \tag{3.14}$$

where we have used the magnetic flux quantum, $\Phi_0 = h/2e$.

This nonlinear inductance is what allows us to create a qubit out of a superconducting circuit. The LC oscillator discussed in the previous section, like all quantum harmonic oscillators, has evenly spaced energy levels. Varying L and C can modify the fundamental frequency ω_c, but the only relevant energy transition remains $\hbar \omega_c$, which drives transitions between all possible energy states simultaneously. To create a qubit, we require a system with a uniquely addressable transition between just two states. The addition of the non-linear inductance bestows the spectrum with anharmonicity that makes this possible. See figure 3.2.

The most common method of adding nonlinearity to a LC circuit is to add at least one Josephson junction by fabricating a superconductor-insulator-superconductor junction in which the insulator is a thin layer of oxide between two superconducting electrodes. Cooper pairs are able to coherently tunnel from one electrode to another. Thus,

current can flow though the junction without dissipation, and a difference in charge accumulates as a result. Different charge states can exist in coherent superpositions. This is the physical embodiment of the superconducting quantum bits that are the main actors in our laboratory.

The structure we have just described is known as the Cooper pair box. Coherent superpositions of charge states in superconducting circuits were first shown in 1998 (Bouchiat et al., 1998). Following this, a veritable zoo of superconducting artificial atoms were developed and studied. The different species are made by shunting the junction with different configurations of inductances and capacitances. Of theses species, the most straightforward to design and control is a "transmon" qubit (Koch et al., 2007; Schreier et al., 2008). Compared to other superconducing qubit species, the transmon enjoys particular robustness against noise sources. We focus on it here because of its simplicity and because it is the species of qubit that we will create in chapter 8.

To give a representative example: An $Al/AlO_x/Al$ junction with an area of 100 nm by 100 nm at the usual transparency has $L_J \approx 10$ nH and $C_J \approx 1$ fF. The self resonance of the junction is approximately 50 GHz, depending on the transparency. [1] A shunting capacitance of around 50 fF brings the resonance of the combined circuit to frequencies in the 5-10 GHz range. (A junction shunted by the "super-inductance" made of many smaller junctions forms a fluxonium (Manucharyan et al., 2009).)

In its simplest implementation, the transmon qubit consists of a single Josephson junction and a parallel capacitor to ground. The energy of this circuit is that of a harmonic oscillator plus a perturbation due to the Josephson effect depending on the junction phase ϕ. Prior to writing the Hamiltonian, let us define a Josephson energy,

$$E_J = \frac{I_c \Phi_0}{2\pi}, \tag{3.15}$$

---

[1]The transparency of the junction is the tunneling probability of Cooper pairs across the barrier, and it is directly proportional to the critical current density.

associated with the transfer of a single electron across the Josephson junction, and the charging energy,

$$E_C = \frac{e^2}{2C_\Sigma}, \tag{3.16}$$

(also called the Coulomb energy) associated with the addition of a single electron to the capacitance. With these definitions, the exact Cooper pair box Hamiltonian is written:

$$\hat{H} = 4E_C(\hat{n} - n_g)^2 - E_J \cos(\hat{\phi}), \tag{3.17}$$

where $\hat{n}$ is the integer number of Cooper pairs that have tunneled through the junction, and $n_g = -C_g V/2e$ is the "gate charge" or "offset charge", which is a continuous variable that represents some junction asymmetry that breaks the degeneracy between positive and negative charge transfers. It can be externally modulated by an applied electric field and is subject to fluctuations (intended or unintended).

Another valid approach is to write the same Hamiltonian in the basis of charge and flux, so that it can be easily compared with the LC circuit in equation 3.2. Using $\hat{\Phi} = \Phi_0 \hat{\phi}$, the Hamiltonian is then written

$$\hat{H} = \frac{1}{2C}\hat{Q}^2 - E_J \cos\left(\frac{2\pi\hat{\Phi}}{\Phi_0}\right). \tag{3.18}$$

These equations can be numerically solved to find the exact eigen-energies. In the lab, we create this device with a designed E_C and E_J set by our engineered physical parameters, including circuit geometry and Josephson junction transparency. In some regimes, however, the gate charge n_g can fluctuate beyond our control. This phenomenon is known as charge noise, and it causes dephasing through changes in the transition frequencies. Fortunately, we can reduce sensitivity to this charge noise by designing the circuit such that E_J/E_C is large (Koch et al., 2007; Schreier et al., 2008). To make this clear, we plot the first three energy levels as a function of gate charge several different values of E_J/E_C in

(a)

(b)

$I = I_0 \sin \dfrac{2\pi\hat{\Phi}}{\Phi_0}$

Current

Flux across junction $(\hat{\Phi})$

(c)

$E_J \cos\hat{\Phi}$

Energy

$\hbar\omega$

Flux across junction $(\hat{\Phi})$
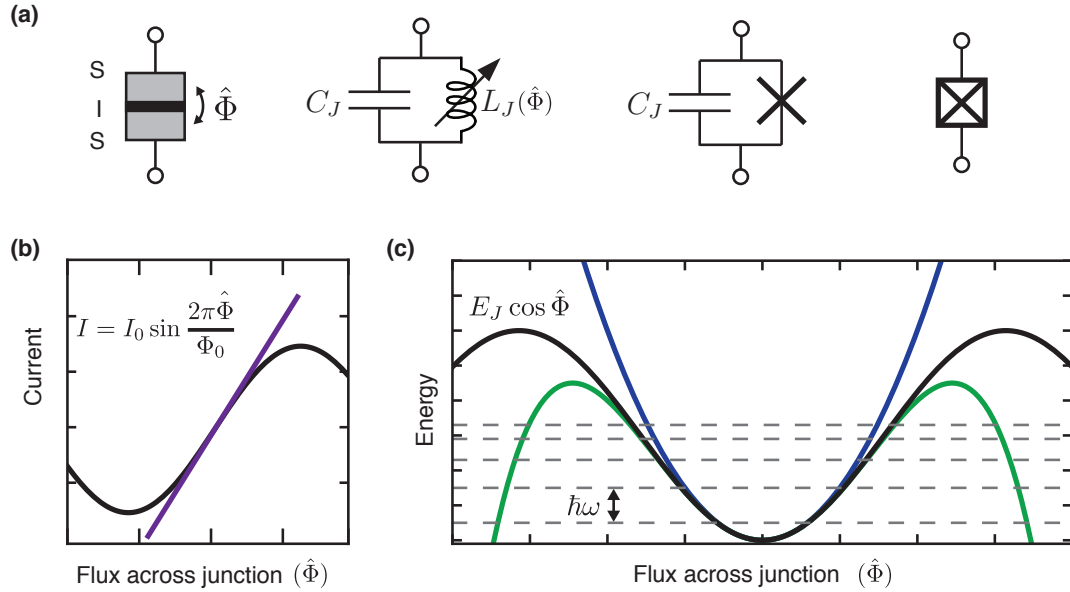
FIGURE 3.2: **Josephson junction as a circuit element.** **(a)** A Josephson junction is created by two superconducting electrodes separated by a thin insulating barrier. Embedded in a circuit, it behaves as an inductance that is nonlinear in flux. Here, we draw four equivalent representations of the Josephson junction as a circuit element. **(b)** The current-flux relationship of the Josephson effect is sinusoidal equation 3.14. To a first order approximation, we can ascribe a linear inductance of $L_J = \phi/I$ to the junction (purple line). **(c)** The energy spectrum of the junction is $E_J \cos\hat{\phi}$ (black curve). Successive approximations corresponding to terms in equation 3.20 are included (blue, green curves), along with the resulting anharmonic eigen-energy spectrum (dashed lines). (Figure adapted with permission from Reagor, 2015. See Copyright Permissions.)

figure 3.3.

It is evident that when E_J/E_C is large, the qubit approaches the behavior of a harmonic oscillator. For transmons, we plan to operate near this limit, where ϕ is small. Therefore, we can expand the cosine term about $\phi = 0$. To lowest order, we recover equation 3.2 directly from equation 3.18 above, with an effective inductance of the Josephson junction given by $L_J = (\frac{\hbar}{2e})^2/E_J$. The result is a simple harmonic oscillator with frequency given by $\hbar\omega_q = \sqrt{8E_J E_C}$. In the first order, there is no nonlinearity.

Next, we will further expand the cosine in the Josephson inductance of equation 3.14,

$$L_J = \frac{\Phi_0}{2\pi I_c \cos\phi} \approx \frac{\Phi_0}{2\pi I_0}\left[1 + \frac{\phi^2}{2} + \mathcal{O}(\phi^4)\right]. \tag{3.19}$$
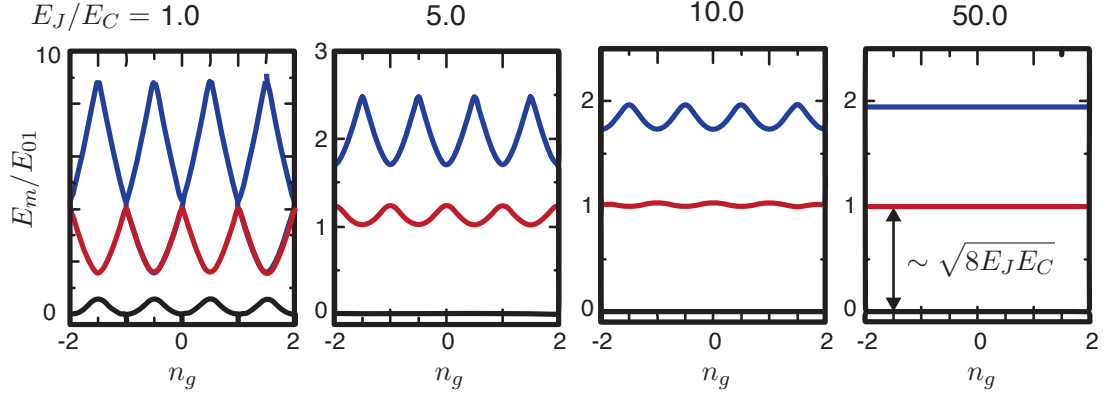
FIGURE 3.3: **Charge noise insensitvity in the transmon regime.** Eigenenergies (first three levels: E_0 in black, E_1 in red, and E_2 in blue) versus gate charge for several ratios of E_J/E_C. Anharmonicity is also reduced with increasing E_J/E_C; but this reduction is geometric whereas charge noise sensitivity is reduced exponentially. (Figure adapted with permission from Koch et al., 2007. See Copyright Permissions.)

Equivalently, the expansion in the Josephson term of the Hamiltonian above is written

$$\hat{H}_J = -E_J \cos \hat{\phi} \approx E_J \left[\frac{\hat{\phi}^2}{2} - \frac{\hat{\phi}^4}{4!} + \mathcal{O}(\hat{\phi}^6) \right]. \tag{3.20}$$

The first two orders of correction, accompanied by the resulting eigen-energy levels, are shown in figure 3.2**(c)**.

This approximation is accurate for $\phi \ll 1$, or equivalently in the flux basis, for $\bar{n}\Phi_{ZPF}/\Phi_0 \ll 1$. Recall from equation 3.7 that $\Phi_{ZPF} \propto \sqrt{Z_c}$. Therefore, a low impedance circuit has less flux noise which lends favorably to this approximation. On the other hand, the trade off is that the low impedance circuit has more charge noise than a higher impedance circuit. The consequences of this effect are evident in the sensitivities to gate charge fluctuations pointed out with the aid of figure 3.3.

Using this expansion (equation 3.20 to fourth order in ϕ), definition equation 3.8, and applying a rotating-wave approximation, the approximate transmon Hamiltonian is

$$\hat{H} = \hbar\omega_q'(\hat{a}^\dagger \hat{a} + 1/2) + \hbar\frac{\alpha}{2}\hat{a}^\dagger\hat{a}^\dagger\hat{a}\hat{a}. \tag{3.21}$$

We have thus renormalized the circuit to be an oscillator with a new frequency

$$\hbar\omega_q' = \sqrt{8E_JE_C} - E_C \tag{3.22}$$

and anharmonicity $\alpha = -E_C/\hbar$.

The transition frequency between the ground state and the first excited state differs from the transition frequency between the first and second excited states by an anharmonicity $\alpha = \omega_{01} - \omega_{12}$. In fact, this is most precisely what we mean by "anharmonicity", and it is this property that allows us to control the level transitions directly with incident microwave pulses. In the transmon limit, $E_J/E_C \approx 50 - 100$, and the anharmonicity is about $3 - 5$ percent of ω_q'. Therefore, we can design transmon qubits of frequencies 5-10 GHz with anharmonicities on the order of 100 MHz. With the resulting energy spectrum, it is possible to manipulate the system with pulses on the timescale of nanoseconds while remaining sufficiently selective to the desired transitions (Houck et al., 2009).

In particular, we wish to restrict operation to a logical subspace consisting of only the first two energy levels of the transmon. Let us thus relabel $\omega_q = \omega_q'$ from this section and rewrite the Hamiltonian as that of a two-level system with energy states $|g\rangle$ and $|e\rangle$:

$$\hat{H}_q = \hbar\omega_q|e\rangle\langle e|, \text{or} \tag{3.23}$$

$$\hat{H}_q = \frac{1}{2}\hbar\omega_q\hat{\sigma}_z. \tag{3.24}$$

Our approach is now readily applicable to the language of quantum information science introduced in chapter 2, and this Hamiltonian describes the "qubit" for the rest of this thesis.

3.4 Circuit QED

By coupling the qubit to a linear resonator, its state can be protected from radiative decay or decoherence from nearby dissipative sources.

In cQED, a system with one (two-level) qubit and one cavity is described by the *Jaynes-Cummings Hamiltonian* (Jaynes and Cummings, 1963):

$$\hat{H}_{JC} = \hbar\omega_c \left(\hat{a}^\dagger \hat{a} + \frac{1}{2} \right) + \frac{1}{2}\hbar\omega_q \hat{\sigma}_z + \hbar g \left(\hat{a}^\dagger \hat{\sigma}_- + \hat{a}\hat{\sigma}_+ \right), \tag{3.25}$$

where g is the interaction rate, and ω_c and ω_q are the cavity and qubit frequencies respectively. The last term represents a dipole interaction between the cavity and qubit. The expression contains the harmonic oscillator ladder operators, $\hat{a}$ and $\hat{a}^\dagger$, as well as operators $\hat{\sigma}_\pm = \hat{\sigma}_x \pm i\hat{\sigma}_y$ and $\hat{\sigma}_z$ that operate on the qubit state. This Hamiltonian is under a rotating wave approximation (RWA), meaning that terms that are counter-rotating (i.e. do not conserve energy) are deleted. [2] In this convenient form, it is a 2 x 2 block diagonal matrix whose eigenstates are

$$|n,+\rangle = \cos\theta_n |n-1, e\rangle + \sin\theta_n |n, g\rangle,$$
$$|n,-\rangle = -\sin\theta_n |n-1, e\rangle + \cos\theta_n |n, g\rangle, \tag{3.26}$$

where $\theta_n = \arctan 2g\sqrt{n}/\Delta$, which is the degree of hybridization of the qubit and cavity. The eigen-energies are $E_{n,\pm} = n\hbar\omega_c \pm \hbar\sqrt{4g^2 + \Delta^2}/2$ and the ground state $E_0 = -\hbar\Delta/2$, where $\Delta = \omega_q - \omega_c$ is the detuning between the qubit and the cavity.

On resonance, when $\Delta = 0$, the eigenstates are just the odd and even combinations of states $|n-1, e\rangle$ and $|n, g\rangle$. An excitation in this cQED system oscillates between these two states with a rate g. This is called a "vacuum-Rabi oscillation" and the g is a common measure of the strength of the interaction between the qubit and cavity degrees of freedom. In circuit QED, the interaction rate g can be hundreds of MHz, sufficient to perform

---

[2]Without taking the RWA, the interaction term is replaced by $\hbar g(\hat{a}^\dagger + \hat{a})\hat{\sigma}_x$.
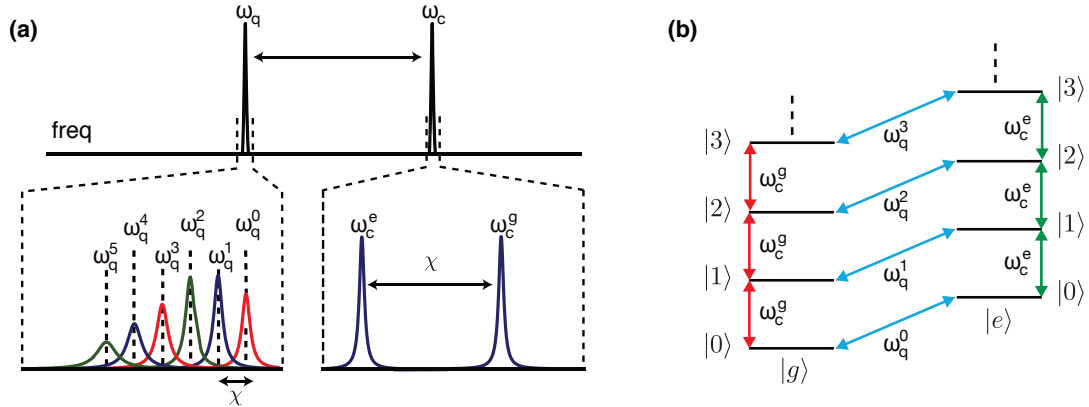
FIGURE 3.4: **Photon number splitting and energy level diagram.** **(a)** In the strong dispersive regime, the qubit and cavity are detuned and χ is large enough compared to the decay rates. The observed effect is photon number splitting of the qubit transition (left) and a cavity peak that depends on the state of the qubit (right). **(b)** The corresponding energy level diagram has the associated transition frequencies labeled. (Figure adapted with permission from Schuster et al., 2007. See Copyright Permissions.)

quantum operations in nanoseconds, but small enough that counter-rotating terms in the Hamiltonian can usually be ignored (RWA). We will discuss the control of this parameter in section 3.5.1.

The physics of the cavity-qubit interaction can take on different characters as the systems hybridize depending upon how close to resonance the two are. Altering the detuning *in-situ* during an experiment can be very useful. For this purpose, the classic transmon design includes two junctions in a gradiometric superconducting quantum interference device (SQUID) configuration. Applying a flux through the SQUID loop modulates the Josephson term of equation 3.25, changing the frequency of the qubit.

3.4.1 Strong dispersive regime

The purpose of cQED experiments is observe the effects of the coupling term and put them to use processing quantum information. In experimental devices, however, the desired effects can be obscured by photon decay at rate κ and qubit decoherence at rate γ. We will say more about the origins of these decay rates in section 5.2. For now, we state that it

is desirable to be able to engineer systems that are in a "strong coupling" regime, where $g \gg \gamma, \kappa$.

When the the coupling is strong and the qubit and cavity are far off resonance from one another ($\Delta = |\omega_c - \omega_q| \gg g$), we can recast equation 3.25 to the dispersive Hamiltonian:

$$\hat{H} = \hbar \left(\omega_r - \chi |e\rangle \langle e| \right) \hat{a}^\dagger \hat{a} + \hbar \omega_q |e\rangle \langle e| \tag{3.27}$$

where $\chi = g^2/2\Delta$. [3] We are in the limit $\chi \gg n\kappa, \gamma$ (where $n = \langle \hat{a}^\dagger \hat{a} \rangle$). Observe that the interaction term representing exchange of excitations in equation 3.25 is gone. Instead, the dispersive interaction produces a shift in cavity frequency that depends on the qubit state. Note that we can also write the dispersive Hamiltonian as

$$\hat{H} = \hbar \omega_r \hat{a}^\dagger \hat{a} + \hbar \left(\omega_q - \chi a^\dagger \hat{a} \right) |e\rangle \langle e|, \tag{3.28}$$

where we have simply regrouped the terms to observe a shift in the original qubit frequency that depends on the number of photons in the cavity. If there is a superposition of photon number states in the cavity, the qubit transition will spit into several peaks separated by χ – a phenomenon we call "number splitting". The consequences of the dispersive interaction are shown schematically in figure 3.4.

As a result of this hybridization, the eigenstates take on a "dressed" form. For instance, the one-excitation dressed states are written

$$|-, 0\rangle \sim -\frac{g}{\Delta} |e, 0\rangle + |g, 1\rangle$$
$$|+, 0\rangle \sim |e, 0\rangle + \frac{g}{\Delta} |g, 1\rangle. \tag{3.29}$$

The fact that the cavity frequency depends on the qubit state is used for non-destructive readout of the qubit state, as described in the next section. In addition, this dispersive

---

[3] This definition for χ is consistent with current notation in the lab, but note that it is different by a factor of 2 from Schuster, 2007. Do not be confused.

interaction can source qubit-cavity entangling operations by making it possible for us to perform qubit gates that are selective on the state of photons in the cavity. Some of these operations can be seen in action in chapter 8 and are described more thoroughly in other publications (Vlastakis et al., 2013).

3.4.2 Qubit readout

The dispersive readout mechanism is described in figure 3.5 and caption. I note that qubit readout can also be achieved through a different mechanism that we call the "Jaynes-Cummings readout", or "high power readout" (Reed et al., 2010; Boissonneault, Gambetta, and Blais, 2010, and Reed, 2013–chapter 6).

3.4.3 Multimode generalization

To describe the physics of current experiments, we need to expand upon the ideas introduced here. To this end, we write a generalized multimode Hamiltonian to fourth order in ϕ and with RWA applied:

$$\hat{H}_{(4)} = \sum_i \hbar\omega_i \hat{a}_i^\dagger \hat{a}_i - \sum_{i \neq j} \hbar\chi_{ij} \hat{a}_i^\dagger \hat{a}_i \hat{a}_j^\dagger \hat{a}_j - \sum_i \frac{\hbar}{2}\alpha_i \hat{a}_i^{\dagger 2} \hat{a}_i^2. \tag{3.30}$$

All modes i in the Hamiltonian have an anharmonicity, α_i, also called self-Kerr, weighted by their participation to the junction phase, as well as a state-dependent shift caused by all the other modes, χ_{ij}, also called the cross-Kerr. The actual system has higher order terms that are sometimes important, but they are not explicitly important in the scope of this thesis.

3.4.4 Black-box quantization analysis

A very effective method for analyzing cQED systems is *black-box quantization* (BBQ) (Nigg et al., 2012). This technique successfully describes the spectrum of all the early transmon
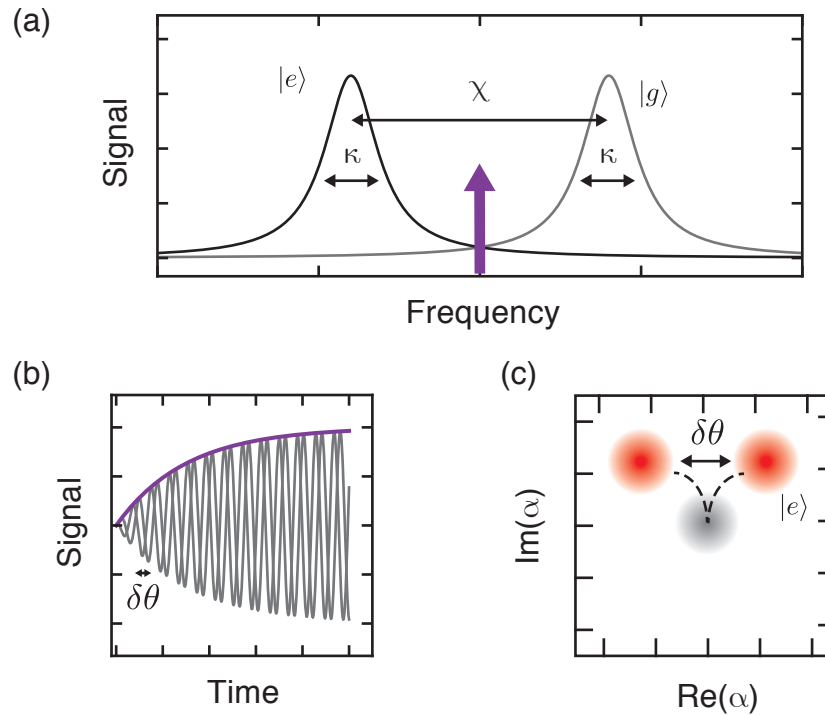
FIGURE 3.5: **Dispersive readout of qubit state. (a)** The frequency of the readout resonator depends on the state of the transmon qubit from which it is detuned. In the strong dispersive regime, the frequency shift χ is greater than the linewidth of the cavity mode, κ, allowing for clear discrimination in spectroscopy. **(b)** A readout pulse at the bare cavity frequency ($\omega_c/2\pi \approx 5 - 10$ GHz, purple arrow in(a)) adds energy to the resonator which then exits through a measurement chain, where it is demodulated to $\sim$20 MHz, digitized, and analyzed by digital demodulation to extract an amplitude and phase (or real and imaginary) profile over time. The envelope of the ring-up is the same regardless of the qubit state, while the phase is different. **(c)** Many iterations of measurement results are histogrammed to reveal the probabilities that the qubit was in $|g\rangle$ or $|e\rangle$ at the time of the readout pulse. Larger $\delta\theta$ enables greater readout contrast. (Figure used with permission from Reagor, 2015. See Copyright Permissions.)

designs and promises application in more diverse multi-qubit-multi-cavity systems. In essence, the analysis involves decomposition of the Josephson junction into a linear and nonlinear part followed by network theory using the junction electrodes as a port. In the next section we will ask, "what is V_ext as seen from the junction?" in order to calculate the dipole interaction strength g. However complicated the rest of the environment, this question is answered if we know the frequency-dependent impedance, $Z(\omega)$, of the exterior environment from the perspective of the junction electrodes. Figure 3.6 makes this viewpoint explicit. In fact, any linear circuit or electromagnetic environment can be transformed to this model with some $Z(\omega)$.

First, we make the approximation that all of the circuit except for the junction non-linearity is treated as a Foster network. [4] That is, the nonlinearity of each mode that arises from hybridization with the Josephson junction is assumed to be a small perturbation to the linear behavior. Under this approximation that the external circuit is linear, non-dissipative ($Z = iX$), and passive, this otherwise mysterious black-box network can be transformed into one of Foster's forms, as in figure 3.6**(b)**. This transformation can go to either a series concatenation of parallel LC resonators (Foster's first form) or a parallel concatenation of series LC resonators (Foster's second form). Either way, the mapping corresponds to a diagonalization of the linearized system of coupled harmonic oscillators. The modes in these Foster networks, represented by individual LC resonators, are uncoupled or independent. Also, the poles and zeros of $Z(\omega)$ completely specify the frequency characteristics of the Foster network. Specifically, the resonance frequencies are given by the real parts of the poles of Z (or the real parts of the zeros of $Y = 1/Z$).

$$Y(\omega) = 1/Z(\omega) = \sum_i \frac{c_i \omega}{\omega_i^2 - \omega^2}, \tag{3.31}$$

with resonances $\omega_i = 1/\sqrt{L_i C_i}$.

---

[4]In our standard approach, the linear inductance L_J is assumed to be part of the environmental circuit as well.

In practice, $Z(\omega)$ can be obtained by analytical circuit analysis or through finite-element simulations. Then, since each mode is independent, Kirchhoff's laws tell us that V_{ext} as seen from the junction is the vector sum of the voltage across the excited modes of the Foster equivalent circuit. $V_{\text{ext}} = d\phi/dt$ for each, so phase contribution from each mode adds as to a total

$$\phi = \sum_i \phi_i = \sum_i \sqrt{\frac{\hbar}{2\text{Im}\left[Y'(\omega_i)\right]}}, \tag{3.32}$$

where $Y'(\omega_i)$, the slope of the admittance at its zero-crossing, appears.

In fact, all Hamilitonian parameters can be extracted knowing L_j as well as ω_i and $Y'(\omega_i)$ for all relevant modes. With these as input parameters, we use QuTIP (Johansson, Nation, and Nori, 2013) to diagonalize the full Hamiltonian to obtain anharmonicities and interaction terms.

Small losses are incorporated in this approach by decomposing the circuit into RLC circuits instead of LC circuits. In this case, the quality factor of the i-th mode is given by

$$Q_i = \frac{\omega_i}{2} \frac{\text{Im}\left[Y'(\omega_i)\right]}{\text{Re}\left[Y(\omega_i)\right]} \tag{3.33}$$

with corresponding lifetime $T_i = Q_i/\omega_i$.

See Nigg et al., 2012 for a more thorough discussion of BBQ quantization, including multi-qubit formalism.
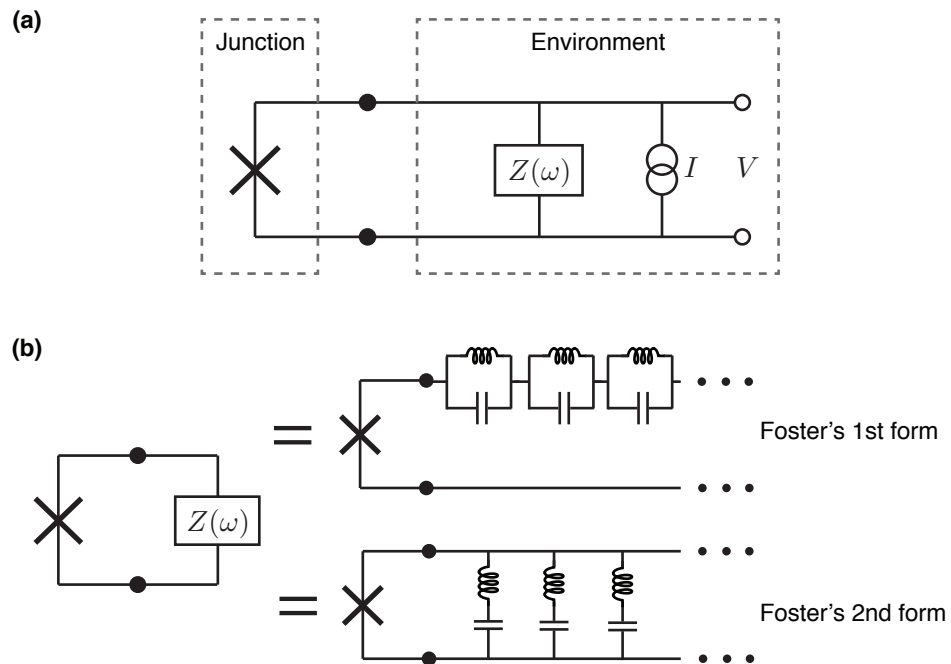
FIGURE 3.6: **Blackbox circuit quantization.** **(a)** A junction's electromagnetic environment can be represented as a complex frequency dependent impedance in parallel with a current source. **(b)** If the environment is assumed to be linear, non-dissipative, and passive, it can be transformed into an equivalent Foster circuit for network analysis. In either of Foster's forms, the constituent LC resonators are independent from one another.

3.5 Experimental implementations

Many cQED experiments in labs around the world have been realized in the last 15 years. Experiments have investigated several variations of qubit species, as well as variations in the structure of the resonator. Furthermore, many are true quantum information processing devices that are composed of multiple qubits and multiple resonators of various types between which the interactions are artfully tailored. In this section, we look at the coupling mechanism behind the interaction of a single transmon qubit and electromagnetic resonator.

3.5.1 Engineered interaction

The first prevalent cQED implementation was that of a qubit strongly coupled to a coplanar waveguide (CPW) transmission line resonator. The CPW transmission line resonator is drawn with its circuit equivalent in figure 3.7. We are interested in creating an overlap of the fields of a qubit mode to those of a standing wave mode of this transmission line. Intuitively, this is achieved by placing the qubit in a region where the voltage oscillation of the resonator mode forces a charge oscillation across the Josephson Junction.

In this section, we will understand how this manifests as the interaction term $\hbar g(\hat{a}\sigma_+ + \hat{a}^\dagger\sigma_-)$. We recognize g as the dipole matrix element for a single quantum of excitation being traded between the qubit and the photon mode.

To know the strength of the interaction g, we will be interested in the voltage or current corresponding to an exchange of one excitation, for instance the loss of one photon from the resonator. From equation 3.7 and equation 3.6 we can write these matrix elements for the charge and flux:

$$\langle g|\hat{\Phi}|e\rangle = \sqrt{\frac{\hbar Z_c}{2}}, \text{and} \tag{3.34}$$

$$\langle g|\hat{Q}|e\rangle = \sqrt{\frac{\hbar}{2Z_c}}. \tag{3.35}$$

These equations express the flux and charge difference between the ground state and the first excited state in the circuit, in terms of the circuit's characteristic impedance. The associated differences in the voltage and current are then simply

$$\langle g|\hat{V}|e\rangle = \langle g|\omega_c\hat{\Phi}|e\rangle = \omega_c\sqrt{\frac{\hbar Z_c}{2}}, \text{and} \tag{3.36}$$

$$\langle g|\hat{I}|e\rangle = \langle g|\omega_c\hat{Q}|e\rangle = \omega_c\sqrt{\frac{\hbar}{2Z_c}}. \tag{3.37}$$

But it will be enlightening to write this in a form that includes the fine structure constant, α as done in Devoret, Girvin, and Schoelkopf, 2007. To do this, we incorporate $\alpha = Z_0 e^2/2h$, where Z_0 is the impedance of free space (or the "vacuum impedance"), given by $Z_0 = \sqrt{\mu_0/\epsilon_0}$. We arrive at the expressions:

$$\langle g|\hat{V}|e\rangle = \sqrt{\frac{1}{8\pi}}\frac{h\omega_c}{e}\sqrt{\frac{Z_c}{Z_0}}\alpha^{1/2}, \text{and} \tag{3.38}$$

$$\langle g|\hat{I}|e\rangle = \sqrt{\frac{1}{8\pi}}e\omega_c\sqrt{\frac{Z_0}{Z_c}}\alpha^{-1/2}. \tag{3.39}$$

Meanwhile, the coupling between a (two-level system) qubit and external circuit can be written as

$$\hat{H}_c = -2e\hat{N}\cdot\hat{V}_{\text{ext}}, \tag{3.40}$$

where $\hat{V}_{\text{ext}} = \hat{Q}_{\text{ext}}/C_J$ is the voltage established by an external charge $\hat{Q}_{\text{ext}}$ on the junction capacitance C_J. By comparison with an atomic interaction of form $H_c = -\vec{p}\cdot\vec{E}(\vec{x})$, we identify $2e\hat{N}$ with the dipole moment of the qubit, for which

$$\langle g|2e\hat{N}|e\rangle = \left(\frac{2E_J}{E_C}\right)^{\frac{1}{4}}e. \tag{3.41}$$

We will consider incorporating the qubit with the transmission-line resonator in two different configurations: Either placing the qubit in the gap between the central conductor
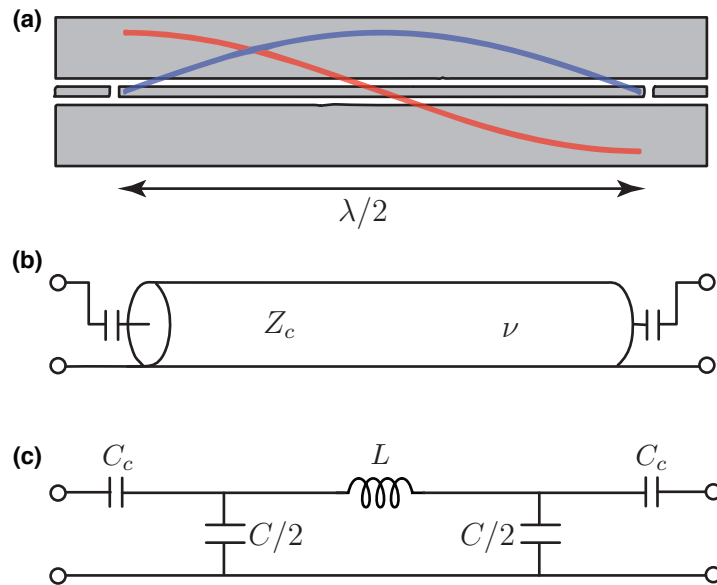
FIGURE 3.7: **Transmission line resonator.** **(a)** Coplanar waveguide (CPW) transmission line res-
onator viewed from the top. Grey areas are superconducting films. Colored curves represent the
spacial variation in voltage (red) and current (blue) profiles over the length of the resonator pertain-
ing to the first (fundamental) standing wave mode. This is a $\lambda/2$ resonance. **(b)** Circuit schematic
of the transmission line resonator. The capacitors are analogous to the mirrors of a Fabry-Perot
resonator. The section of transmission line has characteristic impedance Z_c and a propagation ve-
locity ν. **(c)** Lumped element model of a resonator corresponding to the $\lambda/2 = \pi\nu/\omega_c$ resonance.
The cavity "mirrors" are the coupling capacitors, C_c.

and the ground plane, as shown in figure 3.8**(a)**, or placing the qubit "in-line" with the central conductor of the resonator, as shown in figure 3.8**(b)**. Qubits are typically fabricated to have dimensions that are much smaller than a wavelength. Therefore, it is possible to make use of lumped-element approximations to evaluate Hamiltonian parameters. Typically, a capacitance network is suitable. In the following analysis we work on resonance, with $\omega = \omega_c = \omega_q$, to work out a dimensionless coupling factor g/ω.

Parallel qubit-resonator coupling.

The first scheme, diagrammed in figure 3.8**(a)**, makes use of a field maximum at the end of the resonator to drive current across the junction. The coupling of the qubit to the resonator is modulated by the capacitance to ground, C_g. Specifically, it is a voltage division:

$$\langle g|\hat{V}_{\text{ext}}|e\rangle = \frac{C_g}{C_g + C_J}\langle g|\hat{V}|e\rangle. \tag{3.42}$$

By combining this with equation 3.40, equation 3.41, and equation 3.38, we arrive at the dimensionless coupling constant

$$\frac{g_\perp}{\omega} = \sqrt{\frac{1}{2\pi^3}}\frac{C_g}{C_g + C_J}\left(\frac{2E_J}{E_C}\right)^{\frac{1}{4}}\sqrt{\frac{Z_c}{Z_0}}\alpha^{1/2}. \tag{3.43}$$

These parameters are under the control of the circuit designer, with some of the other consequences regarding the anharmonicity and sensitivity to noise having been mentioned earlier in this chapter.

In the case of small E_J/E_C (Cooper Pair Box), this finding is written more compactly as

$$\frac{g_\perp}{\omega} = \frac{e\beta V_0}{\hbar\omega} = \beta\sqrt{\frac{Z_c e^2}{2\hbar}}, \tag{3.44}$$

where $V_0 = \sqrt{\hbar\omega/2C}$ is the root-mean-square voltage due to vacuum fluctuations in the circuit, [5] and $\beta = C_g/(C_g + C_J)$ describes the voltage division (Schuster, 2007).

---

[5] The RMS vacuum voltage fluctuation comes from solving $\frac{1}{2}\frac{1}{2}\hbar\omega = \frac{1}{2}CV_0^2$

The situation in this coupling scheme is similar to that of an atom in an optical cavity of cavity QED. However, atoms are small, and there is great flexibility advantage in circuit design. Another way to look at this same coupling scheme is in terms of the qubit's dipole coupling to the electric field fluctuations in a cavity of volume V (Schoelkopf and Girvin, 2008). Consider the resonator as a section of transmission line, as pictured in figure 3.7**(b)**. Imagine it has radius r, in which case the entire mode volume is $V = \pi r^2 \lambda/2$. For the quantum harmonic oscillator ground state, we would write

$$\frac{\hbar\omega}{4} = \frac{\epsilon_0}{2} \int E^2 dV = \frac{\epsilon_0}{2} E_0^2 V, \tag{3.45}$$

were E_0 is the root-mean-square electric field at the location of the atom due to vacuum fluctuations. Plugging in the mode volume and substituting for $\lambda = 2\pi c/\omega$, where c is the speed of light,

$$E_0 = \frac{1}{r} \sqrt{\frac{\hbar\omega^2}{2\pi^2 \epsilon_0 c}}. \tag{3.46}$$

Now, the vacuum Rabi frequency is given by energy $\hbar g = dE_0$. Let the dipole moment $|\vec{p}| = eL$ in the direction of the electric field fluctuations, with e being the electron charge and L indicating the size of the qubit. Following this, we can write the dimensionless coupling constant in terms of the relevant length scales:

$$\frac{g}{\omega} = \frac{L}{r} \sqrt{\frac{e^2}{2\pi^2 \epsilon_0 \hbar c}} = \frac{L}{r} \sqrt{\frac{2\alpha}{\pi}}. \tag{3.47}$$

Note the appearance of α, just as in equation 3.43. In the circuit QED case, it is possible that $V \ll \lambda^3$ and $L/r \to 1$. In contrast, the cavities employed for cavity QED have larger mode volumes and the real atoms have smaller dipole moments. In practice, cQED circuits are commonly designed to have $g/\omega \sim 10^{-2}$. This is much stronger than the cavity QED analog of an atom in an optical trap, for which typical couplings are $g/\omega \sim 10^{-6}$.

Series ("in-line") qubit-resonator coupling.
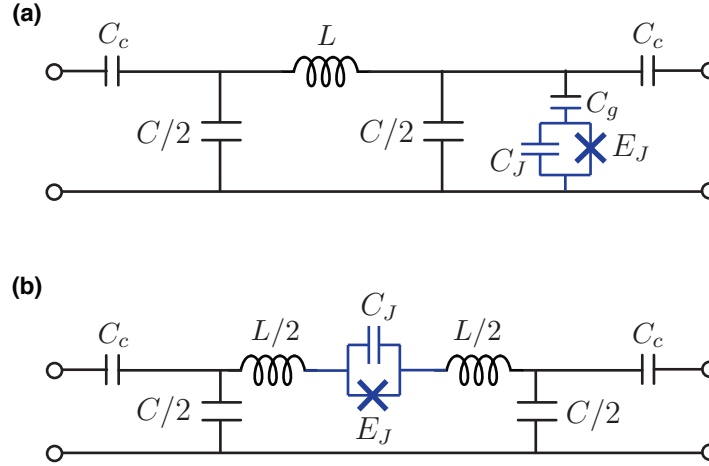
FIGURE 3.8: **Circuit schematics of two different schemes for coupling a Josephson junction qubit to a cavity resonator.** **(a)** The junction is placed in the insulating gap of the transmission line and couples via its voltage oscillations. **(b)** The junction is embedded in the central conductor of the transmission line and is coupled to its current oscillations. (Figure adapted with permission from Devoret, Girvin, and Schoelkopf, 2007. See Copyright Permissions.)

The second scheme, diagrammed in figure 3.8**(b)**, involves placing the qubit directly in the path of the center conductor. Though this "in-line" configuration is not the one used for most current experiments in our lab, we address it here to demonstrate the remarkable interaction strength that can be achieved in cQED. Here, the qubit couples directly to the charge of the resonator, meaning $V_{\text{ext}} = \hat{Q}/C_J$. By combining this with equation 3.40, equation 3.41, and equation 3.39, we arrive at the dimensionless coupling constant

$$\frac{g_{\parallel}}{\omega} = \frac{1}{8\pi} \left(\frac{E_C}{2E_J} \right)^{\frac{1}{4}} \sqrt{\frac{Z_0}{Z_c}} \alpha^{-1/2} \tag{3.48}$$

The coupling in this configuration can be extremely strong, as we have emphasized by writing it in this way, finding a negative power of $\alpha = 1/137$. Also, note that $\sqrt{Z_0/Z_c} > 1$. Taking for example, values of $E_C/2E_J = 100$ and $Z_c = 50 \ \Omega$, the dimensionless coupling rate is ≈ 20. This falls into the "ultra-strong" coupling regime (Ciuti and Carusotto, 2006; Bourassa et al., 2009) where RWA does not apply.

3.5.2   3D Cavity cQED

The same cQED-enabled physics that we have been discussing can be harnessed when the transmission line resonator is replaced with a 3D cavity resonator. Incorporation of a transmon qubit and a rectangular 3D cavity in a strong dispersive regime resulted in major gains in coherence times (Paik et al., 2011). Not surprisingly, 3D cavities immediately became very popular in the growing community of cQED experimenters. The most basic type of 3D cavity is a rectangular waveguide cavity, but other geometries are proving useful in cQED as well (Reagor et al., 2016).

The dimensions of a rectangular cavity determine the spectrum of resonant modes. The transmon is fabricated on a substrate, which is cut to size and placed with carefully chosen orientation in the cavity. An SMA connector delivers and receives signals from the internal cavity and qubit modes. The effective mode volume of 3D cavity resonators is greatly increased compared to "planar" transmission line cavities (figure 3.7) or compact resonators (Geerlings et al., 2012) of the same frequency. The most striking advantage to this approach is that a 3D cavity has a longer lifetime T_1, or a larger quality factor $Q = \omega_c T_1$, than a small planar circuit made of the same materials. This is due to reduced participation ratios in lossy materials. (We will discuss this further in section 5.2.) We also note that the larger mode volume necessitates a larger qubit extent in order to achieve a sufficiently high dipole coupling rate $g \sim 100$s MHz.

The 3D transmon has longer coherence times ($T_1 \sim T_2 \sim 100~\mu s$) than "planar" superconducting qubits, and we identify several reasons leading to this. First, the larger dimensions of the 3D qubit have the beneficial effect of lowering dielectric participation ratios (more in section 5.2.4). Second, radiation losses (section 5.2.2) for the 3D qubit are small and simple to calculate because the qubit is completely encapsulated in the cavity. Housing the qubit in vacuum surrounded by perfect superconducting cavity walls is impeccable microwave isolation. Compare this "clean" RF environment to that of a planar qubit, which may have stray capacitance coupling it to nearby parts of the circuit, wirebonds,

PCB, epoxy, or box modes of the experimental package. Additionally, in experimental scenarios in which the qubit lifetime is "Purcell-limited" (see section 8.6.1), the coupling of a qubit to a cavity with a higher Q will enhance the lifetime of the qubit.

Now that we have discussed some advantages, let us consider two analytical approaches to calculating g for qubits encapsulated in 3D cavities. Note that the 3D transmon of Paik et al., 2011 is essentially an antenna in a box. Electrodes on either side of the Josephson junction build up a potential V_{ext} manifested from dipole coupling to the surrounding electromagnetic mode of the cavity.

An oscillating electric dipole $\vec{p}$ radiates power (Jackson, 1998)

$$\langle P \rangle = \frac{\mu_0 |\vec{p}|^2 \omega^4}{12\pi c} \tag{3.49}$$

where we indicate with angle brackets that this is a time-averaged quantity. For this rough calculation, we will estimate that the dipole moment is $|\vec{p}| = eL$, where e is the electron charge and L is the length of the qubit antenna. The radiated power obeys $\langle P \rangle = \Gamma \hbar \omega$, where Γ is the radiative decay rate of the transition. Fermi's Golden Rule tells us that the decay rate to a continuum of states is $\Gamma = g^2/\omega$. Putting it all together and simplifying to arrive at an expression in terms of the fine structure constant α:

$$\begin{aligned}
g &= \sqrt{\omega \Gamma} \\
&= \sqrt{\frac{\mu_0 |\vec{p}|^2 \omega^4}{6hc}} \\
&= \sqrt{\frac{\mu_0 e^2 L^2 \omega^4}{6hc}} \\
&= \sqrt{\frac{2\pi^2 \mu_0 e^2 L^2 \omega^2}{3\sqrt{\epsilon_0 \mu_0} h \lambda^2}} \\
&= \frac{2\pi \omega L}{\lambda} \sqrt{\frac{1}{3} \frac{e^2}{2h} \sqrt{\mu_0 \epsilon_0}} \\
&= \frac{2\pi \omega L}{\lambda} \sqrt{\frac{\alpha}{3}}.
\end{aligned} \tag{3.50}$$

(We have used $\omega/2\pi = c/\lambda$ and $c = 1/\sqrt{\epsilon_0\mu_0}$ as well as the definition of $\boldsymbol{\alpha}$.) We find that the dimensionless coupling constant has the same form as equation 3.43:

$$\frac{g}{\omega} \sim \frac{L}{\lambda}\boldsymbol{\alpha}^{1/2}. \tag{3.51}$$

Indeed, 3D cavities can couple to qubits inside with the same order of magnitude as transmission line resonators, and the coupling strength can be modified by adjusting L/λ.

We can also describe the 3D cavity-qubit coupling with an equivalent circuit. The layout is straightforwardly mapped to a circuit like that of figure 3.8**(a)**. Just as we found in the last section, there is a voltage division

$$\langle g|\hat{V}_{\text{ext}}|e\rangle = \beta\langle g|\hat{V}|e\rangle \tag{3.52}$$

where we now generalize $\beta = C_g/C_\Sigma$ for the voltage division, where C_Σ is the total capacitance, which you will recall is related to the charging energy as $E_C = e^2/2C_\Sigma$. The coupling constant is then given exactly by equation 3.44. The capacitances are modified by shaping of the antenna electrodes as well as the surrounding cavity geometry, and adjusting the location of the qubit with respect to the cavity mode. In order to calculate the relevant capacitances in practice, electrostatic simulations and/or electromagnetic mode simulations are conducted in addition to an analytical approach.

3.6 A dynamic toolbox

Now the reader can appreciate that several characteristics of cQED are encouraging for its prospects in quantum computation. Though we have not discussed the other physical implementations at length, we experimentalists enjoy that cQED manipulations and measurements are done with all electronic control using off-the-shelf microwave generators and coaxial cables. As we have shown in this chapter, strong coupling between the

qubit and cavity is readily accessible. This is dissimilar to atomic qubits, for example. Furthermore, the field has sustained exponential growth in qubit coherence times as a result of improvements in design and materials. Therefore, cQED is an attractive platform for exploring quantum control of photons in the microwave realm.

One can probably imagine that the flexibility of circuit design affords the cQED experimentalist with a wide range of potential quantum systems, some of which are viable for application in quantum information processing. Countless variations on the coupling schemes laid out in figure 3.8 are possible, and can be modeled by the addition of inductors and capacitors in additional circuit branches. Multiple qubits and multiple cavities are combined in increasingly complex networks.

We make another observation about transmons that sets them apart from other physical implementations listed in section 2.2. These quantum objects are mesoscopic in nature, composed of many millions of atoms. Yet, as we have discussed in this chapter, they are definitively quantum. First, they possess discrete energy levels. Second, they can exist in superpositions of their eigenstates. Third, they undergo transitions between their eigenstates accompanied by absorption or emission of electromagnetic energy. As a consequence, they interact with harmonic oscillator modes with completely analogous physics to that of atoms in optical cavities in cavity QED. For this reason, we can fondly call superconducting qubits "atoms with wires", and they are truly engineerable quantum systems.

Chapter 4

Multilayer microwave integrated quantum circuits

4.1 Scalability

4.1.1 Introduction

In 1965, when state-of-the-art integrated circuits had only ten components, Gordon Moore made a now-famous prediction: the number of transistors on a production integrated circuit would double every two years (Moore, 1965). This has held true to present times, enabled and accompanied by astounding technological achievements.

Quantum circuits are a comparatively nascent, but nevertheless extremely lively subject of research and development. Rather than observing a steady increase in the number of components, we presently see a healthy rise in qubit lifetimes. Amazingly, the relevant lifetimes achieved in experiments have increased exponentially since the superconducting qubit's inception over 15 years ago. This is a trend that we like to refer to as "Schoelkopf's law" (figure 4.1). It is unknown how long this trend can persist. Research will doubtless continue with the aim of reducing materials' dissipation effects on qubits. In addition, for every incremental gain in coherence times, it becomes increasingly important to develop

scalable hardware schemes that are suitable for such delicate systems. This is the motivation for much of the work in this thesis.
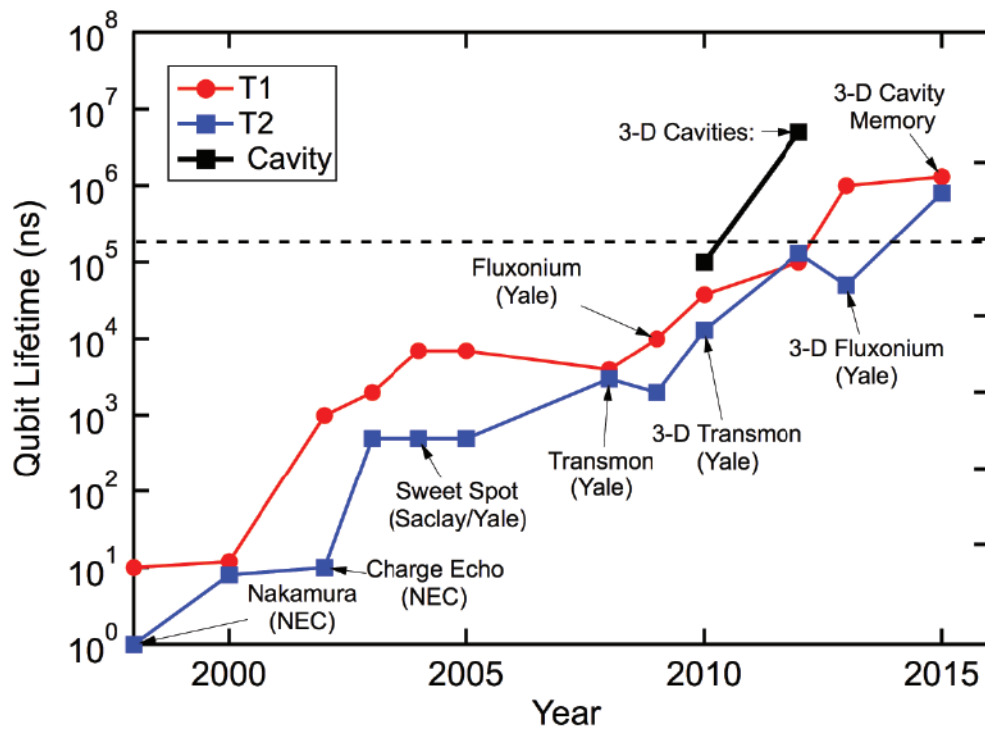
FIGURE 4.1: **Schoelkopf's Law for the coherence times of superconducting circuits.** The coherence of state-of-the-art superconducting quantum circuits has doubled approximately every nine months. (Reproduced from (Devoret and Schoelkopf, 2013), updated in (Reagor, 2015).)

Superconducting quantum circuits share several important advantages with classical computing architectures: For one, devices are created in the solid state and their properties can be fully engineered through circuit design and mass produced by lithographic fabrication. Further, electromagnetically coupling qubits to superconducting transmission lines enables communication of quantum information, rapid multi-qubit gates, and entangling operations between elements on or off the chip (Barends et al., 2014; Reed et al., 2012; Roch et al., 2014; Majer et al., 2007; Steffen et al., 2013; Loo et al., 2013). Finally, electronic control and measurement are achieved through microwave signals carried to and from the device by wires and cables. In addition to this high capacity for quantum electrical engineering, the lifetimes of quantum states in such systems have continually risen due to improvements in design and selection of high quality materials. As a consequence, superconducting circuits fulfill many of the necessary requirements for universal quantum computation, as evidenced by recent experimental realizations of a large suite of desired building blocks (Divincenzo, 2000; Ladd et al., 2010; Perez-Delgado and Kok, 2011).

In general, scaling up quantum information devices will require connecting orders of magnitude more circuit elements than today's experimental devices without sacrificing coherence. In particular, building a fully functional, fault-tolerant quantum computer requires error rates to remain below the threshold for quantum error correction (Gottesman, 2010; Knill, 2005). At the same time, the different components must retain the ability to selectively interact with each other while being externally addressed and accurately controlled. Finally, they must be mass producible in a reliable and precise manner. These criteria cannot be achieved by simply replicating and connecting currently available cQED hardware.

4.1.2 Challenges in scaling cQED circuits

Superconducting quantum circuits are presented with crucial challenges that prevent a scaling strategy similar to that of classical integrated circuits. The strong electromagnetic

interactions of the qubits allow for efficient entanglement and control, but make them also especially susceptible to undesired couplings that degrade quantum information. This "cross-talk" results in either undesirable mixing of quantum states or decoherence. High isolation to prevent these effects is especially important as long-lived qubits ($Q \approx 10^6 - 10^9$; 10 kHz – 10 Hz) must also be coupled to high-speed (10 MHz – 1 GHz) elements for read-out, control, and feedback. Various strategies are employed in complex superconducting circuits, including large scale detector arrays, to mitigate cross-talk (Noroozian et al., 2012; Audley et al., 2004; Zmuidzinas, 2012; Wenner et al., 2011b; Chen et al., 2014; Vesterinen et al., 2014; Bunyk et al., 2014; Lee and Lee, 1998). On a small scale, these unintended couplings can be minimized by spectral and/or spatial separation among elements on a single chip. However, with increasing number of elements, the former approach faces an increasingly crowded spectrum. The latter becomes ineffective when the device package grows in size and consequently supports unintended electromagnetic modes that can mediate detrimental couplings between elements. These effects become more problematic as circuits must move beyond tens of qubits, requiring chips greater than a wavelength ($\sim$cm) in size.

Increasing complexity and computation power of a quantum computer is unlikely to be achieved by miniaturization of its constituent elements. Most of the superconducting circuit elements in devices to date have dimensions of 3-30 mm, which is approximately the wavelength of microwave light they contain. It is also understood that increasing the density of elements through simple miniaturization is subject to a trade-off between size and coherence due to dissipative materials. This trade-off has been established in super-conducting resonators and qubits, where larger features provide a reduced sensitivity to surface losses (Wenner et al., 2011a; Geerlings et al., 2012; Reagor et al., 2013; Wang et al., 2015). Moore even pointed out in his predictions about the scaling up of classical circuits that larger volumes are accompanied by a coherence advantage: While considering large-value capacitors and inductors in linear circuits, Moore says, "By their very nature, such

elements require the storage of energy in a volume. For high Q it is necessary that the volume be large..." (Moore, 1965).

With coherence being *the* critical attribute to maintain, we conclude that miniaturization is a lower priority. Simply miniaturizing existing elements in order to achieve higher density is both unnecessary and detrimental to coherence, thereby requiring even more qubits in an error-correction overhead. The hardware platform for quantum circuits must instead literally be *scaled up*, implying that the physical size of a quantum computer will increase with the number of qubits it contains. The parts which are not coherence-critical, however, ought to be miniaturized: control wiring, connectors, and packaging.

Scaling up quantum circuits also encounters a challenge in connectivity. A large number of qubits and resonators have to be selectively coupled to each other with very low loss. This requires more internal connections between circuit elements than can be achieved in a single plane, demanding signal crossovers that are generally hard to implement with high isolation (Chen et al., 2014; Jeffrey et al., 2014). Even in planar architectures that only require nearest-neighbor coupling, such as the surface code (Fowler et al., 2012), additional connections are needed for measurement and control purposes. As a result, development towards low-loss three-dimensional connections has emerged as a pressing need. A superconducting quantum computer will also require a scalable input/output interface that provides external connections with much higher density and isolation than techniques that are presently employed, such as wire bonding.

Therefore, the outstanding task is to design a hardware platform that allows large number of quantum components to couple through intended and controllable channels, while suppressing any other interactions. In addition, crucial properties of the quantum circuit, such as qubit and resonator frequencies, anharmonicities, and mutual interaction strengths must be more predictable and reproducible than what has been necessary to date.
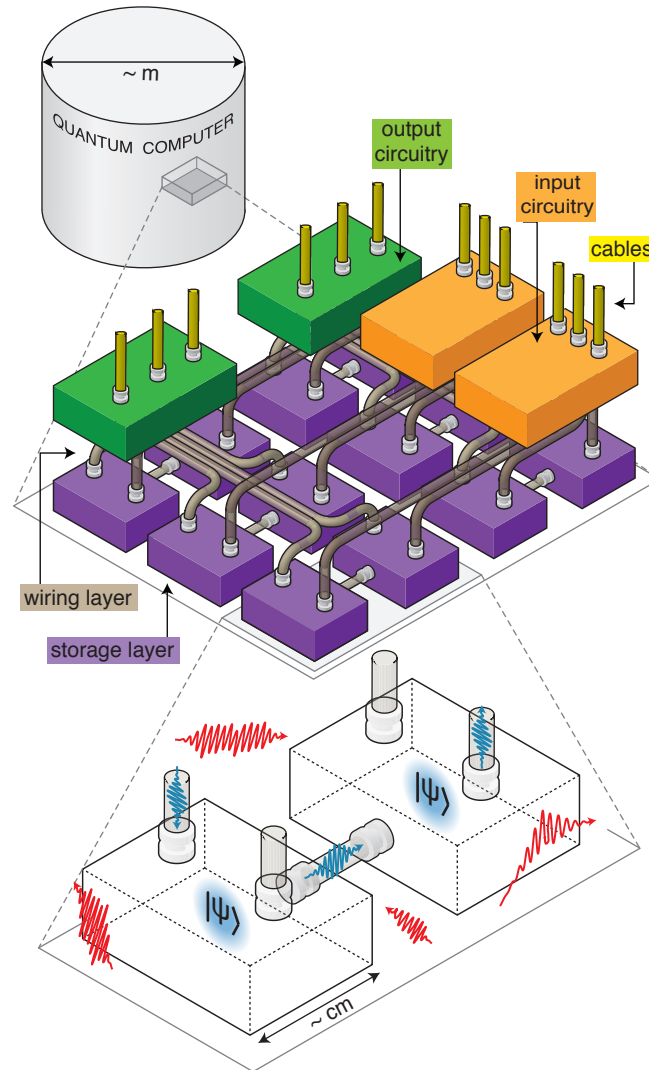
FIGURE 4.2: **Conceptual sketch of a quantum computer.** A large quantum information processor can be composed of many individual modules with precisely managed connections. These modules consist of enclosures approximately a wavelength in size (cm) containing superconducting circuit elements, including Josephson-junction qubits. While only a few modules are sketched here, a quantum processor composed of millions of these components can occupy the payload space of industry standard dilution refrigerators (m^3). (Figure used with permission from Brecht et al., 2016. See Copyright Permissions.)

4.2 Quantum hardware of the future

It should soon be possible to construct a scalable quantum computer that overcomes these challenges by incorporating other technologies into the cQED architecture. This can be achieved by dividing the quantum circuit into subsystems and shielding each one with a three-dimensional superconducting enclosure, as sketched in figure 4.2. The enclosures, represented as boxes in the figure, suppress cross-talk by providing a high degree of electromagnetic isolation. Some house planar circuits containing multiple qubits, some contain input and output circuitry, and others are themselves 3D cavity resonators serving as quantum memories (chapter 7, Brecht et al., 2015).

Quantum information can be stored efficiently in the states that reside in storage modules with minimal loss and high isolation. Modules of input circuitry may include filtered RF control lines and bias wiring, and output circuitry may include quantum limited amplifiers, filters and switches. Key requirements of the device are addressability via a large number of external connections, indicated by yellow tubes at the surface, and internal selective coupling and isolation, indicated by grey tubes. Unlike the modules, these interconnects can be smaller than a wavelength and require negligible space. Each component is well isolated from cross-talk and environmental effects (red wave packets) by its enclosure, and components interact only by transmission through shielded channels (blue wave packets).

The use of intentionally designed 3D modes as quantum elements also alleviates the need for suppressing spurious package modes. [1] Within each shielded module, circuit complexity can be kept manageable, and the engineering of different modules can be mostly independent. Interconnects between individual modules are then created using superconducting transmission lines. 3D shielding allows for the implementation of a large

---

[1]"Package modes" are resonances that are not intended for use in the device, but arise anyway due to the complex boundary conditions of the surroundings. Participating materials possibly include a chip, PCB, metal box, package, sample mount, etc. The circuit engineer must conscientiously design the entire system in order to avoid package modes that are close in frequency or coupling strength to the important device modes.

number of internal and external connections, shown as wires in figure 4.2, without introducing cross-talk or sacrificing coherence. A dilution refrigerator payload space of one cubic meter can accommodate a device containing millions of these components, each with linear dimensions on the order of one centimeter. This general hardware architecture is compatible with any superconducting circuit, and particularly necessary for the scalable implementation of a complex device requiring quantum coherence.

As an approach for creating this concept, we introduce the multilayer microwave integrated quantum circuit (MMIQC), which combines the advantages of integrated circuit fabrication with the long coherence times attainable in 3D cQED, shown schematically in figure 4.3. The shielding enclosures are formed using established techniques from the MEMS industry (Rebeiz, 2003). For example, recesses can be created in silicon wafers by masking and subsequent etching. The removal of bulk substrate material to create 3D features with precise dimensions is known as "micromachining". The etched wafers are then patterned with metal, aligned, and bonded to one another to form integrated circuitry and shielding. Devices can be fabricated in a single foundry to produce a compact monolithic structure of macroscopic size containing components made with lithographic precision. This hardware platform is suited for integrating a wide variety of cQED components and utilizes a number of existing technologies.

FIGURE 4.3: **General schematic of a multilayer microwave integrated quantum circuit (MMIQC).** (Figure is on the next page.) **(a)** Layers are made of silicon wafers with features etched out of the bulk using micromachining techniques to create enclosures that serve as high-Q resonators and as shielding for internal components. Superconducting metalization (blue) covers the walls of these enclosures and enables low-loss wafer-to-wafer bonding of the layers. Dense planar input/output circuitry, including filters, switches and amplifiers can be embedded in other layers. RF and DC vertical interconnects carry signals between layers, and wirebonding or ball-grid connection can be used to interface with external control and measurement electronics. **(b)** A cross-section of the rectangular cavity resonator shows interlayer aperture coupling between the cavity and transmission lines above. **(c)** 3D superconducting transmission lines could be constructed using membranes (green) in the micromachined structure. Some of these can be populated with qubits and act as a compact low-loss quantum bus. (Figure used with permission from Brecht et al., 2016. See Copyright Permissions.)

a

wafer substrate

shielding enclosures

superconducting film

multilayer signal interconnect

input circuitry →

output circuitry →

storage layer →

wiring layer →

connectorization →

b

wafer-to-wafer bonding

apertures

microstrip

~ 500 µm

~ cm

c

shielded coupling line

inner superconductor

~ mm

Top view:

qubits

~ mm
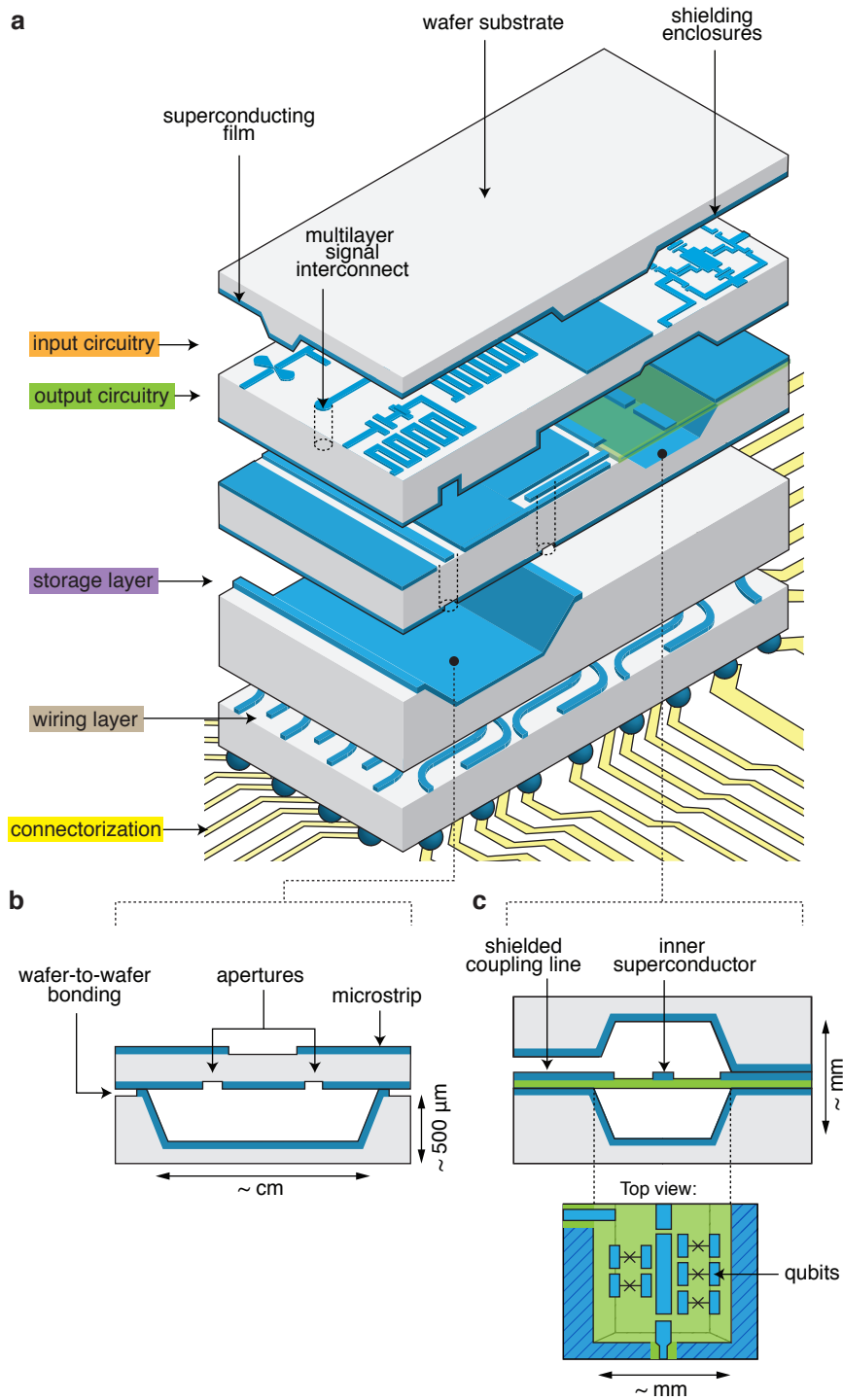
4.3 Characteristics of MMIQCs derived from existing technology

Many of the design problems we have mentioned are not unique to quantum computers, and have known solutions in different contexts. In this section, we will discuss some of the existing solutions and point out ways that they can be directly applied in the MMIQC platform, as well as contrast between contexts such as room-temperature versus cryogenic, DC versus microwave, and quantum versus classical.

4.3.1 3D cavities and isolation

A prominent feature of the MMIQC is 3D isolation provided by superconducting enclosures. Some of these enclosures form high-Q cavity resonators (figure 4.3**(b)**). These are circuit elements in themselves: quantum memories with precise frequencies. We learned in chapter 3 that a resonator such as this is one of the two key characters in cQED (the other being the qubit), so there may be many thousands of these cavities in future MMIQCs. Micromachined cavity resonators with $Q \sim 100$ have previously been demonstrated with normal metal coatings, and are used in low-loss multi-cavity microwave filters (Harle, 2003; Brown, Blondy, and Rebeiz, 1999; Papapolymerou et al., 1997). These are a 20-year-old established technology, and existing methods can be extended to accommodate superconducting coatings to achieve the higher Qs required for storing quantum states. The cavity resonator is also the most quintessential component of the MMIQC that can prove the viability of a superconducting bond isolation strategy. This is the subject of chapter 6 and chapter 7.

The second function of these enclosures is to provide shielding for embedded planar (or quasi-planar) circuitry. It is a well-known and effective practice to use metalized enclosures to prevent radiative loss and cross-talk in vertically integrated microwave circuits. See the summary in Katehi, Harvey, and Herrick, 2001 and examples in Takahashi, 2001;

Lee and Lee, 1998; Herrick, Katehi, and Kihm, 2001; Henderson et al., 2000; McRae et al., 2017. In these cases, the enclosures serve as bulk microfabricated electromagnetic *packaging* necessary for adequate microwave hygiene. [2]

4.3.2 3D transmission lines

Another important feature of the MMIQC is the use of shielded superconducting transmission lines connecting elements on the same layer (Figure 4.3**(c)**. Micromachining has previously been used to remove substrate in both normal metal and superconducting transmission lines to reduce dielectric loss. Notably in superconducting circuits, removal of silicon around superconducting TiN and NbTiN CPW microwave resonators was shown to reduce surface dielectric losses (Sandberg et al., 2012; Bruno et al., 2015). A similar strategy was shown to reduce dielectric loss in room-temperature microwave CPWs 15 years earlier (Herrick, Schwarz, and Katehi, 1998). Other current work in superconducting circuits for cQED reduces dielectric loss by design of vacuum-gap stripline multi-layer structures without the use of micromachining (Minev, Pop, and Devoret, 2013; Minev et al., 2016b; Lewis, Henry, and Schroeder, 2017).

Much of the other existing work on micromachined transmission lines in normal metals makes heavy use of metalized walls for shielding or to serve as the outer conductor of the transmission line (a feature not present in Bruno et al., 2015; Herrick, Schwarz, and Katehi, 1998). While this distinction is a continuous one, the shielding can be considered the outer conductor of the transmission line if it is in close enough proximity to dramatically influence the characteristic impedance of the line to a traveling wave. An early theoretical analysis (Dib et al., 1991) of this idea concludes that the surrounding conductor reduces radiation compared to traditional CPWs. Multiple styles of multilayer low-loss micromachined transmission lines have been developed in normal metals and feature 3D shielding

---

[2] By microwave hygiene, we mean the precise control of the electromagnetic modes in a wide frequency range that might couple to the qubit (or other device). This is important because any mode, when coupled to a qubit's degrees of freedom, can hybridize with low-Q parasitic modes, introducing loss.

(Chi and Rebeiz, 1996; Blondy et al., 1998; Brown, Blondy, and Rebeiz, 1999; Katehi, 1997; Garro, 2003; Reid, Marsh, and Webster, 2006; Drayton and Katehi, 1995). For instance, a diagram and photos of one style of 3D transmission line is reproduced in figure 4.3. Garro, 2003 contains a literature review summarizing and comparing the several styles.

For integration throughout the MMIQC, these types of transmission lines can be modified to replace the normal metal with superconducting coating. Similar to cavity resonators, some of these 3D transmission lines require high quality superconducting bonds to tame both dissipative loss and cross-talk. Some 3D transmission line geometries, however, are less sensitive to the quality of the bonds. This sensitivity depends on the distribution of the currents of the propagating mode. We will say more on this subject for cavities and sections of 3D transmission lines used as resonators in section 5.2.5.

4.3.3 Vertical interconnects

To route signal communication between layers, MMIQCs must contain many layer-to-layer transitions of wires and transmission lines. The connectivity advantage of vertically integrated circuitry is extreme, as summarized by Davis et al., 2005 and suggested by the schemes shown in figure 4.4. However, engineering these vertical interconnects is much more difficult when dealing with high-frequency microwave signals, and more challenging still when the materials are superconducting. MMIQCs will employ superconducting versions of layer-to-layer microwave interconnects (Herrick, Yook, and Katehi, 1998; Herrick, Katehi, and Kihm, 2001; Farrington and Iezekiel, 2011). Two particular examples are reproduced in figure 4.5. Some of these vertical interconnects in the MMIQC may be required to carry signals at single-photon power levels, requiring extraordinarily pure transmission. Recently, several cQED research groups have begun development of such vertical interconnects.

A second type of layer-to-layer signal transfer can be made through apertures. Coupling of the cavity resonators to one another or to planar transmission lines can be achieved,
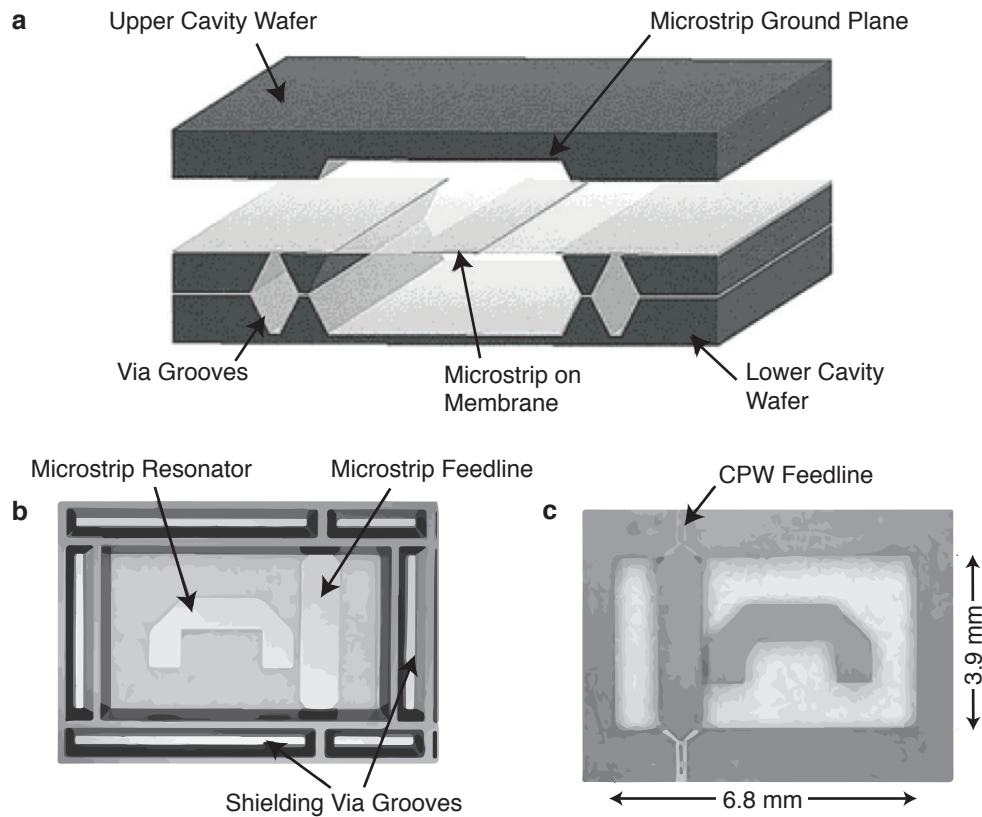
FIGURE 4.3: **3D transmission line on membrane.** A transverse cross-section of the three-wafer stack used to create low-loss room-temperature membrane-supported microstrip resonators in Brown, Blondy, and Rebeiz, 1999 is shown in **(a)**. The circuit (middle) wafer of a 29 GHz microstrip resonator in bandstop filter configuration (or what we will call "hanger" in chapter 5) is shown from **(b)** bottom view and **(c)** top view. The upper and lower cavity wafers are not shown separately, but are comparatively simple. (Figure used with permission from Brown, Blondy, and Rebeiz, 1999. See Copyright Permissions.)
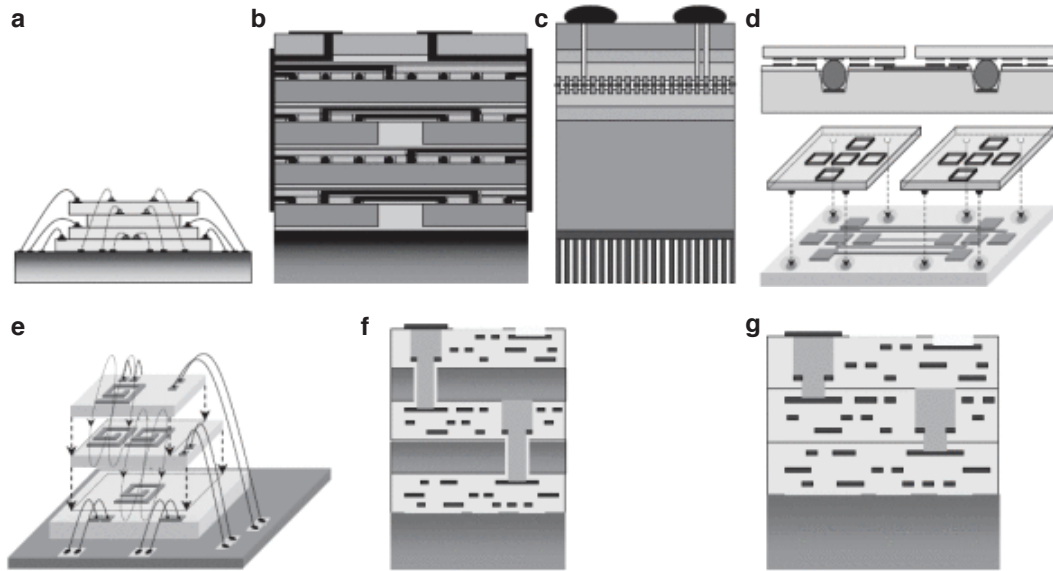
FIGURE 4.4: **Vertical interconnect schemes.** Illustration of vertical interconnect technologies: **(a)** wire bonded **(b)** microbump–3D package **(c)** microbump–face-to-face **(d)** contactless–capacitive with buried bumps **(e)** contactless–inductive **(f)** through via–bulk **(g)** through via–silicon on insulator. (Figure used with permission from Davis et al., 2005. See Copyright Permissions.)

for instance, through apertures in the metalization of the enclosure through which electromagnetic field radiates, as done in some room temperature microwave cavities and multicavity filters (Harle, 2003; Brown, Blondy, and Rebeiz, 1999; Papapolymerou et al., 1997). This is the type of coupling that is implemented later in this thesis. This aperture-type layer-to-layer coupling is distinct from the vertical interconnects mentioned above in that the apertures provide a large range of couplings (coupling Qs) between local modes. The interconnects mentioned above, however, ideally support unity transmission of traveling signals.

4.3.4 Vias

Vias are simply holes in the substrate wafers that may or may not be metalized. The holes can be made in silicon wafers by wet or dry etching, and these are sometimes abbreviated TSVs (through-silicon-vias). For TSVs that are small, or of high aspect ratio, non-trivial methods have been developed to etch or metallize them. For facilities with the capabilities,
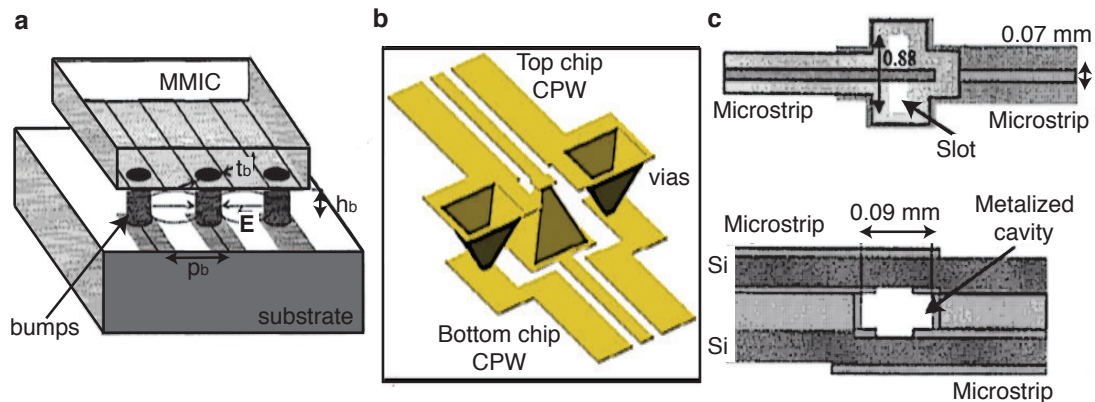
FIGURE 4.5: **Examples of microwave vertical interconnects.** **(a)** Face-to-face bump-bonded interconnect of a CPW from Krems et al., 1996, in which the height h_b, thickness t_b, and pitch p_b of the bumps are considered as parameters affecting the transmission of the transition. **(b)** CPW wafer-to-wafer interconnect using wet-etched metalized vias. (From Herrick, Yook, and Katehi, 1998.) **(c)** A multilayer microstrip transition. The ground of the two microstrips is connected through a short section of a narrow waveguide which carries the EM power from one side of the transition to the other. (From Herrick, Yook, and Katehi, 1998.) (Figures used with permission from Krems et al., 1996; Herrick, Yook, and Katehi, 1998. See Copyright Permissions.)

however, it can be a robust process. Etching the holes can be done with wet or dry processes, or laser ablation. Metalizing the holes is achieved by either electroplating, atomic layer deposition (ALD), plasma enhanced chemical vapor deposition (PECVD), sputtering, or solder injection, depending on the application. Metalized vias see use in multilayer ICs for embedded signal routing. TSVs are used in such high-volume manufactured classical ICs as CMOS image sensors and stacked 3D DRAM.

Vias will be necessary on some layers throughout a MMIQC in order to suppress field leakage and resulting cross-talk. It is a common practice in single-layer microwave circuits to use metalized vias to electrically tie together ground-planes on the front and back sides of a chip (Wu, Scholvin, and Alamo, 2004). In order to be effective, vias for this purpose should be distributed with spacing of less than a quarter wavelength. Vias for this purpose do not need to be circular holes, and they do not always need to be high aspect ratio. For example, the vias in the device shown in figure 4.3 are millimeters long grooves made in the same wet-etch step as the enclosures or membrane relief. Linder et al., 1994 also describes an accessible technical approach using wet-etching to create square vias that is

a trivial variation to the wet etching of the enclosures. High aspect ratio vias would only be necessary when connected to localized modes, in which case they must be designed to minimize radiation loss (section 5.2.2). Deep reactive ion etching (DRIE) or femtosecond pulsed ultra-violet laser ablation can achieve aspect ratios exceeding 10:1 height to radius.

Another practical reason that open vias may be necessary in the MMIQC is to allow air to be pumped out of the enclosures. The device is placed in a cryogenic refrigerator with a vacuum chamber that is evacuated to $\sim 10^{-6}$ Torr. If no route for air is available, the enclosures sealed with superconductor would be hermetic, and the differential pressure due to an atmosphere trapped inside may explode the wafer stack.

4.3.5 Dense I/O connectorization

Future MMIQCs will require high-density connectivity to external measurement and control circuitry. For dense connectorization, we anticipate the incorporation of methods commonly used in integrated circuits, such as ball grid arrays and flip-chip bonding (Miller and Jhabvala, 2012; Lau, 1996). A interposer layer may be purposed for routing wires to spatially distributed bump-to-bump or bump-to-pad interfaces with a substrate PCB. In addition to wiring density, these types of vertical connections allow signal routing to elements otherwise inaccessible from the edges of chips by other circuitry. One current effort to increase density and allow connections to these embedded elements at high sensitivity is the so-called "Quantum socket"(Béjanin et al., 2016).

For signal routing between large MMIQCs and room temperature operation and measurement electronics, coaxial cables that we currently use in experiments may eventually be replaced by flexible ribbons of high-density superconducting microwave transmission lines. Currently, flexible superconducting Nb transmission lines on thin film polyimide (microwave $\tan \delta \sim 10^{-5}$) are being investigated over 1-20 GHz bandwidth and wide power range specifically for quantum computing applications(Tuckerman et al., 2016). Low frequency cryogenic ribbon-looms are commercially available, but other prior work

on microwave frequency cryogenic flexible transmission lines can be found in millimeter-wave detectors with heterodyne focal plane arrays, where they must carry a 1-10 GHz IF signal (Harris et al., 2012; McGarey et al., 2014). Like the quantum computer, this application is also concerned with the trade-offs between thermal conduction between temperature stages and crosstalk between closely spaced signals.

4.4 Prior high-density multilayer superconducting ICs

4.4.1 RSFQ and RQL circuits

Early exploration of Josephson junction ICs aimed to use the junction as a lossless switch that reproduced the voltage characteristics of the vacuum tube or semiconductor transistor. Schemes of this type were known collectively as Josephson "latching logics" or Josephson computation. Notably, the "superconducting supercomputer" program at IBM in Yorktown Heights, NY, ran from 1969-1983 (Anacker, 1980).

Afterwards, significant technological development was accomplished by those working on Rapid Single-Flux Quantum (RSFQ) logic infrastructure (Bunyk, Likharev, and Zinoviev, 2001; Brock, 2001). RSFQ technology consists of superconductor ICs that enable high-speed digital logic at low-power with quantum accuracy. Using mixed-signal systems operating at 100+ GHz, and lying at the intersection of RF and digital domains, it is intended to perform classical logic operations using radically different IC hardware that is better suited than modern semiconductor ICs to address complications associated with high clock-speeds, interconnect delays, and dissipative heating. In particular, RSFQ logic uses the lossless ballistic transport of single quanta of magnetic flux, or "fluxons", as the digital data manipulated by gates.

The RSFQ research effort was strong between 1985 and 2000, with specific applications in wireless communications, ultra-high throughput networks, and supercomputing. During that time, prototypes reached the level of very large scale integration, or "VLSI".

However, the effort lost speed in 2000 with increasing attention and funding redirected to quantum computing research. Nevertheless, MIT-Lincoln Labs currently produces circuits with 18,000+ Josephson junctions and 8-10 layers. These multi-layer circuits consist of alternating layers of niobium and PECVD SiO_2 dielectric, with niobium stud vias and $Nb/Al-AlO_x/Nb$ trilayer Josephson junctions. The multilayer structure does not use wafer bonding; instead it is constructed layer-by-layer with alternating steps of deposition and chemical mechanical planarization, which helps maintain component yield and uniformity.

A more recently developed cousin of the RSFQ logic family is reciprocal quantum logic (RQL) (Herr et al., 2011). RQL uses reciprocal pairs of single flux quantum pulses to encode logical bits. Both power and clock are provided by multi-phase alternating current signals on the order of 10 GHz. In comparison to RSFQ, RQL gates dissipate negligible static power because they include no intentionally resistive elements. Circuits operating under these two logic families share the same fabrication process.

The main difference between a cQED-based quantum computer and RSFQ/RQL circuits is the requirement for isolation of localized high-quality microwave modes in close proximity to control circuitry. In RSFQ/RQL, the Josephson junctions are used as fast switches which turn fluxon transfer on and off rapidly, while in cQED they must sustain coherent oscillations at the single-photon level for as long as possible. Likewise, RSFQ/RQL circuits are less sensitive to losses in the dielectric support substrate between layers because the superconducting lines do not function to sustain high-Q modes, as they must in cQED. Nevertheless, scaling these superconducting circuits has many of the same system-level concerns as a quantum computer when it comes to I/O connectorization, packaging, and certain interconnects.

4.4.2 Detectors

Another area which can lend important technological guidance to MMIQC engineers is in detectors for sub-mm astronomy and other infrared (IR) imaging. For instance, the SCUBA-2 detector contains a grid of 10,000+ pixels, each of which consists of a transition-edge sensor (TES) fabricated on a silicon nitride membrane and is coupled to a single SQUID on a multiplexed backplane (Audley et al., 2004). The multiplexed SQUID backplane (Chervenak et al., 1999) was developed at NIST and can be hybridized with several types of superconducting detector using indium bonds. One will also serve as the backplane for the Near Infrared Spectrometer (NIRSpec) device on the James Webb Space Telescope (JWST) scheduled to be launched within the next two years. NIRSpec's focal plane is also combined with a micro-shutter array containing $\approx 250,000$ shutters 100×200 μm in size that can mechanically open and close by individual electronic actuation to form multiple apertures to different objects in the sky. This is an excellent example of a large-scale device that utilizes micromachining, superconducting vertical interconnects in the form of indium bump bonds, and Josephson junctions, as well as micro-electromechanical systems.

4.5 MMIQC development

4.5.1 Hybridization opportunities

Other existing quantum circuit elements of various geometries can be readily incorporated into the MMIQC. These include planar fabricated qubits, which can be situated inside shielding enclosures on non-metalized surfaces. Integration of transmon qubits and micromachined cavities is the subject of chapter 8. As shown in Figure 4.3c, some modules or buses coupled to several qubits can even be made on membranes to further suppress dielectric loss, as was demonstrated in normal metal filters (Chi and Rebeiz, 1996; Blondy et al., 1998). It is also possible to incorporate low-participation quasi-2D devices such

as superconducting whispering gallery mode resonators (Minev, Pop, and Devoret, 2013; Minev et al., 2016b). Practical quantum information processing will require more sophisticated on-chip input/output circuitry under active development, such as quantum-limited amplifiers (Castellanos-Beltran and Lehnert, 2007; Bergeal et al., 2010; Macklin et al., 2015; Lecocq et al., 2017), circulators (Sliwa et al., 2015; Kerckhoff et al., 2015; Lecocq et al., 2017), and switching elements (Pechal et al., 2016; Chapman et al., 2016).

Moreover, the platform is compatible with integration of classical control electronics in close proximity to the quantum device. When incorporated with adequate isolation, such "cold electronics" may even be included in the same structure as the quantum elements. One consequence of such close proximity would be reduced latency in feedback circuits (eliminating delays of 10s of nanoseconds needed for transmission through cables leading in and out of a refrigerator). It is possible that eventual quantum computers will make use of embedded RSFQ or RQL circuitry (section 4.4.1) to control pulse timings on different qubits, post-processing logic, or in-situ measurement-based entanglement of qubits. In fact, this kind of integration is already being pursued at Northrup Grumman (Miller and Naaman, 2016).

4.5.2 New challenges

While many features and components of the MMIQC make use of existing technologies, there are certain aspects of the design that will require the development of novel techniques. This includes the fabrication of micromachined superconducting enclosures, both for use as cavity resonators and as shielding. In particular, enclosures with high quality RF isolation will require a low-loss bond between two wafers that are etched and coated with a suitable superconductor. The first step in investigating the feasibility of such devices is to fabricate and evaluate 3D superconducting cavity resonators. This is the subject of chapter 6 and chapter 7. There, we demonstrate 3D micromachined resonators with high quality superconducting seams and planar multilayer coupling.

The second major challenge to making such a multilayer structure useful for cQED is to engineer coupling between 3D modes and qubits, and also to other embedded planar circuitry. This is the subject of chapter 8, in which we provide a proof-of-principle device that includes a micromachined cavity and a transmon. The scheme implemented there, however, is not the only one possible.

It is not expected to be trivial to incorporate the many transmission lines, wiring, and filtering that must be added to provide suitably shielded connections between subsystems as well as to the outside world. Even after high-density vertical transitions like those of figure 4.4 and the use of multiplexing schemes, the microwave signals must be carried by many coaxial cables to and from the classical world so that we can engage and ultimately make use of whatever quantum processing occurs inside. One concern is the massive heat load of many hundreds of connections between the operating temperature of the quantum computer and the lab electronics. Excessive cooling power or advances in cryogenics may be necessary to make the required connections possible. Another likely strategy is to place control units, feedback units, and classical processing units inside the refrigerator along with the QIP system. Therefore, this concern is another reason to emphasize MMIQCs' integrability with non-quantum electronics.

4.6 Conclusion

In summary, practical implementation of complex quantum circuits will require innovative approaches to scaling up. In the platform of cQED, the goal is to create integrated QIP circuits with multiple interconnected cavities, qubits, and embedded control wiring while also obeying the principles for minimizing materials losses, and providing the high isolation and shielding that quantum states require. We emphasize that the most pressing need in achieving this goal is not the miniaturization of circuits, but the maintenance of high coherence. We conclude that the solution is likely to heavily employ superconducting 3D enclosures, as sketched in figure 4.2. This chapter proposes a lithographic approach for

fabricating quantum circuits that incorporate superconducting enclosures in a multilayer structure (figure 4.3). The eventual complete demonstration of the MMIQCs described here could enable the large-scale fabrication of sophisticated systems for quantum information processing.

Chapter 5

Microwave resonators

In [chapter 3](#) we introduced the quantum harmonic oscillator as an integral part of the cQED system. Each discrete mode of an electromagnetic resonator is a harmonic oscillator that can be treated as in [chapter 3](#) in combination with a qubit to access cQED physics. Long lived 3D cavities are of particular use in cQED circuits for their potential to be used as quantum memories. Cavities can be significantly longer lived than the qubits, reaching single-photon lifetimes as long as 100 ms ([Kuhr et al., 2007](#)).

Furthermore, resonator measurements can often serve as valuable aids to help us probe loss mechanisms that may also affect qubits fabricated with commonalities. An important sector of the scientific community aiming to scale up cQED devices seeks to understand and minimize various loss mechanisms affecting both resonators and qubits. It is an on-going effort to determine the exact performance of superconducting metals and the dielectric loss-tangents of substrates and material interfaces at microwave frequencies, single-photon powers, and cryogenic temperatures. In this chapter, we will discuss the framework with which to think about the effects.

We will first introduce the basic properties of several of the physical realizations of resonators that have come to be useful in cQED. Next, we will discuss the coherence limits of resonators, including an enumeration of individual loss mechanisms accompanied by a formalism for accounting for the affects of each of them on the resonator's quality factor. The next section explains the methods used to measure superconducting resonators

in the quantum regime and how to extract useful data. We end with a section showing measurements of sets of cavities with the important variable being "seam loss." The measurements will show that the performance of resonators can be severely limited by such seam losses and that in such cases significant improvements to lifetime can be accessed by making changes is the design of cavity geometry and the materials employed.

5.1 Physical realizations

5.1.1 Planar transmission line resonators

Consider a planar transmission line resonator, as drawn in figure 3.7**(a)**. The transmission line may be of several types, including microstrip, coplanar waveguide, slotline with or without backside ground plane. The impedance of the line is determined by the inductance and capacitance per unit length as $Z_0 = \sqrt{l/c}$. An electromagnetic signal can travel down the line. If the signal encounters a discontinuity in impedance, some of the signal is reflected with a complex reflection coefficient

$$\frac{V^-}{V^+} = \frac{Z - Z_0}{Z + Z_0}, \tag{5.1}$$

where V^- and V^+ are the incoming and outgoing waves. When the discontinuity is a short ($Z = 0$) or an open ($Z = \mathrm{inf}$), the magnitude of the reflection coefficient is unity. The fact that two of these reflections can create a standing wave is used to construct resonators in planar circuits. For instance, for a segment of transmission line of electrical length L terminated at both ends by opens has a fundamental resonance with wavelength $\lambda = 2L$. Because of this standing wave resonance, it is called a $\lambda/2$-resonator, and it has higher order modes at all integer multiples of frequency $c/2L$. The boundary conditions may instead be open on one end and short on the other, and in this case the fundamental resonance occurs at $\lambda = 4L$. It is called a $\lambda/4$-resonator, and it has higher order modes at all integer multiples of frequency $c/4L$.

5.1.2 Compact resonators

Compact resonators, like planar transmission line resonators, are made by thin-film metal deposition and lithography on a substrate. However, the pattern creates a largely inductive region in parallel to a largely capacitive region. The inductive region is simply a thin length of wire, and the capacitor is two pads of metal separated by a gap. In the *lumped element* approximation, there is a resonance in which the voltage of the capacitor oscillates 90 degrees out of phase with the current in the inductor. However, in the compact resonators usually employed for microwave superconducting circuits the elements are slightly smaller than a quarter-wavelength, so this lumped approximation is not exactly correct. The name *compact* indicates that these resonators are much smaller in size than the transmission line resonators, while still not behaving in exactly in the lumped element approximation.

One key difference from transmission line resonators is that compact resonators do not have equally spaced resonances; rather, factors of 5 between the fundamental resonance and the second resonance are commonly designed. Truly lumped resonators can display much larger ratios (Geerlings, 2013).

5.1.3 3D cavity resonators

A cavity resonator consists of a region of vacuum surrounded by metal that provides boundary conditions for electric field oscillations inside. The field corresponding to the lowest frequency of the possible oscillations is the fundamental mode. We have already appealed that 3D cavity resonators need not contain a dielectric substrate whatsoever, instead taking advantage of lossless vacuum to store nearly all of their field energy. We will discuss dielectric loss in section 5.2.4. In addition to the lack of a dielectric substrate, the other advantage of a cavity design is that there are no printed circuit boards, wirebonds, or glue to interfere with the mode.

Several styles of 3D cavity resonators are well-known, including cylindrical cavities, spherical cavities, and coaxial stub cavities. The coaxial stub cavity has recently become
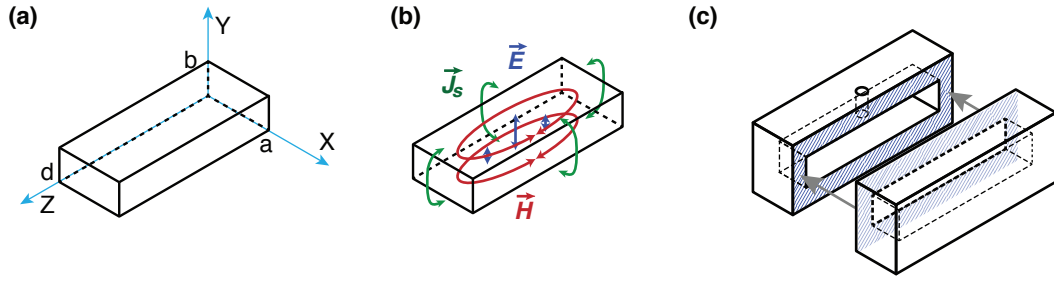
FIGURE 5.1: **The rectangular cavity resonator. (a)** Convention for the axis orientation and dimensions of the rectangular cavity adhered to in this thesis. **(b)** The TE101 (fundamental) mode of the rectangular cavity is shown by it's electric field (blue arrows), magnetic field (red arrows), and surface currents (green arrows). **(c)** Cavity used in some cQED experiments (Paik et al., 2011).

the resonator of choice for many experiments in the Schoelkopf lab, playing a key role in

Reagor et al., 2016; Blumoff et al., 2016; Wang et al., 2016; Pfaff et al., 2016. In this thesis,

we will concentrate on the rectangular cavity resonator.

Rectangular cavity resonators:

A rectangular cavity is composed of a length of rectangular waveguide shorted on both

ends. It can be designed to be about a cubic inch in volume with resonant modes in the

microwave frequencies, stores the majority of the electromagnetic energy in vacuum, and

is readily machined.

We follow the labeling conventions of Pozar, 2005. The rectangular cavity shown in

figure 5.1 has resonance frequencies corresponding to variations in standing wave patterns

in each of three dimensions. The variations are indexed to define different modes. The

frequencies of the TE_{mnl} and TM_{mnl} modes are given by

$$f_{mnl} = \frac{c}{2\pi\sqrt{\mu_r \epsilon_r}}\sqrt{\left(\frac{m\pi}{a}\right)^2 + \left(\frac{n\pi}{b}\right)^2 + \left(\frac{l\pi}{d}\right)^2}. \tag{5.2}$$

The quantity including the square root and excluding the preceding constant is the resonant wavenumber, k_{mnl}. We also define the propagation constant governing transmission

of ,

$$\begin{aligned}
\beta_{mn} &= \sqrt{k^2 - k_c^2} & (5.3) \\
&= \sqrt{k^2 - \left(\frac{m\pi}{a}\right)^2 - \left(\frac{n\pi}{b}\right)^2} & (5.4)
\end{aligned}$$

where the top line is the form for propagation constant in an arbitrary waveguide with cutoff wavenumber k_c (which is a fixed function of the cross-sectional geometry of the guide perpendicular to the direction of propagation), and the second line specifies the cutoff wavenumber for the TE_{mn} and TM_{mn} rectangular waveguide modes.

The fields of the rectangular cavity's TE10l mode are given by:

$$\begin{aligned}
E_z &= E_0 \sin\left(\frac{\pi x}{a}\right) \cos\left(\frac{l\pi z}{d}\right) & (5.5) \\
H_x &= \frac{-jE_0}{Z_{TE}} \sin\left(\frac{\pi x}{a}\right) \cos\left(\frac{l\pi z}{d}\right) & (5.6) \\
H_z &= \frac{j\pi E_0}{k\eta a} \cos\left(\frac{\pi x}{a}\right) \sin\left(\frac{l\pi z}{d}\right) & (5.7)
\end{aligned}$$

where $k = \sqrt{(\pi/a)^2 + (\pi/b)^2 + (l\pi/c)^2}$ is the wavenumber, $Z_{TE} = k\eta/\beta_{10l}$, and $\eta = \sqrt{\mu/\epsilon} = 2\pi f_{10l}\mu/k$ is the wave impedance. These fields are sketched with arrows in figure 5.1.

5.1.4 Hybrid forms

Some types of resonator do not fit neatly into one of the above categories.

The *whispering gallery mode* ring resonator from Minev, Pop, and Devoret, 2013 consists of symmetric rings of patterned on two wafers held in close proximity aligned to one another. A great advantage of this type of resonator is that there is a high level of field confinement in the vacuum between the two conducting paths. There is therefore very small dielectric participation, but increased conductor participation compared to either 3D cavities or traditional planar circuits.

A *coaxline* (Axline et al., 2016) consists of a superconducting microstrip line on a narrowly cut substrate chip that is surrounded by a close-fitting tubular superconducting outer-conductor. This design is flexible to link several types of planar fabricated components, including qubits and filters, along with the resonator. Additionally, it is highly integrable with 3D cavity designs in a way that bypasses the need for seams entirely. For example, this is put to use in our lab in the works: Wang et al., 2016; Blumoff et al., 2016; Pfaff et al., 2016.

A *micromachined transmission line* is of similar structure to the coaxline, but created by etching, metal patterning and bonding of two or more wafers. As discussed in section 4.3.2, many styles of micromachined transmission lines have been developed at room temperature. Like the coaxline, they have a central conductor and an outer conductor that participates in the mode as well as prevents radiation loss and interference. The difference from the coaxline, however, is that the construction is by layered wafers, making seams an integral aspect, and these have not yet been fully developed for cQED.

I make a note now about systematics. Often times, a distinction is drawn between "planar" or "2D" resonators and "3D" resonators. This dichotomy is descriptive but it also a simplistic one; and if taken literally it is ultimately a misleading one that neglects important aspects of microwave engineering. Ultimately, the fields of any microwave circuit are quite 3D, as we have claimed in the previous chapter.

Instead of a dichotomy, there is a continuum of device designs with more or less confinement of fields near the surface of a substrate versus in a conductor-bounded volume. For instance, transmission line resonators are not necessarily "planar" at all. The "hybrid" 2D/3D forms mentioned above can all be considered some form of transmission line resonator, though they are certainly not completely "planar". First, the ring resonator is a vacuum stripline with circular boundary conditions. Next, the coaxline is a mixture of two types of transmission lines: a microstrip and a coaxial cable. The same is true for a micromachined transmission line. Some planar resonators are of this kind, but compact
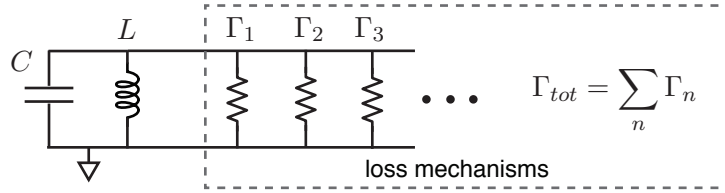
FIGURE 5.2: **Dissipation from separable loss mechanisms combines additively.**

resonators or lumped element resonators are not. Analogously for cavities: rectangular and cylindrical cavities are sections of waveguide, whereas a Helmholtz resonator is not.

These diverse forms have varied possibilities and applications. In the next section, we describe a formalism for assessing general resonator losses. Each loss mechanism plays a role in all resonators, but sometimes to very different degrees. Our aim is to quantify this.

5.2 Loss mechanisms

We have mentioned the quality factor several times already in this thesis. This section is dedicated to understanding all of the known loss mechanisms can limit the quality factor:

$$Q = \omega \frac{\text{Total energy stored}}{\text{Total power dissipation}} = \omega T_1 = \frac{\omega}{\kappa} \tag{5.8}$$

In a circuit with characteristic impedance Z_c, the general expression for the quality factor is

$$Q = \frac{1}{Z_c \text{Re}\,[Y]\,|_{\omega=\omega_0}}. \tag{5.9}$$

The total Q of the whole system includes the losses from various sources, each with

$$\frac{1}{Q_n} = \frac{1}{\omega} \frac{\text{power dissipated in component } n}{\text{total energy stored in system}}. \tag{5.10}$$

The sources add according to

$$\frac{1}{Q_{\text{tot}}} = \sum_n \frac{1}{Q_n}. \tag{5.11}$$

That is, power can be dissipated in any of the various sources with particular rates Γ_n that accumulate in a simple sum, as depicted in figure 5.2:

$$\frac{1}{Q_{\text{tot}}} = \frac{\Gamma_{\text{tot}}}{\omega E_{\text{tot}}} = \frac{1}{\omega E_{\text{tot}}} \sum_n \Gamma_n \tag{5.12}$$

In some of the analysis that follows in this section, we will write the individual Q's of each component as $\frac{1}{Q_n} = \frac{p_n}{q_n}$, where we have a participation ratio, p_n, which is the fraction of the total energy that is stored in the nth component, and q_n is some intrinsic unit contribution to the quality factor of the component.

In the following subsections, we will consider five different loss mechanisms that contribute to the total quality factors according to

$$\frac{1}{Q_{\text{tot}}} = \frac{1}{Q_c} + \frac{1}{Q_{\text{rad}}} + \frac{p_{\text{cond}}}{q_{\text{cond}}} + \frac{p_{\text{diel}}}{q_{\text{diel}}} + \frac{y_{\text{seam}}}{g_{\text{seam}}}. \tag{5.13}$$

We will discuss external (or coupling) loss, radiation loss, conductor loss, dielectric loss, and seam loss in that order. Keep in mind that there may be more than one contributor for each of these mechanisms in a particular resonator. For example, two different types of dielectric would add as separable terms $\frac{p_{\text{diel},1}}{q_{\text{diel},1}}$ and $\frac{p_{\text{diel},2}}{q_{\text{diel},2}}$.

5.2.1 External loss

Physically measuring a resonator provides a total Q that differs from the internal Q. We define total, internal, and coupling quality factors [1] by

$$\frac{1}{Q_{\text{tot}}} = \frac{1}{Q_{\text{int}}} + \frac{1}{Q_c}. \tag{5.14}$$

---

[1]Sometimes Q_c is written Q_{ext} instead.

In the case of two ports there is an input and output coupling Q, related by

$$\frac{1}{Q_c} = \frac{1}{Q_{\text{in}}} + \frac{1}{Q_{\text{out}}}. \tag{5.15}$$

Coupling to the external world induces loss. Often times, the resonator is capacitively coupled to an external transmission line with an impedance of 50 Ω for measurement. Whatever the structure of the external port, the resonator is damped in the process.

To generalize the damping of a LC resonator capacitively coupled to an external load, we can recast the capacitive series coupling into a parallel admittance Y_{ext} that damps the mode. This calculation follows (Schuster, 2007; Reagor, 2015), and is accompanied by figure 5.3. We begin by writing the external admittance

$$Y_{ext} = \frac{1}{R + 1/j\omega C_c} \tag{5.16}$$

$$= \frac{j\omega C_c}{1 + j\omega C_c R} \tag{5.17}$$

$$\approx j\omega C_c + \omega^2 C_c^2 R, \tag{5.18}$$

where the last step takes the approximation that the coupling is weak ($\omega C_c \ll R$). Then, the total admittance of the circuit including the resonator and external admittance is

$$Y_{\text{tot}} = 1/j\omega L + j\omega(C + C_c) + \omega^2 C_c^2 R. \tag{5.19}$$

The characteristic impedance is $Z_0 = \sqrt{L/(C + C_c)}$. Therefore, inserting this and $\text{Re}\,[Y]$ into equation 5.9, we obtain a result for the coupling Q as a function of the coupling capacitance. In the approximation of weak coupling,

$$Q_c = \frac{1}{\omega_0^2 C_c^2 Z_0 R}. \tag{5.20}$$
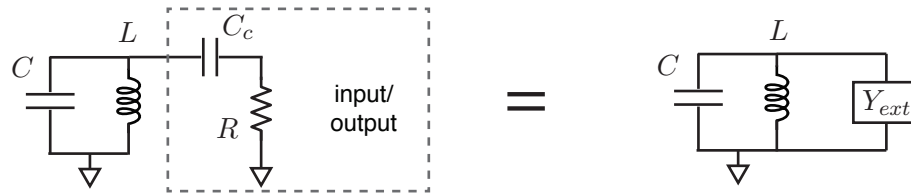
FIGURE 5.3: **External loss of a resonator.**

5.2.2 Radiation loss

In addition to loss to an externally coupled circuit or transmission line, energy of an open resonator can be lost to the vacuum in the form of radiation. Except in the case of cavity resonators, which are fully enclosed, it may be difficult to exactly calculate radiation loss analytically.

As a simple radiation loss example, let us consider a 3D cavity with a small hole. We will perform a simple calculation for the maximum Q of a cavity with an aperture of radius r_0. If $r \ll \lambda$, the loss out the aperture can be approximated as dipole radiation out into half-space. In what follows, we will calculate this loss by considering the electric and magnetic dipole radiation separately. The effects are combined by adding the power radiated from both the electric and magnetic dipoles. An example is plotted in figure 5.4.

Electric dipole radiation:

At the aperture, if the radius is smaller than the wavelength, there is an oscillating dipole moment

$$\vec{p}\,e^{i\omega t}$$

which radiates power. The magnitude of the dipole moment depends on the shape of the aperture. [2] For a circular aperture in the center of the broad wall,

$$|\vec{p}| = \epsilon_0 \alpha_e E_0 = \epsilon_0 \left(\frac{2}{3} r_0^3 \right) E_0, \tag{5.22}$$

and the orientation is perpendicular to the wall. The average power radiated from a dipole into space is (Jackson, 1998)

$$P_{\text{rad}} = \frac{1}{4\pi\epsilon_0} \frac{|\vec{p}|^2 \omega^4}{3c^3}. \tag{5.23}$$

Dividing by 2 for half-space radiation and inserting $\vec{p}$, the power radiated from such a circular aperture in a cavity wall is

$$P_{\text{rad}} = \frac{1}{2} \frac{E_0^2 \epsilon_0 r_0^6 \omega^4}{27\pi c^3}. \tag{5.24}$$

The total energy stored in the electric field inside the cavity is

$$W_e = \int \frac{1}{2} \epsilon_0 E_0^2 dV = \frac{1}{2} \epsilon_0 |E_0|^2 abd. \tag{5.25}$$

The resulting decay time is

$$T_1 = W_e / P_{\text{rad}} = \frac{27\pi c^3 abd}{r_0^6 \omega^4}, \tag{5.26}$$

---

[2] For example, a rectangular slot of length l and width d, and $\vec{H}$ across the width of the slot, the polarizabilities are

$$\alpha_e = \frac{\pi l d^2}{16} \qquad\qquad \alpha_m = \frac{\pi l d^2}{16} \tag{5.21}$$

These approximations for the circular and rectangular apertures are provided in Collin, 1990.

and the corresponding quality factor is

$$
\begin{aligned}
Q &= \omega T_1 \\
&= \frac{27\pi c^3 abd}{r_0^6 \omega^3} \\
&= \frac{27\pi}{(2\pi)^3} \frac{abd}{r_0^3} \left(\frac{\lambda}{r_0}\right)^3.
\end{aligned}
\tag{5.27}
$$

Note the sensitivity to the radius is $Q \propto r_0^{-6}$, and keep in mind that these expressions are based on an approximation with $r_0 < \lambda$. In the last step, we have written the dimensionless quantity in terms of the product of two volume ratios: the volume of the cavity to the effective "volume" of the aperture times the "volume" of a wave to the effective "volume" of the aperture. If the aperture is placed elsewhere on the broad wall, a factor of $|\sin \frac{\pi x}{a} \sin \frac{\pi z}{d}|^2$ appears in the denominator. This displacement of the aperture can only make the Q_{rad} larger; Q_{rad} is limited most harshly for a central aperture because that is where the E-field is strongest.

Magnetic dipole radiation:

Now we do the calculation for the effective magnetic dipole moment of the circular aperture:

$$
\vec{m} = -\alpha_m \vec{H}_t = -(\frac{4}{3}r_0^3)\vec{H}_t
\tag{5.28}
$$

For the transverse component of the magnetic field, we can write the following, keeping in mind that both H_x and H_z may be non-zero on the broad wall.

$$
|H_t|^2 = E_0^2 \left(\frac{1}{Z_{TE}^2} \sin^2 \frac{\pi x}{a} \cos^2 \frac{\pi z}{d} + \frac{d}{Z_{TE}a} \cos^2 \frac{\pi x}{a} \sin^2 \frac{\pi z}{d} \right)
\tag{5.29}
$$

where we have used equation 5.6, equation 5.7, and $\pi/k\eta a = d/aZ_{TE}$. The total power radiated from a magnetic dipole is (Jackson, 1998)

$$P_{\text{rad}} = \frac{Z_0}{12\pi}k^4|\vec{m}|^2. \tag{5.30}$$

Dividing by 2 for half-space radiation and inserting the above expression for magnetic dipole, we get

$$
\begin{aligned}
P_{\text{rad}} &= \frac{1}{2}\frac{1}{12\pi}Z_0 k^4 \left[-\frac{4}{3}r_0^3 \left(\frac{E_0}{Z_{TE}} \right) \right]^2 \\
&= \frac{1}{2}\frac{1}{12\pi}\frac{16}{9}\sqrt{\frac{\mu_0}{\epsilon_0}} \left(\frac{\omega}{c} \right)^4 r_0^6 \left(\frac{E_0}{Z_{TE}} \right)^2 \\
&= \frac{2}{27\pi}\sqrt{\frac{\mu_0}{\epsilon_0}} \left(\frac{\omega}{c} \right)^4 r_0^6 \left(\frac{E_0}{Z_{TE}} \right)^2.
\end{aligned}
\tag{5.31}
$$

Now, the contribution to the decay time due to magnetic field radiation is

$$
\begin{aligned}
T_1 &= W_e/P_{\text{rad}} \\
&= \frac{1}{2}\epsilon_0|E_0|^2 abd/P_{\text{rad}} \\
&= \frac{27\pi}{4}\epsilon_0\sqrt{\frac{\epsilon_0}{\mu_0}}abd \left(\frac{c}{\omega} \right)^4 \frac{1}{r_0^6}Z_{TE}^2.
\end{aligned}
\tag{5.32}
$$

Or, substituting $Z_{TE} = k\eta/\beta$, and $c = 1/\sqrt{\epsilon_0\mu_0}$,

$$
\begin{aligned}
T_1 &= \frac{27\pi}{4}abd \left(\frac{c^3}{\omega^4} \right) \frac{1}{r_0^6} \left(\frac{k\eta}{\beta} \right) \\
&= \frac{27\pi c^3 abd}{r_0^6 \omega^4} \left(\frac{k\eta}{4\beta} \right).
\end{aligned}
\tag{5.33}
$$

The limit on Q due to the magnetic radiation is therefore

$$
\begin{aligned}
Q &= \omega T_1 \\
&= \frac{27\pi c^3 abd}{r_0^6 \omega^3} \left(\frac{k\eta}{4\beta} \right) \\
&= \frac{27\pi}{(2\pi)^3} \frac{abd}{r_0^3} \left(\frac{\lambda}{r_0} \right)^3 \left(\frac{k\eta}{4\beta} \right).
\end{aligned}
\tag{5.34}
$$

Note that these results resemble the expressions for the lifetime and Q limited by electric field radiation, equation 5.26 and equation 5.27, except for the factor of $\frac{k\eta}{4\beta}$. Also, keep in mind that these expressions are modified by some sines and cosines found in equation 5.29 if the aperture is translated away from center. The magnetic dipole radiation is maximized when the aperture is at the edges of the broad wall and zero when the aperture is centered.
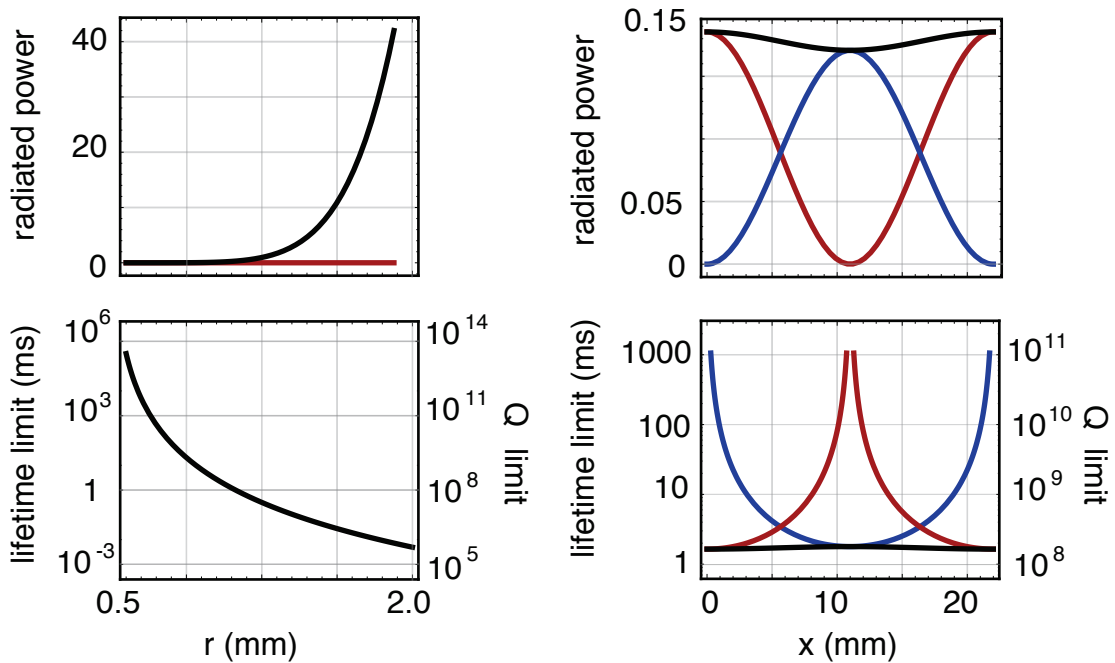
FIGURE 5.4: **Radiation loss in a 3D cavity example.** Radiated power and consequences for lifetimes and quality factors for electric (blue) and magnetic (red) dipole and combined electric and magnetic (black) calculations. The rectangular cavity dimensions are $24 \times 22 \times 0.3$ mm, and the wall is considered infinitely thin. The graphs as a function of radius have fixed position in the center of the cavity's broad wall (where the total radiation is all from electric dipole). The graphs versus position have a fixed aperture radius of 0.75 mm.

What if the wall is not infinity thin? A non-zero wall thickness L creates a short section of waveguide which attenuates fields that would radiate the cavity. Therefore, we expect any wall thickness to reduce the radiation loss compared to the case of an aperture in an infinitely thin wall. The propagating circular waveguide mode TM01 is excited at the cavity wall, and is attenuated by a factor of $e^{-2\beta_{TMmn}L}$, where β_{TMmn} is the propagation constant of the mode that is principally excited in the waveguide, given by

$$\beta_{TMmn} = \sqrt{k^2 - \left(\frac{p_{mn}}{r_0}\right)},\tag{5.35}$$

where k is the wavenumber corresponding to the cavity resonance. In the simple case of electric dipole radiation from the center of the broad wall, the propagating mode that is principally excited is TM01, and the first zero of the zeroth Bessel function is $p_{01} \approx 2.4$. Elsewhere on the wall, other modes may also be excited and contribute to propagation with their own exponential attenuation. See Pozar, 2005–section 3.4 for descriptions of these propagating modes in circular waveguides and a handy table for numerical evaluations.

5.2.3   Conductor loss

A superconductor possesses a complex surface impedance $Z_S = R_S + jX_S$ as described in Zmuidzinas, 2012. The components are a surface resistance R_S and a surface reactance $X_S = \omega\mu\lambda$, where λ is the penetration depth. "Surface Q," or Q_S refers to the ratio X_S/R_S, but here we prefer to write $q_{\text{cond}} = Q_S = \omega\mu_0\lambda/R_S$ instead. The effect of conductor loss on a resonator can be expressed using the magnetic fields of the resonator as follows.

$$\frac{1}{Q_{int,M}} = \frac{R_S}{\omega\mu_0\lambda}\frac{\lambda\int_S |H|^2 dA}{\int_V |H|^2 dV} = \frac{p_{\text{cond}}}{q_{\text{cond}}}.\tag{5.36}$$

The quantity p_{cond} is the participation ratio of the conductor's surface impedance. Notice that it is a dimensionless quantity that is proportional to the resonator's surface-to-volume ratio weighted by the magnetic field. The numerator of the second fraction is the magnetic field energy stored in the super-current-carrying portion of the superconducting walls, while the denominator is the total magnetic field energy of the mode.

p_{cond} is equivalently called the kinetic inductance fraction, and is often denoted elsewhere by α. What is this kinetic inductance? When current flows in a wire it induces a magnetic flux, and this is associated with what we normally think of as inductance. In addition to energy stored in these magnetic fields, there is also kinetic energy present from to the mass of the electrons. In normal metals, this kinetic inductance is masked by substantial resistivity. In a superconductor, however, the kinetic inductance can become significant. Some astronomers put this effect to use in arrays of circuits with high p_{cond} functioning as Microwave Kinetic Inductance Detectors (MKIDs) (Mazin et al., 2002; Day et al., 2003). In these, photon flux from space is detected by way of quasiparticle signals to which the pixels/resonators are sensitive by $\sim p_{\mathrm{cond}}$. In section 7.6, we will show how p_{cond} can be experimentally extracted from resonator measurements.

Since we will later be concerned with micromachined rectangular cavity resonators, we will now write an expression for p_{cond} in terms of the cavity dimensions (defined by figure 5.1(a). The numerator integral is

$$\lambda_L \int_S |H|^2 dA = \lambda_L \frac{E_0^2 \lambda^2}{2\eta^2} \left(\frac{ab}{d^2} + \frac{bd}{a^2} + \frac{a}{2d} + \frac{d}{2a} \right).$$
(5.37)

Dividing by the total energy, equation 6.13, we have

$$p_{\mathrm{cond}} = \lambda_L \frac{\lambda^2}{\epsilon_0 \eta^2} \left(\frac{1}{d^3} + \frac{1}{a^2} + \frac{1}{2bd^2} + \frac{1}{2a^2b} \right).$$
(5.38)

If the cavity height is the only changing parameter,

$$p_{\text{cond}} \propto 1/b + \text{const.} \tag{5.39}$$

5.2.4 Dielectric loss

Dielectrics have a loss tangent that characterizes their dissipation. The loss tangent of a dielectric insulating material with permittivity of $\epsilon = \epsilon' - j\epsilon''$ is defined as $\tan\delta = \epsilon'/\epsilon''$ and it is usually frequency dependent. Intrinsic crystalline sapphire (Creedon et al., 2011) and silicon (Martinis and Megrant, 2014) might have loss $\tan\delta < 10^{-6}$. The quality factor of the material is $q_{\text{diel}} = 1/\tan\delta$. The quality factor, loss tangent, and participation ratio are related by

$$\frac{1}{Q_{\text{diel}}} = p_{\text{diel}}\tan\delta = \frac{p_{\text{diel}}}{q_{\text{diel}}}. \tag{5.40}$$

The dielectric participation ratio is

$$p_{\text{diel}} = \frac{\int_{\text{diel}} \epsilon |E|^2 dV}{\int_{\text{tot}} \epsilon |E|^2 dV} \tag{5.41}$$

where the numerator integrates over the dielectric and the denominator integrates the total amount of electrical energy in the resonator. This approach applies to account for the effects of both dielectrics in bulk and as surface layers of dielectric.

Let us create an expression specified for surface participation. Assume that the metal of a resonator is uniformly coated in a layer of dielectric of thickness t and relative permittivity ϵ_r. This is a reasonable description of the total dielectric loss in a 3D cavity resonator that is otherwise filled with vacuum, as the surfaces of its walls are likely covered in a layer of oxide a few nanometers thick. The description also applies to the oxide that grows on an evaporated metal as one of several dielectric loss contributors in a planar circuit. The effect on the resonator can be expressed using the electric fields of the resonator as follows.

$$\frac{1}{Q_{int,E}} = \frac{\epsilon_r t \int_S |E|^2 dA}{Q_{\text{diel}} \int_V |E|^2 dV} = \frac{p_{\text{diel}}}{q_{\text{diel}}}. \tag{5.42}$$

Surface layers of dielectric can consist of oxides, residual organics, and/or adsorbed water, with separate participation ratios and loss tangents at the metal-substrate, substrate-air, and metal-air interfaces. Loss at these interfaces is currently the limiting factor for the T_1 of transmons in cQED (Wenner et al., 2011a; Wang et al., 2015). In particular, in the work of Wang et al., 2015, a new study combined with a survey of the published data for 3D transmons and finds that all data points with a single-step aluminum lift-off process [3] place a bound on the metal-surface interface of $\tan \delta \geq 2.6 \times 10^{-3}$, whereas some transmons fabricated with subtractively patterned MBE aluminum (Barends et al., 2013) or titanium nitride (Chang et al., 2013) have a slightly improved metal-surface interface (down to $\tan \delta = 0.9 \times 10^{-3}$). [4] To improve T_1, researches seek to both improve interface quality using cleaning methods and innovate low-participation designs (Bruno et al., 2015; Chu et al., 2016).

Since we will later be concerned with micromachined rectangular cavity resonators, we will now write an expression for p_{cond} in terms of the cavity dimensions (defined by figure 5.1(a). The numerator integral is

$$\epsilon_r t \int_S |E|^2 dA = \epsilon_r t E_0^2 \frac{ad}{2} \tag{5.43}$$

Dividing by the total energy, equation 6.13, we have

$$p_{\text{diel}} = \frac{\epsilon_r t}{b}. \tag{5.44}$$

The dielectric participation ration scales inversely with the cavity height.

---

[3] See section A.5 for this fabrication process.

[4] These numbers assume a dielectric surface thickness of $t = 3$ nm and $\epsilon_r = 10$. Different assumptions would change the $\tan \delta$ values but not impact qualitative conclusions and meaningful comparisons made in Wang et al., 2015; Chu et al., 2016.

5.2.5   Seam loss

All cQED devices are assembled from several parts. The connections between components that carry RF energy can introduce dissipation in the form of spurious contact resistance at seams. Frequently, 3D cavities are machined in two parts and then assembled, such that the cavity itself possesses a seam where pieces of bulk metal meet. In this section, we will incorporate the seam loss into our understanding of all cavity losses. At the interface of two metal parts, there may be voids, oxide layers, and/or superconducting weak links. Therefore, the seam may be responsible for loss that is either radiative, ohmic, or dielectric in microscopic nature. However, for the remainder of this section, we will avoid discussion of the detailed microscopic mechanisms of the loss. Instead, we develop a prescription to weight the seam's contribution to loss based on cavity geometry and seam position. The goal is to account for seam loss analogously to previous sections on conductor and dielectric loss.

We now quantify the dependence of seam losses on the cavity geometry. We model the seam as a distributed port around a path $\vec{l}$ with a total length L and total conductance G_{seam}. The cavity fields are accompanied by surface currents $\vec{J}_s$ that may pass across the seam and dissipate power. The total power dissipated by the seam is

$$P_{\mathrm{dis}} = I^2 R_{\mathrm{seam}}/2 = \frac{I^2}{2G_{\mathrm{seam}}}. \tag{5.45}$$

The average current contributing to dissipation is found by integrating the component of $\vec{J}_s$ perpendicular to the seam line:

$$|I|^2 = \int_{\mathrm{seam}} |\vec{J}_s \times d\vec{l}|^2 = L \int_0^L |\vec{J}_s \times \hat{l}|^2 dl. \tag{5.46}$$

Let a cavity mode of frequency ω and total energy E_{tot} be damped solely by seam losses. Then, the mode has a quality factor Q_{seam} given by

$$\frac{1}{Q_{\text{seam}}} = \frac{1}{\omega}\frac{P_{\text{dis}}}{E_{\text{tot}}} = \frac{1}{G_{\text{seam}}}\left[\frac{L\int_{\text{seam}}|\vec{J}_s \times \hat{l}|^2 dl}{\omega\mu_0\int_{\text{tot}}|\vec{H}|^2 dV}\right] = \frac{y_{\text{seam}}}{g_{\text{seam}}}, \tag{5.47}$$

where the field $\vec{H}$ is integrated over the volume V of the mode. We identify the expression in square brackets as the admittance, Y_{seam}, of the cavity presented to the seam. This admittance is zero when the seam is placed such that there are no perpendicular surface currents. In order to compare intrinsic seam properties in different cavity constructions, we introduce the conductance per unit length $g_{\text{seam}} = G_{\text{seam}}/L$ and admittance per unit length,

$$y_{\text{seam}} = Y_{\text{seam}}/L = \frac{\int_{\text{seam}}|\vec{J}_s \times \hat{l}|^2 dl}{\omega\mu_0\int_{\text{tot}}|\vec{H}|^2 dV} \tag{5.48}$$

Both g_{seam} and y_{seam} have units of $[\Omega\text{m}]^{-1}$. Using this model, we can associate y_{seam} with the seam location and cavity fields and g_{seam} with materials properties in the seam region.

Note that we do not attempt to break the $1/Q_{\text{seam}}$ expression into two unitless quantities as in the form $p_{\text{seam}}/q_{\text{seam}}$. Such a distinction would require making an explicit assumption about the microscopic geometry localized at the seam. Analagous explicit assumptions of a particular length scale were made in the dielectric loss (thickness of dielectric t found in p_{diel}) and conductor loss (penetration depth λ_L found in p_{cond}) discussions. However, we do not wish to make such a claim about the microscopic nature of the seam of a cavity, instead choosing to remain general. The formulation in equation 5.47 enables us to map measured Q to a conductance per unit length and use this as a figure of merit comparing different cavities with different seam locations and materials. The advantage of this model is that we do not need to make any geometrical assumptions to define a seam region.

5.3 Resonator measurement methodology
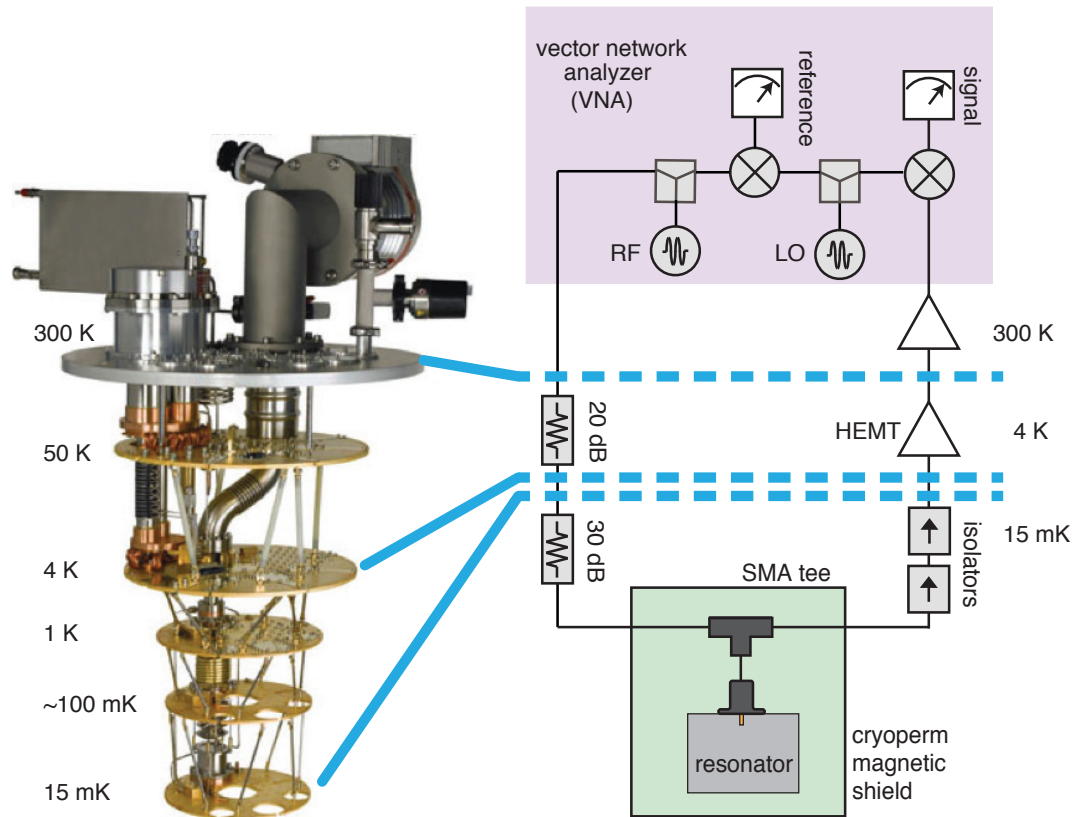
FIGURE 5.5: **Dilution refrigerator and schematic for cavity measurement.** (Left) The interior of a dilution refrigerator with approximate temperatures of each plate. The payload experiments are thermally anchored to the baseplate. (Right) A wiring diagram shows a standard configuration that was used for measuring cavity resonances in this thesis. A VNA (purple box) is used to measure transmission through the experiment. Resonators under test are connected to the signal line in either a transmission (not shown) or hanger configuration.

5.3.1 Superconducting resonator measurement setup

Resonators to be tested are first characterized using a VNA at room temperature and suitable couplers are made. Then, the resonator is mounted to a bracket thermally anchored to baseplate of a closed-cycle He-3/He-4 dilution refrigerator from Oxford, which reaches

a base temperature ≈ 15 mK. The schematic for resonator measurements is shown with an image of the refrigerator in figure 5.5.

5.3.2 Fitting resonance line-shapes to extract quality factor

Transmission configuration:
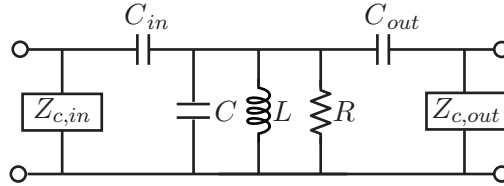
FIGURE 5.6: **Circuit diagram of a resonator in the transmission measurement configuration.**

In a cavity transmission measurement, shown in figure 5.6, the power of an incoming wave is split into a reflected, dissipated, and outgoing part $P_{\text{in}} = P_{\text{ref}} + P_{\text{dis}} + P_{\text{out}}$.

A measurement of S21 near a resonance f_0 is a Lorentzian in linear units,

$$\frac{P_{\text{out}}}{P_{\text{in}}}(f) = A_0 \frac{\delta f}{(f - f_0)^2 + \delta f^2/4} + B_0, \tag{5.49}$$

which can be fit to obtain f_o and the linewidth δf (FWHM). The maximum is $|S_{21}|^2 = 4A_0/\delta f$ and the quality factor is $Q_{\text{tot}} = f/\delta f$ by definition.

It is possible to separate the total Q into coupling and internal Qs in a transmission measurement only if it is calibrated. First, we know that

$$|S_{21}|^2 = \frac{4Q_{\text{tot}}^2}{Q_{\text{in}}Q_{\text{out}}} \tag{5.50}$$

If we assume $Q_{\text{in}} = Q_{\text{out}} = Q_c$, then we arrive at $Q_c = Q_{\text{tot}}/|S_{21}|$.

If $Q_{\text{int}} > Q_c$, we say the cavity is *overcoupled*. A very strongly overcoupled transmission peak approaches 0 dB, meaning unity transmission. In the *critically coupled* case, $Q_{\text{tot}} = Q_{\text{int}}/2 = Q_c/2 = Q_{\text{in}}/4 = Q_{\text{out}}/4$, assuming symmetric coupling. Then $|S_{21}|^2 = 1/4 = -6$ dB. Also, $|S_{11}|^2 = 1/4$ and $\frac{P_{\text{dis}}}{P_{\text{in}}} = 1/2$. If *undercoupled*, $|S_{21}|^2$ is small.

Note that equation 5.50 is only true if the transmission S-parameter is measured at the resonator ports. However, cables, attenuators and amplifiers in the measurement setup impose frequency-dependent offsets. To use equation 5.50, the setup must be calibrated or the background subtracted.

Hanger configuration:
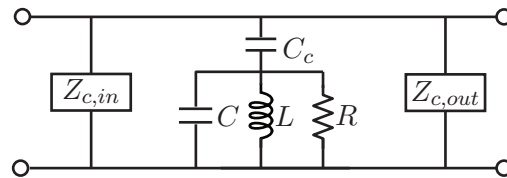
FIGURE 5.7: **Circuit diagram of a resonator in the hanger (or shunt) measurement configuration.**

A different way to measure a resonator is to use a microwave-T to place the resonator between the center conductor and ground of the measurement transmission line, as diagrammed in figure 5.7. On resonance, power is coupled to the resonator and dissipated inside, while off-resonant frequencies simply transmit along the line. Measurements in this "hanger" or "shunt" configuration have the advantage that the resonance can be fit to extract coupling and internal Qs without knowledge of offset in total transmission level. The far off-resonant behavior of the measurements serve as a calibration that enables extraction of the internal and coupling Qs. Derivations of this technique are found in Khalil et al., 2012, and Geerlings, 2013. A summary of applicable results is found in Reagor, 2015–chapter 5.1.

Simple resonator models predict a dip in S21 symmetric about the resonance ω_o with linewidth $\Delta\omega$ as power is coupled from a feedline to the resonator. Typical measurements display an asymmetric dip due to reflections in the feedline to which the resonator is capacitively coupled. See Geerlings, 2013–Appendix A or Probst et al., 2015. The lineshape

TABLE 5.1: **Hanger resonator** Q_c/Q_i. On resonance, the dip in transmission with the hanger configuration is simply Q_c/Q_i, enumerated in dB for convenience in this table.

Q_c/Q_i	$|S_{21}|^2$ (dB)
0.01	-40
0.1	-20
0.3	-12
0.5	-10
1	-6
2.5	-3
4	-2
10	-0.8
100	-0.08

is described by

$$|S_{21}| = 1 - \frac{\frac{Q_{\text{tot}}}{Q_c} - 2iQ_{\text{tot}}\frac{\delta\omega}{\omega_o}}{1 + 2iQ_{\text{tot}}\frac{\omega-\omega_o}{\omega_o}}. \tag{5.51}$$

On resonance, the insertion loss is

$$|S_{21}| = 1 - \frac{Q_{\text{tot}}}{Q_c} = \frac{Q_c}{Q_c + Q_{\text{int}}} \tag{5.52}$$

One can estimate both the total Q and ratio of coupling to internal Qs at a quick glance. See table 5.1. At critical coupling ($Q_{\text{int}} = Q_c$), the dip of a hanger resonance is -6 dB. If the resonator is far undercoupled $Q_{\text{int}} \ll Q_c$, the dip is very small, making it difficult to measure, especially at low powers. In the overcoupled case, $Q_{\text{int}} \gg Q_c$ and the total (loaded) Q may be limited by the coupling Q, hindering accurate determination of internal Q.

To extract this information accurately, the best method is to fit the data near resonance in the complex plane, as we illustrate in figure 5.8. Measurements are most efficient if the measurement points are taken at frequencies evenly spaced about the circle in
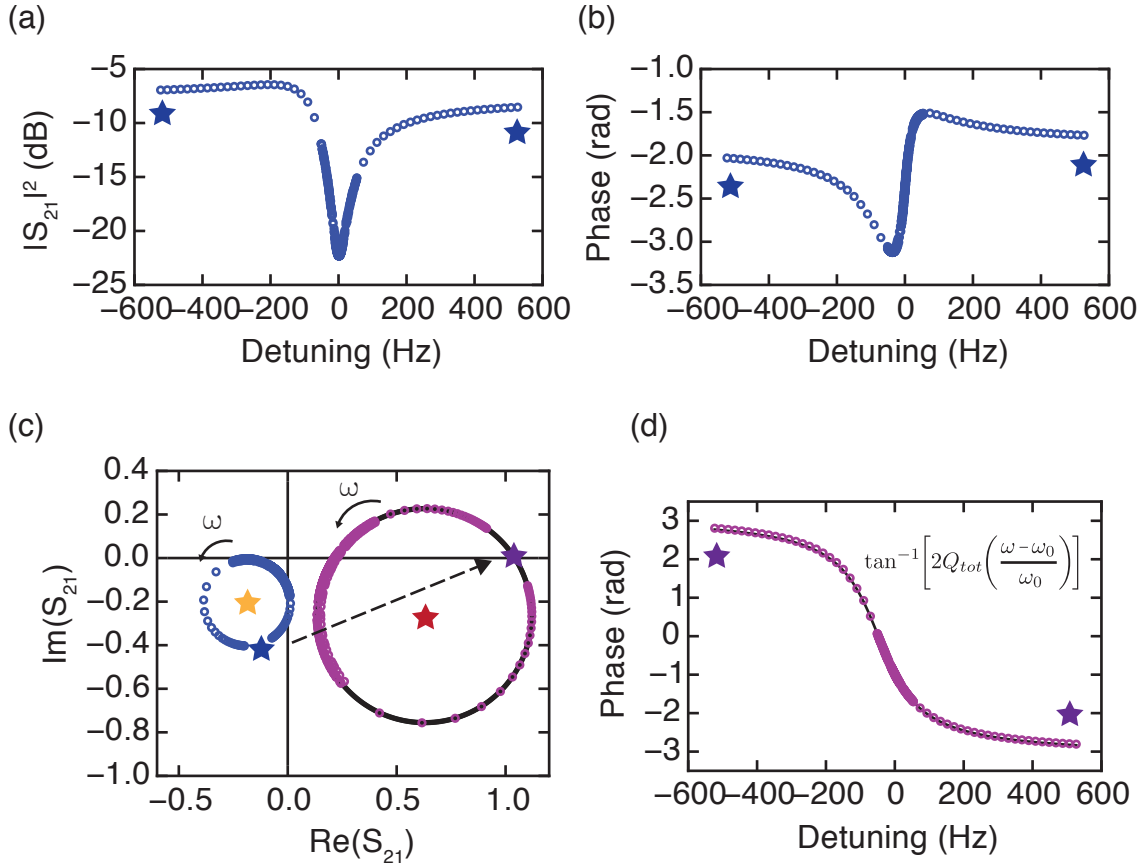
FIGURE 5.8: **Fitting quality factors in the complex plane. (a) (b)** Raw data (blue) for the transmitted signal through a shunt resonator. Because the VNA is not calibrated at the ports of the device, we must transform the signal in post-processing by the far detuned signal levels. Transformed data is purple. **(c)** A convenient representation for the signal is to evaluate the best-fit circle along the parametric angle $\theta(\omega)$ to give the rato $Q_{\text{tot}}/Q_{\text{int}}$. **(d)**The phase wraps at a rate given by Q_{tot}. (Figure used with permission from Reagor, 2015. See Copyright Permissions.)

$(\text{Re}\,[S_{21}]\,,\text{Im}\,[S_{21}])$. Ideally, the resonance is a circle as follows:

$$S_{21} = 1 - \frac{Q_{\text{tot}}}{2Q_c}\left(1 + e^{2i\theta}\right) \tag{5.53}$$

Several realities of our experimental setup cause the measured lineshape to differ from this ideal form. First, impedance mismatches are inevitably present, and there is the possiblity

of cross-talk. The effects can be accounted for by allowing an imaginary component of the coupling Q. Furthermore, both loss and phase-delay are accumulated through coaxial cable on both sides of the resonator. These two effects can be accounted for with a scaling term $Ge^{j\omega\tau}$, where τ is the electrical delay and G is a complex gain. Therefore, in reality we have a lineshape that can be modeled (Probst et al., 2015) as

$$S_{21} = Ge^{j\omega\tau} \left[1 - \frac{Q_{\text{tot}}}{2Q_c} \left(1 + e^{2i\theta} \right) e^{-i\epsilon} \right]. \tag{5.54}$$

The non-idealities have the effect of scaling, rotating and displacing the resonance circle, and sometimes the resultant distortions are severe, but almost always possible to transform back to the form in equation 5.53.

5.3.3 Extracting photon number

This subsection explains how to approximate the steady state circulating energy $\bar{n}$ during a cavity measurement. Recall that $Q_{\text{tot}} = \omega/\kappa$. Contributing to the decay rate κ is the rate of energy leaving the resonator through intentional coupling, ω/Q_c, as well as all of the internal losses discussed earlier in this chapter. One or more of these internal loss mechanisms can depend on the stored energy in the resonator, and we have yet to completely understand all parts of this. One of the more studied power dependent mechanisms is the dielectric dissipation due to two-level systems (TLSs), causing Q_{int} increase and then saturate at higher photon numbers (Geerlings, 2013). We measure and discuss these power dependent effects for our devices later in section 7.5. For now, let our interest in studying such loss mechanisms motivate our calculations of circulating powers.

Circulating energy in a resonator is related to average photon number by

$$E_c = \hbar\bar{n}\kappa, \tag{5.55}$$

where $\kappa = \omega/Q_{\text{tot}}$. The average number of photons in the resonator is

$$\bar{n} = \frac{E_c Q_{\text{tot}}}{\omega \hbar}. \tag{5.56}$$

A steady state of develops when there is rate of incoming energy (P_{in}), outgoing energy (P_{out}), and a rate of energy that is dissipated due to loss inside the resonator (P_{dis}). The circulating energy (E_{circ}) is the steady state energy that exists in the driven resonator. If the drive is turned off, ωE_{circ} refers to the rate at which photons leave either through coupling to the outside or internal dissipation. For the case of an under-coupled cavity ($Q_c \gg Q_{\text{int}}$) for example, the circulating energy can be much greater than the dissipated power. We can formulate the internal Q in terms of the dissipated power in the following way:

$$Q_{\text{int}} = \frac{\omega W_m}{P_{\text{dis}}}, \quad \text{where} \tag{5.57}$$

$$P_{\text{dis}} = \hbar \omega_0 \bar{n} \kappa_{\text{int}}, \tag{5.58}$$

where $\kappa_{\text{int}} = \omega/Q_{\text{int}}$. The average number of photons in the resonator is

$$\bar{n} = \frac{P_{\text{dis}} Q_{\text{int}}}{\omega \hbar}. \tag{5.59}$$

Exploring this relationship a little further, let us write

$$\frac{1}{Q_{\text{tot}}} = \frac{E_{\text{circ}}}{W_m} = \frac{1}{Q_{\text{int}}} + \frac{1}{Q_c} = \frac{P_{\text{dis}}}{\omega W_m} + \frac{1}{Q_c}. \tag{5.60}$$

We find that the circulating energy and the dissipated power are related through the coupling Q as

$$\omega E_{\text{circ}} - P_{\text{dis}} = \frac{\omega W_m}{Q_c}. \tag{5.61}$$

We can calculate the power dissipated in the cavity as a ratio to the input power ($P_{\text{dis}}/P_{\text{in}}$) in terms of parameters we pull from the measured resonance peaks (Qs and

S-parameters). [5] This ratio depends on the configuration in which the measurement of known P_{in} is done. We can use a VNA to measure of the insertion loss $|S_{21}|^2 = P_{\text{out}}/P_{\text{in}}$ (or $|S_{21}| = V_{\text{out}}V_{\text{in}}$) while driving with a controllable P_{in}.

Transmission configuration:

A quick estimate of the input power in transmission can be made by thinking of output VNA power and additional attenuation before the resonator. For example, there may be -60 dB of attenuation on the input lines of the fridge and an additional -3 dB per 6-foot length of blue coax cable. You can also do a measurement of the chain without the cavity as a calibration.

Let us begin with

$$|S_{21}|^2 = \frac{P_{\text{out}}}{P_{\text{in}}} = \frac{4Q_{\text{tot}}^2}{Q_{\text{in}}Q_{\text{out}}}. \tag{5.62}$$

The on-resonance reflected power from input (return loss) is

$$
\begin{aligned}
|S_{11}|^2 = \frac{P_{\text{ref}}}{P_{\text{in}}} &= 1 - \frac{P_{\text{dis}}}{P_{\text{in}}} - \frac{P_{\text{out}}}{P_{\text{in}}} \\
&= 1 - \frac{4Q_{\text{tot}}^2}{Q_{\text{in}}Q_{\text{int}}} - \frac{4Q_{\text{tot}}^2}{Q_{\text{in}}Q_{\text{out}}}.
\end{aligned}
\tag{5.63}
$$

So we infer that

$$\frac{P_{\text{dis}}}{P_{\text{in}}} = \frac{4Q_{\text{tot}}^2}{Q_{\text{in}}Q_{\text{int}}}. \tag{5.64}$$

Equipped with this ratio, one may then use equation 5.59 to find the average number of photons circulating in the resonator in terms of the quality factors (if known) and input power:

$$\bar{n} = \frac{4}{\omega\hbar}\frac{Q_{\text{int}}Q_{\text{tot}}^2}{Q_{\text{in}}Q_{\text{out}}}P_{\text{in}}. \tag{5.65}$$

---

[5] In doing so, we can talk about voltage or power ratios in linear units or in decibels, which are related by

$$(\text{dB}) = 10\log_{10}(\text{ratio in linear units}).$$

We now try to develop and expression using S-parameters. If the coupling is symmetric ($Q_\text{in} = Q_\text{out}$), equation 5.14 and equation 5.3.3 combine to give us

$$Q_\text{in} = \frac{2Q_\text{tot}}{S_{21}}, \quad \text{and} \tag{5.66}$$

$$Q_\text{int} = \frac{Q_\text{in}Q_\text{tot}}{Q_\text{in} - 2Q_\text{tot}}. \tag{5.67}$$

This enables us to write

$$\frac{P_\text{dis}}{P_\text{in}} = 2(1 - S_{21})S_{21}. \tag{5.68}$$

What if the input and output coupling is different? Let $Q_\text{in} = \gamma Q_\text{out}$. Then

$$|S_{21}|^2 = \frac{4Q_\text{tot}^2}{\gamma Q_\text{out}^2}. \tag{5.69}$$

After expanding equation 5.14 and solving for internal Q,

$$Q_\text{int} = \frac{\gamma Q_\text{tot}Q_\text{out}}{\gamma Q_\text{out} - (1 - \gamma)Q_\text{tot}}. \tag{5.70}$$

The ratio of the power dissipated in the cavity to the input power becomes

$$\frac{P_\text{dis}}{P_\text{in}} = \frac{4Q_\text{tot}^2 \left(\gamma Q_\text{out} - (1 + \gamma)Q_\text{tot}\right)}{\gamma^2 Q_\text{out}^2 Q_\text{tot}}, \tag{5.71}$$

or, expressed in terms of insertion loss,

$$\frac{P_\text{dis}}{P_\text{in}} = \frac{2|S_{21}|}{\sqrt{\gamma}} - (1 - \gamma)|S_{21}|^2. \tag{5.72}$$

Equipped with this ratio and knowing the input power, one may then use equation 5.59 to find the average number of photons circulating in the resonator.

Hanger configuration:

In a hanger measurement, you can use the baseline away from resonance to infer P_in. It

is also possible to extract the circulating power in a cavity under measurement in a hanger configuration by the lineshape and input power alone. To begin, we analyze the circuit in figure 5.7 at the obvious node. First, current conservation gives

$$I_{\text{in}} = I_{\text{ref}} + I_c + I_{\text{thru}}. \tag{5.73}$$

Next, the voltage at the node is

$$V_{\text{in}} + V_{\text{ref}} = V_{\text{thru}} = V_c. \tag{5.74}$$

So we can write

$$V_{\text{thru}} = V_c = S_{21}V_{\text{in}}, \quad \text{and} \tag{5.75}$$

$$V_{\text{ref}} = V_{\text{in}}(S_{21} - 1). \tag{5.76}$$

We can also express

$$
\begin{aligned}
I_c &= I_{\text{in}} - I_{\text{ref}} - I_{\text{thru}} \\
&= I_{\text{in}} - (S_{21}I_{\text{in}} - I_{\text{in}}) - S_{21}I_{\text{in}} \\
&= 2I_{\text{in}} - 2S_{21}I_{\text{in}}.
\end{aligned} \tag{5.77}
$$

Then, substituting, the dissipated power is

$$
\begin{aligned}
P_{\text{dis}} &= (2I_{\text{in}} - 2S_{21})S_{21}V_{\text{in}} \\
&= 2P_{\text{in}}(1 - S_{21})S_{21}.
\end{aligned} \tag{5.78}
$$

Then, using equation 5.52, we can write the required power fraction in terms of either insertion loss alone or Qs:

$$\frac{P_{\text{dis}}}{P_{\text{in}}} = 2(1 - S_{21})S_{21} \tag{5.79}$$

$$\frac{P_{\text{dis}}}{P_{\text{in}}} = \frac{2Q_{\text{int}}Q_c}{(Q_c + Q_{\text{int}})^2}. \tag{5.80}$$

Note that this is the identical result as for the transmission configuration with symmetric coupling, equation 5.68.

Knowing the input power, we can now relate the circulating power in a resonator of a certain Q_{int}, to the number of photons with equation 5.56, as

$$\bar{n} = \frac{Q_{\text{int}}}{\omega\hbar}\left(2(1 - S_{21})S_{21}\right)P_{\text{in}} \tag{5.81}$$

$$= \frac{2}{\omega\hbar}\frac{Q_{\text{int}}^2 Q_c}{(Q_c + Q_{\text{int}})^2}P_{\text{in}}, \tag{5.82}$$

where we have again used equation 5.52. Alternatively, in terms of Q_{tot} and Q_c only, we can write

$$\bar{n} = \frac{Q_{\text{int}}}{\omega\hbar}\left(2\frac{Q_{\text{tot}}}{Q_c}\left(1 - \frac{Q_{\text{tot}}}{Q_c}\right)\right)P_{\text{in}}$$

$$= \frac{2}{\omega\hbar}\left(\frac{Q_c Q_{\text{tot}}}{Q_c - Q_{\text{tot}}}\right)\frac{Q_{\text{tot}}}{Q_c}\left(1 - \frac{Q_{\text{tot}}}{Q_c}\right)P_{\text{in}}$$

$$\bar{n} = \frac{2}{\omega\hbar}\frac{Q_{\text{tot}}^2}{Q_c}P_{\text{in}}. \tag{5.83}$$

5.4 Seam loss in 3D cavities

We now put the techniques in this chapter to use in studying the effects of seam loss (section 5.2.5) in 3D cavities. Before we begin this discussion, note that the planes along which the rectangular cavity may have a seam in construction are defined as shown in figure 5.9.
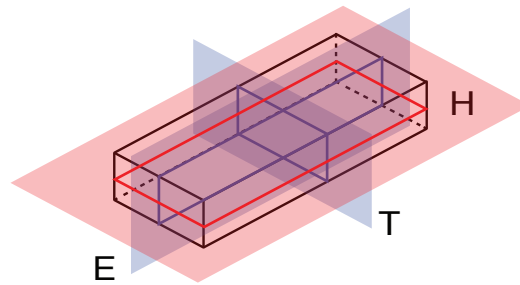
FIGURE 5.9: **Planes along which the rectangular cavity may have a seam in construction.** The blue E-plane is parallel to the electric fields and propagation direction of waveguide, were it not truncated to form a resonator. The red H-plane is parallel to all magnetic fields. Perpendicular to both of these is the transverse plane, or T-plane shown in blue, which intersects the propagation direction of the waveguide.

5.4.1 Microwave cavity choke

One design solution to reduce loss at a seam is a *choke*. Choke flange couplers are commonly used to join sections of waveguide, as shown in figure 5.10**(a)**. They are essentially branch waveguides, one-half wavelength long, in series with the main waveguide (Ridenour, 1948 - section 2.17). For ease of manufacture, the choke groove is often circular, even if the waveguide is rectangular. The radius and depth of the groove are so chosen that no current flows across the joint between the choke and the flange. The outer groove is itself a section of low-impedance coaxial line excited principally in the TE102 mode. This groove is made to be a quarter wavelength ($\lambda/4$) deep so that the minimum-current point occurs at the flange contact, as shown in figure 5.10.

The principle of a $\lambda/4$ choke groove, while typically used in waveguide flanges, can also be effective for use in 3D cavities. For example, in a study on cavity QED with Rydberg atoms uses superconducting lead-plated copper and niobium cylindrical cavities that must have a gap between two halves of their construction so that field can be coupled to a beam of atoms inside. A choke groove was added to reduce the radiation loss in such split cylindrical cavities to the effect of improving the Q by two orders of magnitude up to $Q = 4 \times 10^7$ (Hughey et al., 1990).

Implementation of a choke groove to rectify seam losses in rectangular cavities has

been a success in the lab. Remarkably, a superconducting aluminum rectangular cavity with an internal Q limited by seam effects to 5000 was brought to $Q = 2.5 \times 10^7$ by implementing a *cover choke* designed for the cavity frequency. Figure 5.10(b) diagrams the "cavity cover choke". Experimentally, cavity dimensions were $a = 19, d = 28, b = 5$ mm and we chose to implement a circular choke. Simulations in HFSS were used to optimize cover choke dimensions of groove diameter, groove depth, groove width and gap. As a starting point, the groove depth should be approximately $\lambda/4 = 8$ mm, as should the maximum distance between the cavity boundary and the groove. Secondly, it is desirable to choose a small (but still possible to machine) groove width and gap in order to perturb the original rectangular cavity mode as little as possible with the added volume. Next, we calculate he total current passing the seam (which is circular) as the integral of surface currents perpendicular to it. Choosing groove width of 12.7 mm and a gap of 0.25 mm, the optimum groove diameter is 35.5 mm and groove depth is 8.4 mm. As noted, this affects a radical improvement in quality factor, and frequency of the cavity's TE101 mode is only slightly perturbed: 9.50 GHz originally versus 9.54 GHz with the cover choke. 9% of the new mode's energy resides in the cover choke.

The cover choke has enabled measurements of micromachined wafers as well (cavity height $b = 0.33$ mm), boosting an aluminium-covered micromachined cavity wafer from $Q = 1000$ to 5.0×10^6. For this measurement, the same cover choke with dimensions described above was used. In this case, 58% of the mode's energy resides in the cover choke. Despite the proven effectiveness in minimizing seam admittance, its bulkiness is a significant detractor, and the principle of a 3D cover choke is incompatible with the MMIQC design. Additionally, the choke introduces additional modes to the spectrum. Though they have little field in the cavity, having extra modes in close proximity is a disadvantage to any design. For the case of the taller cavity, the nearest extraneous mode is 500 MHz away, and in the case of the micromachined cavity, the nearest extraneous mode is 400 MHz away.
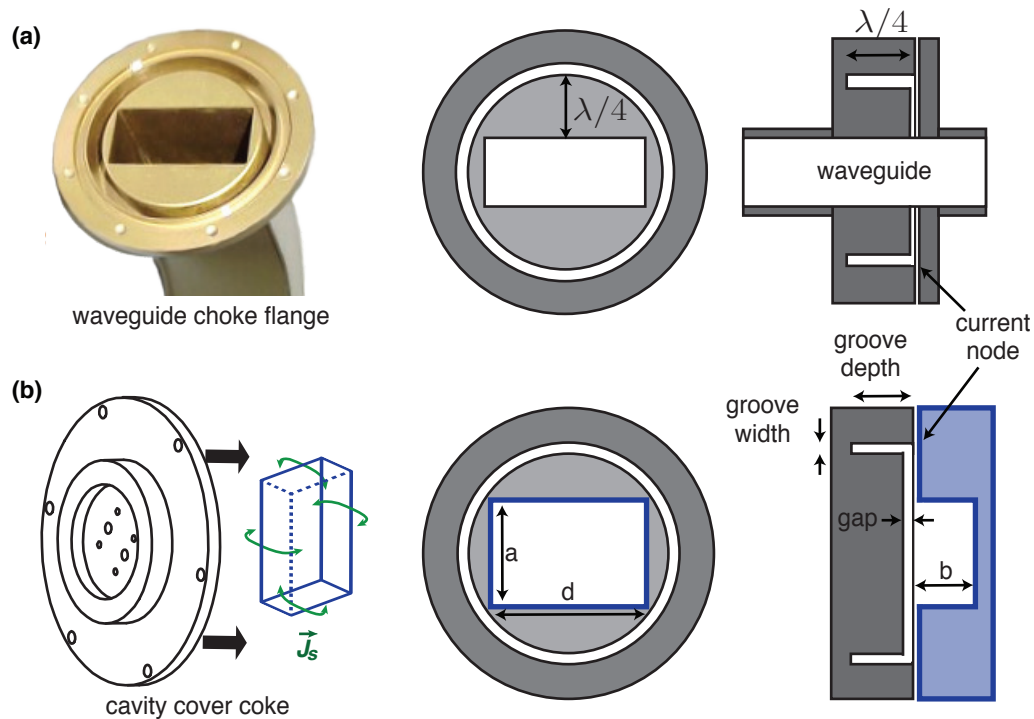
FIGURE 5.10: **Microwave choke flange and cavity cover choke.** **(a)** Microwave chokes are frequently used in waveguide flanges. The groove is placed a quarter wavelength away from the waveguide and machined a quarter wavelength into the flange block. This way, there is a microwave *short* at the bottom of the groove, placing a current node at the joint of the waveguide-to-waveguide junction. This reduces radiation and seam losses at the joint. **(b)** The same principle can be applied to a cavity resonator (blue) with a seam in the H-plane. We modify the geometry of the "cover" (grey) such that the seam occurs at a surface current node.

Attempts to apply a choke groove to the rectangular cavity with an E-plane seam (figure 5.1(c)) are not effective. Quality factors were not improved in either of three attempted cases: (1) a cavity with symmetric E-plane seam, (2) a cavity with symmetric E-plane seam loaded with a sapphire chip to dielectrically perturb fields asymmetrically, (3) a cavity with a 10% asymmetric E-plane seam.

5.4.2   Aluminum 3D cavities with various seam configurations

Figure 5.11 presents several measurements of internal quality factors for rectangular cavity resonators. We first discuss the cavity geometries with reference to the aluminum cavity

quality factors (red points). These devices were machined in bulk metal to various geometries and assembled with several seam locations to study the effect different y_seam. The left-most geometry represents a symmetric cavity geometry like those used in 3D cQED experiments (figure 5.1**(c)**, which is assembled in two halves that meet at a seam in the E-plane. Machining imprecision of ± 2 mils may cause deviation from the ideal $y_\mathrm{seam} = 0$, and this is the reason we draw a break with an estimate admittance on the horizontal axis for this geometry. In bulk aluminum, these cavities typically have $Q_\mathrm{int} = 10^6 - 10^7$. Pure ($> 4$N) aluminum cavities, when chemically etched, have higher Q_int due to reduced surface loss.

To study the losses at the seam, we machined mating cavity parts in aluminum alloy to have either a 5% or 10% asymmetry along their length such that, once assembled, the E-plane seam was not centered (figure 5.11**(b)**). The increased y_seam is accompanied by 60% and 85% reductions in Q_int compared to the cavity with symmetric E-plane seam. We also constructed cavities of similar dimensions with seams in the H-plane (figure 5.11**(c)**). Aluminum cavities with H-plane seams (figure 5.11**(c)**) had quality factors limited to 5×10^3. The cavities with the most seam admittance (figure 5.11**(d)**) are made with a height of 300 μm, which is feasible to micromachine in a wafer. In addition to the discussed sensitivity to seam losses, these thin cavities are also more sensitive to surface and conductor losses when compared to larger cavities, with participation ratios scaling inversely with cavity height. It is clear from our measurements, however, that the dominant loss mechanism for these aluminum cavities is related to the seam. Taking $g_\mathrm{seam} = 10^4 \,/\Omega\mathrm{m}$ as a likely limit for the aluminum alloy cavities, this implies an average total conductance of $G_\mathrm{seam} = 1/\left[1.25\,\mu\Omega\right]$.
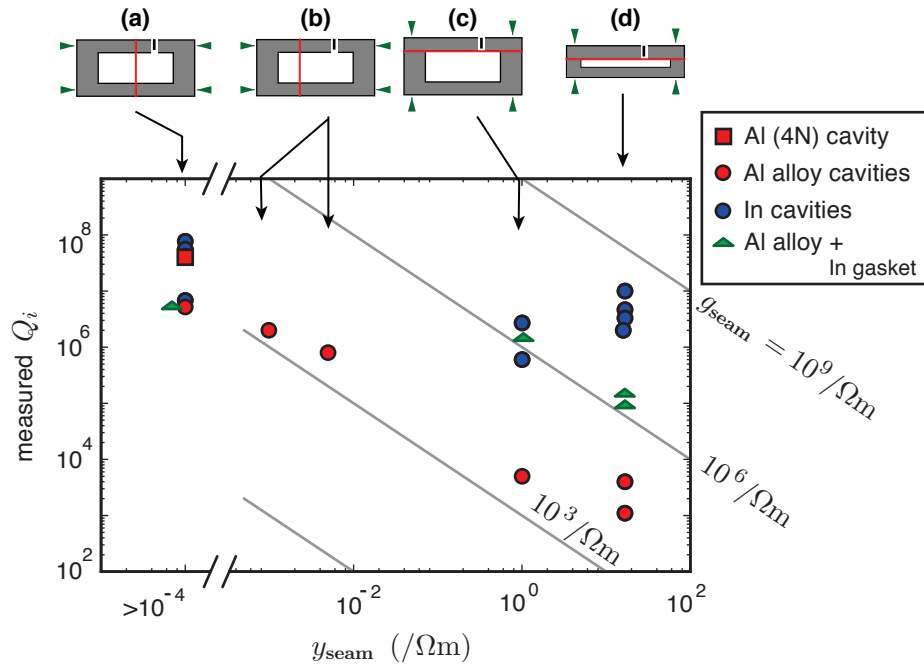
FIGURE 5.11: **Measured quality factor versus seam admittance.** Internal quality factors of cavity resonators plotted against seam admittance. Each y_{seam} is calculated using the known fields of the cavity geometry and a seam path. Grey lines correspond to several g_{seam} values. **(a)-(d)** Pictorial descriptions show a T-plane cross-section of several cavity constructions. Dimensions of cavities of types (a)-(c) were approximately $33 \times 18 \times 5$ mm. The dimensions of cavity type (d) were $28 \times 19 \times 0.3$ mm and $22 \times 24 \times 0.3$ mm. All cavities were coupled using a pin in a sub-cutoff waveguide, measured in hanger configuration at 20 mK, and had TE101 resonances between 9.45 - 9.54 GHz. The two halves of all the cavities were bolted together with four screws that remained during measurement, applying force indicated by green arrows.

5.4.3 Indium 3D cavities

We are interested in how the choice of superconductor affects the conductor, dielectric, and seam losses of cavities. This thesis concerns the use of indium resonators mainly because of its utility for wafer bonding, which we will arrive at in chapter 7. As we know, micromachined cavities in bonded wafer stacks have geometrical constraints that conventionally machined cavities do not. But we do not let that discourage us from employing a variety of cavity geometries to determine bounds on the loss mechanisms in cavities using this material. In this section, we show experiments using conventionally machined cavities with indium walls.

Indium is extremely ductile and soft, making it impractical to machine in bulk. Therefore, the cavity geometries were created in bulk OFHC (oxygen free high conductivity) copper and then electroplated with indium. The thickness of the indium must exceed the penetration depth [6] The thickness of material electroplated onto a concave object can be highly non-uniform, with less material being deposited on the interior corners. Therefore, the electroplated layer was made copiously thick to ensure that the interior corners of the cavities were coated.

The blue points in figure 5.11 do not trend downward with a line of constant conductance with increasing seam admittance. Therefore, none of these cavities are likely to be limited by losses at their seams. The upper-right-most point places a bound on indium-indium seam conductance at $g_{\text{seam}} = 10^8 /\Omega\text{m}$, meaning that the total conductance of the cavity can be at least as high as $G_{\text{seam}} = 1/[70\,\text{n}\Omega]$. The same measurement also places a bound on the conductor loss (see section 5.2.3) of the indium surface of $Q_S = q_{\text{cond}} > 3 \times 10^3$. This follows having calculated $p_{\text{cond}} = 1.8 \times 10^{-4}$. With this satisfactory bound, and a seam conductance far exceeding that of aluminum, we conclude from these machined cavity experiments that indium is a viable candidate for construction of seams in MMIQCs.

5.4.4 Indium gasket

Let us assume we want to use cavities machined in aluminum. Can we improve the quality factors by adding indium just around the seam? After a simple experiment, it was found that this indium gasket strategy is effective up to a level of conductance $g_{\text{seam}} \approx 10^6 /\Omega\text{m}$.

The experiment was conducted by applying an indium gasket to some previously measured aluminum alloy (6061) cavities of figure 5.11 measurements. The cavities were opened, the mating surfaces buffed with fine grain sandpaper (to remove surface oxide), then sonicated in acetone and methanol for several minutes each. Then, a 0.5 mm gage

---

[6]The penetration depth of superconducting bulk crystalline indium was measured to be 43 nm at 3 GHz (Dheer, 1961).

indium wire was laid around the perimeter about 2 mm away from the cavity wall in one part, and the mating part was bolted on. The cavities were then measured with the same couplers at ~ 15 mK for fair comparison. Referring to the H-plane cut cavities, the application of an indium gasket to cavity type **(c)** boosted the internal Q from 5,000 to 1.5 million. The application of an indium gasket to cavity type **(d)** boosted the internal Q from 1,300 to 250,000. These cavities with indium gaskets are placed on the graph as green triangles. Symmetric E-plane cavities are not improved by application of indium gasket. However, it is standard practice in the lab to use an indium gasket around the seam of these cavities when there are qubits inside because the substrate chip (either sapphire or silicon) is a dielectric perturbation that disturbs the symmetry of the cavity mode, necessarily increasing the admittance to the seam.

5.5 Conclusion

In this chapter we have broadly covered microwave resonators. After introducing several different forms they may take (transmission line, compact, 3D cavity, or hybrid forms), we used a *participation* framework to account for different loss mechanisms that affect the quality factor. Then, we described how superconducting resonators are characterized in the lab.

The experiments shown in the last section clearly show the importance of the seam as a loss mechanism. Furthermore, it is possible to choose geometrical designs with attention to currents at the seam location. The choice of material also affects seam loss, and in this section we have established that indium is a promising candidate for low-loss superconducting seams in 3D cavities. In chapter 7, we will investigate other aspects of indium as a bonding material and as a superconductor. First, we concentrate on making and measuring 3D rectangular cavities in silicon wafers.

Chapter 6

Micromachined cavity resonators

6.1 Introduction

In this chapter, we cover micromachined cavity resonators, including the methods of etching a cavity pit in a wafer, coating it with superconductor, and bonding components together in four different coupling schemes for measurement. Our discussion of coupling schemes will include simulations and measurements.

6.2 Fabrication

This section concerns the lithographic masking, etching and metalizing of the pits in silicon wafers that form micromachined rectangular cavities. We have claimed that the resulting superconducting resonator devices are an important demonstration of viability for all of the superconducting enclosures quintessential to MMIQCs. These fabrication procedures are also listed step-by-step, with more details but less discussion, in appendix A.

6.2.1 Bulk etching

There are several options for removing material to create a large rectangular pit in a wafer. The most convenient method for our purpose is a chemical wet etch of potassium hydroxide (KOH) into silicon substrate masked by silicon nitride. Another silicon wet etch option
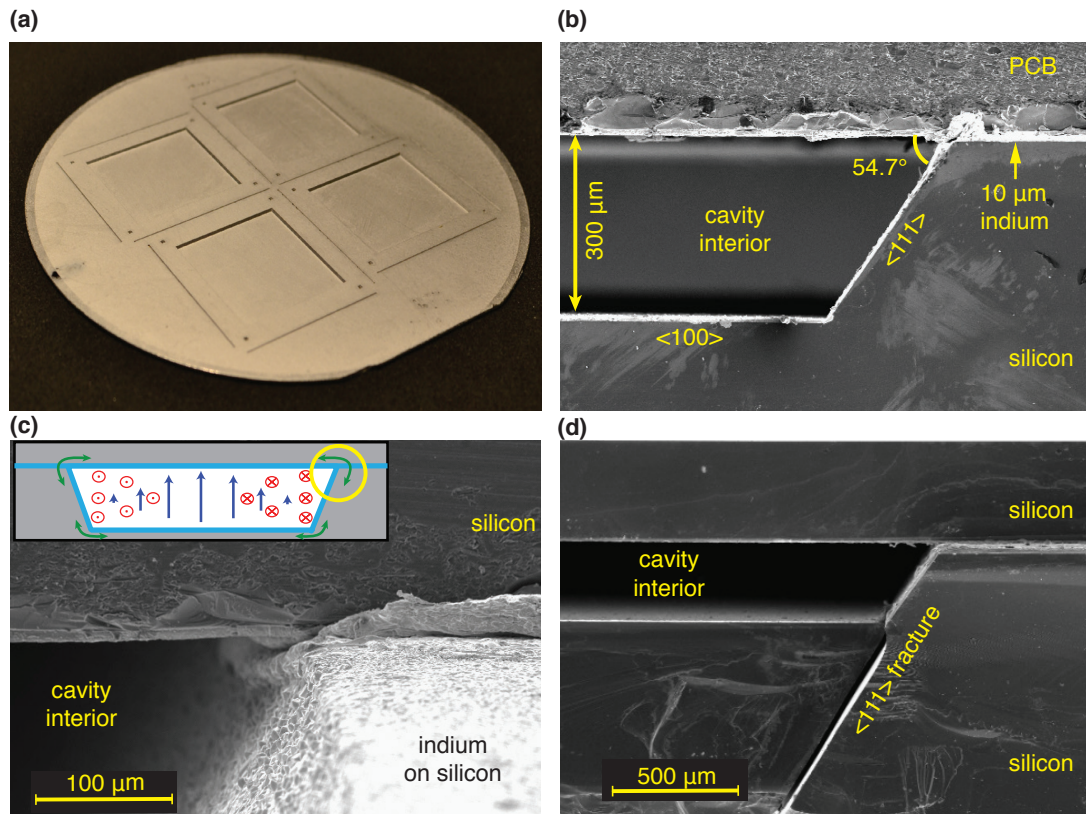
FIGURE 6.1: **Pictures of micromachined cavities. (a)** A 100 mm diameter silicon wafer can accomodate four rectangular cavities with frequency ≈ 9.5 GHz. The wafer is shown after cavity etching and indium electroplating. **(b)** An SEM cross-section of the assembled cavity shows the depth of the cavity and the angle of the side wall as determined by silicon's crystal planes. **(c)** An SEM image showing indium deforming at the contact region (indicated with the cartoon inset, where electric fields are blue, magnetic fields are red, and surface currents are green). **(d)** An SEM image showing a fractured 1 mm thick cavity chip.

is tetra-methyl-ammonium hydroxide (TMAH) masked by silicon oxide. Both methods were tried. The benefits of KOH over TMAH are:

- Depositing and etching nitride is faster, easier, and safer than growing oxide.

- The mask selectivity is an order of magnitude better. [1]

- KOH is considered less toxic than TMAH, though they are both caustic/corrosive.

---

[1]The mask selectivities are 480:1 for TMAH etch of silicon masked with our grown silicon oxide versus 6300:1 for KOH etch of silicon masked with our PECVD nitride.
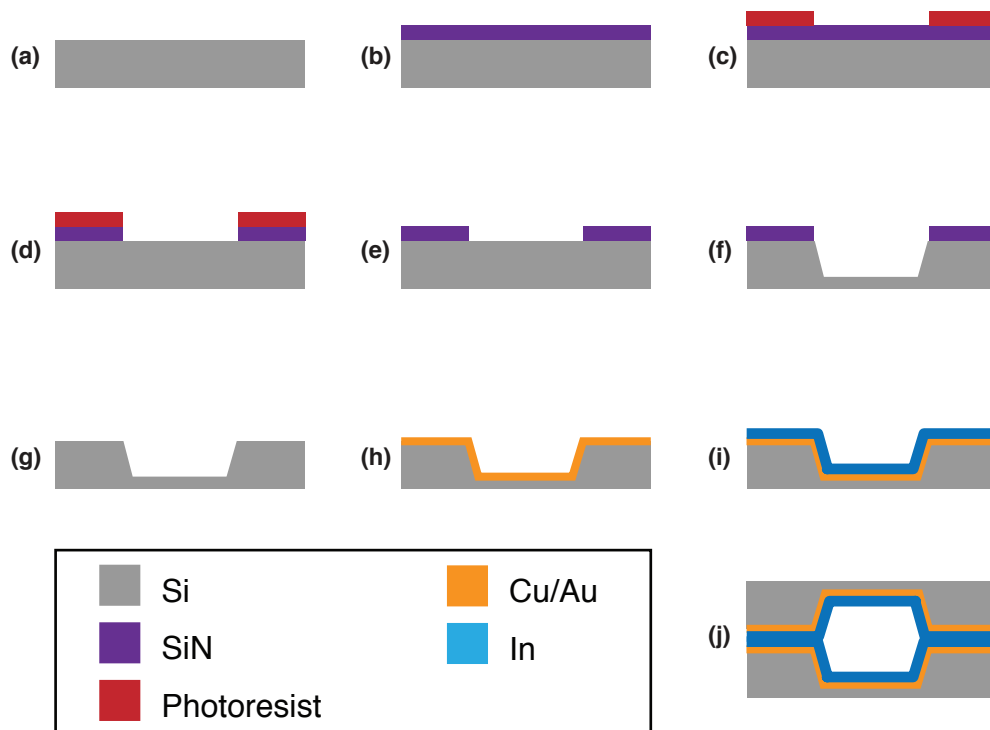
FIGURE 6.2: **Fabrication steps for micromachined cavities.** Beginning with a Silicon wafer **(a)**, a nitride mask is created **(b)-(e)**, the silicon is etched **(f)**, the mask is removed **(g)**, and the wafer is metalized **(h)-(i)**.

- KOH etch is a much faster silicon etchant than TMAH, by a factor of 3-5 times, meaning that the cavity etches we will describe take a total of about 3 hours rather than 10.

The negative aspects of using a KOH etch are:

- The resultant surface roughness is higher due to increased etch speed.

- It leaves a residue salt of potassium (K^+) which is incompatible with MOS or CMOS processing.

Dry etching options, such as DRIE, were not explored for creating the cavity, because it was suspected that the side-walls especially would be comparatively rough and difficult to completely coat with metal.

Following figure 6.2, we begin with a silicon wafer 500-1000 μm thick in (100) orientation **(a)**. First, the wafer is cleaned by sonication in solvents and dip in BOE to remove

native oxide. Next, a 150 nm layer of silicon nitride is deposited by PECVD **(b)**. A mask with large rectangles is transfered into the nitride layer by photolithography with S-series positive photoresist **(c)** followed by plasma etching ($CHF_3 + O_2$) the nitride **(d)** and removing the photoresist **(e)**.

Next, the cavity recesses are etched by a KOH bath **(f)**, wherein the following redox reaction occurs:

$$Si + 2OH^- + 4H_2O \rightarrow Si(OH)_2^{2+} + 2H_2 + 4OH^- \tag{6.1}$$
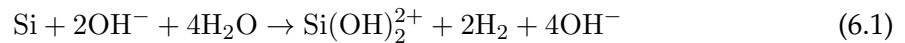
The crystalline silicon dissolves accompanied by a release of hydrogen gas bubbles. The etch bath consists of 30% by weight KOH in water with 1% Isopropanol added as a surfactant intended to reduce surface roughness. At 88°C, it etches silicon with a rate 95 μm/hr. The etch rate has an exponential dependence on temperature. A slower option is the same bath set to 75°C for etch rate 50 μm/hr. Since etch bath reactants are not significantly consumed by individual wafer etches, the bath is saved in a closed jug and reused for many wafer etches. To maintain consistent etch rate, water must be added to compensate for evaporative loss. For the cavities in this chapter, KOH was used to create 22×24 mm rectangular pits to depths around 300 μm deep. Desired depth is achieved by knowing the etch rate and stopping the etch with copious DI water rinsing at the appropriate time.

The wet etch is anisotropic with selectivity to silicon's (100) : (111) planes, resulting in a rectangular recess with sidewalls determined by the crystal planes. An angle of 54.7°results, as seen in figure 6.1. These angled sidewalls are actually beneficial when it comes to metalizing the 3D structures. In section 6.4, we will find that the perturbation to the cavity frequency is small. The bottom of the pits have an RMS surface roughness of $R_q = 20 - 40$ nm. We measure a selectivity of 30:1 between the (100) : (111) crystal planes, which results in an undercut of the mask of about 2% of the cavity depth. Additionally, the PECVD nitride mask is etched at 15 nm/hr at 88°C, indicating a mask selectivity of 6300:1.

After the KOH etch, the nitride mask can be removed (figure 6.2**(g)**) by either plasma etching ($CHF_3 + O_2$) or hydroflouric (HF) acid. Because we wish to remove potassium

salts left over from KOH etch, we choose the HF option because it also dissolves the salts. [2] 40 minutes in BOE 5:1 is more time than needed for nitride mask removal, but it is the recommended time for salt residue removal. The salt crystals are visible by optical microscope before this removal step, especially on the angled sidewalls, but disappear after this removal step. The presence of the salt is also sometimes visible by the naked eye as hazy white residue regions.

6.2.2 Electroplating

After the pits are created and the wafer cleaned, the wafer is metalized (figure 6.2**(h)-(i)**). The wafer is coated by e-beam evaporation with 6 nm titanium and 100 nm copper or gold which serves as a conducting layer onto which 10 μm of indium is electroplated, forming the cavity walls. Refer to appendix A for more information on the electroplating process.

6.2.3 Bonding

Finally, the cavity chips are diced out of the wafer and paired with a mating component that both forms the final remaining wall of the microwave cavity and permits measurement of the resonant mode, and they are united in holy indium matrimony. The mating component to which the etched chips are bonded depends on the coupling scheme being employed, and we will discuss several of these in the next section. You will see that this mating component can be of several materials including silicon, bulk copper, or PCB, each also electroplated with a layer of indium.

Some mechanical concerns that must be considered when bonding micromachined silicon wafers to one another or various other materials are ennumerated in section 7.3. In fact, the entirety of the next chapter is dedicated to process development of indium bonding, so we suspend detailed discussion of indium bonding until then.

---

[2]Another common way to remove the potassium salt residue after KOH etch is 20 minute immersion in a self-heating solution of 1:1:1 H_2O : H_2O_2 : HCl. This solution removes the salt, but does not etch the nitride. This is useful in cases of nitride membrane relief.

6.3 Coupling

6.3.1 Pin coupling

In what is commonly called "pin coupling", a coaxial transmission line carries that carries signals between room-temperature instruments and the cavity resonator has an abrupt transition in a port to the cavity. The center pin of the coaxial cable comes to an end, and the propagating signal exponentially decays in a short section of narrow circular waveguide to evanescently reach the cavity mode, as illustrated in figure 6.3. This is the most common means by which signals are coupled with 3D cavities in cQED, and it is already covered thoroughly.
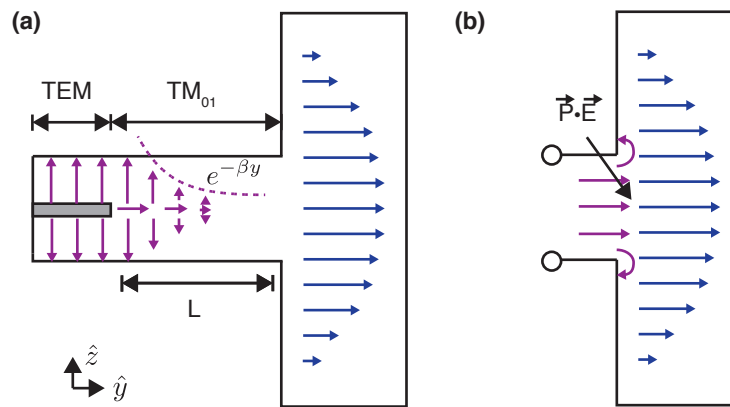
FIGURE 6.3: **Pin coupling. (a)** Signals from the coaxial line (TEM) are coupled to a propagating circular waveguide mode (TM01), which has a decay length given by the cutoff propagation constant β. **(b)** Coupling between the circular waveguide and a rectangular cavity is well-described by a dipole excitation approximation of a circular aperture since the radius of the circular waveguide is small compared to the wavelength. (Figure used with permission from Reagor, 2015. See Copyright Permissions.)

Let us briefly explain the mechanism here before showing that this method can be used to measure micromachined cavities too. The abrupt transition of coaxial transmission line to sub-cutoff cylindrical waveguide excites many of the waveguide propagating modes, but particularly the TM01 waveguide mode transmits the most power. Propagation constants of the TM0m (azimuthally symmetric) modes of the circular waveguide with radius
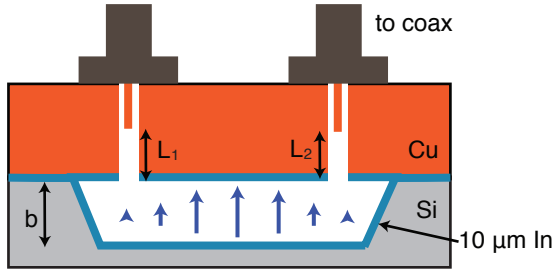
FIGURE 6.4: **Pin coupling micromachined cavity.**

r_0 are

$$\beta_{TM0m} = \sqrt{k^2 - \left(\frac{p_{0m}}{r_0}\right)^2} \tag{6.2}$$

where p_{0m} is the mth zero of the zeroth Bessel function $J_0(x)$. The cutoff frequency of the waveguide is the frequency below which the propagation constant becomes imaginary, which is

$$\omega < \frac{p_{0m}c}{r_0}. \tag{6.3}$$

The waveguide into which the pin extends is a small enough radius such that the signals will be below the cutoff frequency. In this case, the Q scales exponentially in the length of the waveguide section L as

$$Q_c \propto e^{-2\beta_{\text{TM01}}L}. \tag{6.4}$$

For example, the cavity lids used for the cavities in this section had cylindrical waveguides of $r_0 = 1.2$ mm, so the dominant mode has $\beta_{TM01} \approx i2$ mm^{-1}, corresponding to an e-folding length of 0.5 mm. [3]

The waveguide opening to the cavity is small compared to a wavelength, so impinging fields on the cavity can be approximated by a dipole excitation, similar to our circular aperture calculation. A derivation for the actual pin coupling to a rectangular cavity (Reagor,

---

[3]To say the waveguide has an e-folding length of 0.5 mm means that the propagating fields lose a factor of e in their *amplitude* for every 0.5 mm that they travel in the waveguide, or equivalently, they lose a factor of e in their *energy* every 0.25 mm.

- section 4.4.2) reveals

$$Q_c \approx \frac{3}{8}\pi^2 \left[\frac{R(1-\Gamma)^2}{\omega\mu_0 r_0} \right] \left(\frac{abd}{r_0^3} \right) \left(\frac{r_i^2}{r_0^2} \right) \left[\sin\frac{\pi x_0}{a} \sin\frac{\pi z_0}{d} \right]^{-1} \tag{6.5}$$

where R is the real impedance of the coaxial line (50 Ω), Γ is a reflection coefficient (in practice, $\Gamma \approx 1/2$), and r_i is the radius of the inner conductor of the coax pin. Note that the coupling is modulated by the location of the aperture on the cavity wall, and that $Q_c \propto r_0^6$, as with the aperture alone.

To employ this method in micromachined cavities, we pair a micromachined pit wafer with a traditionally machined block with the cylindrical waveguide ports, as shown in figure 6.4. The block is electroplated in indium by a vendor (Component Surfaces) to a thickness of 10 μm.

6.3.2 Transmission line to aperture coupling

FIGURE 6.5: **Quality factors of superconducting micromachined resonators with the described aperture coupling scheme.** Quality factors from simulation and measured devices are compared in **(a)**, while a cartoon of the cross-section of an aperture-coupled device is shown in **(b)**. There is a single aperture of radius r positioned in the center of the cavity beneath a CPWG in the top PCB chip (figure 6.6). All measurements were taken at temperatures ≈ 20 mK and the lineshape was fit to obtain Q_{tot}, Q_c, and Q_{int}. Simulated values are obtained using HFSS's eigenmode solver with 50 Ω wave ports terminating each end of the CPWG. The blue dashed line shows the expected scaling $Q_C \propto 1/\omega r^6$.

A multilayer planar-fabricated coupling method is achieved by omitting metalization in a small circle on the cavity wall positioned below a transmission line. This aperture coupling scheme is diagrammed in cross-section in figure 6.5**(b)**, and the device components are shown in figure 6.6**(a)-(c)**. For radius $r \ll \lambda$, the radiation of field E_0 through the aperture can be modeled as that of a dipole with $\vec{p} = \frac{2}{3}\epsilon E_0 r^3$ oscillating at the cavity resonance frequency ω. The scaling of the coupling is therefore predicted to be $Q_C \propto r^{-6}$ (see section 5.2.2).

We conducted several measurements of micromachined cavities in this style. The cavity chips were paired with PCB coupling lids. The chosen transmission line was a CPWG with a center strip width comparable to the diameter of the aperture and comparable to the dielectric height to ensure sufficient overlap with fields radiating from the aperture (strip width $w = 625$ μm, gap $G = 762$ μm, height $h = 762$ μm). We also found that including metalized vias in the PCB improved the transmission spectrum, and these vias are 300 μm in diameter and through-plated with copper. In figure 6.5**(a)**, we show results from four such devices made with different aperture radii. Measured coupling Qs compare well with simulation. Internal Qs measured here are less than 500,000, which we attribute to seam losses at the indium-indium bond.

Though radiation of field out the aperture is necessary to provide a means of coupling, the aperture must be kept small enough to prevent excessive radiative loss, discussed in section 5.2.2. Using equation 5.27, we find that for $r = 0.75$ mm, $Q = 10^6$. For $r = 0.675$ mm, $Q = 5 \times 10^6$. The fact that our measurements of Q_{int}, shown in figure 6.5, do not meet these values, and do not increase for decreasing aperture radius, indicates that radiation loss out the aperture is not the limiting factor.

6.3.3 Lateral loop coupling

The two methods of coupling discussed so far (pin and aperture) require multi-layer or vertical transfer of field energy. It is also possible to couple to the rectangular cavity from
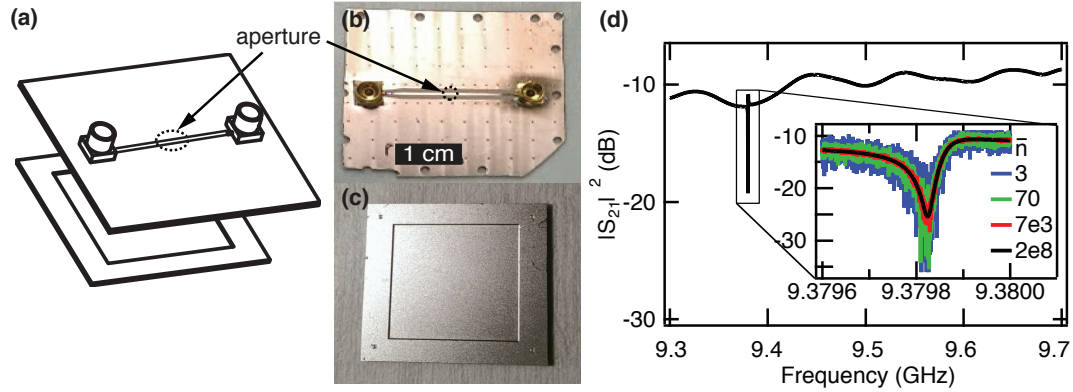
FIGURE 6.6: **Superconducting micromachined cavity with aperture readout.** **(a)** Sketch of a transverse plane cross-section of the device. **(b)** The top chip is made in TMM10i PCB and contains Cu plated vias and 10 μm In is electroplated on the back side. An aperture (dashed circle, $r = 675$ μm) is omitted in the back side metalization to permit coupling of cavity fields through the dielectric to the CPWG trace above. **(c)** The bottom chip consists of a $22 \times 24 \times .3$ mm rectangular pit metalized with 10 μm In. **(d)** A 500 MHz range of the transmission spectrum of the device measured at 20 mK shows the TE101 resonance. A fit to the asymmetric lineshape yields $Q_{int} = 4.6 \times 10^5$ and $Q_c = 1.4 \times 10^5$. (Figure adapted with permission from Brecht et al., 2015. See Copyright Permissions.)

within the same layer, which we call lateral coupling. Since the electric field is zero at the edges of the cavity that can be accessed laterally, we can instead couple to the magnetic field directly, which is strong at the edges of the cavity. The probe consists of a loop of current that can be inserted in a tunnel in the same layer as the cavity. The loop has a magnetic dipole aligned to the local orientation of the cavity magnetic field, as shown in figure 6.7**(b)**. A propagating waveguide mode translates this dipole moment to the resonator with an exponentially reduced amplitude, similar to our findings in section 6.3.1.

The principle is illustrated for micromachined cavities in figure figure 6.7. The blue points and bottom axis show that a range of coupling strengths can be accessed by adjusting the position of the loop probe, or the cavity-coupler distance. When the probe is inside the waveguide, retraction from the cavity's edge increases the coupling Q approximately exponentially. Stronger coupling is reached when the probe is inserted inside the cavity itself. The position of the sub-cutoff waveguide along the cavity wall can also be varied to affect coupling strength. The location of strongest coupling is in the middle (position 0.5).
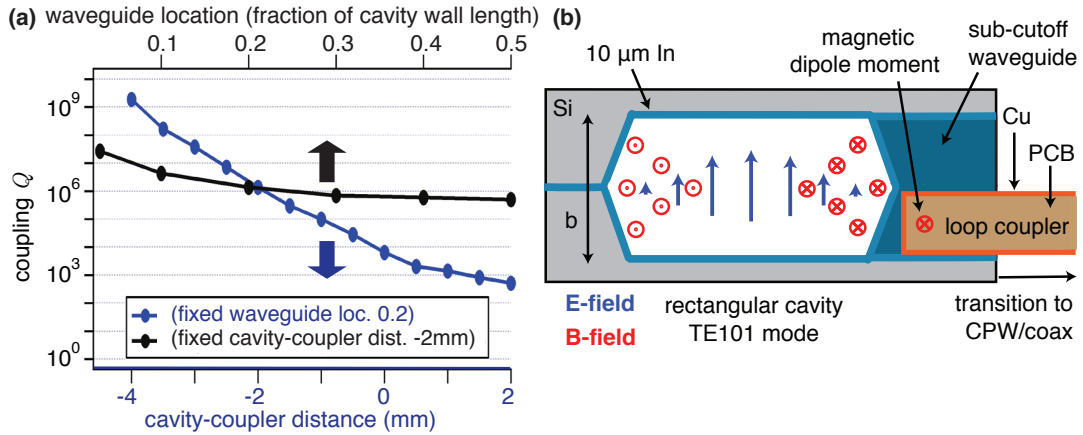
FIGURE 6.7: **Lateral loop coupling principle.** **(a)** Simulated coupling Qs for a loop coupler scheme. The blue points and bottom axis show that a wide range of coupling strengths can be accessed by adjusting the lateral position of the loop probe, or the cavity-coupler distance. Negative values of cavity-coupler distance indicate that the tip of the loop probe is retracted into the sub-cutoff waveguide, and positive values indicate protrusion of the loop probe into the cavity. The black points and top axis show that the position of the sub-cutoff waveguide along the cavity wall can also be changed as a parameter that affects coupling, and that the location of strongest coupling is in the middle (0.5). **(b)** A cross-section of the cavity and sub-cutoff waveguide "tunnel" in which the loop coupler probe is inserted.

In this location, the sensitivity of the exponential dependence of coupling to cavity-coupler distance is also maximized. With this in mind, if it is difficult to control the exact placement of the loop probe, it may be advantageous to reduce the sensitivity of exact cavity-coupler distance by choosing a waveguide position at 0.2, for instance.

In contrast to the pin coupling case of section 6.3.1, here there is not azimuthal symmetry in the under-cutoff waveguide. Additionally, the waveguide is actually a hexagon and the current loop does not generate a perfect dipole excitation of a single propagating mode. Higher TE and TM waveguide modes both may contribute to power transmitted between the loop probe and the cavity. Propagation constants of the TM modes of a circular waveguide are (Pozar, 2005 - section 3.4)

$$\beta_{TMnm} = \sqrt{k^2 - \left(\frac{p_{nm}}{r_0}\right)^2},$$
(6.6)

where p_{nm} is the mth root of the nth Bessel function $J_n(x)$. Similarly, propagation constants of the TE modes are

$$\beta_{TEnm} = \sqrt{k^2 - \left(\frac{p'_{nm}}{r_0}\right)^2},$$ (6.7)

where p'_{nm} is the mth root of the first derivative of the nth Bessel function $J'_n(x)$

Because of the orientation of the loop, we expect to primarily excite the circular waveguide mode TE11 (Reagor, 2015–section 4.5.2). We expect the coupling Q to scale exponentially with the length of tunnel between the loop and cavity L as

$$Q_c \propto e^{2\beta_{TE11}L}.$$ (6.8)

Since this is an approximation, it is worth noting that additionally higher modes would change the slope of the blue points (which ideally fall on a line of slope β for $L < 0$) in figure 6.7(a). In our case, the dimensions of the sub-cutoff waveguide tunnel are shown in figure 6.8(d). Approximating the tunnel as a circular waveguide with radius $r_0 \approx 400$ μm, the relevant propagation constant for a 10 GHz signal is $\beta_{TE11} \approx i3.4$ mm^{-1} (using $p'_{11} = 1.841$). The cutoff frequency for this mode is 200 GHz, and the e-folding length is 0.15 mm.

Implementation of this strategy in the lab (see device in figure 6.8) faced a few challenges. First, construction of the loop coupler itself required a specialized procedure of milling and copper electroplating steps with our (LPKF) circuit board creation tools. Specifically, copper is through plated on the vertical tip and the coupler's conducting line is recessed into the top of the stick to prevent shorting between it and the tunnel into which it is inserted. Second, a transition from coaxial cable to CPW to the coupler was made with a taper pattern and wirebonding conducted after mechanical insertion into the tunnel. Third, we suspect poor quality indium-indium bonding of the two chips forming the cavity and tunnel. A waveguide with a poor quality seam along the propagation axis is known to support unwanted signal pathways like parallel-plate transmission. In this way, the poor quality seam results in cross-talk between two probes that would otherwise see
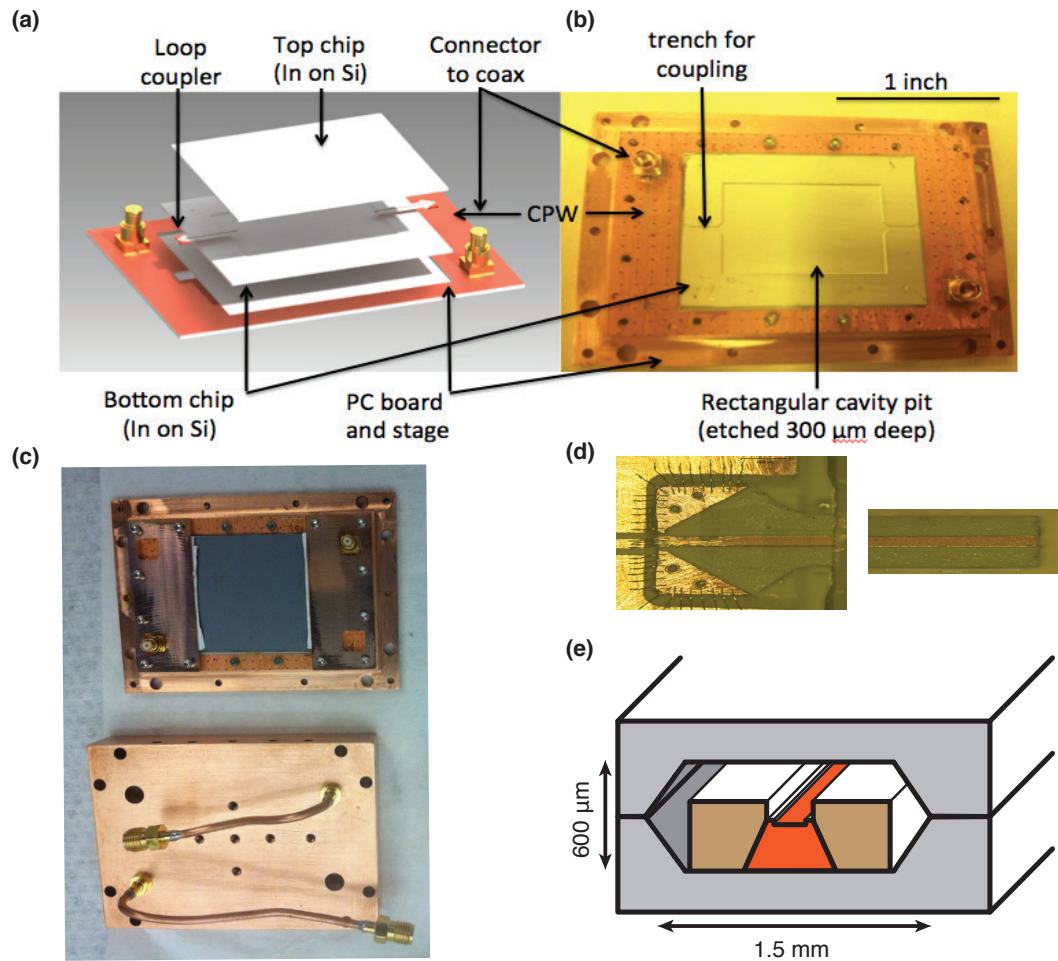
FIGURE 6.8: **Lateral loop coupling micromachined cavity device.** **(a)** An exploded diagram and **(b)** photograph of a micromachined cavity chip, it's mounting PCB, and trenches that hold loop couplers described in this section. **(c)** A photo of the assembled cavity and copper shims that cover the CPW-to-microstrip transition (top), and the cover (bottom). **(d)** Magnification of the loop coupler including the CPW-to-microstrip transition. **(e)** Cross-section of the tunnel with end of loop coupler, where orange is copper (to scale).

transmission only on cavity resonance. The combination of these issues resulted in an unacceptable spectrum dominated by cross-talk. The cavity resonance was also visible, however, so it should be possible to employ the lateral loop coupling principle effectively if there is reliably good wafer bonding and an improved CPW-to-loop coupler transition.

6.3.4   Lateral CPW coupling

We now consider a second type of lateral coupling. Like the loop coupling method, this scheme involves a probe entering near the cavity wall though a tunnel created in the same layer and with the same etch as the cavity. We pattern the probe as a CPW transmission line on the wafer that forms one of the tunnel walls, as shown in figure 6.9. The benefits are lithographic definition of the probe geometry and position, as well as elimination of the need to mechanically insert a separate piece by hand. Lateral CPW coupling is therefore sure to be more precise and robust.

An analysis of the coupling mechanism, i.e. in terms of dipole excitation of the tunnel waveguide modes, is less clear now than in the other coupling schemes that we have discussed. The tip of the CPW probe line can be terminated in either an *open* or a *short*, but in both cases there is no obvious electric or magnetic dipole that can be simplistically oriented to align with cavity fields, at least without some accompanying symmetric cancellation. However, perhaps because the terminated CPW is dominated by fringing fields, and these are not symmetric, coupling undoubtedly occurs. Coupling strength is best determined by simulation, and in figure 6.9 we show examples of two sizes of CPW terminated in both open and short tips.

I do not present experimental attempts for this coupling scheme. It is apparent from simulation that this scheme cannot be operated in cavity transmission mode (two loop couplers, where the ideal S_{21} signal from one to the other is minimal except on resonance) because a significant fraction of the signal propagates through the bottom wafer at a wide range of frequencies. The propagation results from a parallel plate traveling mode between
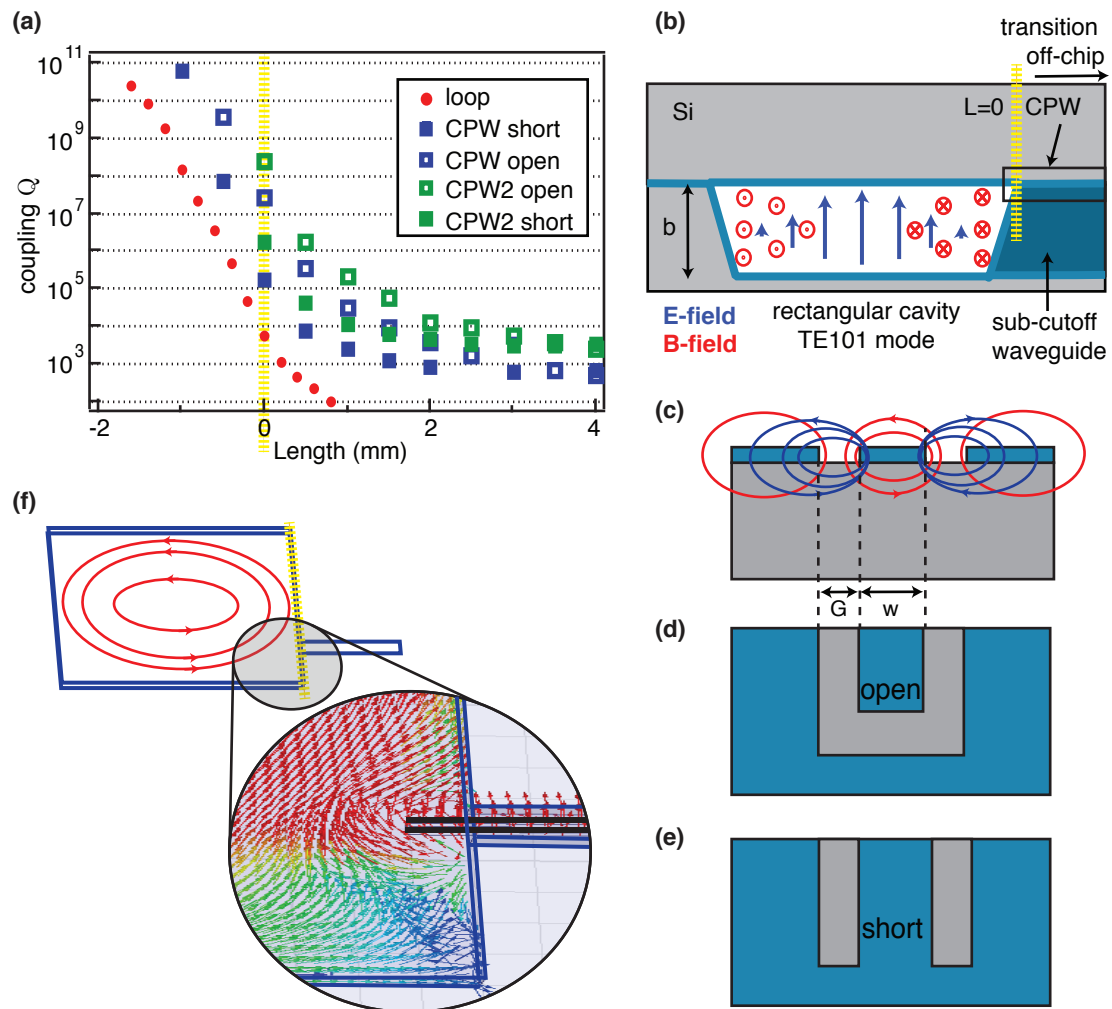
FIGURE 6.9: **Lateral CPW coupling to micromachined cavity.** **(a)** Simulated coupling Q as a function of the length that the probe penetrates into the cavity for the loop probe of section 6.3.3 as well as four types of lateral CPW probes. The yellow dotted line at the cavity edge is 0, negative lengths correspond to retraction into the tunnel, and positive lengths correspond to insertion into the cavity. **(b)** A cross-section of the cavity and sub-cutoff waveguide "tunnel" in which the CPW (fabricated on the upper wafer, black box) or loop probe resides. **(c)** A cross-section showing the fields of a CPW that hybridize with those of the sub-cutoff waveguide and/or cavity. These simulations concern CPWs with parameters $[w, G]_{CPW} = [50, 86.7]$ μm and $[w, G]_{CPW2} = [20, 35.5]$ μm and that may terminate in either an open, **(d)**, or a short, **(e)**. **(f)** We show that the position of the tunnel along the cavity wall, which is another tunable parameter, is fixed to 20% in this case. The small colored arrows show magnetic field vectors that qualitatively suggest the nature of the coupling between the CPW short at $L = 1$ mm (black lines in inset) and the cavity (red is high and blue is low field magnitude).

the metal layers surrounding cavity chip dielectric, to which fields from the CPWs couple. In simulation, the problem can be remedied by creating a perfect conducting barrier between the two ports. In actuality, the analagous result can be achieved using conducting vias in the cavity wafer. This is a valuable observation: developing metalized vias is probably necessary to prevent cross-talk in much of the CPW circuitry of MMIQCs section 4.3.4.

6.4 Frequency shift in wet-etched rectangular cavity

The asymmetric wet etch of KOH in silicon results in a cavity shape that differs slightly from a rectangular prism. How much does this effect the field distribution or change the frequency of the modes?

We follow Pozar, 2005–section 6.7 to add a general shape perturbation to the rectangular cavity. We will derive an expression for the change in frequency due to the change in shape due to the sloped sidewalls that result from a chemical wet etch of silicon. The "original cavity" is a rectangular cavity with dimensions $a \times b \times c$ as seen in figure 5.1(a). We will add a triangular prism at each of the four vertical walls to create the "etched cavity".
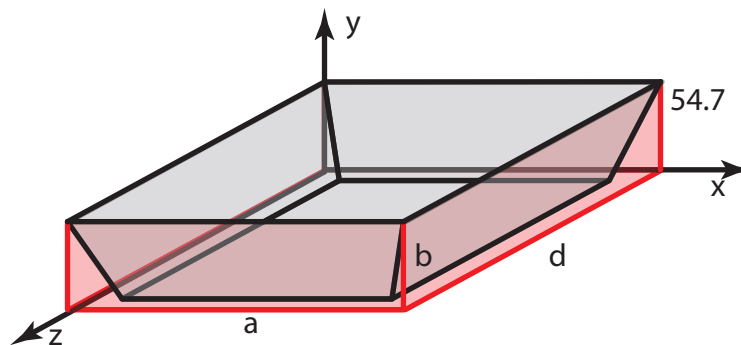
FIGURE 6.10: **Shape perturbation of the etched cavity.** The original cavity is $a \times b \times d$ rectangular prism. Red triangular prisms highlight the volumes that differ between the original rectangular cavity and the actual etched cavity.

Let us denote the fields and frequency of the original cavity $\vec{E}_0$, $\vec{H}_0$, and ω_0, and denote the fields of the etched cavity $\vec{E}$, $\vec{H}$, and ω. The exact shift in resonance frequency is

$$\omega - \omega_0 = \frac{-j \int_{\Delta S} \vec{E}_0^* \times \vec{H} \cdot d\vec{s}}{\int_V \left(\epsilon \vec{E} \cdot \vec{E}_0^* + \mu \vec{H} \cdot \vec{H}_0^* \right) dv} \tag{6.9}$$

Though this is exact, it is not very useful since we do not initially know $\vec{E}$, $\vec{H}$, and ω. To go further, we make some perturbative assumptions. First, we assume that the field at the new wall is the same as it would be at the original wall: $\vec{E} = \vec{E}_0$ and $\vec{E} = \vec{E}_0$. Second, we assume that the change in surface area is small: $\Delta S = S_0 - S \ll S_0$. Also assume that the total energy in the original and perturbed cavities is the same. Then, using conservation of power it is simple to show that the fractional change in the frequency is

$$\frac{\omega - \omega_0}{\omega_0} \approx \frac{\int_{V_0} \left(\mu|\vec{H}_0|^2 - \epsilon|\vec{E}_0|^2 \right) dv}{\int_{V_0} \left(\mu|\vec{H}_0|^2 + \epsilon|\vec{E}_0|^2 \right) dv}. \tag{6.10}$$

This can be written in terms of stored energies as

$$\frac{\omega - \omega_0}{\omega_0} \approx \frac{\Delta W_m - \Delta W_e}{W_m + W_e}. \tag{6.11}$$

For our rectangular cavity, the electric stored energy is

$$W_e = \frac{\epsilon}{4} \int_{V_0} E_y^* E_y dv \tag{6.12}$$

$$= \frac{\epsilon}{16} abd E_0^2, \tag{6.13}$$

and the magnetic stored energy is

$$W_m = \frac{\mu}{4} \int_{V_0} H_x^* H_x + H_z^* H_z \, dv \tag{6.14}$$

$$= \frac{\mu}{16} abd E_0^2 \left(\frac{1}{Z_{TE}^2} + \frac{\pi^2}{k^2 \eta^2 a^2} \right) \tag{6.15}$$

$$= \frac{\epsilon}{16} abd E_0^2. \tag{6.16}$$

In the last step, we have simplified by noting that $Z_{TE} = k\eta/\beta = k\eta/\sqrt{k^2 - \left(\frac{\pi}{a}\right)^2}$, so the expression in parentheses is equal to $1/\eta^2 = \epsilon/\mu$. We arrive at the expected result that the stored electric and magnetic energies are equal on resonance.

For our etched cavity, we are adding a shape perturbation for the volume of trapezoidal prisms along the lengths of each of the narrow walls. We will neglect the corners. The volume of the original cavity is $V = abd$. Our perturbation is written

$$\Delta V \approx ab^2 \tan\theta + db^2 \tan\theta \tag{6.17}$$

$$= (a + d)b^2 \tan\theta \tag{6.18}$$

where $\theta = 54.7\,°$is the angle defined by the silicon crystal planes (100) and (111).

The fields on the left/right walls ($z = 0, z = d$) are $\vec{E} = 0$ and $\vec{H} = -\frac{jE_0}{Z_{TE}} \sin\frac{\pi x}{a} \ \hat{x}$, and the fields on the front/back walls ($x = 0, x = a$) are $\vec{E} = 0$ and $\vec{H} = \frac{j\pi E_0}{k\eta a} \sin\frac{\pi z}{d} \ \hat{z}$. Therefore, $\Delta W_e = 0$ and we only have to work on the magnetic energy that would have been stored in ΔV were it to have th fields of the original cavity. There is a cancellation of a factor of two for pairs of symmetric walls and a factor of one half in the volume of a

triangular prism. We calculate

$$\Delta W_m = \frac{\mu}{4} \int_{\Delta V} H_x^* H_x + H_z^* H_z \, dv \tag{6.19}$$

$$= \frac{\mu}{4} \left[\int_0^a b^2 \tan\theta \frac{-E_0^2}{Z_{TE}} \sin^2 \frac{\pi x}{a} \, dx + \int_0^d b^2 \tan\theta \frac{\pi E_0^2}{k\eta a} \sin^2 \frac{\pi z}{d} \, dz \right] \tag{6.20}$$

$$= \frac{\mu}{4} E_0^2 b^2 \tan\theta \left[-\frac{k^2 - (\pi/a)^2}{k^2 \eta^2} \int_0^a \sin^2 \frac{\pi x}{a} \, dx + \frac{\pi^2}{k^2 \eta^2 a^2} \int_0^d \sin^2 \frac{\pi z}{d} \, dz \right], \tag{6.21}$$

where we have again expanded Z_{TE} as above. Noting that results of the two integrals are $a/2$ and $d/2$, and again substituting $1/\eta^2 = \epsilon/\mu$, we continue simplifying,

$$\Delta W_m = \frac{\epsilon}{8} E_0^2 b^2 \tan\theta \left[-a \frac{1}{k^2} \left(k^2 - (\pi/a)^2 \right) + \frac{d}{a^2} \frac{\pi^2}{k^2} \right] \tag{6.22}$$

$$= \frac{\epsilon}{8} E_0^2 b^2 \tan\theta \left[-a + \frac{\pi^2}{k^2} \frac{1}{a} + \frac{\pi}{k^2} \frac{d}{a^2} \right]. \tag{6.23}$$

We now can apply this knowledge to equation 6.11 and know the approximated frequency shift is

$$\frac{\omega - \omega_0}{\omega_0} \approx \frac{\frac{\epsilon}{8} E_0^2 b^2 \tan\theta \left[-a + \frac{\pi^2}{k^2} \frac{1}{a} + \frac{\pi}{k^2} \frac{d}{a^2} \right]}{\frac{\epsilon}{8} abd E_0^2} \tag{6.24}$$

$$= \frac{b \tan\theta}{ad} \left[-a + \frac{\pi^2}{k^2} \frac{1}{a} + \frac{\pi}{k^2} \frac{d}{a^2} \right]. \tag{6.25}$$

One can recall that the wavenumber $k = \omega_0 \sqrt{\mu\epsilon}$. We have arrived at an expression for the frequency shift of the etched cavity in terms of parameters of the original cavity and θ.

Now we apply this to the cavity dimensions used here: $a = 22, b = 0.30, c = 24$ mm. The original frequency is $\omega_0/2\pi = 9.24933$ GHz. The fractional frequency change is 0.0043, meaning the new frequency of the etched cavity is 0.43 percent higher than original: $\omega/2\pi = 9.28877$ GHz. This is checks out with common sense, since we expect the etched cavity to have a higher frequency than the original cavity, but a lower frequency than the rectangular cavity that could fit inside (having dimensions $a - 2b\tan\theta \times b \times d - 2b\tan\theta$),

which in this example would be a limit of 9.42393 GHz. We can conclude that for $b \ll a, d$, the frequency shift is less than half a percent.

6.5 Summary

The first superconducting micromachined cavities, complete with a multilayer aperture coupling scheme, are showcased in Brecht et al., 2015. This marks a success in proving the viability of such devices and methods that can be extended towards the MMIQC hardware architecture described in chapter 4. However, in working with such devices, it was apparent that more work was need to develop methods to produce *reliably robust* indium-mediated wafer-to-wafer bonds. In the next chapter, we characterize both the indium material and the bonding process in several dimensions. Then, in chapter 8, we will return to the micromachined cavity and incorporate a transmon qubit.

Chapter 7

Superconducting wafer bonding with indium

We focus on indium because of a few remarkable properties. First, we know that it is a superconductor. Second, it is extremely malleable and ductile, meaning that it readily deforms without losing toughness. Furthermore, it maintains this ductility at low temperatures. For this reason, it is commonly used for hermetic sealing gaskets in cryogenics. Refer to table B.1 for some superconducting parameters of indium compared to those of aluminum and niobium, which are two metals commonly used in superconducting circuits.

Being a trivalent metal, indium is chemically similar to aluminum. In industry, the largest end-use for indium is in the form of thin-film coatings of its alloys, such as indium tin oxide (ITO), in liquid crystal displays, solar cells, etc. Indium-semiconductor compounds are used in infrared detectors and high-speed transistors. In this thesis, we concentrate on pure indium and its application in cQED as an inter-wafer bonding medium. [1]

---

[1] On an historically interesting note, indium made its first appearance for use in superconducting circuits in the in the form of lead-gold-indium alloy Josephson junctions because of stability advantages over the first Josephson junctions, which were made with lead. This development occurred in the 1970's at IBM (Greiner, 1971; Lahiri and Basavaiah, 1978). These alloy junctions were subsequently replaced by the more reliable Niobium and Aluminum junctions.

We begin this chapter by providing a brief background on wafer bonding. Second, we review existing work on wafer bonding using *indium bumps*, followed by a presentation of indium bumps that we have fabricated in the lab. Next, in section 7.3, we discuss some of the mechanical considerations relevant to indium bonding silicon wafers, including some observations from benchtop examinations of the indium's deformation and shear. In section 7.5, we use 3D resonators with indium walls to study the surface of indium. First, we examine the response of resonator to varying circulating power, concluding that dielectric losses are as small as those found in aluminum cavity counterparts (suggesting similar q_{diel}). We also discuss some nonlinear effects that were observed in 3D resonators with high seam participation and at very large circulating powers. In section 7.6, we again use 3D resonators to examine indium's surface impedance by tracking the change in frequency as temperature is swept across the superconducting transition. This allows us to extract q_{cond} and the penetration depth. Additionally, in section 7.7, we track the DC resistivity of indium across the superconducting transition. Lastly, in section 7.4, we discuss experiments using stripline resonators as test-devices to allow us to probe the conductivity (g_{seam}) of indium bonds.

7.1   Background on wafer bonding

Wafer bonding is a crucial aspect of 3D integration. There are several different methods, reviewed by Fan and Tan, 2012, that we briefly summarize here to provide context and reasoning for the choice of pure indium in this thesis.

First, thermocompression bonding, also referred to as diffusion bonding or solid-state bonding, is a process in which clean metallic surfaces are brought into contact with applied force and heat. Atoms migrate across the surfaces of the two crystal lattices during crystal lattice vibration and the two surfaces become bonded to one another through this atomic diffusion across surfaces, grain boundaries, and the bulk. Applied heat, force, and optional ultrasonic force encourages the process. Thermocompression bonding has established use

in gold, copper and aluminum, which are all metals with high diffusion rates. Gold is an ideal metal for this process because it does not have an oxide, is very ductile, and has low melting point. Gold thermocompression bonding was used in the MMICs of Brown, Blondy, and Rebeiz, 1999; Blondy et al., 1998; Papapolymerou et al., 1997; Katehi, 1997; Chi and Rebeiz, 1996, to name a few. Copper bonding requires temperatures $> 400°C$ and an oxide-cleaning strategy, and it is employed industrially on the wafer-scale (Chen and Tan, 2012). Aluminum bonding requires temperatures $> 500°C$, pressures twice that required for copper, and forming gas to break through surface oxide because aluminum does not diffuse through its oxide at all (Cakmak et al., 2009; Farrens, 2008). [2] As of very recently, thermocompression bonding of indium is being investigated for the application of multilayer superconducting quantum circuits (McRae et al., 2017). [3] The conditions for aluminum thermocompression bonding, however, require a temperature not compatible with Josephson junction circuits.

A material property relevant to thermocompression bonding is a metal's self-diffusion rate. The rate of self diffusion follows $D = D_0 e^{-A/RT}$, where D_0 is the self-diffusion constant, A is the activation energy, T is temperature, and $R = k_B N_A$ is the gas constant. Indium's self-diffusion rate becomes significant at half the activation energy of copper and gold.[4]

The second type of bonding is eutectic bonding, in which two metal species are combined with energy from heat, voltage, and/or ultrasonics to activate and then solidify a eutectic system. A eutectic system is an alloy in which transformation between solid and liquid states can occur at a specific alloy concentration as well as temperature. That is,

---

[2] We had EVG perform aluminum thermocompression bonding test on a micromachined cavity device with 1 μm e-beam evaporated aluminum on both wafers. The etched cavity part of the silicon wafer broke under the required force.

[3] This work conducts bonding of bulk indium surfaces 150 nm thick at 190°C, which is above the melting point (156°C) so that the indium reflows to create the bond. DC indium-to-indium bond resistance measured in this work is 515 nΩmm^{-2} at 10 mK. This work also corroborates our findings that bonded indium devices can withstand multiple cooling cycles, as well as "several minutes of high-power sonication".

[4] For copper, D_0 = 0.5 cm^2/s, and Q = 47 kcal/mole (Kuper et al., 1954).
For gold, D_0 = 0.091 cm^2/s, and Q= 42 kcal/mole (Makin, Rowe, and Leclaire, 1957).
For indium, D_0 = 2.7-3.7 cm^2/s, and Q = 19 kcal/mol (Dickey, 1959).

the phase diagram of a eutectic alloy has a *eutectic point* at a unique atomic or molecular percentage ratio and temperature at which there coexists two solid phases and a liquid superlattice. This is the melting point of the eutectic and it is lower than that of either species. Not all binary alloys have eutectic points. Eutectic wafer bonds are commonly made in systems of Si/Au, Si/Al, In/Au, Cu/Sn, Au/Sn and Al/Ge. We suspect that many of these eutectic combinations would not be good superconductors. Transient liquid phase (TLP) bonding is a variation of eutectic bonding that involves sealing wafer surfaces together by melting and then cooling a low-melting-point interfacial layer between parent metal layers under conditions such that an intermetallic joint results. The In/Au system is ideal for this technique (Welch and Najafi, 2008).

Other bonding methods make use of conducting paste or nonconductive adhesives and these are not of interest to us here. We will now focus on thermocompression bonding of pure indium because we expect good superconducting behavior and because it has a high self-diffusion rate at relatively low temperatures.

7.2   Indium bump bonding

Indium may be pattered into "bumps" before use in bonded multilayer structures. These bumps may either serve as individual electrical interconnects, as in ball-grid-arrays, or form electromagnetic boundary conditions, e.g. around the perimeter of a micromachined cavity. They may also only provide mechanical support of the wafer assembly (e.g. in SCUBA-2 Audley et al., 2004).

For wafer-scale bonding for the purpose of creating electromagnetic boundary conditions, there are two advantages of patterning indium bumps rather than simply covering large areas with bulk indium. First, patterning bumps reduces the effective bulk modulus of the entire bond area, thus requiring less force for the same deformation. Second, there is space for the indium bumps to deform, which allows for the surface oxide to be sheared or broken through. The result is a superior electrical and mechanical bond.

Indium may be deposited by either electroplating or thermal evaporation. While it is also possible to sputter Indium, the process is notably messy and the resultant surface is comparatively very rough. In many cases, the indium is deposited on top of an existing metal or stack of metals, referred to as under-bump-metal or UBM. Different applications require particular UBM stacks for their conductivity and physical interface properties, among other considerations. In many cases, the indium bumps are pattered and then heated above melting point (156°C), allowing the indium to liquefy and reflow under the influence of its surface tension and adhesion to nearby surfaces, resulting in smooth rounded tops or sometimes spheres resting on top of UBM pads. For high yield uniform spheres, the UBM must repel liquid indium, but it is also desirable to have good adhesion between the indium and the UBM pad. Reflowing indium bumps to form spheres is done in order to create smooth surfaces of high hight uniformity. It has also been found that the shear strength is increased after reflow (Huang et al., 2010; Huang, Xu, and Luo, 2009). We do not experiment with reflow in this thesis.

Indium bump bonding is an established industrial technique. Unfortunately, however, much of the methodology exists in the realm of unpublished trade secrets. For instance, major development has occurred under military contractors such as Raytheon for the application of infrared/night-vision sensors. In table A.4, we draw attention to what can be gleaned from published works on indium bump fabrication and bonding. There are several notable observations. First, all electroplaters use the indium sulfamate bath from Indium Corp. They all use a soluble indium anode, while in our process we have used an insoluble titanium anode. Third, most of the works mention the need for a post-lithography dry-etch or plasma cleaning for satisfactory plating and we have also found this to be a crucial step. All works in which the indium bumps are re-flowed perform the reflow in a hydrogen or forming gas oven to limit surface oxidation. Lastly, the grain size of electroplated indium is smaller for reduced current density and/or a reverse-pulse-plating (RPP) profile (Volpert et al., 2010) and we also find this to be the case.

(a)

(b)

500 μm

10 μm
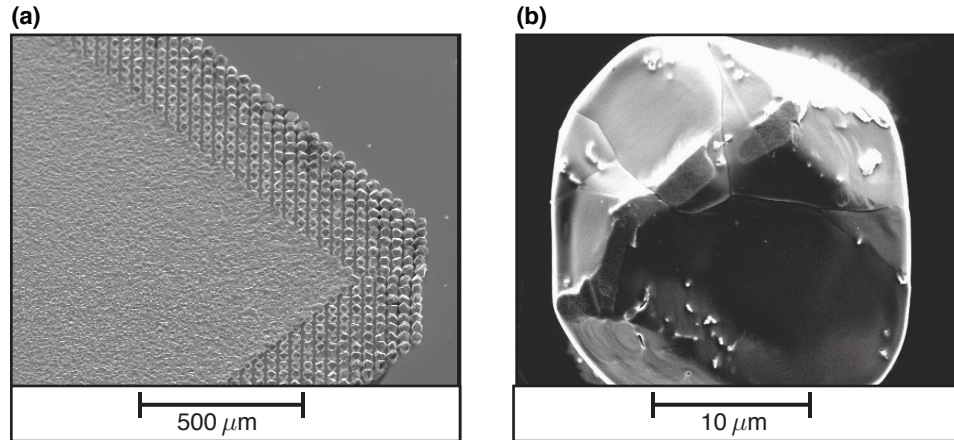
FIGURE 7.1: **Electroplated indium bumps (SEM images). (a)** View from 45° tilt showing a layout of 12 rows of 20×20 μm indium bumps in a 60 μm staggered pitch (fill-factor 22%) around a region of blanket indium coverage. In this image, one can notice that the bumps on the corner are taller than those in the interior. In this pattern, the corner bumps tended to grow ~1.75 times the height of the interior bumps, even with RPP. **(b)** Top-down view of a single indium bump. Some grain boundaries are visible. The small spots and "trails" are of unknown origin.

7.2.1 Fabrication

We have made indium bumps in the lab using an electroplating process described in section A.2. First, a conducting layer of 10 nm Ti and ~150 nm Au or Cu is deposited on the wafer by e-beam evaporation. During electroplating, the wafer acts as a cathode and a thick photoresist prevents electrodeposition of indium on the masked areas. In the end, the photoresist is washed away with solvents. Bumps are displayed in figure 7.1.

A method to reduce surface roughness and improve height uniformity across the wafer is reverse-pulse-plating (RPP), in which the current in the plating cell is modulated from positive to negative. The result is that material is deposited and removed in an alternating way to result in a net positive deposition with smoother edges than develop under constant direct current plating. An example of this effective technique is shown in figure 7.2.

Additionally, we are able to grow indium bumps on a layer of preexisting indium. This is of interest for micromachined cavities and similar structures that require a continuous superconducting joint over a large area. The process differs from that of table A.3 in that
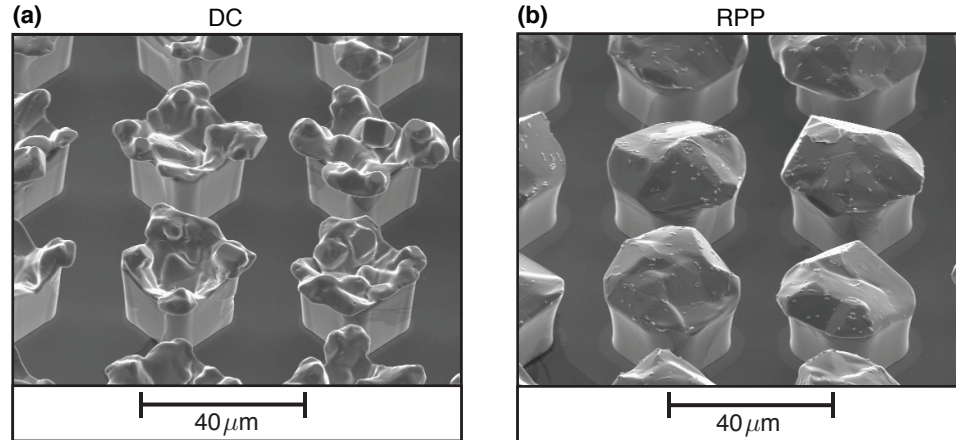
FIGURE 7.2: **Indium bumps made with DC and reverse-pulse-plating.** SEM images at 45° tilt of 20×20 μm indium bumps in a 60 μm staggered pitch (fill-factor 22%). **(a)** Constant current plating with average current density $\langle J \rangle = 3.8$ mA/cm². **(b)** Reverse-pulse-plating profile with time-averaged current density $\langle J \rangle = 3.8$ mA/cm², and profile: 0.5 ms at $10\langle J \rangle$ reverse bias, 1.5 ms at $10\langle J \rangle$ forward bias, 8.0 ms off, repeat.

a first electroplating step covers all of the Cu with ∼1 μm of In, over which a thick photoresist plating mask is created (task 8). Then, the fresh indium surface is cleaned with the usual pre-wet solution, which etches the oxide, and the rest of the indium is electroplated (task 9b-c). Figure 7.3 shows images of this success. This process may introduce another indium-indium interface, but we do not know the consequences of this in detail.
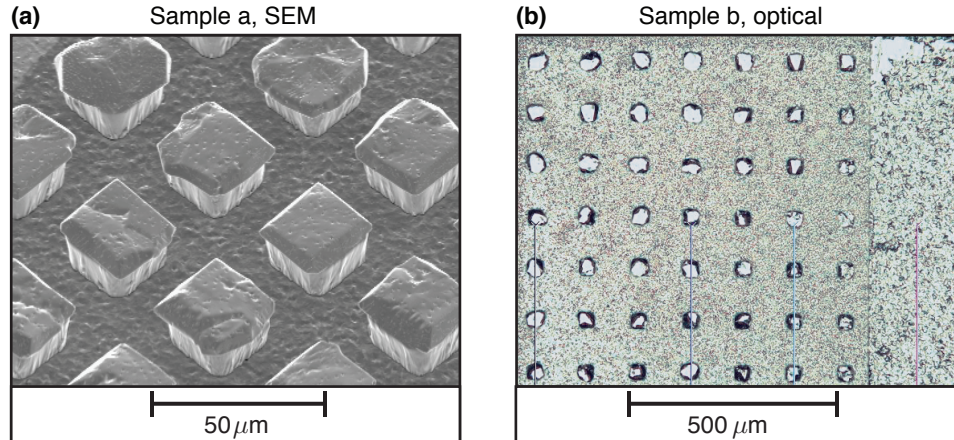
FIGURE 7.3: **Electroplated indium bumps on a layer of indium. (a)** SEM image (45° tilt) of a sample of 25×25 μm bumps at 50 μm pitch 15 μm tall on top of a 2 μm layer of indium. **(b)** Optical microscope image of a sample of 20×20 μm bumps at 100 μm pitch 20 μm tall on top of a 2 μm layer of indium.

7.3 Mechanical considerations

Indium is the softest metal that is stable in air (Reed et al., 1988). The Young's (or elastic) modulus of indium is 11 GPa, which is much lower than typical metals. For instance, aluminum and gold are two more commonly encountered metals that are known for their softness, and their Young's moduli are 69 and 79 GPa respectively. The softness results from deformation-induced recrystallization. Indium has an exceptionally low melting point (156°C = 430 K) and a high boiling point (2353 K). The temperature dependence of indium's tensile properties, strength and strain-hardening, is similar in form to metals such as copper and aluminum when considering the homologous temperature (scaled by the melting point). As an example, because the melting point is so low, the strain-hardening of indium at cryogenic temperatures is similar to that of copper at room temperature, implying a considerable ability to dynamically recover from deformation at low temperatures.

Because it is so soft, pure indium is not suitable for structural applications larger than

millimeter scale. As such, there are few publications that focus on the mechanical properties of indium. Reed et al., 1988 studies tensile strength and ductility between 4 and 295 K, and Iliev et al., 2017 reviews what is available and adds additional mechanical experiments of unique application to indium. In particular, compared to other metals indium has an exceptionally large "size effect," which is a deviation from classical theories of plastic and elastic structures, according to which the nominal strength of a structure is independent of structure size. Indium has a viscoplastic response on the large scale [5] , but deviates strongly when bulk indium is subject to $\sim 100~\mu$m of indentation or beams < 1 mm thick are subject to bending.

Because the grains are so prominent in the images of indium shown in this chapter, we briefly note on this. The crystal structure of pure indium is body-centered tetragonal, which is slightly distorted from the face-centered cubic structure of aluminum. Because of this, physical properties of indium crystals (such as thermal expansion and elasticity) are slightly anisotropic. It can undergo "crystal twinning," in which two separate crystals share the same lattice points in a symmetrical way. Twinning occurs more readily when indium is stressed at low temperatures (Reed et al., 1988). Additionally, indium can grow "whiskers," which are long filaments of single crystal grown out of the surface either spontaneously or in response to stress. Tin and silver notably behave in this way, as do a great many other metals (Zhang, Zhang, and Sun, 2015). While the whisker growth mechanism is not fully understood, the resulting single crystal filaments can be made intentionally (Werner, Tidecks, and Johnston, 1985) and some indium whiskers $\sim$mm long and $\sim~\mu$m in diameter have been used to measured to probe superconducting characteristics (Damaschke and Tidecks, 1989; Overcash et al., 1971). We have not observed these whiskers in

---

[5] Viscoplasticity describes inelastic behavior that is rate-dependent. That is, the deformation of the solid depends on the rate at which a load is applied. It is distinguished from (visco)elasticity, in which any application of stress causes reversible deformation, by the presence of a yield stress over which the material deforms and does not return. The difference between rate-independent plasticity and viscoplasticity is that viscoplastic materials not only permanenly deform under load, but they continue to undergo a *creep* flow over time under the influence of a continuously applied load. For metals and alloys, the viscoplastic mechanism usually becomes dominant at temperatures greater than a third of the melting temperature.

work with electroplated indium.

One important mechanical consideration is the possibility of fracture of the substrate chip during bond. Silicon is a brittle crystal. Its fracture stress is 7000 MPa (10^6 psi), with stress concentration factors of 33 possible at sharp corners produced by anisotropic etching (Petersen, 1982; Sooriakumar et al., 1995). Thermal contraction differences between different material substrates can increase stress concentration. However, we can expect a layer of indium to shear to accommodate the contraction of the substrates. (We will justify this expectation in section 7.3.2.)

The mechanical characteristics of an oxide layer that develops on the surface of indium are important as well. A pure indium surface will develop an oxide layer 3 nm thick immediately upon exposure to air in ambient conditions, then continue to grow until it passivates at a thickness of 8-10 nm over the course of about three days (Indium Corporation, 2016). This oxide can be removed with hydrochloric acid, formic acid, or by a plasma process (Indium Corporation, 2016; Greer et al., 2009). A specially developed plasma process is intended to remove indium oxide and replace it with indium nitride, which is more brittle in character, easily cracking upon bump deformation (Schulte, 2013). Indium oxide, on the other hand, is described as a tough leathery layer.

7.3.1 Deformation of bumps under bond and separation.

Figure 7.4 shows a side-view of our indium bumps under deformation. The chips with 25×25 μm indium bumps ∼15 μm in height were first cleaned with 10% HCl to remove the oxide and then bonded with a force that caused the height of the bumps to reduce by half. Notice that a new layer of oxide grew, and that ruptures or cracks in it are visible in the SEM images. When the two chips are pulled apart by hand in **(b)**, pairs of bumps that are well-bonded remain adhered at the interface, ripping the indium of one bump apart from the chip. In some cases, however, the oxide layer is not broken through and the flattened bumps separate in a way that indicates that no metallic inter-diffusion has taken place **(c)**.
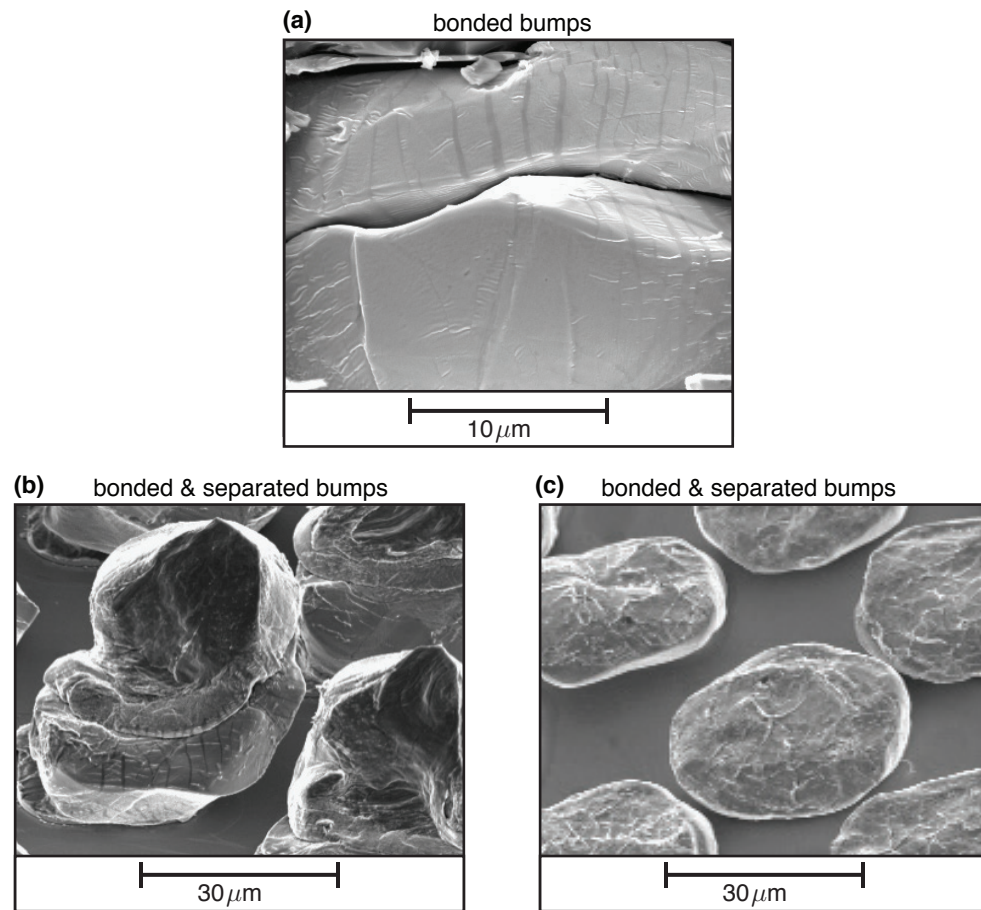
FIGURE 7.4: **Indium bumps bonded and separated (SEM). (a)** A view from the side while opposing bumps are bonded together. **(b)** A view from 45° tilt after chips with bumps have been bonded and then separated. In both images, ruptures in the indium oxide are visible as cracks on the surface of the bumps in both images.
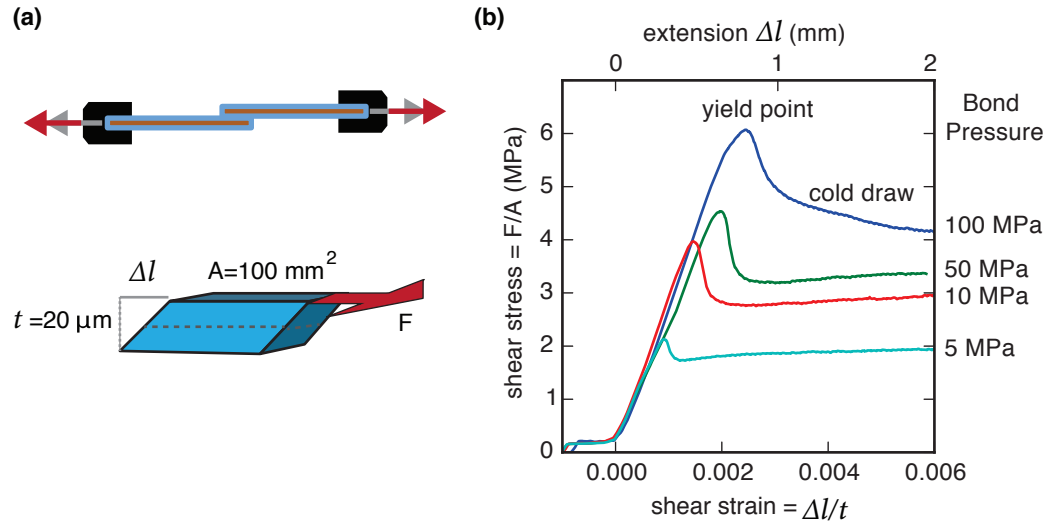
FIGURE 7.5: **Shear test results for indium.** **(a)** Cartoon of the test samples (top), which are two strips of copper each coated in 10 μm of electroplated indium and bonded together before being clamped on the edges for shear pulling; and a cartoon of the block of bulk indium (bottom) under shear deformation due to the applied force F. **(b)** Shear stress-strain curves collected for several samples bonded at different pressures. To compensate for mounting differences, the data were shifted horizontally to make the initial rise in stress occur at zero strain for all samples.

7.3.2 Shear tests of indium bonds

We performed some shear tests of our electroplated indium. The samples consisted of strips of copper (20×100 mm) electroplated with 10 μm of indium (by Component Surfaces), aligned to an indium contact region of 20×5 mm bonded with the Instron at several compressive forces. All samples were bonded at room temperature with a force profile that ramped to target over 1 minute and held at target for 5 minutes before release. After bonding, the samples were loaded to tensile test mounts and pulled at rate of 0.010 mm/s. Shear stress-strain curves were collected for several samples bonded at different pressures and shown in figure 7.5. To compensate for mounting differences or an initial slide in the clamps, the data were shifted horizontally to make the initial rise in stress occur at zero strain for all samples. The fact that copper strips were used as a substrate has negligible

effect. [6]

The indium shears elastically for some time before reaching a peak load. This maximum is the yield point or shear strength. Afterwards, the material continues to "cold draw" for a very long time. The range of the shear axis corresponds to a total extension of 2 mm. The largest shear strength was measured for a sample of indium that was bonded at 100 MPa of pressures, and shear strength was 6 MPa. The slope before the peak load provides the shear modulus: $\frac{F/A}{\Delta l/t}$. The measured shear modulus for all samples was approximately 2.6 GPa, which did not vary with applied bond pressure. The accepted value for pure indium's shear modulus is 3.7 GPa. The "toughness" of a material can be found by integrating the stress-strain curve to the point of failure, and it is an indication of how much energy can be absorbed. Using the blue curve for 20 μm of indium bonded at 100 MPa, the toughness is about 70 J/m^3.

An indium layer of this thickness can easily shear enough to accommodate difference in thermal contraction between copper and silicon over the scale of a 100 mm wafer. Taking a generous estimate of the differential thermal contraction, let us assume that silicon does not change in size at all [7] and that copper changes by a total of 0.3% between room temperature and 15 mK (Pobell, 2007). In that case, there would be 150 μm of shear travel required. This extension is far below the yield point for our 20 μm slab of indium.

In this section we have discussed room-temperature shear tests on bulk indium bonds. Additionally, we observe from numerous thermal cycling tests, in which samples were dunked in liquid nitrogen to rapidly cool from room temperature to 77 K, that indium-indium bonds between silicon, copper, and TMM10i PCB do not fail (indium separation or substrate cracking) with any repeatable pattern. Beyond these simple checks that we have done on full-coverage indium, the stress induced by thermal contraction during cryogenic

---

[6]The Young's modulus of copper is 120 GPa, which is much greater than the shear strength of indium being probed. The copper strips are expected to extend by $\sim$50 μm under the maximum force applied (600 N at the peak of the blue curve), which is a 2.5% effect over the full extension range of 2 mm.

[7]The percent change between room temperature and 7 K is 0.023% in Middelmann et al., 2015, which reports coefficient of thermal expansion of single-crystal silicon accurate to the order of 1×10^{-9}/K

cycling of indium bumps is of interest to the pixelated multilayer detector systems that we have previously mentioned. The subject is thoroughly addressed with both numerical simulations and experimental measurements in Cheng, Liu, and Silberschmidt, 2012.

7.4 Bonded stripline resonators

For application in MMIQCs, the relevant metric for superconducting bonds is their RF conductance. Earlier in this thesis, data in figure 5.11 showed that 3D cavity resonators composed of indium have dramatically increased seam conductance compared to those made of aluminum. In this section, we describe a test structure designed to probe bond conductance, and we push this bound higher.

Physics background.

In chapter 5, we discussed the effect that seam loss can have on 3D cavity resonators. The description in terms of seam admittance is applicable to all microwave resonators, cavities and planar resonators included. In order to systematically access any seam admittance, a planar stripline resonator can be designed with several superconducting bonds interrupting the continuous strip of metal. A stripline containing no bonds has $y_{\text{seam}} = 0$, while striplines containing more bonds in locations where the standing wave current is high access $y_{\text{seam}} > 0$. To do this, the parts of the stripline are fabricated on two chips that are then aligned and bonded together, as shown in figure 7.6.

The purpose of these stripline experiments is to isolate the fabrication parameters that have the most important effect on the superconducting bond quality. It is therefore important that the seam loss at the bonds is the dominant loss mechanism in the device. If another loss mechanism, dielectric loss for example, were dominant, we expect to see the quality factors unchanging with varying y_{seam}. Parameters that we suspect affect the seam conductance include the purity of the indium, indium bump size and pitch, pre-bond

cleaning procedures, bond pressure profile, bond temperature, and optional post-bond annealing temperature profile.

Fabrication of devices.

The stripline chip pairs were fabricated on a sapphire substrate. First, a liftoff process with optical lithography was used to create a pattern in copper. [8] Next, a second optical lithography step used a thick photoresist designed for use in electroplating (AZ9260) to mask off areas of the chip where indium is not allowed. Then, the wafer-electroplater described in appendix A was used to deposit indium on all exposed copper regions. Appendix A also contains an illustration of these fabrication steps, generalized to any pattern made by the masked-electroplating method.

Once the pattern is fabricated, the wafer is diced into pairs of chips which are then aligned and bonded. This thesis describes early experiments in which this process is somewhat crude compared to methods that are currently being developed. Specifically, the pairs of chips were manually aligned and bonded with the aid of a custom jig. The jig is diagrammed in figure A.3.

The stripline chip pairs were packaged in an aluminum tube housing that we have termed the "coaxline," (Axline et al., 2016) illustrated in figure 7.6**(e)**. This package is considered seamless, meaning that the only seams at the clamped ends of the chips have negligible admittance in the resonator modes. The two ends of the parent chips are individually clamped by pieces of metal at the end of the tube housing. Though here we show a transmission pin-coupled coaxline, most of the bonded striplines were measured in a multiplexed version of the hardware containing five resonators at a time. Microwave

---

[8] A possible concern is the effect of the normal conductor beneath the indium. Any effect that there is, however, would be identical for all of the striplines, including those with no bonds. To examine this, preliminary measurements of solid indium-on-copper striplines (with no bonds) were conducted. These devices are the left-most blue diamonds in figure 7.7. They reach the maximum Q that is possible to measure in this package. We are therefore satisfied that the presence of the normal conductor is not playing a significant role in the dissipation of the mode in question.
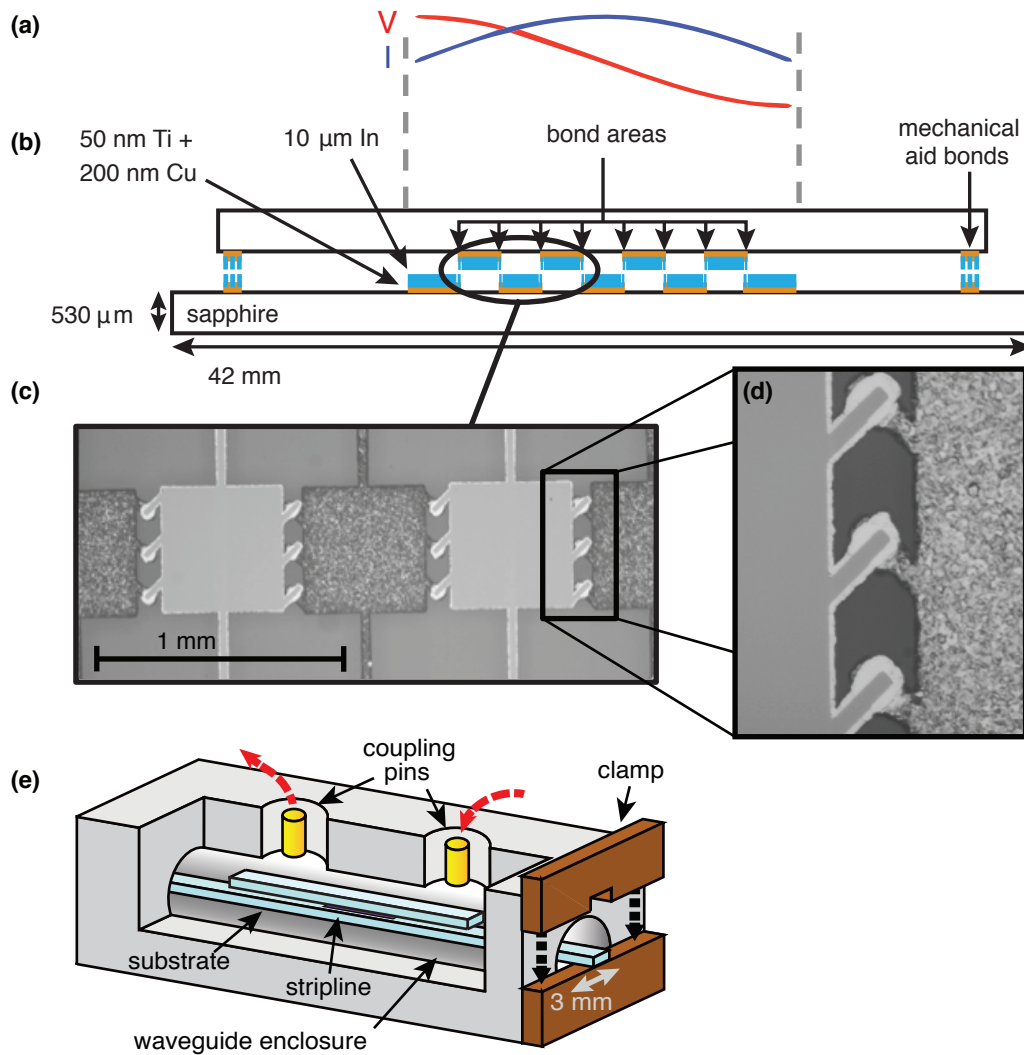
FIGURE 7.6: **Stripline resonator experiment with indium bonds.** The stripline is a $\lambda/2$ transmission line resonator, which supports a fundamental mode with voltage (red curve) and current (blue line) are shown in **(a)**. The stripline is composed of two chips that are bonded together to form a conducing line interrupted by a variable number of bond regions, as **(b)** shows in cross-section. The indium layer (light blue) is on top of the conducting seed layer (orange). The bottom chip is diced to size 42×2 mm and the top chip is diced to size 35×2 mm. To provide mechanical stability to the pair of bonded chips, groups of bonds in addition to the bond areas under test are necessary and placed at the two ends of the chips. In **(c)**, we show an image from an optical microscope viewing through the top chip. Since sapphire is clear, the reverse side of the top chip pattern and the indium of the bottom chip pattern are visible. A zoom-in of a single bond region is shown in **(d)**. The bond region consists of three overlapping fingers; each overlapping area is approximately 20×20 μm. The bonded chip stacks are loaded into a coaxline package, as shown in **(e)**, for measurement.
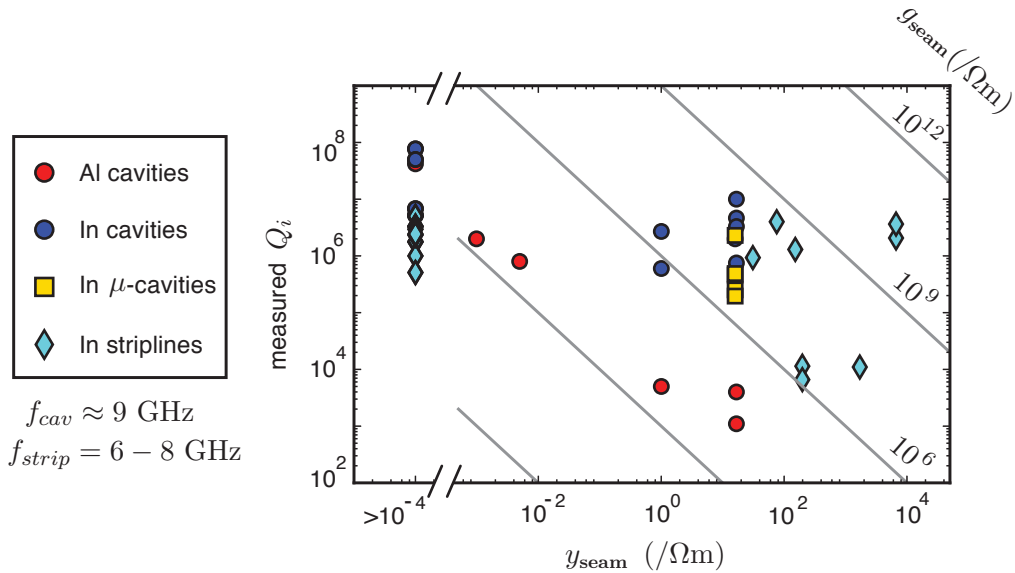
FIGURE 7.7: **Measured quality factor versus seam admittance for cavities and striplines.** Internal quality factors of resonators plotted against calculated seam admittance. Note that this graph builds upon figure 5.11.

signal is coupled to the striplines via a wire positioned coaxially in a tube running perpendicular to the stripline housing tubes. This is a "hanger" measurement (section 5.3.2) whose coupling strength depends on the distance from the wire to the end of the stripline. This coupling strength is therefore set in fabrication by the placement of the stripline relative to the ends of the chips, but small adjustments can be made in the placement of the chips in the clamps. The hanger measurement is suitable for frequency multiplexing several resonators.

Measurements and discussion.

The measured internal quality factors of the bonded striplines are plotted versus calculated seam admittance as blue diamonds in figure 7.7. We make several observations. First, observe that there is no evidence of a trend following seam conductance, even in this range of higher seam admittances. The achieved bond quality is highly inconsistent, as evidenced by the scatter in the points as well as the fact that some resonators did not appear

in spectroscopy at all. Nevertheless, it is fruitful to observe that the upper-right-most point sets a new bound on the conductance that it is possible to achieve in indium-indium bonds: $g_{\mathrm{seam}} \geq 10^{10}$ /Ωcm. Lastly, we note that stripline resonators of all seam admittances tested can approach the horizontal limit of $Q_{int} = 7 \times 10^6$, which is actually the maximum that is possible to measure, as it is the limit on Q imposed by p_{cond} of the aluminum package surrounding the indium chip (Axline et al., 2016).

7.5 Indium 3D resonators

First attempts at improving the quality factor of micromachined cavities through the application of indium bumps were not successful. Of four attempted cavities, the best performance was $Q_i = 2.0 \times 10^5$, whereas $Q_i = 2.7 \times 10^6$ was reached with full-coverage 10 μm thick indium. The reason could be poor uniformity in bump height over the large area of the cavity, or residual photoresist among the bumps. More notes on these experiments are found in table B.2, and they are represented as yellow squares in figure 7.7.

The resonators that we will discuss in this section were made with full-coverage indium (not bumps). Observing internal quality factor change with respect to circulating power can inform us about loss mechanisms that are present. In particular, dielectric loss is the suspect for a specific kind of trend. A rise and then plateau of Q at higher powers is well-documented (Gao et al., 2008; Khalil, Wellstood, and Osborn, 2011; Geerlings, 2013) and is attributed to the saturation of two-level fluctuator systems (TLSs) which are microscopic and thought to be distributed throughout an amorphous oxide layer on the surface of the superconductor. In this section, we will show our observation of this plateau in an indium 3D resonator. Then, we will discuss another dramatic change that is occasionally observed in resonators with high y_{seam} and speculate on its origin.

7.5.1 Power dependence with TLS signature

Physics background.

TLSs can collectively be significant source of dissipative loss at low powers, especially for resonators with high dielectric participation (see section section 6). They cause dissipation by absorbing power from the resonator and then decaying with some lifetime of their own to an external bath. At increasing powers, more of the TLSs are permanently excited, which creates a bottleneck in this avenue for dissipation. In other words, the population of TLSs becomes saturated at high circulating powers and the resonator's Q plateaus. The relationship is given by

$$\frac{1}{Q_i} \propto \frac{\tanh(\frac{\hbar\omega}{k_B T})}{\sqrt{1 + E^2/E_s^2}}, \tag{7.1}$$

where E is the RMS electric field in the resonator and E_s is a saturation electric field (Barends et al., 2010; Khalil, Wellstood, and Osborn, 2011). The value of E_s depends on the distribution of TLSs in the resonator, which can be modeled by solving the Bloch equations for the TLS density matrix (Burin, Khalil, and Osborn, 2013), but this is not generally known. Additionally, the TLS states can be partially saturated due to temperature, as accounted for by the $\tanh()$ in the numerator.

Measurement and discussion.

Using the measurement methodology described in section 5.3, various resonators were characterized at a range of powers. An example of a high quality factor resonator is an indium e-plated 3D cavity with a symmetric E-plane cut; data for which is shown in figure 7.8. Equation 5.82 is used to estimate the circulating photon number in the cavity. For this measurement, $Q_c = 8 \times 10^7$. Single photon powers require $P_{in} \approx 200$ dBm at the port of the cavity. The dilution refrigerator setup had approximately 75 dB of attenuation between the spectroscopic probe tone, from a VNA in this case, and the cavity. The minimum output from the VNA is -85 dBm, and an additional 40 dB of physical attenuation is

added to the VNA port in order to obtain the lowest power data. Measurements at single photon levels required about 10 hours of averaging time for a single spectroscopic VNA trace, even with a HEMT at 77°K and an additional 30 dB amplifier at room temperature. The data show a plateau in internal quality factor, indicating a saturation of TLSs after about a factor of two change from the quality factor at single-photon levels. Similarly, a micromachined cavity was also found to have about a factor of two difference between the high and low power internal Qs: 2.3×10^6 at $\bar{n} \geq 10^6$ versus 1.2×10^6 at $\bar{n} \approx 1$.

Comparing these findings with literature and what has been found in the lab, there are several things to note. First, 3D resonators tend to show a very small amount of power dependence compared to planar resonators due to their low dielectric participation. The TE011 mode of cylindrical cavity shows no power dependence at all thanks to having $p_{\text{diel}} = 0$ (Reagor et al., 2013). A coaxial $\lambda/4$ resonator (Reagor et al., 2016) was found to have a factor of four difference between the high power Q (6.1×10^7 at $\bar{n} \approx 10^6$) and low power Q (1.5×10^7 at $\bar{n} \approx 1$), due to its dielectric participation (2×10^{-7}). Planar aluminum, niobium, and NbTiN circuits on sapphire typically have a factors of 5 to 10 between high and single-photon powers (Khalil, Wellstood, and Osborn, 2011; Geerlings, 2013; Barends et al., 2010; Gao et al., 2008). We do not have a similar planar indium circuit with which to compare to these results. However, power dependence measurements of indium striplines in a coaxial package (figure 7.6**(e)**) reveal a factor of 2-3 between high and single-photon powers, which matches what is observed for aluminum striplines in the same package (Axline et al., 2016). We conclude that indium surfaces do not introduce TLS dissipation significantly larger than other metals that have been studied.
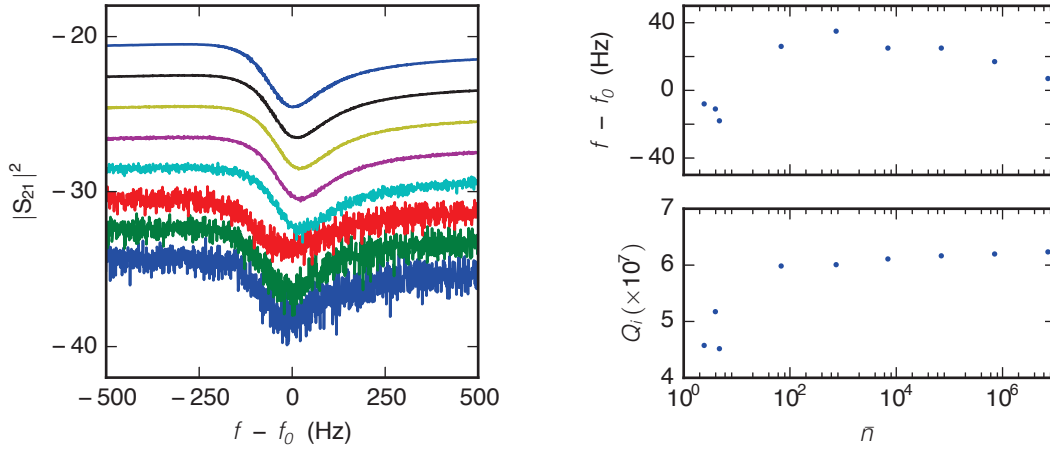
FIGURE 7.8: **Power dependence of indium 3D cavity.** This data is from the second cooldown of a rectangular cavity with a symmetric E-plane seam (type (a) from figure 5.11) machined in OFHC copper and electroplated to thickness of $100\ \mu$m indium. The resonance $f_0 = 9.49279983$ GHz and successive traces are offset by $+2$ dB. Note that a TLS saturation plateau is reached with less than a factor of two between high power and low power internal Qs.

7.5.2 Cases of nonlinear resonance

Different power-dependent behavior that is not explained by TLS excitation is occasionally exhibited in cavities with high y_{seam}. At very high circulating powers, we see a nonlinear response and bifurcation consistent with a Duffing oscillator. In this section, we will make some observations about these high-power effects. However, note that the usual cQED experiments do not operate in such regimes. It could be that the appearance of high-power nonlinearities can be an indicator of poor bonding at the seam, but otherwise are of no consequence to the operation of the device at lower powers. Therefore, this section exists to remark on experimental observation but is not relevant to the claims of this thesis.

Physics background.

A damped and driven Duffing oscillator is described by the ordinary differential equation

$$\ddot{x} + \delta\dot{x} + \alpha x + \beta x^3 = \gamma\cos(\omega t), \tag{7.2}$$

where δ is the damping factor, α controls the linear stiffness, and γ and ω are the amplitude and frequency of the driving force. The so-called Duffing term βx^3 controls the amount of nonlinearity in the restoring force. Notice that when $\beta = 0$, we have the damped and driven simple harmonic oscillator with linear frequency response. In general, the frequency response solution of the Duffing oscillator takes the form (Jordan, 2007)

$$\left[\left(\omega^2 - \alpha - \frac{3}{4}\beta z^2 \right)^2 + (\delta\omega)^2 \right] z^2 = \gamma^2, \tag{7.3}$$

where z is the amplitude of the steady-state solution $x(t)$ at a given driving frequency ω. In certain parameter ranges, the frequency response is not a single-valued function. When $\beta < 0, \alpha > 0$, the frequency response shifts and eventually overhangs downwards in frequency, and this is called the "soft" regime of the Duffing oscillator. On the other hand, when $\beta > 0, \alpha > 0$, the frequency response shifts and eventually overhangs upwards in frequency, and this is called the "hard" regime of the Duffing oscillator.

Previously, nonlinear dynamics, bifurcations and hysteresis were found and studied in planar superconducting resonators (Abdo et al., 2006; Golosovsky, Snortland, and Beasley, 1995). These works studied thin film Nb/NbN resonators, and the resonance frequency shifts down with increasing power, like that of a soft Duffing oscillator. Other works have observed similar behavior and offer explanations involving weak links and thermal effects (Chin et al., 1992; Cohen et al., 2002) or vorticies (Golosovsky, Snortland, and Beasley, 1995).

Soft Duffing nonlinearity at very high powers.

Figure 7.9 shows transmission amplitude and phase data from an indium-plated rectangular cavity with an H-plane seam (type **(a)** from figure 5.11, $y_{\mathrm{seam}} \approx 1$). Plots of amplitude and phase over a range of high powers are consistent with a soft Duffing nonlinearity with a bifurcation beginning at a circulating power of $\bar{n} \approx 5 \times 10^6$.
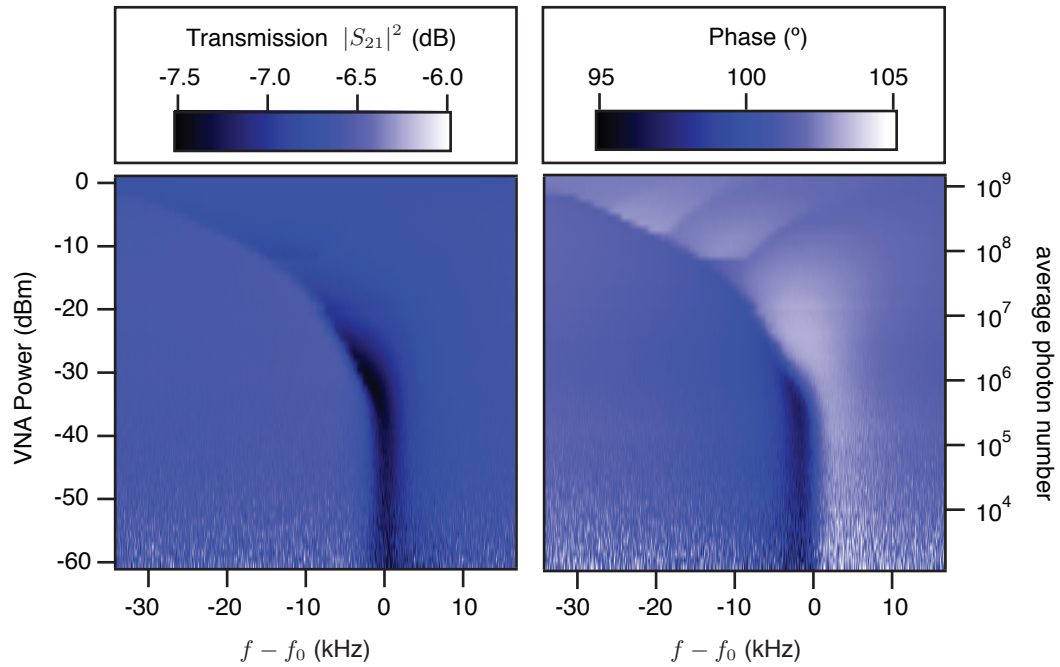
FIGURE 7.9: **Soft Duffing nonlinearity at high powers.** This data is from a rectangular cavity with an H-plane seam (type **(a)** from figure 5.11, $y_{\text{seam}} \approx 1$) machined in OFHC copper and electroplated to thickness of 30 μm indium. We show amplitude and phase over a range of high powers. The resonance $f_o = 9.531435$ GHz, coupling $Q_c = 3.3 \times 10^7$. Low power $Q_{int} = 2.4 \times 10^6$, while a nonlinearity takes over at higher powers, with bifurcation beginning at $\bar{n} \approx 5 \times 10^6$.

We can speculate on the source of this soft Duffing nonlinearity. The imperfect super-conducting bond may include an ensemble of nonlinear elements, such as SIS junctions of random transparencies and weak links, that act in parallel with the resonator. When heated or driven past their various critical currents, their inductance contribution decreases and this is observed by a change in resonance frequency that depends on circulating power in the cavity. By this model, where the imperfect seam adds parallel inductance, we expect the resonance to shift to lower frequency with higher powers as the inductances are shorted.

This is not a unique feature of indium cavities. Similar effects were also observed in high-seam participation cavities with poorly bonded (merely clamped in contact) aluminum-aluminum and niobium-aluminum seams (first three devices of table B.2). In these early cavities, it was also observed that the resonance frequency was highly sensitive to changes in external magnetic fields.

Hard Duffing-like nonlinearity.

Extreme power-dependent behavior was found in one experiment with high indium-indium seam participation. An example of the anomalous behavior is shown in figure 7.10, where we show a resonance of an indium micromachined cavity passing through a bifurcation regime. First, note that the transmission resonance has a total Q of 10^4, which is unusually low. The resonance is found to increase in frequency by 1.2 MHz, first entering a bifurcation regime and then returning to a nearly Lorentzian lineshape. This is one mode of a multi-mode device akin to the one featured in chapter 8. It is identified with the micromachined cavity because of its frequency, but also note that several other unintended modes exist in the device: there are modes at 4.73 and 5.76 GHz which behave in a similar nonlinear fashion. In addition to possessing large y_{seam}, it is suspected that these lower frequency modes are also dielectrically loaded with silicon.

We would like to estimate the circulating power in the mode during this phenomenon using equation 5.65. We can do so if we assume that the coupling is accurately described
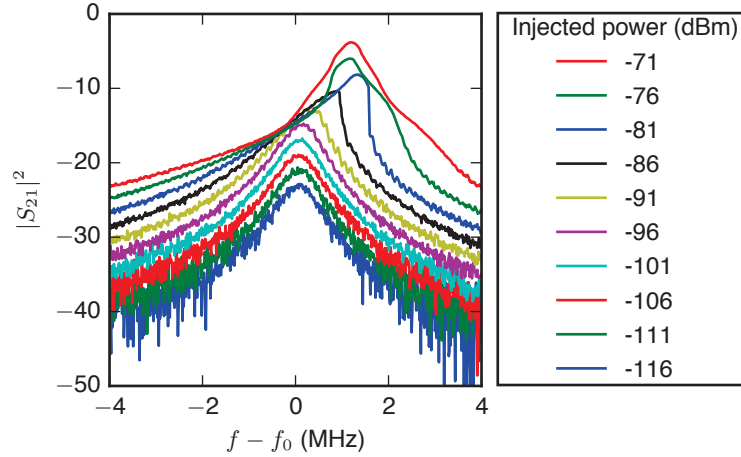
FIGURE 7.10: **Anomalous power dependence of indium 3D cavity.** This is a transmission resonance with $f_0 = 9.26252$ GHz, and $Q_{tot} = 10^4$ at low powers. It was found in a failed multi-mode MMIQC device of the type featured in chapter 8, along with several extra modes of similar behavior. Since there is uncertainty in Q_{int} and Q_c for this mode, we leave the scale in P_{in} at the cavity port. Successive traces are offset by $+2$ dB.

by our HFSS simulation, in which $\kappa_\mu/\kappa_r = 10^{-6}$. However, this is not likely to be accurate because the mode's total Q is lower than expected and there also may be unintended channels of coupling. If we do make this assumption, however, we expect $\bar{n} \approx 2300$ at injected power -86 dBm, at the onset of the nonlinearity.

It would seem that this is an example of a hard Duffing nonlinearity. As in the case described above, we speculate that the imperfect superconducting bond may include an ensemble of nonlinear elements, such as SIS junctions and weak links, this time acting in series with the resonator, adding inductance. When heated or driven past their various critical currents, their inductance contribution decreases and this is observed by a shift to higher frequency with higher powers. Unlike the previous case, the bifurcation here is only for a narrow power range. It could be that in high power ranges all of the superconducting weak links that are providing the nonlinearity become shorted, leaving us with a new linear resonator of higher frequency and only slightly reduced Q.

7.6 Temperature dependence of 3D indium microwave resonator

Resonator performance may be affected by the surface impedance of the superconductor itself (Zmuidzinas, 2012). The effect can be assessed by observing changes in the resonator's center frequency and internal quality factor as a function of temperature. In this section, we will briefly describe this effect and show temperature sweep data from cavity resonators made of indium. First, T_c can be readily identified from a microwave resonator's frequency shift near the transition. The behavior also indicates the kinetic inductance ratio, which we call p_{cond}, and the penetration depth.

Physics background.

As discussed in section 5.2.3 on conductor losses, superconducting resonators can be sensitive probes of the complex surface impedance $Z_S = R_S + j\delta X_S$. We write a differential surface reactance δX_S because an exact volume is not accessible. The relation we observe is

$$\frac{1}{q_{\mathrm{cond}}} + 2j\frac{\delta f}{f} = \frac{p_{\mathrm{cond}}}{\omega \mu_0 \lambda}\left(R_S + j\delta X_S\right). \tag{7.4}$$

Note the presence of the conductor participation ratio (or kinetic inductance fraction, denoted elsewhere α), p_{cond}, which is geometry-dependent, and the penetration depth, λ, which is material dependent only but changes as a function of temperature along with the superconducting energy gap. We will look at the change in quality factor and frequency separately, and expect

$$\frac{\delta f}{f} = \frac{f(T) - f(0)}{f(0)} = -\frac{p_{\mathrm{cond}}}{2}\frac{X_S(T) - X_S(0)}{X_S(0)} = -\frac{p_{\mathrm{cond}}}{2}\frac{\delta \lambda}{\lambda}, \tag{7.5}$$

$$\delta\frac{1}{q_{\mathrm{cond}}} = \frac{1}{q_{\mathrm{cond}}(T)} - \frac{1}{q_{\mathrm{cond}}(0)} = p_{\mathrm{cond}}\frac{R_S(T) - R_S(0)}{X_S(0)}. \tag{7.6}$$

Note that the frequency change depends only on the change in surface reactance, which effectively shortens the penetration depth at increasing temperatures. The change in quality factor arises from a chance in surface resistance.

The superconductor's surface impedance is related to the normal state surface impedance $Z_n = R_n + jX_n$ as

$$Z_S \propto Z_n \times (\sigma_1 + j\sigma_2)^\nu, \tag{7.7}$$

where σ_1 and σ_2 are dimensionless conductivities of Mattis-Bardeen theory (Mattis and Bardeen, 1958). In the superconducting state, the surface reactance is much larger than the resistance: $\sigma_2 \gg \sigma_1$, and (Tinkham, 1996)

$$
\begin{aligned}
R_S &\propto R_n \sigma_1 \sigma_2^{\nu-1} \tag{7.8}\\
X_S &\propto R_n \sigma_2^\nu. \tag{7.9}
\end{aligned}
$$

The exponent ν indicates whether the superconductor behaves in the clean (or London) limit, for which the mean free path is greater than the coherence length and $\nu = -1/3$, or the dirty (or Pippard) limit, for which the mean free path is much less than the coherence length and $\nu = -1/2$ (Nam, 1967b; Nam, 1967a). The penetration depth is defined as

$$\lambda = \frac{X_S}{\omega \mu_0}, \tag{7.10}$$

and the surface conductor quality factor is $q_{\text{cond}} \approx \sigma_2/\sigma_1$.

BCS theory predicts a universal form for the energy gap Δ versus reduced temperature, $\bar{t} = T/T_c$: (Tinkham, 1996–section 3.6.2)

$$\frac{1}{N(0)V} = \int_0^{\hbar\omega_D} \frac{\tanh\left(\frac{\hbar}{k_B \bar{t}}\sqrt{\xi^2 + \Delta^2}\right)}{\sqrt{\xi^2 + \Delta^2}} d\xi, \tag{7.11}$$

Where $\omega_D = \Theta_D k_B/\hbar$ is the Debye frequency, $N(0)$ is the density of states at the Fermi level and V is the BCS interaction strength. The values for indium and aluminum are included in table B.1. This describes the characteristic shape for the gap rolling off to 0 at $\bar{t} = 1$. We numerically solve it to tabulate a table of values for $\Delta(\bar{t})$ and use it in the numerical
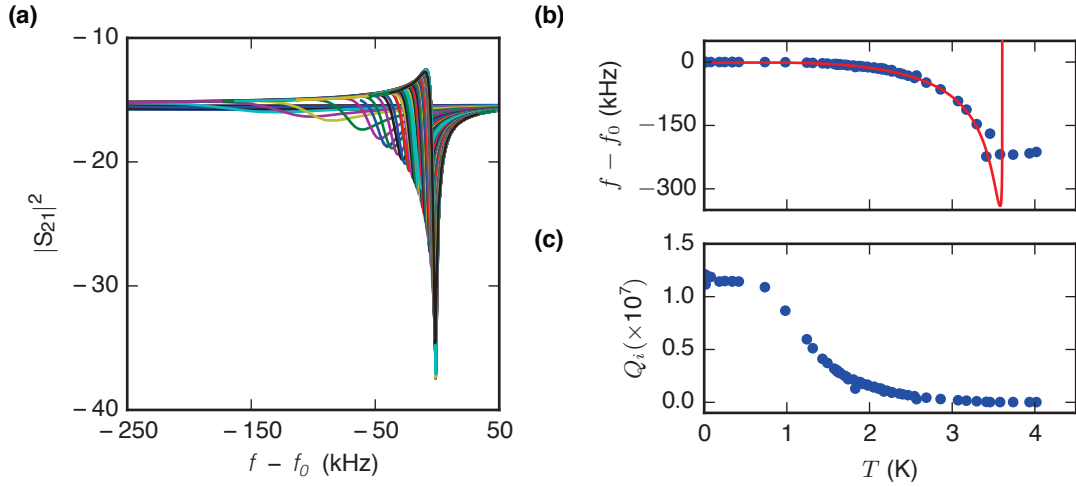
FIGURE 7.11: **Fitting temperature dependence to BCS theory. (a)** The frequency of an indium cavity resonator ($f_0 = 9.738$ GHz) was tracked from 15 mK across the superconducting transition temperature at approximately 3.4 K. **(b)** The frequency shift of the resonator is proportional to the surface reactance of the superconductor (equation 7.5). Using the BCS integrals allows independent determination of T_c and p_{cond}. **(c)** Internal quality factor versus temperature. The shape of the roll-off is described by the rise in surface resistance – see figure 7.12.

integration of the Mattis-Bardeen expressions for AC conductivities σ_1, σ_2, following the procedure of (Reagor et al., 2013; Reagor, 2015) but replacing ω_D and $N(0)V$ for indium. See Reagor, 2015–section 5.1.5 for details and prior measurements of 3D resonators made of aluminum and measured in our lab.

Measurement and discussion.

We show temperature dependence of a 3D rectangular resonator with indium walls in figure 7.11. The central frequency shifts by a maximum of 23 parts per billion from one side of the superconducting transition to the other. The frequency should reach a minimum value at T_c, where $\hbar\omega = 2\Delta$ and resonant Cooper-pair breaking occurs, then stabilize as a normal state surface impedance is reached. While our data points have not captured this narrow pair-breaking regime exactly, there is a clear transition near the expected T_c, so we apply the discussed fitting method. The best fit results in $p_{\text{cond}} = \alpha = 4.5 \times 10^{-5}$ and $T_c = 3.46$ K. The accepted value for indium's T_c is 3.4 K, so something may be amiss
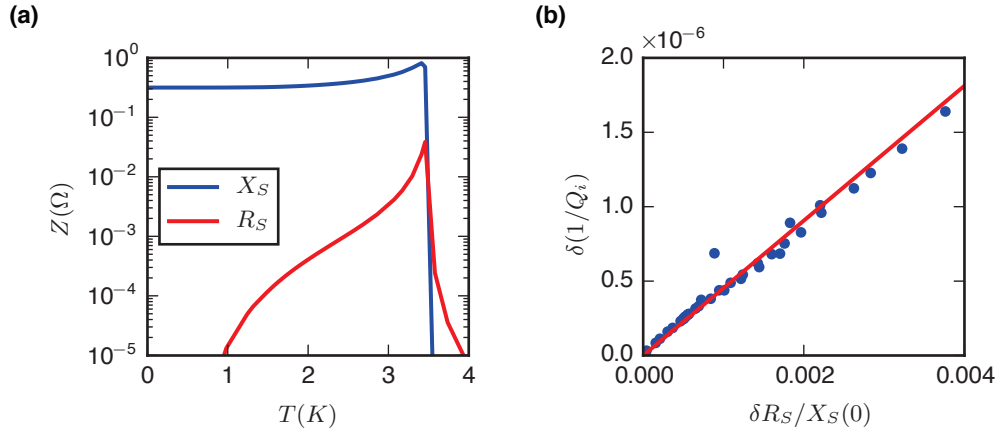
FIGURE 7.12: **Fitted surface impedance of indium resonator. (a)** We plot the real (red) and imaginary (blue) parts of the surface impedance resulting from numerical integration of the Mattis-Bardeen conductivities using a table of values for the gap of indium $\Delta(\bar{t})$ and fitting to our resonator's frequency response data. Increasing temperature brings a rise in surface resistance (real conductivity σ_1). **(b)** Plotting the change in inverse quality factor versus $R_S/X_S(0)$ ideally results in a line with slope p_{cond} (equation 7.6). The solid red line fit yields $p_{\mathrm{cond}} = 4.5 \times 10^{-5}$, corresponding to $\lambda = 23$ nm.

in thermalization of the resonator or density of data points in the region near T_c. The corresponding penetration depth is $\lambda = 23$ nm. Dheer, 1961 reports 46 nm, measured at 3 GHz.

We look more closely at the results of the fit by examining the the surface reactance and surface resistance versus temperature in figure 7.12. We fit to the conductivities and show the components of surface impedance as they relate with equation 7.8-7.9; the data best agreeing with the Pippard limit of a dirty superconductor with $\nu = -1/2$, as is also the case with bulk high-purity aluminum measured in our lab. The change in inverse quality factor versus $\delta R_S/X_S(0)$ results in a line with slope p_{cond} vis-à-vis equation 7.6 with good agreement.

The temperature-sweeping procedure for gathering such data is easily employed in a dry-cycle dilution refrigerator only up to about 1.5 K. This is sufficient to investigate aluminum resonators, for which $T_c \approx 1.2$ K. Temperature control is achieved by resistive heaters and automated PID control, but this is not possible at temperatures above about

1.5 K because the helium mixture becomes unstable and begins to evaporate, creating a thermal link that rapidly warms the baseplate. To collect well-thermalized data points between 3 and 4 K, a different strategy is necessary. It involves warming to just above 4 K and then recondensing with a small amount of helium present in the precool circuit. In the condensation step of a usual cooldown, the precool circuit is emptied and condensation occurs quickly, but in this case the small additional thermal link slows the cooling to allow better thermalization of the indium cavity under test. In this data set, the cooling rate between 4 and 1.5 K was -1.9 mK per second. Downward swept points in this range are combined with upward swept points from 15 mK to 1.8 K for the graph and fit. The fact that the warming and cooling sweeps mostly overlap in the coinciding temperature range is encouraging evidence for sufficient thermalization. However, we must be slightly suspicious of this fit to BCS theory, as it yields a T_c that is 50 mK greater than the accepted value of 3.41 K. In the next section, we find T_c with a DC measurement.

7.7 DC resistivity of indium versus temperature

We just saw that T_c can be identified from a microwave resonator's frequency shift near the transition. A second (and simple) way to measure T_c is to simply observe the DC resistance of a wire as the temperature is brought across the transition.

Physics background.

Thanks to its low Debye temperature, the resistance versus temperature curve of pure indium has very good sensitivity down to T_c. Because of this, long thin indium wires have been used to make low temperature resistance thermometers appropriate for $3.4 < T < 300$ K (Logvinenko, Mikhina, and Mende, 1984). Precisely at T_c, the resistivity abruptly drops to 0 as the metal enters a superconducting state.

Along with identifying T_c, the temperature dependence of the resistivity can reveal additional properties of the metal, chiefly whether it contains significant impurities. Above

the Debye temperature, resistivity is dominated by electron-phonon scattering, which scales linearly with temperature. At very low temperatures, but above the superconducting transition, resistivity is dominated by electron-defect scattering, which is temperature independent. Therefore, if defects are present, the residual resistivity ratio defined as $RRR = \rho(273 \text{ K})/\rho(T_c + \epsilon)$ is an indicator for purity of a metal. There is also an intermediate region around $T \approx \Theta_D/3$, where resistivity has contributions from both phonon and defect scattering; and in this region resistivity follows approximately $\rho \sim T^5$.

Measurement and discussion.

I measured DC resistance of a long thin indium wire versus temperature using a Dynacool PPMS (Physical Property Measurement System). The test device was a 20 μm wide wire totaling 205 mm long that meanders to fit on a 6×6 mm chip of sapphire. It was fabricated by optical lithography and electroplating of indium (appendix A); the wire consisting of ∼1 μm indium atop ∼150 nm copper. The accepted values for room temeprature bulk resistivity of indium and copper are 8.4×10^{-8} and 1.7×10^{-8} Ωm respectively. From the dimensions of our wire, the expected room temperature resistance is 860 Ω in the indium layer and 1200 Ω in the copper layer, adding in parallel to 500 Ω. Resistance data were collected in a four-point-probe setup, wherein a current is applied and the voltage is measured to provide $R = V/I$. This method nullifies contributions from contact resistances at the probe (wirebonds) or between the copper and indium transition at this pad.

The device and data are shown in figure 7.13. We observe the a superconducting transition between 2.80 - 2.95 K. The data shown include cooling (lefthand step at 2.80 K) and heating (righthand step at 2.95 K). Above the superconducting transition but below 10 K, we see that the resistance is dominated by electron-defect scattering. The sample has $RRR = 70$. In order to separate the contribution of both the copper and indium layers to this residual resistivity, we need to do another measurement of only copper.

The accepted T_c for indium is 3.4 K, and the fact that we observe a clear transition at 2.9 K may indicate impurity in our material. A previous study (Bruynseraede et al., 1971)
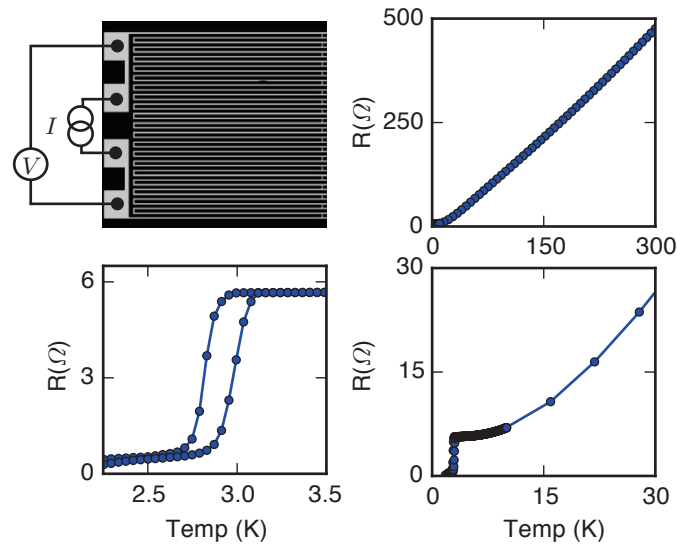
FIGURE 7.13: **Indium wire resistance versus temperature.** The device is a 205 mmm long wire consisting of ~1 μm indium atop ~150 nm copper. Voltage was measured in a four-point-probe configuration with excitation current 10 μA. Here, one set of resistance data are plotted in three different scales. From 10 to 1.8 K, the data were collected in 40 mK steps with software controlled feedback designed to prevent overshooting of temperature setpoints in both cooling and warming sweeps. The discrepency between steps, however, is evidence of imperfect thermalization of the sample. $T_c = 2.9 \pm 0.1$ K.

on electroplated indium attributed reduced T_c to organic contaminants present in the metal that originated from the electroplating bath. This study found transition temperatures of 2.4 K for metal plated from an indium floroborate bath and and 3.3K for metal plated from an indium sulfate plating bath. Our indium is plated from an indium sulfamate plating bath (see appendix A).

7.8   Conclusion

In summary, we began this chapter discussing wafer bonding, including the use of indium bumps. We have fabricated indium bumps using a masked electroplating process in the lab, but their application around the perimeter of micromachined cavities did not improve quality factors over the cavities bonded with full-coverage indium. Wafer bonding with indium has some mechanical considerations that we have discussed with the aid of the

literature and our own simple observations of deformation and shear. Essentially, the extreme malleability of indium across a wide temperature range makes it an ideal candidate as a bonding material in 3D integration for cryogenic applications.

Next, we looked closely at microwave resonators made of indium. First, we used bonded stripline resonators as a test-bed to establish a bound on indium bond conductance of $g_{\mathrm{seam}} \geq 10^{10}$ /Ωcm. Then, we found that varying the circulating power in a 3D resonator reveals a plateau consistent with TLS saturation in a thin dielectric layer (nm oxide) at losses very similar to those found in aluminum 3D resonators. Then, we commented on power-dependent bifurcation regimes that present themselves in resonators with H-seam construction (high y_{seam}). This sort of power dependence is not unique to indium, as similar behavior is found in 3D aluminum cavities with H-seam construction (however, it may not appear as dramatically because of the wider linewidth).

We then examined the surface impedance of indium by observing the change in frequency and quality factor with respect to temperature, successfully fitting to BCS theory in the dirty limit to find a penetration depth of 23 nm, which is roughly half the value reported in the literature. This microwave measurement also yielded a value for indium's critical temperature of 3.46 K. Tracking the DC resistance of a long indium wire through the superconducting transition, however, revealed $T_c = 2.9 \pm 0.1$ K.

Having concluded this assessment of indium's suitability as a superconductor and bonding material, the next chapter returns to cQED.

Chapter 8

Transmons in the MMIQC

This chapter concerns the integration of qubits with micromachined cavities. To begin, we explain why this is not a trivial matter of replicating the common methods in either existing planar or 3D cQED circuits. We then show the design, fabrication, and characterization of a quantum device containing a transmon qubit coupled to a superconducting micromachined cavity for the first time. Before concluding, we touch on two reasonable modifications to devices of this kind.

8.1   Coupling challenge

Coupling between a resonator and a qubit occurs via shared electric and magnetic fields of their respective modes. However, there is an orientation challenge to address in order to produce strong coupling of qubits to micromachined cavities. In planar circuits, qubits coupled to the metal of a transmission line resonator capacitively and/or inductively. In traditionally machined 3D cavities, the qubit electrodes form a dipole antenna – it is fabricated on a separate chip and then inserted into the cavity to align with the cavity fields. We have discussed these schemes in chapter 3, and they are diagrammed in figure 8.1**(a)-(b)**. It would be impractical to use the same scheme for coupling qubits to micromachined cavities because of the extreme aspect ratio imposed by the wafer height. While it is certainly

163
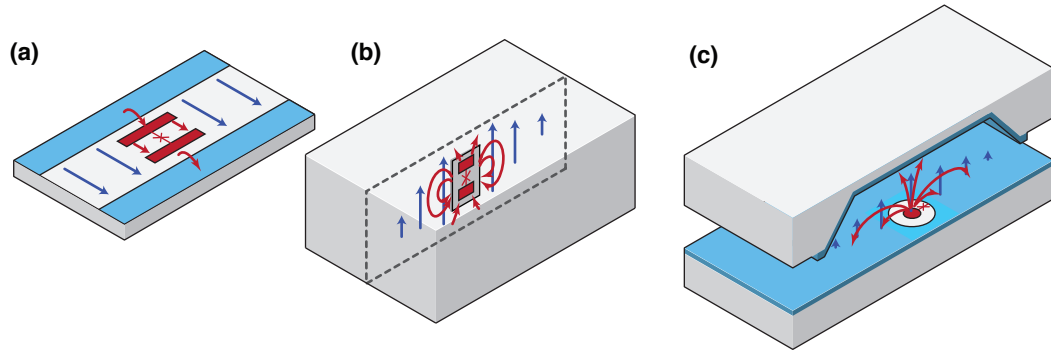
FIGURE 8.1: **Transmon coupling orientations.** Illustrations of dipole coupling in cQED. Electric dipole moment orientations for typical transmons are fabricated to align with **(a)** the electric field of a planar transmission line resonator or **(b)** the electric field of an encapsulating 3D cavity. Blue arrows show electric field lines of the each resonator's fundamental mode, and red arrows show electric field lines of the transmon mode. **(c)** The aperture transmon fields couple to the fundamental mode of the micromachined cavity. For clarity, the diagram shows an exploded cross-sectional view of two substrate wafers, and it is not to scale.

possible to follow the same strategy as larger 3D cavities, it would require precise assembly of small components and/or non-standard lithography methods, so we would like to avoid these complications. Instead, we desire to achieve the same coupling while limiting ourselves to planar fabrication and wafer stacking. It is possible to pattern electrodes on one of the cavity walls such that the electromagnetic fields couple to those of the cavity, as suggested by figure 8.1**(c)**.

8.2 The aperture transmon

The coupling of an to a resonator using fields that are out of the plane of transmon fabrication (Minev et al., 2016a) is described in the context of two separate experiments in Minev et al., 2016b and Brecht et al., 2017. The design consists of an annular opening in the broad wall of the cavity, creating a central electrode which is connected to the wall (ground-plane) by one or more leads containing one or more Josephson junctions. For out-of-plane coupling to occur, there must be significant capacitance between the central electrode and

proximal metal of the opposite cavity wall. We have come to call this geometry an "aperture transmon." The mechanism can be understood by analyzing the overlap between the electric fields of the transmon mode and those of the adjacent cavity mode(s), and also by an equivalent circuit model.

Before moving on, we compare the aperture transmon to two other works. First, the "concentric transmon" (Braumüller et al., 2016) consists of a circular electrode connected by a two Josephson junctions to an annular outer electrode, backed by a continuous groundplane on the flipside of the chip. This gradiometric (frequency-tunable by flux-bias) transmon is lauded for its comparatively large magnetic dipole moment, which could be used to establish site-selective $\hat{Z}$-coupling between neighboring qubits in an array (Sandberg et al., 2016), while the superconducting back-plane reduces radiation loss and cross-talk by cancellation with image-charges (Sandberg et al., 2013). Second, Rahamim et al., 2017 reports on the out-of-plane coupling through a dielectric layer between a transmon and a resonator in which a Josephson-junction (in the transmon) or a thin inductive wire (in the resonator) separates a circular inner electrode and an annular outer electrode. The transmon and resonator are aligned on opposite sides of a sapphire chip and accessed by coaxial cables positioned normal to the chip on both sides, and operated in either reflection or transmission. The coupling is very strong ($g/2\pi > 450$ MHz) because of the close proximity through dielectric of ϵ_r=10. The dielectric participation of both modes is very large, and the qubit decay time $T_1 = 4$ μs is likely Purcell limited. The advantage advertised in this work is the simple non-contact out-of-plane coupling to external control wiring, possibly extensible to larger 2D arrays.

8.2.1 Fields of the aperture transmon

Consider an aperture transmon design in which the opening in the metal has the shape of a circle of radius r_o and the inner electrode is disk of radius $r_i < r_o$. The circles are concentric and the inner disk electrode is connected to the outer metal by a lead interrupted by a

Josephson junction. To get a rough estimate of the coupling strength to expect, we can approach the problem in a similar way to the derivation in section section 3.5. First, we need to obtain an expression for the dipole moment of the annulus structure in terms of r_i and r_o.

We start with an analytic approach to study the electrostatic field in two limiting cases. Begin with a large conductor plane with an annular ring removed, and assume that a voltage V_0 is applied across the annulus. There will there be an electric field across the gap as well as an electric field pattern out of the plane. The total field has quadrupole-like fields which point in opposite directions on either side of the plane.

In the limiting case of an infinitely thin annulus $r_i \approx r_o$ (figure 8.2(a)) is treated by Jackson, 1998–problem 3-12. The potential at any point in space round such an annulus is given in cylindrical coordinates (thin annulus of radius r centered at $\rho = 0$ in an infinite conducting sheet $z = 0$) by the integral expression

$$\Phi(\rho, z) = rV_0 \int_0^\infty J_1(kr)J_0 k\rho e^{-kz} dk. \tag{8.1}$$

The field is that of two opposing dipoles of identical magnitude pointing out of the annular plane in both directions:

$$|\vec{p}| = \frac{4\pi\epsilon_o}{3}V_0 r^2. \tag{8.2}$$

In the limit of no central island at all ($r_i = 0$, (figure 8.2(b))), this is a circular aperture. In the presence of an incident E-field, the field on the other side can be approximated as a dipole with r^3 dependence (equation 5.22),

$$|\vec{p}| = \frac{2}{3}\epsilon r_o^3 E_o. \tag{8.3}$$

As the radius of the inner island goes from 0 to r_o, there must be some smooth correspondence between the fields in these two limits. The actual system to which we want to

(a)   **(b)**

$$r_i \approx r_o \equiv r$$

V_0 r_o

$\uparrow E_0$

$\mathbf{p} \propto r^2$ $\mathbf{p} \propto r_o^3$

$\mathbf{p} \propto r^2$
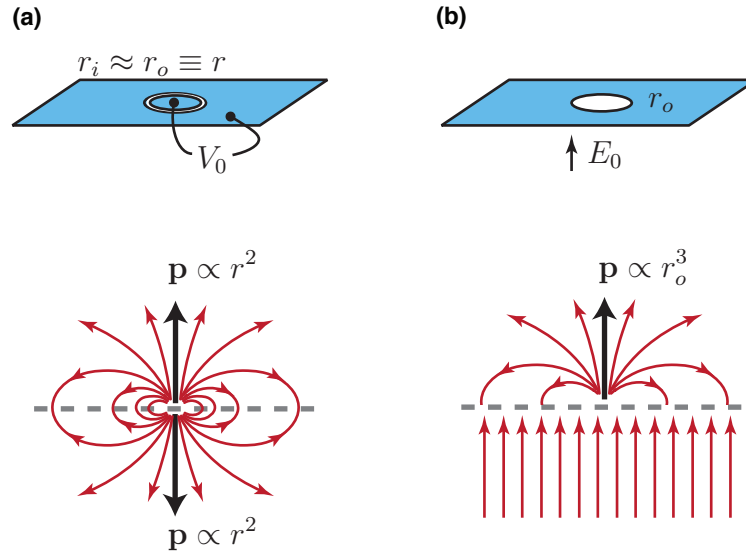
FIGURE 8.2: **Dipole fields of an annulus and aperture.** Illustrations of electric field (red arrows) corresponding to two limiting cases of the annular ring excised from a conducting sheet. **(a)** In the limit of a narrow annulus with applied voltage V_0, the field contains components of opposing dipoles matching equation 8.2. **(b)** In the limit of a circular aperture, an incident field generates a dipole matching equation 8.3.

apply this understanding is complicated by several effects. First is the presence of a nearby conductor: The distance from the annulus island to the wall of the micromachined cavity is on the same order as the annulus dimensions. Furthermore, the fields are affected by the presence of the dielectric substrate. Finally, we have eventually chosen a shape that differs from the circular annulus. In practice, an analytic expression for the fields or coupling strength is difficult and not the best avenue for design.

If we now imagine inserting such a structure in the middle of the cavity, the contribution from the two identical opposing dipole moments (in $+/- \hat{y}$, the direction of the cavity height) would cancel and the coupling would be nullified. When placed nearer to one wall, the capacitance between the two conductors and the cavity wall creates an asymmetry, leaving a net electric dipole moment in line with the cavity field. The presence of a dielectric, i.e. the chip upon which the structure may be fabricated, can further enhance

this asymmetry and therefore the coupling to cavity fields. Additionally, our intuition suggests that coupling will be increased with reduced height of the cavity. We are therefore encouraged that this structure is a strong candidate for pairing qubits with micromachined cavities in the MMIQC vision. We will proceed in the next section with designing the structure directly on a wall of the cavity such that only one of the two opposing dipole moments couples to the cavity field.

Note that, were it not for the cavity, such an electrode structure in a planar circuit would be especially prone to radiation loss. The aperture transmon was in fact first inspired by microwave patch antennae, which are intended to send and receive far-field radiation signals. The dipole radiation description and accompanying far-field equations will not directly apply in our case, however, because the opposite wall of the cavity is definitively near-field. Patch antennae come in a variety of shapes and sizes, but we note especially the annular slot antenna (Al-Zoubi, Yang, and Kishk, 2009; Sun et al., 2013) and a complementary structure: an annular ring microstrip antennae. We are not unaware of the existing body of microwave engineering research, including analyses of optimum ring dimensions aiming to maximize radiation efficiency and bandwidth of similar structures. For example, Sun et al., 2013 contains some relevant discussions on designing TM01 and TM02 modes of annular ring slot antennas backed with dielectric and air layers. Some patch antennae are backed with micromachined cavities in order to enhance outward radiation efficiency (Zheng et al., 1998).

We have discussed the electric field of the aperture transmon because it provides the relevant imagery for understanding the coupling of the qubit and cavity in the chosen configuration. Our strategy is to create overlap of electric field (charge differences, voltages), and this is equivalent to a capacitive coupling. As shown in figure 8.3, the coupling is strongest when the qubit is in the center of the chip, where the electric field of the cavity is maximum. The dual strategy is to create overlap of magnetic field (moving charges, currents), and this is described as an inductive coupling. From the graph, we conclude

cavtiy height (ŷ) = 300 μm
width (x̂) = 22 mm
length (ẑ) = 24 mm

r_i = 500 μm, r_o = 800 μm

z-displacement
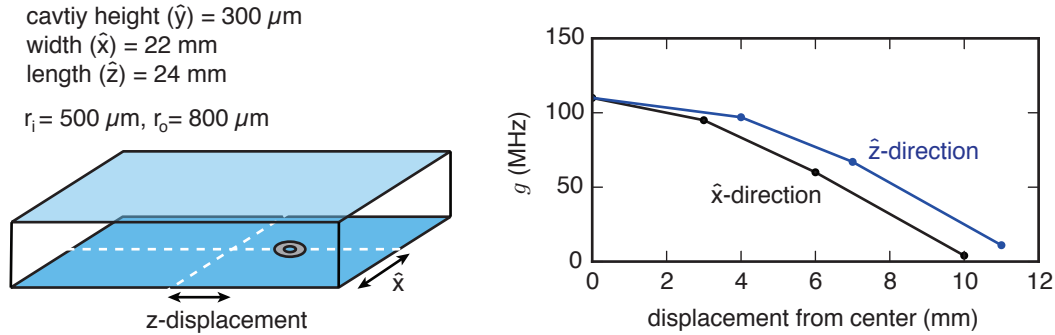
FIGURE 8.3: **Coupling rate versus position on cavity wall.** With the geometry of the cavity and aperture transmon electrodes fixed, we plot the simulated (HFSS) resonant coupling rate g versus lateral position of the transmon on the cavity wall. The coupling is strongest in the center of the cavity (where the electric field is maximum) and becomes very small near the edges of the cavity, which is evidence that this electrode geometry is targeted towards capacitive coupling, and that any inductive coupling contribution is small.

that for a fixed aperture transmon electrode shape, the capacitive coupling depends on the lateral position in the expected sinusoidal way. Furthermore, the inductive coupling is very small in comparison, even near the walls of the cavity where the magnetic field is the largest. This is reasonable because only a very small fraction of the total magnetic energy is localized near the aperture transmon.

We can compare this situation to the coupling configurability in the aperture transmon and whispering gallery resonator device (Minev et al., 2016b). In that device, it is possible to target either capacitive or inductive coupling with high efficiency. Furthermore, the ring-shaped resonator has two orthogonal TEM modes nearby in frequency and with mode structures that are similar only with a 90° rotation. The transmon can be positioned around the ring at an area of high electric field or an area of high magnetic field with respect to either of the modes. Coupling strength to each mode is adjusted by the aperture transmon's placement around the ring and size of inner electrode and outer aperture. Here, the magnetic coupling can make a large contribution to the total because it is acceptable for the aperture to span a large fraction (~90%) of the resonator's width. In the micromachined cavity, strong inductive coupling could conceivably be accomplished

by creating a long aperture that spans a significant fraction of the cavity width or even perimeter. However, this approach is problematic for reasons relating to both increased seam loss (section 8.6.3) and radiation loss. Therefore, we keep it simple by using a centered aperture transmon and discussing capacitive coupling with a circuit model next.

8.2.2 Aperture transmon and cavity circuit model
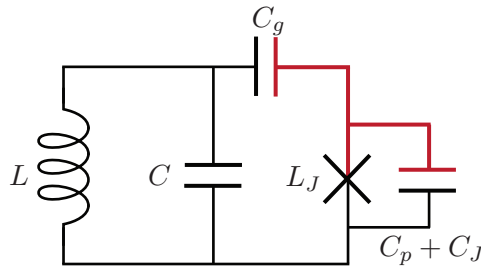
FIGURE 8.4: **Aperture transmon and cavity circuit model.** The red part of the circuit maps to the central island of the aperture transmon geometry. C_g is the capacitance between the central island and the opposite cavity wall. C_p is the capacitance across the annulus. The Josephson junction has an inductance L_J and a small capacitance C_J.

Analogously to our exercises in section 3.5 for existing cQED hardware designs, a circuit picture elucidates the relationships between device geometry and coupling strengths. As before, the 3D layout is straightforwardly mapped to a circuit like that of figure 3.8**(a)**. An equivalent circuit for the aperture transmon embedded in the cavity wall is drawn in figure 8.4. A single Josephson junction connects the central island to the rest of the cavity wall. It is accompanied by a junction capacitance (C_J), which is small compared to the other capacitors in the system: First, there is a capacitance across the open annulus between the island and the rest of the lower cavity wall (C_p). Second, there is a capacitance across the gap between the island and the opposite wall of the cavity (C_g). Lastly, there is capacitance C associated with the walls of the cavity, which combines with an effective inductance L to create the LC-resonator characteristic of the cavity's fundamental mode at frequency $\omega_\mu = 1/\sqrt{LC}$.

We have the case of equation 3.43, which we re-write as

$$\frac{g}{\omega} = \sqrt{\frac{1}{2\pi^3}} \left(\frac{2E_J}{E_C}\right)^{\frac{1}{4}} \sqrt{\frac{Z_c}{Z_0}} \beta \boldsymbol{\alpha}^{1/2}, \tag{8.4}$$

where

$$\beta = \frac{C_g}{C_g + C_p + C_J}. \tag{8.5}$$

Substituting the fine structure constant, we can write this as

$$g = \frac{1}{2} e\omega \sqrt{\frac{Z_c}{\pi^3 h}} \left(\frac{2E_J}{E_C}\right)^{1/4} \beta. \tag{8.6}$$

While this equation is more precise, we will now plot β and a corresponding g assuming that the qubit is a simple two level system; using $g = eV_0\beta/\hbar$, where $V_0 = \sqrt{\hbar\omega_\mu/2C}$ (equation 3.44). Voltage excitations in the cavity mode correspond to ones across the junction scaled by β, a capacitance ratio that determines a voltage division in the circuit. The capacitances are modified by adjusting the geometry of the qubit electrodes as well as that of the surrounding cavity geometry and any dielectric that is present, and adjusting the location of the qubit on the cavity wall. We perform electrostatic simulations of the relevant capacitances to investigate relationships to geometry. Some such relationships are shown in figure 8.5. These trends are useful guides device design. However, we note that our device will be in the transmon regime, where the reduced anharmonicity complicates the otherwise simple Jaynes-Cummings model of equation 3.25. Instead, we will consider equation 8.7 and perform Black Box Quantization to determine the target parameters.

8.3 Designing a two-cavity/one-qubit device

The purpose of the experiment is to demonstrate strong coupling between a single micro-machined cavity and a single qubit embedded in its wall. As we have noted, the annular structure has fields on both sides, and we intend to fabricate it directly on the wall of the
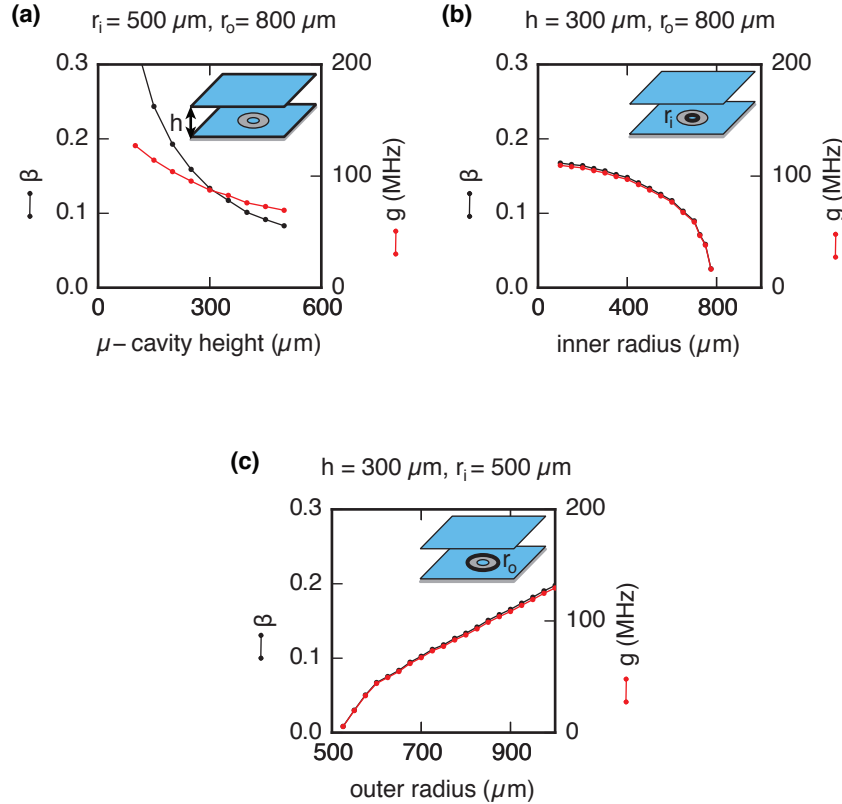
FIGURE 8.5: **Relationships of the capacitance ratio β (black) and coupling rate g (red) versus three geometrical variations.** These results were obtained using ANSYS Maxwell® to model the capacitance matrix of a set of three conductors while including the dielectric: 325 μm slab of silicon. The capacitance ratio $\beta = C_g/(C_g + C_p + C_J)$ is plotted in black and the coupling rate g is plotted in red. **(a)** Coupling increases with reduced micromachined cavity height by way of increasing gap capacitance C_g. **(b)** Coupling increases with smaller r_i, but with weakening dependence as r_i becomes smaller than h. **(c)** Coupling increases with larger r_o, and the relationship is linear when $r_o > 1.5r_i$.

micromachined cavity. Therefore, the first experimental device design actually includes two cavities – one placed on each side of the qubit. The second 3D cavity is added to the other side of the qubit to provide microwave control of the system. This "readout" cavity is traditionally machined and has pin-to-coax input/output ports as described in section 6.3.1. The integration of the machined 3D cavity demonstrates the aperture transmon's bipartite coupling and provides a convenient way of connectorizing the device. The

device also displays a hybrid multilayer construction, including silicon wafers and conventionally machined metals united by indium bonding on flat surfaces. It is shown in figure 8.6.

Our goal is to design a system in the the strong dispersive limit, where the frequency detuning between each resonator and the qubit is much greater than the interaction rate ($|\Delta| \gg g$) and the interaction rate is much greater than the decay rates of the qubit or cavity ($g \gg \kappa_q, \kappa$). In this strong dispersive limit, we approximate the applicable Hamiltonian as

$$\frac{H}{\hbar} = \sum_i^{q,\mu,r} \omega_i a_i^\dagger a_i - \sum_{i \neq j}^{q,\mu,r} \chi_{ij} a_i^\dagger a_i a_j^\dagger a_j - \frac{\alpha_q}{2} a_q^{\dagger 2} a_q^2 \tag{8.7}$$

where the three modes are labeled q for the qubit, μ for the micromachined cavity and r for the readout cavity. This Hamiltonian differs from equation 3.30 only in that we ignore the anharmonicities of the non-qubit modes.

The shape and position of the aperture transmon affect properties of the system between which trade-offs arise. For example, the size of the inner island must be large enough to create a measurable g by a significant capacitance contribution C_g. However, if the inner island is too large, the anharmonicity E_C is reduced, limiting speed of manipulation pulses. The coupling between the qubit and the micromachined cavity, $\chi_{q\mu}$, and that of the qubit and the readout cavity, χ_{qr}, are also adjusted by choice of heights of each cavity and thickness of qubit substrate. We also consider how the transmon geometry affects the surface participation ratios (see section 8.6.2).

Note that our chosen construction imposes a constraint on the cavity frequencies. As is evident in figure 8.6(a), the readout cavity is dielectrically loaded by the qubit chip. Also, the components must be sized such that the readout cavity completely surrounds the transmon chip and intersects the cavity chip. Therefore, the readout cavity must be significantly lower in frequency than the micromachined cavity. In designing multimode cQED systems in practice, it is usually preferable to order frequencies such that the qubit
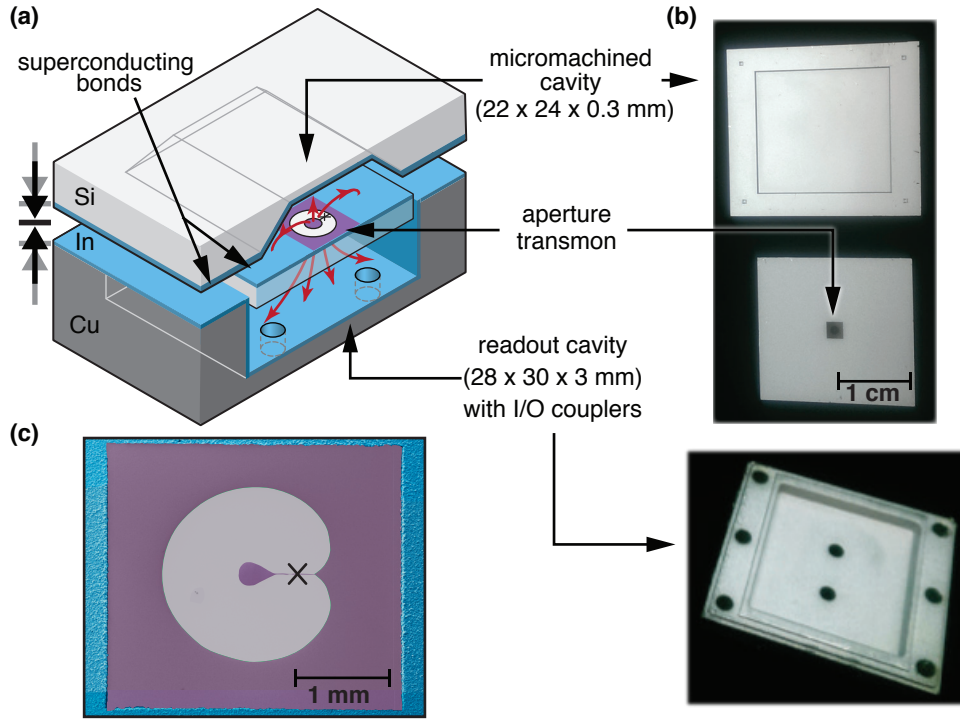
FIGURE 8.6: **Prototype MMIQC device.** **(a)** Sketch of device. For clarity, the image shows an exploded cross-sectional view that is not to scale. The annular structure has electric dipole moment components in two opposing directions, both perpendicular to the plane of fabrication. Red arrows show electric field lines of the transmon mode, and the transmon chip is shown semi-transparent. **(b)** Photograph of the micromachined cavity chip (top), transmon chip (below), and readout cavity (bottom). **(c)** False colored SEM image of the aperture transmon, with silicon in gray, aluminum in purple, and indium in blue. An 'X' indicates the Josephson Junction position, interrupting a 50 μm wide lead connecting the inner island to the remainder of the cavity wall.

is the lowest, followed by the long-lived memory cavity, followed by the readout cavity. An experimenter might prefer this to avoid complications or loss from higher modes of the over-coupled readout cavity, which we will cover in section 8.6.1. In our case, a junction inductance L_J is chosen such that the transmon frequency lies between those of the readout and micromachined cavities: $\omega_r < \omega_q < \omega_\mu$.

Finally, we impose that the qubit exist in the transmon regime to avoid coherence limitations by charge noise (illustrated by figure 3.3). We require that $E_J/E_C > 50$. Recall from section 3.3 that $E_C = e^2/2C_\Sigma = -\hbar\alpha_q$, and $E_J = \left(\frac{\Phi_0}{2\pi}\right)^2/L_J$. A range of junction inductances between 4 and 8 nH is preferable for ease and reliability of fabrication. For the

design featured in this chapter, the target anharmonicity $\alpha_q = -E_C = -204$ MHz, and the Josephson energy $E_J/h = \Phi_0^2 L_J/2\pi h = 39$ GHz place the device well into the transmon regime ($E_J/E_C = 193$).

8.3.1 Simulation and black-box quantization analysis

We perform a full 3D electromagnetic simulation of the entire system using the finite element Maxwell equation solver HFSS, followed by black-box quantization analysis. The simulation includes the Josephson junction as a linear inductance in parallel with a lumped port. First, an *eigenmode* simulation solves for the steady-state resonances of the system. Second, a *driven modal* simulation solves for the response of the system to a drive at the qubit port. From this, we extract either $Y(\omega)$ or $Z(\omega)$ in a spectrum covering the three relevant modes. The qubit geometry is parameterized and optimetrically varied to perform many separate eigenmode and driven modal simulations.

Black-box quantization (BBQ, Nigg et al., 2012) is a phenomenological methodology used to treat a Josephson junction in the presence of an environmental admittance. As we covered in section 3.4.4, the junction is decomposed into its linear inductance and a non-linear parallel inductance, and the phase of the junction is expanded to 4th order. All Hamiltonian parameters can be extracted if we have access to the the admittance spectrum $Y(\omega)$ (or impedance spectrum $Z(\omega) = 1/Y(\omega)$) of the system as seen from the junction port. In fact, all that is needed is L_J, the resonances ω_i, and the corresponding slopes $Y'(\omega_i)$. The participation ratios of all the modes in the junction phase fluctuations can be found with equation 3.32. The Hamiltonian is then numerically analyzed to produce the dressed resonances, anharmonicities α_i, and χ_{ij}'s.

8.3.2 Transmon geometry

With all of our design considerations in mind, we chose the following transmon geometry. The shape of the aperture cut from the outer conductor is a cardiod described by

$$\text{outer} \begin{cases} x &= \frac{r}{2}\left(2\cos t - \cos 2t + \frac{1}{2}\right) \\ y &= \frac{r}{2}\left(2\sin t - \sin 2t\right) \end{cases}, 0 \le t < 2\pi. \tag{8.8}$$

The inner island is a piriform curve described by

$$\text{inner island} \begin{cases} x &= b\left(\frac{1}{2} - 2\sin t\right) \\ y &= b\cos t\left(1 + \sin t\right) \end{cases}, 0 \le t < 2\pi. \tag{8.9}$$

These shapes were chosen in order to easily parameterize simulation variations. They are not necessarily the optimal shapes for maximizing coupling strengths and minimizing surface losses. Nevertheless, these shapes produce a satisfactory design with parameter choices $r = 750\ \mu$m and $b = 100\ \mu$m. This shape is seen in figure 8.6(c).

Earlier trials simply used circular apertures (with r_o) and inner islands (with r_i). The cardioid/piriform shape was preferred in later iterations because simulations predict reduced surface dielectric participations, mainly affected by the length of the leads (see section 8.6.2).

8.4 Fabrication

The device is fabricated as three separate parts that are finally bonded together. The process for the transmon chip is outlined in table A.2. It begins with a 325 μm thick (100)-orientation double-side-polished silicon wafer with resistivity $\rho > 10$ kΩcm. First, a gold pattern is defined on what will be one of the cavity walls using optical lithography and liftoff. The deposition is 10 nm of titanium followed by 100 nm of gold by e-beam evaporation. Second, the qubit is fabricated by e-beam lithography and a double-angle shadow

evaporation of an aluminum Josephson junction (section A.5), followed by liftoff. The featured device of this chapter, e.g., contained a single Josephson junction of dimension 500×500 μm, which had a room temperature resistance of 4.35 kΩ. The outer region of the aluminum qubit layer overlaps the gold to form a continuous ground plane. Third, the aluminum is masked with photoresist and the gold pattern on the wafer is electroplated with indium to a thickness of 10 μm. See details in figure 8.16 and a discussion of the possible losses due to this ground plane transition in section 8.6.3.

The fabrication process for the micromachined cavity chip was described in section 6.2 and is outlined in table A.1. The readout cavity is machined in OFHC copper and electroplated to a thickness of 30 μm by an external vendor. The surface indium thickness is greater than that of the chip components in order to ensure complete coverage of the interior corners of the cavity. The components are all flat indium surfaces, with no bump patterning as explored in chapter 7.

The three components are bonded together between parallel plates of an Instron-5969 at 120°C in two steps. The two chips are bonded together first with 1 kN, followed by the bond of the readout cavity part to the cavity chip using 5 kN. These forces equate to 5 and 25 MPa over the indium contact area of 200 mm^2. For each bond, the force is ramped from 0 to the target over 1 minute and then held at the target for 5 minutes. Immediately prior to bonding, indium oxide is etched away with a solution of 10% HCl for 5 minutes, followed by DI water, acetone and methanol washing. However, the transmon chip is not subjected to a pre-bond etch because the hydrochloric acid damages the aluminum. Once the stack is bonded, a cover piece made of OFHC copper (not pictured in figure) protects it (but does not clamp it) and allows mounting to a thermalization bracket.

Once assembled, pin-to-coax couplers are tuned to provide $Q_{\text{in}} = 430,000$ and $Q_{\text{out}} = 42,000$ to the readout cavity. The device is thermally anchored to the baseplate of a dilution refrigerator reaching a base temperature of 15 mK. A cryoperm shield protects the device from magnetic fields.

8.5 Measurements

In this section, we will show successful cQED operation in this new hardware with measurements of coherence times and interaction rates between each mode. The measurements are performed in a setup diagrammed and explained in figure 8.7 and figure 8.8. The results are summarized and compared to simulation in table 8.1. The remainder of this section walks through how each of these parameters are measured. Much of this description is fairly standard cQED device characterization, with the exception of a few specialties due to the fact that we have restricted ourselves to a single pair of input/output ports for the three-mode system.

TABLE 8.1: **Measured device parameters.** The cross-Kerr interaction with the qubit mode is denoted χ_{qi}, and anharmonicity is α_i. Simulated parameters are in italics, and all other parameters are measured except the anharmonicities of the cavities, which are calculated by $\alpha_i = \chi_{qi}^2/4\alpha_q$ (Nigg et al., 2012).

Mode	Readout cavity	Qubit	μ-Machined cavity
Frequency (MHz)	6973.4	7351.4	9377.2
[simulated]	*6945.1*	*7322.0*	*9258.0*
$\alpha_i/2\pi$ (MHz)	-0.012	-209.8	-0.002
[simulated]	*-0.004*	*-204.3*	*-0.002*
$\chi_{qi}/2\pi$ (MHz)	-3.84	-	-1.17
[simulated]	*-3.22*	*-*	*-1.25*
$\chi_{ri}/2\pi$ (MHz)	-	-	-0.020
[simulated]	*-*	*-*	*-0.004*
T_1 (μs)	1.0	6.4	34.3
T_2^R (μs)	-	9.5	-
T_2^{echo} (μs)	-	11.7	-
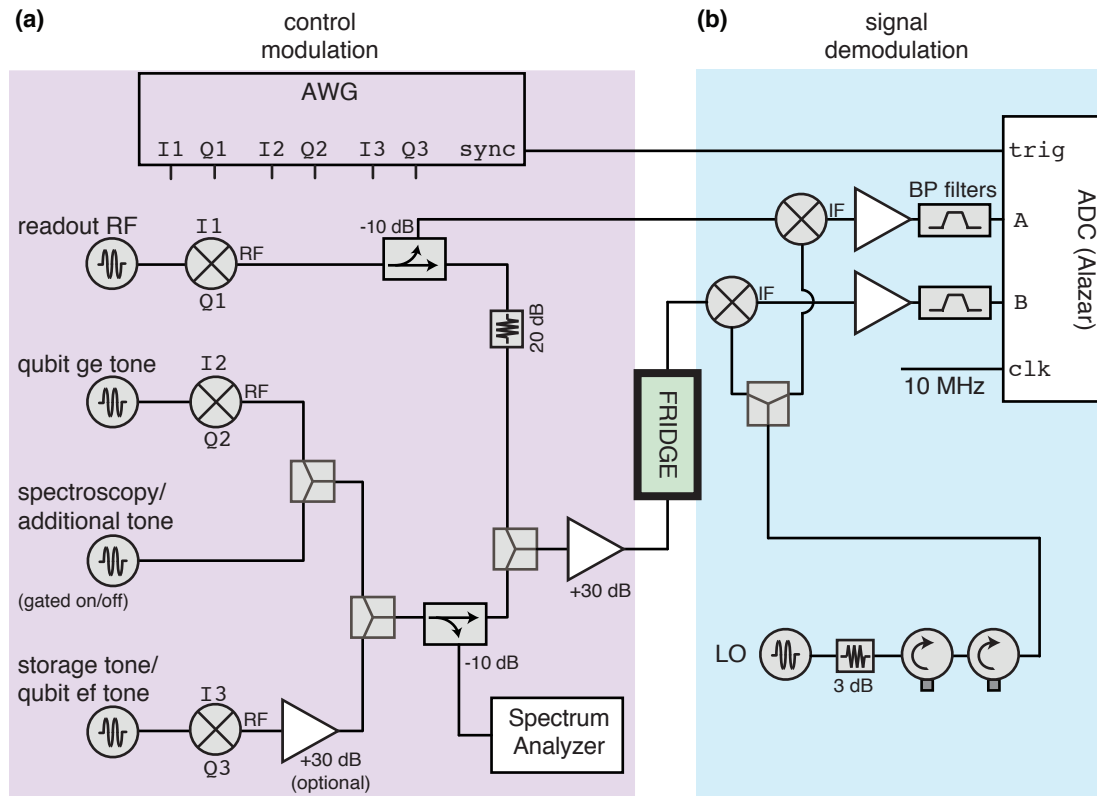
FIGURE 8.7: **Transmon measurement chain: signal modulation/demodulation.** We diagram the measurement chain used in this chapter. It consists of an interferometric heterodyne detection, in which a *signal* branch that passes through the readout cavity in transmission is compared against a *reference* branch at room temperature. **(a)** Control and readout signals are created at room temperature by IQ-modulation of RF generator tones with envelopes from channels of an arbitrary waveform generator (AWG, Tektronix 5014C). The mixers are Marki IQ0618LXP, and the drawing omits lines of AWG signal to the *I* and *Q* ports, but note that each of these also contain 10 dB attenuation to achieve better resolution from the AWG's DAC range. **(b)** The output signals of the signal branch and reference branch are separately demodulated in hardware (using Marki M8-0420MS double-balanced mixers – though image reject mixers may also be used here) to an IF of 50 MHz. The signal is then passed through a gain block (Stanford SR445A) and band-pass filtered to 41-58 GHz. Then, ADC by an AlazarTech 9870 samples the two channels each at 1 gigasample per second and functions as a 2 GB FIFO memory capable of asynchronous acquisition and data transfer to computer RAM where it is processed real-time. In software, each measurement record is demodulated by projecting the signal-(I,Q) onto the reference-(I,Q) to obtain a resulting (I,Q) for each record that is is then averaged over many experimental records to desired accuracy. Unshown: Each signal generator, the AWG, and the ADC card are all referenced to a common 10 MHz rubidium atomic clock for frequency stability, and measurement repetitions are triggered with a square wave to the AWG by a function generator that is also referenced to this clock.
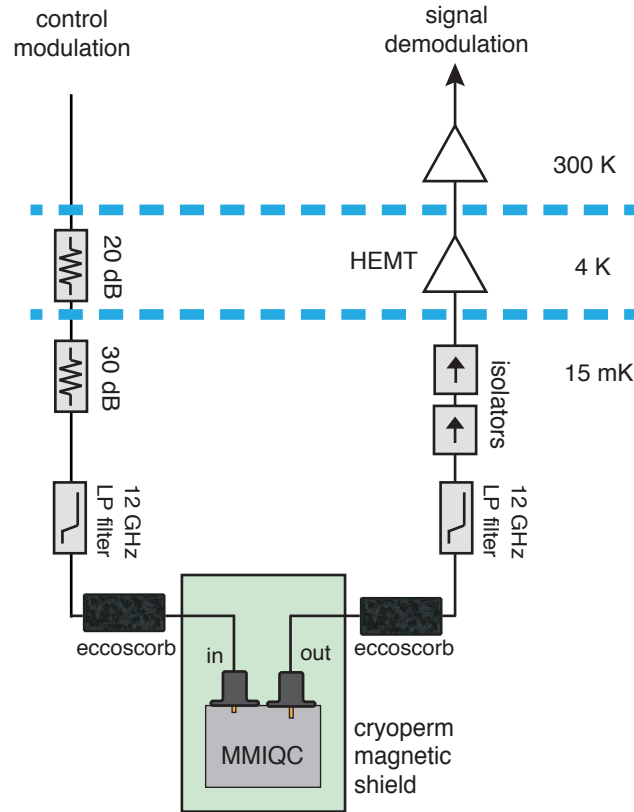
FIGURE 8.8: **Transmon measurement chain: cryogenic portion.** The signal branch of the previous figure consists of the measurement chain inside the fridge diagrammed here. It resembles that of figure 5.5, with a few additions to protect against noise that is known to effect qubit T_2 (Geerlings, 2013). Namely, it is now standard to surround the experiment on both the input and output side with "eccosorb" filters that absorb IR radiation[1], and low pass filters from K&L Microwave that reflect unwanted signal 12-26 GHz. The HEMT is from Low Noise Factory and provides ampilifcation in 7-10 GHz.

---

[1] The eccosorb filter consists of a short section of transmission line in which the dielectric is absorptive to high frequency radiation. We make them in the lab using Emerson & Cuming CR-110, which has a roughly linear attenuation versus frequency curve that becomes significant above 18 GHz and presumably continues throughout the IR spectrum. This material is typically used for anti-reflective coatings in radar applications.

8.5.1 Spectroscopy and pulse tune-up

The qubit state is detected by its dispersive effect on the readout cavity, as described in section 3.4.2. The dispersive coupling rate of the qubit to the readout cavity is $\chi_{qr}/2\pi = -3.84$ MHz, corresponding to interaction strength $g/2\pi = 38$ MHz. The qubit mode is found near the frequency expected by simulation by *pulsed two-tone spectroscopy*, in which a pulse of variable (swept) frequency is sent to the cavity followed by a readout pulse on the readout cavity resonance. Once the qubit is found in this way, the precise dispersive readout frequency and power are optimized by maximizing the contrast with and without an excitation pulse on the qubit.

Since there are no additional couplers to the micromachined cavity, dispersive readout is also the only way that the photon-state of the micromachined cavity is measured. According to simulation, the coupling of the micromachined cavity to the pin couplers is $Q_c = 2.3 \times 10^7$. [2] However, we do not observe the resonance in direct spectroscopy. Instead, two-tone spectroscopy reveals a qubit-mediated dispersive shift of the readout cavity when the micromachined cavity frequency is probed.

Once the qubit frequency is found, a *Rabi oscillations* can be performed. This ensures that the resonance found in spectroscopy is actually a two-level system, and also allows us to calibrate (or "tune up") a π-pulse, which is needed before much else can be done in the system. In a Rabi experiment, a resonant microwave tone is applied to the qubit with either a fixed duration and variable power (called a *power Rabi*) or a fixed power and variable duration (called a *time Rabi*). The resonant tone rotates the qubit around the X-axis of the Bloch sphere by an amount proportional to the time or power applied. After the pulse, the Z-projection measurement of the qubit gives a probability of the qubit being in

---

[2]This is calculated by an eigenmode HFSS simulation in which the only source of dissipation is the 50 Ω external lines, as described later in section 8.6.1. Given the total quality factor of the micromachined cavity, we might have expected to see a ~ 1 dBm deep resonance dip for this resonator in hanger configuration as described in section 5.3. However, our configuration is plainly not such that this resonator is in hanger shunting the measurement transmission line to ground. Instead, it is filtered from the transmission line by the machined readout cavity.

the excited state: $\sin^2(\tau\Omega_R/2)$, where τ is the amount of time the pulse is applied and Ω_R is the Rabi rate, which is directly proportional to the power of the pulse applied. To tune up a π-pulse, we usually choose a length of time and a pulse shape (square, Gaussian, etc.) and perform a power Rabi so that a π-rotation corresponds to a reasonable DAC value and voltage generated at room temperature. Once a π-pulse is tuned up, we know for instance that the same pulse shape at half of the amplitude will result in a $\pi/2$-pulse. The pulse shape and length can be modified, along with appropriate change in amplitude, such that the pulse occurs with greater or less spectral content (and thus selectivity to exact frequency transitions).

8.5.2 Coherence times

Measurements of the qubit coherence times are shown in figure 8.9. The qubit relaxation time is $T_1 = 6.4 \ \mu$s, which is on the order of lifetimes of other 3D transmons recently produced on similar silicon substrates with similar methods(Chu et al., 2016). [3] The qubit dephasing time T_2 is measured by monitoring the decay of *Ramsey oscillations*. We detune our pulse generator from the qubit frequency by Δ and apply two $\frac{\pi}{2}$-pulses separated by a variable delay. The detuning serves to effectively apply a Z-gate at a rate Δ. For reasonable detunings Δ, the qubit state oscillates between having been rotated back to the original state $|g\rangle$ and the excited state $|e\rangle$ as a function of the delay time. Qubit dephasing causes the amplitude of this oscillation to decay exponentially. We find $T_2^R = 9.5 \ \mu$s. Applying a *Hahn echo* adds an additional π-pulse exactly in between the two $\frac{\pi}{2}$-pulses, thus refocusing some of the dephasing. The result is $T_2^{\text{echo}} \approx 1.8 T_1$.

---

[3] The highest coherence qubit made with aluminum lift-off on silicon without suspension in Chu et al., 2016 had $T_1 = 23 \ \mu$s, and was subject to oxygen plasma ash (Glow Research AutoGlow barrel ashing chamber) after e-beam resist development (100 W, 10 sec), and after final chip dicing and resist removal (100 W, 3 minutes). The aperture transmon qubits of this chapter incorporated the brief post-development oxygen plasma ash but not the final oxygen plasma ash because indium was not allowed in the ashing chamber.

  The range of coherence times we have been producing in our lab is less than has been proven possible on silicon substrate, as previous qubits made in aluminum on silicon have reached. For example, MIT-LL is now consistently producing qubits on silicon with $T_1 \approx$60 - 70 μs (Yoder et al., 2017). We suspect, but have not yet confirmed, that the silicon wafers used in (Brecht et al., 2017; Chu et al., 2016) ((100)-orientation, resistivity $\rho > 10^4$ kΩcm from Crystec and SiliconQuest) were not of the lowest $\tan\delta$ available.
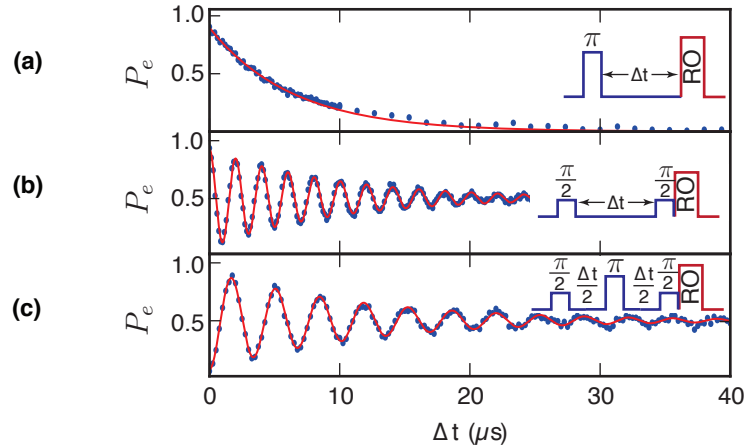
FIGURE 8.9: **Qubit coherence times. (a)** Qubit energy relaxation is fit to a single exponential (red line) with $T_1 = 6.4$ μs. P_e is the probability that the qubit is measured in the excited state. **(b)** Ramsey dephasing time $T_2^R = 9.5$ μs, measured here using 400 kHz detuning from the qubit frequency. **(c)** A Ramsey experiment with a Hahn echo sequence cancels some fluctuations in qubit frequency, and we find $T_2^{\text{echo}} = 11.7$ μs, measured here using 300 kHz detuning from the qubit frequency.
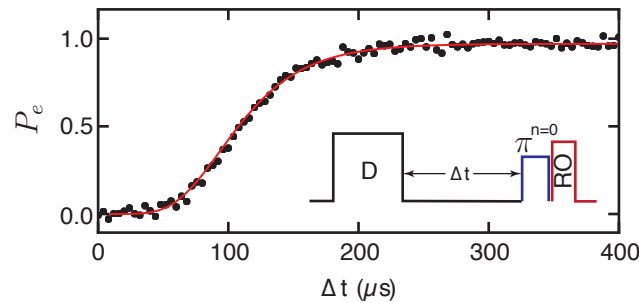
FIGURE 8.10: **Micromachined cavity lifetime.** Energy decay of the micromachined cavity is measured by applying a large displacement to this cavity, followed by a variable delay, followed by a spectrally narrow selective π-rotation of the qubit conditioned on there being no photons in the readout cavity ($n = 0$). A poissonian decay fit (red line) yields $T_1 = 34.7$ μs. At 9.4 GHz, this decay time corresponds to a quality factor of $Q = 2$ million.

The micromachined cavity has a lifetime of $34.7\,\mu s$, which corresponds to a total quality factor $Q = 2$ million at single-photon energies. We measure this by first loading the cavity with many photons by a powerful displacement pulse, waiting a variable time, then applying a π-pulse on the qubit that is spectrally narrow to select on there being 0 photons in the readout cavity. The result is described by a Poissonian decay as the cavity returns to the $n = 0$ state and the selective π-pulse begins to actually excite the qubit (see figure 8.10). The readout cavity has a lifetime of $1\,\mu s$, which is intentionally limited by over-coupling to achieve fast readout. This is observed by the linewidth of the cavity resonance, as well as the exponential "ring-down" after a cavity excitation of many photons.

8.5.3 Qubit anharmonicity and excited state population

The qubit anharmonicity, $\alpha_q = \omega_{ge} - \omega_{ef}$, is known once both of the transitions are found. Finding the ω_{ef} transition is made easy by applying a π-pulse on the ω_{ge} transition before sweeping a spectroscopy tone in the expected region. In this device, we find the ω_{ge} peak with associated $\alpha_q/2\pi = -210$ MHz. There is also a two-photon transition $\omega_{gf}/2$ that can be detected at some spectroscopy powers.

Once the second transition frequency is found, a Rabi experiment prepended by the ω_{ge} π-pulse can be used to tune up a ω_{ef} π-pulse. This two-step Rabi experiment can be repeated with an without the initial ω_{ge} π-pulse and the resulting Rabi contrasts compared to find the fraction of the population that is ambiently excited. Conducting this experiment, we find that the thermal population of the qubit excited state is $< 3\%$.

8.5.4 Demonstration of strong dispersive regime cQED

Next, we find interaction strengths sufficiently large in relation to the coherences by showcasing some standard cQED operations. These measurements are shown in figure 8.11. In spectroscopy, we observe both **(a)** resolved photon number splitting of the qubit and **(b)** a qubit-state dependent shift of the micromachined cavity. In both cases, the peaks are
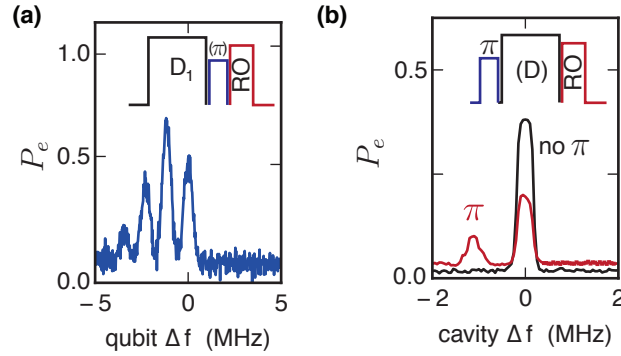
FIGURE 8.11: **Demonstration of strong dispersive cQED in the MMIQC. (a)** We observe number splitting of the qubit in spectroscopy after a calibrated displacement of the micromachined cavity, resulting in a one-photon coherent state. The spacing between the peaks indicates $\chi_{q\mu}/2\pi = 1.17$ MHz. **(b)** The micromachined cavity is dispersively displaced by $\chi_{q\mu}/2\pi = 1.17$ MHz when the qubit is in the excited state. We show the spectroscopy of a $\sigma = 1$ μs Gaussian cavity pulse followed by dispersive readout with (red) and without (black) a prepended qubit π-pulse ($\sigma = 500$ ns Gaussian). Note that over half the population decays during the cavity spectroscopy tone – a trade-off with enhanced resolution of the two peaks.

separated by the dispersive coupling rate $\chi_{q\mu}/2\pi = -1.17$ MHz. If one assumes that $g = \sqrt{\chi_{q\mu}\Delta}$ at a detuning of $(\omega_q - \omega_\mu)/2\pi = -2.03$ GHz, this corresponds to $g/2\pi = -49$ MHz.

Upon excitation of the cavity by a resonant pulse, a *coherent state* is created. A coherent state $|\beta\rangle$ has photon number probabilities given by:

$$P(n, \beta) = e^{-|\beta|^2} \frac{|\beta|^{2n}}{n!} \tag{8.10}$$

This explains the distribution of heights of the several peaks in the number-split qubit spectrum: they correspond to the qubit resonance at photon number 0 at detuning 0 and the shifted qubit resonance at photon numbers 1, 2, 3, ... found at increasing values of negative detuning.

Likewise, the micromachined cavity resonance is dispersively shifted downward by $\chi_{q\mu}/2\pi$ when the qubit is excited (figure 8.11**(b)**). We show the cavity spectroscopy around $f = 9377.2$ MHz of a Gaussian pulse with $\sigma = 1$ μs, followed by dispersive readout on the readout cavity with (red) and without (black) a prepended qubit π-pulse (Gaussian with
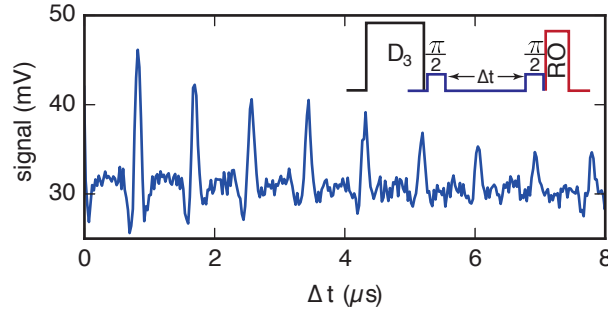
FIGURE 8.12: **Micromachined cavity memory.** In Ramsey interferometry following a displacement of the micromachined (memory) cavity, we observe revivals of the qubit state occurring at integer multiples of $2\pi/\chi_{q\mu} = 0.855 \ \mu$s. In this case, the displacement is a $n = 3$ coherent state. We repeat the previously done experiment (Vlastakis et al., 2013).

$\sigma = 500$ ns). Here, we show that the dispersive shift can be clearly resolved if a spectrally narrow cavity spectroscopy tone is used, but at the expense of $\sim 70\%$ population decay that occurs during this pulse.

As one simple demonstration of the micromachined cavity's utility as a quantum memory, we perform Ramsey interferometry following a displacement denoted D_3 that initializes the micromachined cavity to a coherent state with an average of 3 photons. See figure 8.12. We prepare the initial state $|\beta\rangle_\mu \otimes \{|g\rangle + |e\rangle\}$, which precesses according to $e^{i\chi_{q\mu}ta^\dagger a|e\rangle\langle e|}$ (Vlastakis et al., 2013). Qubit state revivals occur at time intervals $2\pi/\chi_{q\mu}$, consistent with our spectroscopic measurements of $\chi_{q\mu}$. One can imagine Bloch vector components for each photon number precessing at different rates $n\chi_{q\mu}$, with the Ramsey pulses causing them to refocus at a time interval that is independent of the size or number distribution of the initial displacement.

8.5.5 Determination of cross-Kerr

A final measurable parameter is the cross-Kerr interaction between the two cavities. The cavity cross-Kerr $\chi_{r\mu}$ is measured by relative comparison of χ_{qr} and $\chi_{r\mu}$ measured by applying a tone near the readout cavity (Leghtas et al., 2015). The procedure is illustrated by figure 8.13. A microwave pulse detuned 3 MHz above the readout cavity induces a Stark
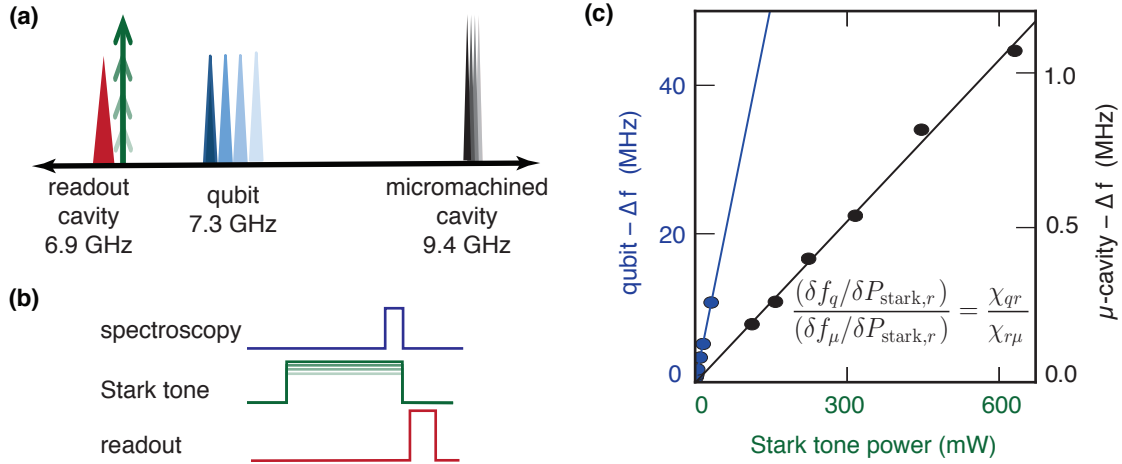
FIGURE 8.13: **Measurement of cavity-cavity cross-Kerr.** A tone detuned 3 MHz above the readout cavity induces a Stark shift that affects both the qubit and micromachined cavity frequencies. **(a)** shows a spectral diagram (not to scale), and **(b)** shows the pulse sequence, where the power of the Stark-shifting tone is varied. The ratio of the slopes $\chi_{qr}/\chi_{r\mu}$ in **(c)** is used to determine $\chi_{r\mu}$.

shift, which precedes single-side-band spectroscopy of both the qubit and micromachined cavity peaks. Both shift downward in frequency with increasing power of the Stark pulse. The slopes of this response are proportional to χ_{qr} and $\chi_{r\mu}$ respectively:

$$\frac{(\delta f_q/\delta P_{\text{stark},r})}{(\delta f_\mu/\delta P_{\text{stark},r})} = \frac{\chi_{qr}}{\chi_{r\mu}}. \tag{8.11}$$

We independently determine $\chi_{qr} = -3.84$ MHz by readout cavity spectroscopy with and without a preceding qubit π-pulse. Finally, we find cross-Kerr $\chi_{r\mu}/2\pi = -20$ kHz, compared to a simulated value of -4.4 kHz.

8.6 Discussion of loss mechanisms

8.6.1 The Purcell effect

The *Purcell effect* refers to the modification of the spontaneous emission rate of an atom (or any quantum emitter) in the presence of a resonant cavity. An atom may only emit a photon into an available state of its environment. When the environment of the atom is a

cavity resonator, the density of states available for photon emission is narrowed to the cavity resonances. This greatly enhances the strength of near-resonance QED interactions, and suppresses off-resonant ones. This effect was discovered by Edward Purcell in the 1940s (Purcell, Torrey, and Pound, 1946), who was studying the decay rate of nuclear magnetic moments.

The Purcell effect has important consequences in cQED circuits. On the one hand, qubits housed in detuned high-quality resonators experience lifetime enhancement. On the other hand, qubit lifetime may be spoiled by a lossy mode nearby in frequency. We are interested in determining if our qubit mode is being limited by a lossy cavity mode. In the dispersive regime, we can approximate that the participation of the hybridized qubit mode in the cavity mode is $(g/\Delta)^2$ (recall equation 3.29). The decay rate that the qubit inherits from the cavity is therefore $(g/\Delta)^2\kappa$. In this device, we might worry about the over-coupled readout cavity lowering qubit lifetime. According to this approximation, we have a limit $T_1^q \leq 2.8$ ms, which is quite safe thanks to the large detuning.

However, this approximation is imperfect in practice. For instance, the Purcell effect is not typically symmetric in Δ, being more pronounced when the qubit frequency is above the cavity frequency (Houck et al., 2008). The asymmetry is in part due to the contribution of higher modes of the lossy cavity. This is the reason it is typically preferable to place the readout cavity (a low-Q mode) below the qubit in frequency. The next mode of the readout cavity is at 10.72 GHz (TE102) The next highest mode is at 15.91 GHz (TE201).

We can use HFSS to predict Purcell loss rates with reasonable accuracy. The method is simple: the physical coupling ports are included (in this case, consisting of pins in undercutoff waveguides) along with lumped $50~\Omega$ resistors representing the coaxial lines. An eigenmode simulation is performed to determine the Qs of the modes. If necessary, the pin length is adjusted such that the readout cavity Q matches the measured one. The Q of the qubit mode is then the Purcell limit, as the only source of loss in the system is the damping of the readout cavity by the $50~\Omega$ ports.

We have verified that qubit and micromachined cavity lifetimes are not limited by the Purcell effect due to the over-coupled readout cavity. We simulated that the upper bounds to the qubit and micromachined cavity lifetimes due to this effect are 200 and 500 μs respectively. In design, the Purcell limit of the micromachined cavity is mitigated by minimizing the area of the annular opening created by the aperture transmon between cavities.

8.6.2 Surface Losses

Also present here are surface dielectric and conductor loss mechanisms that are broadly studied in superconducting circuits. Earlier, we placed a sufficiently high bound on the quality of indium $q_{\mathrm{cond}} > 3 \times 10^3$) that it is unimportant in this device. Instead, the lifetime of the qubit mode is likely limited by dielectric loss. We apply theory of participation ratios discussed in section 5.2.4 to the qubit mode, as in Wang et al., 2015; Chu et al., 2016. The two-step simulation method described in Wang et al., 2015 was performed on several representative design variations. In order to extract participation ratios for comparison to other designs, we assume that the surface losses occur in layers of thickness 3 nm and that the layers have a dielectric constant of $\epsilon_r = 10$.

The particular shapes of the electrodes in figure 8.6(c) are designed to reduce dielectric loss near the surfaces. The aperture transmon has smooth edges that are easily parameterized for optimization that includes consideration of surface participation ratios. For the chosen geometry, the simulated metal-substrate surface participation is 6.08×10^{-4}, substrate-air participation is 3.24×10^{-4}, and metal-air participation is 3.56×10^{-5}. These numbers are most similar to the "C" (a.k.a. "gap-mon") devices measured on silicon in Chu et al., 2016. All three types of surface participation are reduced by shortening the length of the thin leads connecting the Junction to the inner island and outer conductor. Additionally, rounding the edges eliminates areas of high field concentration that would localize around sharp corners in a circular annulus.

8.6.3 Seam Losses

We have discussed in section 5.2.5 that all quantum circuits are subject to sources of loss associated with packaging and assembly that become more severe as complexity increases. Loss occurs at seams where there is finite conductance, g_{seam}, and non-zero admittance to surface currents, y_{seam}^i, which may limit a mode i's coherence time to $T_1 = g_{\text{seam}}/y_{\text{seam}}^i \omega_i$. In a multilayer architecture, these seams are present in the bonds between layers and interfaces between different materials.

In this device, there are two types of seams that contribute to loss. The first consists of In/In bonds around the perimeter of the cavities. Using simulated surface currents, we calculate the admittance in the micromachined cavity mode to be $y_{\text{In/In}}^\mu = 16.0$ /Ωm. For the qubit mode, $y_{\text{In/In}}^q = 0.02$ /Ωm, which is smaller because the surface currents are localized away from the In/In bond. If it is assumed that the In/In bond is the only source of loss, and the conductance is $g_{\text{In/In}} \approx 10^8$ /Ωm (based on similar devices in chapter 5), it would limit the micromachined cavity to lifetime $100\ \mu$s.

The second type of seam is a Al/Au/In transition in a 3×3 mm square shape around the Al aperture transmon region. The conductance of this seam, $g_{\text{In/Au/Al}}$, was determined by an independent series of measurements using stripline resonators (similar to those of section 7.4) detailed in figure 8.14. In this experiment, we measured quality factors of stripline resonators in which the seam in question is the dominant loss mechanism. Microstrip resonators were fabricated on sapphire substrate with the same series of fabrication steps described for the transmon wafer. The resonator chips were loaded in a multiplexed version of the coaxial stripline package shown in figure 8.14(e) and measured at 15 mK. The measured internal quality factors of these resonators are plotted against seam admittance in figure 8.14(d). The blue line is the best fit of the data to $Q_i = g_{\text{seam}}/y_{\text{seam}}$ using linear least-squares regression in the log-log domain, which yields $g_{\text{seam}} = (4.2^{+0.6}_{-0.5}) \times 10^5$ /Ωm. We expect that improvement is possible using cleaning methods, the exploration of which can be the subject of future study.

An important design choice is the location and participation of the seams - including the interfaces between different layers on the transmon chip, and the two different indium bonds by which the device is integrated. Several possible paths for the seam near the transmon are drawn as white dotted lines in figure 8.15. The corresponding seam admittances for both the qubit and cavity modes are numerically calculated in table 8.2. The table also lists limits on qubit and cavity lifetimes assuming the independently measured conductance. We conclude that this seam may limit the lifetime of the qubit or the cavity if it is not placed with intention to minimize its admittance. The path used for the actual device is the 3×3 mm square.
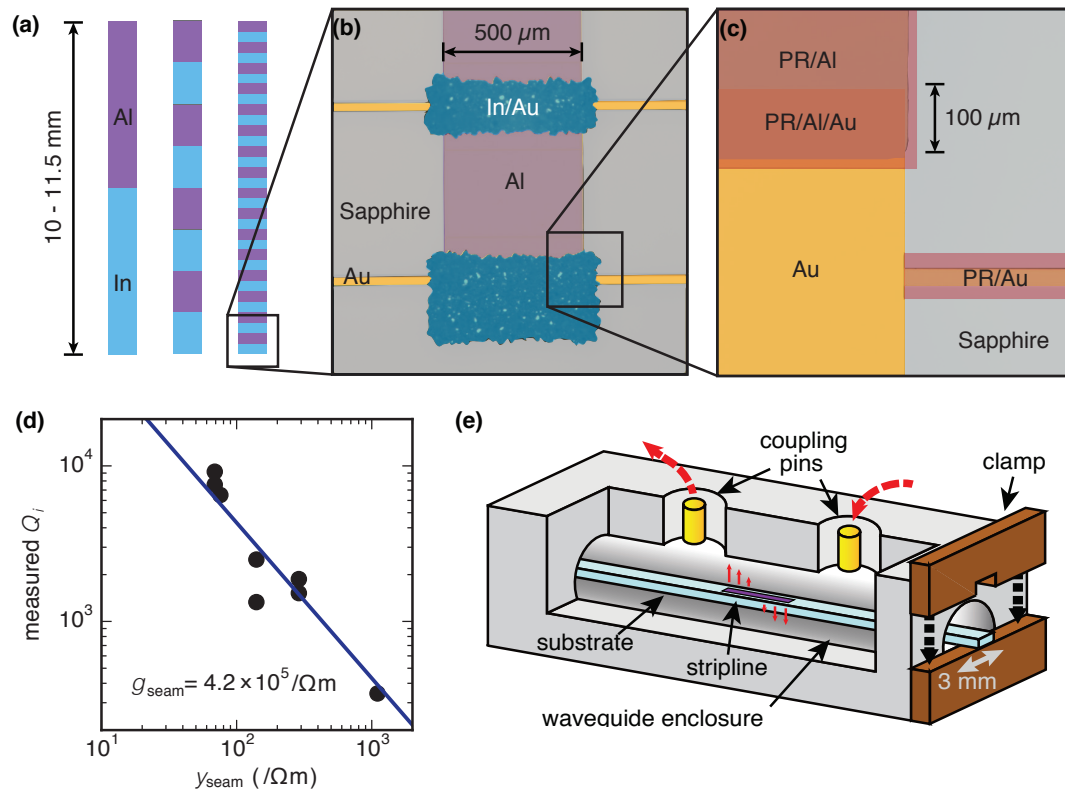
FIGURE 8.14: **Metal contact seam stripline resonators.** Stripline resonators were used to measure the conductance of the seam in question. **(a)** Each device is a rectangular strip of conductor with transitions from Al (purple) to In (blue) that resemble those of the device featured in the main text as closely as possible. Devices were made with various numbers of transitions, and varying lengths to produce fundamental half-wave modes in the 7-8 GHz range. **(b)** Optical microscope image of and end of one device. Three transition regions are visible. False coloring is applied for clarity. **(c)** Optical microscope image showing an intermediate fabrication step, which is featured in cross section in figure 8.16. False coloring is applied for clarity. **(d)** Measured internal quality factors of the several devices of varying seam admittances. The blue line is the best fit of the data to $Q_i = g_{seam}/y_{seam}$ using linear least-squares regression in the log-log domain, which yields $g_{seam} = (4.2^{+0.6}_{-0.5}) \times 10^5$ /Ωm. **(e)** Each device is inserted into a tube-like coaxial stripline package before measurement at 15 mK. (Figure used with permission from Axline et al., 2016. See Copyright Permissions.)
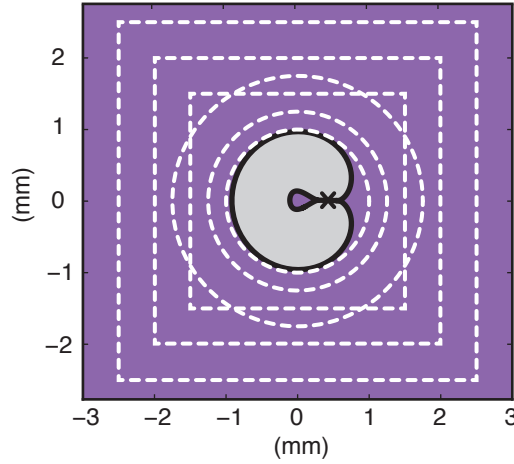
FIGURE 8.15: **Possible seam paths.** White dotted lines show seam paths that were considered for the In/Au/Al transition. The electrode geometry (black lines) is fabricated in Al (purple) on Si (grey), defined by curves following equation 8.9 and equation 8.8 with $r = 750$ μm and $b = 100$ μm. The purple area inside the white dotted line is Al evaporated in a double-angle fashion simultaneous to the Josephson-junction. The purple area outside the white dotted line is In, and extends to form one wall of the micromachined cavity. The corresponding seam admittances for both the qubit and cavity modes are numerically calculated in table 8.2.

TABLE 8.2: **Limits on qubit and storage cavity lifetimes derived from seam admittances.** The qubit mode y_{seam} values are found from HFSS simulation of the design featured here. Storage mode y_{seam} is calculated analytically by integrating surface currents of rectangular cavity's TE101 mode, and agrees with simulation. The inferred lifetime limits are $T_1^{q,\mu} < g_{\text{seam}}/y_{\text{seam}}\omega_{q,\mu}$, assuming $g_{\text{Al/Au/In}} = 4.2 \times 10^5$ /Ωm, and using $\omega_q/2\pi = 7.3$ GHz, and $\omega_\mu/2\pi = 9.25$ GHz. *The last line computes limits imposed by the indium-to-indium bond around the perimeter of the micromachined cavity using $g_{\text{In/In}} = 1 \times 10^8$ /Ωm.

seam	y_{seam}^q (/Ωm)	y_{seam}^μ (/Ωm)	max T_1^q (μs)	max T_1^μ (μs)
In/Au/Al circle, r=1.00 mm	7.955	0.0114	1.1	640
In/Au/Al circle, r=1.25 mm	1.565	0.0467	5.8	160
In/Au/Al circle, r=1.75 mm	0.382	0.161	24	57
In/Au/Al square, 3×3 mm	0.524	0.172	17	42
In/Au/Al square, 4×4 mm	0.187	0.398	49	18
In/Au/Al square, 5×5 mm	0.096	0.756	96	9.6
In/In, cavity perimeter*	0.0239	15.96	91000	108
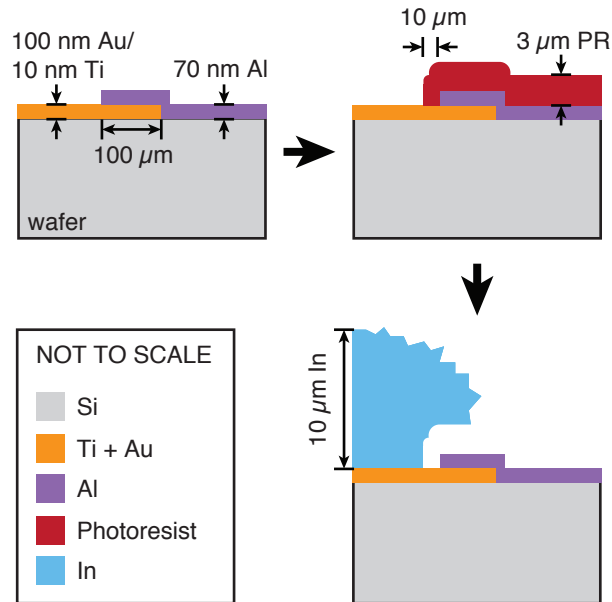
FIGURE 8.16: **Conceptual drawings of the Al/Au/In seam region.** The region is shown in cross-section during two intermediate fabrication steps (top) and the final product (bottom). The drawing portrays the rugged surface of the indium (blue). Note that the In overlaps the Al such that Au is not seen when imaged from above, as in figure 8.6**(c)**. Nevertheless, current transiting this seam must pass from superconducting In through 100 μm normal Au to superconducting Al.

Now we take a closer look at the seam in question. Figure 8.16 shows the seam region in cross-section. Current transiting this seam must pass from superconducting In through 10 μm normal Au to superconducting Al. Any superconductor proximity effect is complicated by the possibility of intermetallics on both interfaces, which we discuss next.

8.6.4 Conductance discussion

The presence of Au is certainly non-ideal. It exists in this process to serve as the conducting layer onto which In is electroplated. Most other conductors are not suitable for In electroplating because of either oxides or incompatible electronegativity. Cu is another appropriate metal for In electroplating. However, we find that DC contact resistance and surface adhesion for Cu/Al is lower than that of Au/Al (at least without experimenting

with cleaning procedures before Al deposition). Therefore, Au is used as the electroplating seed layer.

It is worth noting that Au is known to interact with the nearby metals in worrisome ways. In particular, Au will form intermetallic compounds with both Al and In. Au_xAl_y intermetallics are known problems in microelectronics and wire-bonding. Two such legendary intermetallics are "white plague" (Au_5Al_2), which has low conductivity, and "purple plague" ($AuAl_2$), which leads to voids at the interface. Our process avoids the high temperatures ($> 624°C$) that produce these compounds, but it is possible that diffusion takes place to form $AuAl_2$ (occurring at $> 400°C$, possibly occurring slowly at lower temperatures), which is also a poor conductor.

Au also diffuses into In, forming the intermetallic $AuIn_2$. This compound was used in some Josephson circuits as a thin film resistor (Lahiri, 1977). This intermetallic is a known problem in indium bump manufacturing methods that involve reflow of the indium (Huang et al., 2010), and diffusion rates of have been measured (Huang et al., 2010; Zhang and Ruythooren, 2008). Our process does not involve molten In. There is concern, that any contaminants in the In, Au or other, can reduce its ductility, which has negative consequences for the conductance of In bonds between layers.

Though evidence of these intermetallics has not been discovered in our samples, they are considered cause for concern. Therefore, fabrication procedures that eliminate the Au layer altogether are being explored for future use. In particular, we plan to deposit In via thermal evaporation instead of electroplating, which eliminates the need for a conducting seed layer. Alternatively, a thin Ti layer between Au and In is an effective diffusion barrier at low temperature (Zhang and Ruythooren, 2008).

8.7 Outlook

Here we will mention two simple extensions to the device featured in this chapter. The first is a way to increase $\chi_{q\mu}$ by a modified electrode geometry and an additional step in

fabrication. The second extension considers replacing the machined readout cavity with a planar readout circuit on the layer above the aperture transmon. This was not attempted as it requires small TSVs.

8.7.1 Increased coupling by etching

We have mentioned that the coupling rates between the qubit and both cavities are affected by the thickness of qubit substrate. In particular, thinner substrate leads to greater coupling between the qubit and micromachined cavity. However, a thinner qubit chip is not advisable with our current bonding method because of fragility concerns. Instead, removing bulk silicon in the vicinity of the aperture transmon was investigated. Beginning with the 325 μm silicon wafer, we remove bulk silicon by nitride-masked KOH etch to create 5×5 mm square pits that are 225 μm deep. We are left with 100 μm thick silicon "windows" on which the aperture transmon can be fabricated opposite the pits.

With much of the bulk dielectric behind the aperture transmon removed, a different electrode geometry is required to achieve a similar qubit frequency and capacitance ratio β without compromising E_J/E_C or requiring an impractically high L_J. For instance, we considered an annular aperture transmon (concentric circles) with $r_i = 125$ μm and $r_o = 800$ μm, which is very close in size to the altered shape of this chapter's featured device. Simulated with the full 325 μm silicon wafer, its parameters (frequencies and χ's are also very similar to those of our featured device. Simulated with the 100 μm "window," however, maintaining the same qubit frequency ($f_q \approx 7.3$ GHz) requires an L_J of 7.75 nH, which is feasible but on the high end of the preferred range, and $\chi_{q\mu} = 2$ MHz. Now consider a larger annulus: $r_i = 150$ μm and $r_o = 1400$ μm. In this case, L_J's between 4.5 and 6.7 nH result in qubit frequencies between 8.3 and 7.2 (respectively) and $\chi_{q\mu}$'s between 20 and 4.6 MHz (respectively). The g's range from 140 to 100 (respectively).

Such devices were fabricated but we did not successfully measure a qubit. We were

able to create the "windows" and carry out all of the successive steps: creating the gold pattern, fabricating the aperture transmon, and electroplating indium, and dicing the wafer. The device was bonded and packaged, but upon cooldown there was no discernible qubit. Only one device was attempted.

Another straightforward way to increase the coupling rate would be to reduce the height of the cavity. In that case, the optimum shape would be smaller.

8.7.2 Planar readout resonator

In future designs, it is possible that the aperture qubit can be addressed using a microstrip on the side of the wafer opposite to the micromachined cavity wall and qubit fabrication, eliminating the machined readout cavity. A portion of this scheme is depicted as a sketch in figure 8.17. What follows is a simple estimation of the range of coupling factors that we would expect between the readout microstrip resonator and an aperture qubit positioned below. We will calculate the maximum possible coupling rate g, which is found with the aperture qubit of dipole moment $\vec{p}$ positioned under an end of the resonator, where the electric field is $\vec{E_q}$. The coupling rate is

$$\hbar g = \vec{E_q} \bullet \vec{p}, \tag{8.12}$$

and our geometrical assumptions constrain the two vectors to be parallel (vertical direction in the figure).

First, we estimate the dipole moment of the first excitation of the aperture qubit. We will use the dipole approximation of a thin annulus given by equation 8.2. Assuming that the voltage difference is that of one photon, $\frac{1}{2}\hbar\omega = \frac{1}{2}CV_0^2$, where C is the capacitance between the center electrode and the outer sheet, which for our devices is around 1 pF. Therefore, $V_0 \approx 2$ μV. Assuming radius $r = 300$ μm, and $\epsilon = 10\epsilon_0$ for silicon, we have $p = 5 - 10 \times 10^{-22}$ msA (or 0.5 electron mm).
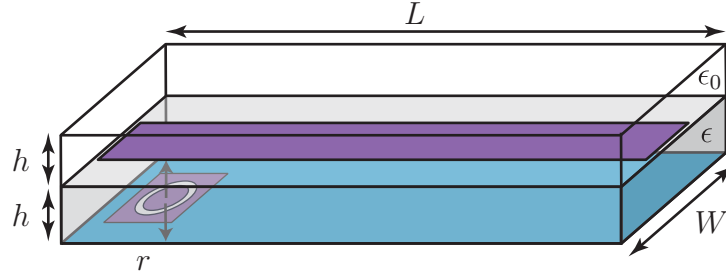
FIGURE 8.17: **Simplified sketch of a microstrip $\lambda/2$ resonator coupling to an aperture qubit.** Purple is aluminum, blue is indium forming a portion of the top wall of a micromachined cavity like the one in this chapter. The semi-transparent grey bottom layer indicates silicon ($\epsilon = 10\epsilon_0$) , while the clear upper layer indicates vacuum in a tunnel. Note that this description supposes boundary conditions that can be instituted in the actual device: the microstrip is surrounded by a conducting housing (slightly larger that the clear $h \times L \times W$ box) as well as thru-wafer vias in the silicon (forming a perimeter slightly larger than the semi-transparent grey $h \times L \times W$ box). The transition to the another transmission line and the following transition off-chip to external coaxial cables is not shown.

Next, we calculate the electric field of the microstrip resonator at the location of the qubit. It is tractable to seek an electrostatic solution by making assumptions about boundary conditions reflecting the geometry in figure 8.17. We will write a rough approximation of the field integration that reflects the sinusoidal character of the voltage ($V \propto \sqrt{E}$) and fixes the total energy to that of one photon:

$$
\begin{aligned}
\frac{1}{2}\hbar\omega &= \int_V \epsilon |E|^2 dV \\
&= (1 + \epsilon_r)\epsilon_0 E_0^2 hW \int_0^L \sin^2 \frac{\pi l}{L} dl \\
&= (1 + \epsilon_r)\epsilon_0 E_0^2 hWL/2,
\end{aligned}
\tag{8.13}
$$

where h, W, and L are the confining dimensions shown in the figure. Assuming a relative dielectric constant of $\epsilon_r = 10$ for silicon, the electric field at the qubit location is

$$
E_q = 10E_0 = \sqrt{\frac{10\hbar\omega}{11\epsilon_0 hWL}}.
\tag{8.14}
$$

Making some reasonable assumptions for geometery ($h \approx 300 \ \mu$m, $W \approx 1$ mm, $L \approx 10$ mm) and using $\omega = 2\pi 7$ GHz, we find $E_q \approx 10 \ $ mV/m.

Putting these last two calculations together with equation 8.12, we find a coupling rate of $g \approx 5$ GHz between the qubit and microstrip. This is sufficiently large, and can be reduced by increasing the height or width (to the effect of $g \propto (hW)^{-1/2}$), or positioning the qubit elsewhere under the microstrip resonator (sinusoidal dependence on position).

8.7.3 Conclusion

The experimental results described in this chapter provide a proof-of-concept for one way to implement a cQED system with a transmon qubit in a superconducting micromachined cavity. We can imagine such a system playing a role in larger MMIQCs. We make a disclaimer that the approach concentrated on for this thesis is certainly not the only one possible for integration of transmons in MMIQCs. For instance, figure 4.3(c) shows qubits in a micromachined transmission line bus. This is essentially a modified coaxial cable, so the coupling strength of would be highly tunable and obey equation 3.47 from the general calculations of section 3.5.1.

Chapter 9

Conclusion

9.1 Future Work

As a result of the exploratory work in this thesis and a confidence that indium bonding will enable more scalable and flexible superconducting circuits, our lab is committing new resources to the development of future MMIQCs. In particular, we have recently installed a dedicated deposition system for thermal evaporation of indium, and at the time of this writing we are about to receive a device-bonder.

Thermal evaporation of indium eliminates many of the difficulties associated with indium electroplating. First, there is no need for a normal metal seed layer, and we anticipate that the contact resistance and microwave seam admittance between aluminum and indium evaporated on top will be an improvement over that measured in electroplated devices. Second, both the surface roughness and the height uniformity across a wafer with any patterning is dramatically improved. Patterns in the indium layer are created by photoresist liftoff or by hard-shadow-masking. Third, we suspect that the evaporated indium is more pure, as it is not at risk of contamination by intermetallic compounds made with a layer of Au, nor organic grain refiners present in the electrplating bath.

The device-bonder is an FC-150 from SET-NA. With its advanced laser-leveling and auto-collimation optics, it will fix two mating surfaces parallel to 20 μradian with active-feedback motorized pitch and roll, and should achieve lateral alignment to ± 1 μm (3σ,

post-bond). It will also provide compression force, height, and temperature control and process monitoring. This should allow the creation of multilayer devices with more reproducible results than previous "improvised" bonding methods.

Another capability which we have mentioned will play a key role in MMIQCs is a process to create and metallize thru-silicon-vias (TSVs). While we are not equipped to apply conformal metalization in high-aspect-ratio vias, for instance by ALD, we can create larger TSVs that apply to certain designs. These can be made by wet or dry etching through an entire wafer thickness, creating angled sidewalls that can be metalized by sputtering or evaporation with a metal of our choosing. These are being incorporated to provide shielding and confinement of propagating modes in micromachined transmission line designs.

The team is actively working on fabricating micromachined cavity and stripline resonator devices that will vet the new tools and provide confidence for larger designs with multiple elements.

9.2 Conclusion

It is an exciting era for superconducting circuits and quantum information processing. At this time, all of the major players in the field of cQED are beginning to strategize about various multilayer constructions, all of which can be categorized as MMIQCs as broadly described in chapter 4. Until now, this has not been strictly necessary as several other challenges relating to coherence and electronic control schemes required attention before the community could work past devices with more than a few quits. It is now time to develop MMIQCs, and it will not be surprising if this activity produces many publications and also breaks into the realm of industrial development in the coming years. At present, labs are beginning to produce circuits using micormachining, superconducting vias, indium bumps and flip chip bonding, motivated for the most part by the need to route the necessary control wiring to internal elements of a 2-dimensional array (or other non-linear

topology of qubits), and to not spoil coherence while doing so. We have approached the transition to multilayer devices with a unique edge.

Starting with the observation that all modes are three-dimensional and all planar circuitry has out-of-plane fields, we emphasize the need for isolation of separate modes as well as the need for inter- and intra-layer coupling routes. Such isolation can be achieved in a multilayer structure embedded with micromachined volumes coated in superconductor that surround regions where planar circuitry resides. Second, we reason that incorporation of high-Q cavity resonators is a natural choice in such a layered structure. Due to their minimal dielectric and conductor participation they can be very high coherence quantum elements.

There were two main challenges that we addressed in this thesis: how to create high quality inter-wafer superconducting bonds, and how to couple a qubit to a cavity in a new configuration. We found that indium is a suitable superconductor for this purpose, and discussed its mechanical and superconducting properties. In the last chapter, we designed and experimentally demonstrated a MMIQC device in the strong-dispersive regime of cQED. There is a myriad of future work that can extend from these findings and be drawn from the vast body of existing engineering work in related fields. These techniques will enable realization of increasingly complex MMIQCs in pursuit of a scalable quantum computer.

Appendix A

Fabrication details

A.1 Recipes

TABLE A.1: **Fabrication steps for micromachined cavities.** See figure 6.2.

substrate: silicon wafer, (100), 100 mm, 0.525 - 1 mm thick is best

Task	Details
1.Clean wafer	a. Acetone, sonicate 2 min b. Methanol, sonicate 2 min c. O_2 plasma clean (Ash) top plate, 300 mT, 175 W, 5 min
2. Deposit nitride	GSI, my recipe, 4 min, 150 nm
3. Create PR mask	a. S1813, spun at 3000 rpm, acl 17, 60 sec b. Bake 115°C, 1 min c. Align with EVG, expose 50 mJ/cm^2 @ 365 nm d. Develop in MF319, 60 sec. DI water rinse e. Post-bake, 115°C, 2 min f. O_2 plasma clean (Ash) bottom plate, 300 mT, 175 W, 3 min
4. Etch nitride	Oxford 80. First O_2 plasma clean of empty chamber, 6 min. 50 sccm CHF_3, 7 sccm O_2, P=5mT, RF 175W, ICP 0W, 3 min
5. Remove PR mask	a. NMP 90°C b. Acetone, sonicate 2 min c. Methanol, sonicate 2 min d. O_2 plasma clean (Ash) top plate, 300 mT, 175 W, 3 min
6. Silicon wet etch	a. 30 sec BOE 10:1 to remove oxide b. KOH at 88°C, spinner 200 rpm. (rate 98 um/hr) c. Stop with DI water after 300 μm depth
7. Remove nitride	BOE 5:1, 30 min (etch rate to nitride is 15 nm/min; this step also removes K salts)
8. Deposit gold	Denton or PETE. 6 nm Ti, 100 nm Au
9. Electroplate indium	a. O_2 plasma clean (ash) top plate, 300 mT, 175 W, 3 min b. HCl 10%, 10 sec. DI rinse. c. Electroplate, 300 mA DC, room temp. (rate is 10 μm/hr when 100% wafer area exposed)

TABLE A.2: **Fabrication steps for aperture transmons embedded in indium groundplane.** This applies to any device in which aluminum Josephson junctions are created, followed by electroplating of indium.

substrate: silicon wafer, (100), 100 mm, 325 um thick, resistivity >7-10 kΩ*cm

Task	Details
1. Clean wafer	a. Acetone, sonicate 2 min b. Methanol, sonicate 2 min
2. create PR mask	a. First prime surface for adhesion: O_2 plasma (ash) top plate, 300 mT, 175 W, 5 min; vapor HMDS b. Spin LOR10A, 4000 rpm, acl 17, 60 sec c. Bake 165°C, 5 min d. Spin S1813, 4000 rpm, acl 17, 60 sec e. Bake 115°C, 1 min f. Align mask and expose 80 mJ/cm^2 @ 405 nm g. Develop MF319, 90 sec h. O_2 plasma clean (ash) bottom plate, 300 mT, 175 W, 3 min
3. Deposit gold	Denton or PETE. 6 nm Ti, 100 nm Au
4. Liftoff gold pattern	a. NMP 90°C for $\sim$ 3 hours or overnight b. Finish with acetone, methanol, N2 dry c. O_2 plasma clean (ash) bottom plate, 300 mT, 175 W, 3 min
5. Ebeam pattern	a. Spin EL13, 5000 rpm, acl 17, 90 sec (500 nm) b. Bake 175°C, 1 min c. Spin PMMA A3, 4000 rpm, acl 17, 90 sec (70 nm) d. Bake 175°C, 20 min e. EBPG write JJ pattern. Dolan bridge. f. Develop. 1:3 MIBK:IPA @ 25°C, 55 sec. IPA rinse 10 sec. N_2 dry.
6. Deposit aluminum (junctions)	a. Preceed load to new plassys with 0_2 clean in asher: bottom plate, 300 mT, 100 W, 10 sec b. Al1: 22.8 nm, -29° c. Oxidation, 15 T, 12 min d. Al2: 68.6 nm, 29° e. Oxidation, 3 T, 10 min
7. Liftoff aluminum	a. NMP 90°C overnight b. Finish with acetone, methanol, N_2 dry
8. Create PR plating mask	a. Spin SC1827, 2000 rpm, acl 17 b. Bake 115°C, 4 min c. Align mask and expose 230 mJ/cm^2 @ 365 nm d. Develop MF319, 60 sec e. Postbake 115°C, 5 min
9. Electroplate indium	a. O_2 plasma clean (ash) top plate, 300 mT, 175 W, 3 min b. HCl 10%, 10 sec. DI rinse. c. Electroplate, 300 mA DC, room temp. (rate is 10 μm/hr when $\sim$100% wafer area exposed)
10. Dice chips	a. Spin SC1827, 2000 rpm, 90 sec b. Bake 115°C, 2 min c. Dice d. Remove resist with NMP, Acetone, Methanol

TABLE A.3: **Fabrication steps for indium patterns.** For creating patterned indium, such as striplines or DC resistance test devices on sapphire or silicon wafers, using electroplating of indium. See figure A.1. Note that this recipe shows copper, rather than gold. Copper is easier to electroplate with quality when there is a pattern in the conducting layer. This is because it fosters better current distribution and has easy-to-clean surface for plating. However, the copper/Al interface is very bad (without any attempt at special cleaning, which could be learned from QP trap devices). That is why I have been using gold for the patchmon devices and copper for striplines. Neither copper nor gold are needed if the indium is evaporated.

substrate: Sapphire, 100 mm, 530 um thick

Task	Details
1. Clean wafer	a. Acetone, sonicate 2 min
	b. Methanol, sonicate 2 min
2. Create PR mask	a. First prime surface for adhesion: O_2 plasma (ash) top plate, 300 mT, 175 W, 5 min; vapor HMDS
	b. Spin LOR10A, 4000 rpm, acl 17, 60 sec
	c. Bake 165°C, 5 min
	d. Spin S1813, 4000 rpm, acl 17, 60 sec
	e. Bake 115°C, 1 min
	f. Align mask and expose 80 mJ/cm^2 @ 405 nm
	g. Develop MF319, 90 sec
	h. O_2 plasma clean (ash) bottom plate, 300 mT, 175 W, 3 min
3. Deposit copper	Old plassys. 6 nm Ti, 100-200 nm Cu
4. Liftoff copper pattern	a. NMP 90°C for ~3 hours or overnight
	b. Finish with acetone, methanol, N_2 dry
8. Create PR plating mask	a. Spin AZ9260, 800 rpm, acl 17, 90 sec (16 um)
	b. Bake 115°C, 3 min. remove edge bead.
	c. Align mask and expose 1000 mJ/cm^2 @ avg of 365 & 405nm
	d. Develop AZ400K 1:4, 8 min
9. Electroplate indium	a. O_2 plasma clean (ash) top plate, 300 mT, 175 W, 3 min
	b. HCl 10%, 10 sec. DI rinse.
	c. Electroplate, 300 mA DC, room temp.
	(rate is 10 $|mu m$/hr when ~100% wafer area exposed)
10. Dice chips	a. Spin SC1827, 2000 rpm, 90 sec
	b. Bake 115°C, 2 min
	c. Dice
	d. Remove resist with NMP, Acetone, Methanol

FIGURE A.1: **Fabrication steps for electroplated indium patterns on wafers.** Corresponds with the steps in table A.3.

A.2   Electroplating Indium

Electroplating (or electrodeposition) is the application of metallic coatings to conductive surfaces by electrochemical processes. A general electroplating circuit consists of the following elements, which can be found in figure A.2, which is a cross-section of our system for electroplating indium on wafer substrates. An electroplating circuit, or cell, contains:

1. An external circuit that provides a source of current, which may be DC or amplitude modulated, and may contain monitoring instruments (ammeters, voltmeters) to regulate voltage and current values applied to the cell.

2. The plating solution itself, which is an acidic liquid "bath"

3. Negative electrodes (cathodes), or the work-piece, which is the material to be plated

4. Positive electrodes (anodes), either made of the metal to be plated (soluble anodes) or a different conducting material which serves merely to complete the circuit (inert or insoluble anodes)

The positive and negative anodes may be either singular or multiple, and they are placed in the bath, completing an electroplating circuit. As the external power source drives current, positive ions of metal are driven in the bath opposite to the flow of electrons. They collect on the cathodes and form a solid deposit. If a soluble anode is used, metal ions dissolve from it to replenish those in the bath.
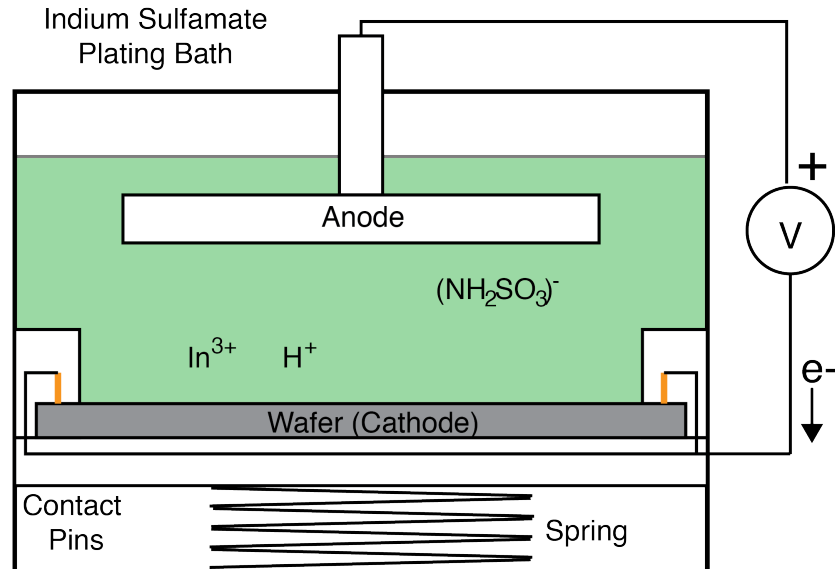
FIGURE A.2: **Indium sulfamate wafer electroplating circuit.** This is a cross-section of the wafer electroplating circuit, which was purchased from Wafer Power Technology. The green area represents the indium sulfamate ($In(NH_2SO_3)_3$) plating bath, which has pH=2. Electrical connection to the wafer (cathode work piece) is made by 24 gold-plated-copper pins spaced around the wafer perimeter. These contact pins are flexible and embedded in a rubber gasket into which the wafer is pressed with a spring. This creates a watertight seal such that the wafer forms the bottom of the bath container. In^{3+} from the solution electrodeposit to form a solid on the areas of the wafer that are both conducting and connected to the circuit. Indium deposit can be masked with common photoresists (figure A.1)

Total amount of material deposited is governed by Faraday's laws of electrolysis. They are basic to both the understanding and the practical use of electrolytic processes. They

may be stated as follows (Ehl and Ihde, 1954):

1. The amount of chemical change produced by an electrical current is proportional to the quantity of electricity that passes.

2. The amounts of different substances liberated by a given quantity of electricity are inversely proportional to their chemical equivalent weights.

Equivalent weight is the molar mass divided by the number of electrons in the balanced redox half-equation. Mathematically, Faraday's laws of electrolysis can be expressed as:

$$Q \propto zm \tag{A.1}$$

$$Q = It = zFn \tag{A.2}$$

where Q is the charged passed, I is the current, t is the time, z is the change in oxidation state, m and M are the mass and molar mass of oxidized or reduced species, $F = 96,485$ C/mol is the Faraday constant, the charge of one mole of electrons, and n is the amount of substance oxidized or reduced.

A.2.1 Electroplating indium on wafers

For this process, an indium sulfamate ($In(NH_2SO_3)_3$) plating bath solution purchased from Indium Corporation is operated at room temperature. In a wafer plating system purchased from Wafer Power Technology[1], a rotating Pt-Ti mesh serves as the insoluble anode and the wafer or PCB work piece serves as the cathode onto which indium precipitates from the bath. A DC current of 300 mA will deposit indium at at rate of 150 nm/min to a final thickness of 10 μm on the full area of the 4 inch diameter substrate. The deposited material is known to be $> 99.9\%$ pure indium.

---

[1]http://waferpower.com

The system here uses an insoluble platinized titanium insoluble mesh anode. This type of insoluble anode utilizes platinum's exceptional conductive properties and corrosion resistance yet still remain economical. It is created by electroplating a very thin layer (typically 2-5 μm) of platinum onto a specially treated activated titanium. This was recommended to us by our contact at Wafer Power (), and it is often used in electroplating of nickel. We are told that the risk with doing this is decreased height uniformity due to changed anode shape and increased surface roughness in the deposit. However, all electroplaters in table A.4 use indium anodes.

Use of an insoluble anode means that indium is depleted from the bath with continued use. We can compute this depletion rate simply by tracking the amount of material deposited. It is possible to add indium wire wound into the anode mesh to replenish indium ions in the bath.

One concern for several of the patterns electroplated in this work is how current distribution affects the uniformity of the electrodeposition. Except for the simplest geometries of a cell, such as when the anode and cathode are concentric, the current is not uniform over the surface of an electrode. In fact, the current distribution on the workpiece electrode surface is complicated. Current will tend to concentrate at edges and points, and unless the resistance of the solution is extremely low, it will flow more readily to parts near the opposite electrode than to more distant parts. Thus, except for the simplest parts subject to electroplating, the thickness of deposit, which depends on the current density, will not be uniform over the surface. Techniques to mitigate this effect include use of specially shaped or moving anodes, and auxiliary anode and cathode structures.

The operating conditions affect the physical properties of the deposited film. It is likely that the response to operating conditions of indium plated using an indium sulfamate ($\text{In}(\text{NH}_2\text{SO}_3)_3$) bath is similar to the responses of nickel plated using a nickle sulfamate ($\text{Ni}(\text{NH}_2\text{SO}_3)_2$) bath. Compared to indium plating, nickel plating with a sulfamate bath is a very commonly conducted industrial process. Conditions which decrease the ductility of

electrodeposited nickel (and correspondingly increase the hardness and tensile strength) are an increase in pH, a decrease in temperature, and an increase in chloride percentage (DisChem, Inc., 2013). For industrial purposes, these operating conditions are carefully controlled to obtain desired properties of the final film.

A.3 Indium Bump Literature Review

TABLE A.4: **Indium bump literature review.** While this is not a comprehensive review of work on the subject, I found these papers to be informative descriptions of indium bump fabrication. EP = electroplating, and UBM = under-bump metallurgy.

source	bump dimensions	indium deposition	mask	UBM (nm)
J. Jiang et al. (2004). "Fabrication of indium bumps for hybrid infrared focal plane array applications". *Infrared physics & technology* **45**.2, 143–151	10 μm diameter post-reflow, 25 μm pitch	thermal evaporation	LOR + AZ P4620 (10 μm, 5 μm undercut)	Ti/Pt/Au
		EP	AZ P4260 (10 μm)	Ti/Pt/Au
C. Broennimann et al. (2006). "Development of an Indium bump bond process for silicon pixel detectors at PSI". *Nuclear Inst. and Meth. in Phys. A* **565**.1, 303–308	50×50 μm, 20 μm diameter post-reflow, 100 μm pitch	sputtering (2-3 μm)	LOR	Ti/Ni/Au (10/50/50)
Y. Tian et al. (2008). "Electrodeposition of indium for bump bonding". In: 58th Electronic Components and Technology Conf. 2096–2100	15-50 μm, pitch 15-100 μm	EP (10 μm)	AZ9260 (20 μm)	Ti/Cu (100/100)
Y. Tian et al. (2014). "Electrodeposition of Indium Bumps for Ultrafine Pitch Interconnection". *J. Electronic Materials* **43**.2, 594–603. ISSN: 1543-186X	25 μm diameter circles, pitch 50 μm.	EP (18 μm)	AZ9260 (20 μm)	Ti/Cu (100/100)
J. J. Coleman et al. (2010). "Optimizing galvanic pulse plating parameters to improve indium bump to bump bonding". *Proc. SPIE* **7590**, 75900F–75900F–11	0.6 - 5 μm diameter	EP, thermal evaporation	AZ51214 (5 μm)	Ti/Cu (20/50)
Q. Huang et al. (2010). "Development of indium bumping technology through AZ9260 resist electroplating". *J. Micromech. Microeng.* **20**, 055035	70×70 μm, 40 μm diameter post-reflow, 100 μm pitch	EP (1μm)	AZ9260 (30 μm)	Ti/Pt/Au (30/20/100)
M. J. Li et al. (2007). "Microshutter array system for James Webb Space Telescope". *Proc. SPIE* **6687**, 668709–668709–13	10×10 μm, 10 μm height, 20 μm pitch	thermal evaporation (10 μm)	Futurexx NR9-8000 (-)	MoN/Cr
M. Volpert et al. (2010). "Indium deposition processes for ultra fine pitch 3D interconnections". In: 60th Electronic Components and Technology Conference (ECTC), 1739–1745	10 μm post-reflow diameter, 15 μm pitch	EP and thermal evaporation	(20 μm)	Ti/Ni/Au

TABLE A.5: **Indium bump literature review – part 2.** Several groups in the cQED community are also beginning to explore indium bump bonding. Here is what we know from presentations at the APS March Meeting, 2017.

source	bump dimensions	indium deposition	mask	UBM (nm)
D. Rosenberg et al. (2017). "3D Integration for Superconducting Qubits". In: APS March Meeting 2017, H46.00001 (MIT Lincoln Laboratory)	15×15 μm, 8 μm high	thermal evaporation	?	Al/Ti/Pt/Au
J. Mutus et al. (2017). "3D Integration of superconducting qubits with bump bonds: Part 1". In: APS March Meeting 2017, H46.00006 (Google, Santa Barbara)	2-8 μm high	thermal evaporation	?	Al/TiN
C. H. McRae et al. (2017). "Thermocompression Bonding Technology for Multilayer Superconducting Quantum Circuits". *arXiv:1705.02435[physics.app-ph]* (IQC, Waterloo)	bulk	sputter	Transene A aluminum etchant	Al/In (150/150)

A.4 Bonding

For many of the devices measured in this work, an Instron 5969 compressive force testing machine is used to bond mating halves with indium contact areas of $50 - 500$ mm^2 at forces between $4 - 40$ kN. Immediately prior to bonding, indium oxide is etched away with a solution of 10% hydrochloric acid (in water) for 5 minutes, followed by DI water, acetone and methanol washing, and nitrogen blow drying.

It is likely that $30 - 40$ Å of oxide develops within minutes of exposure to air before the bond is conducted (Indium Corporation, 2016). If left out at room temperature in ambient conditions, the indium oxide will continue to build up to eventually self-passivate at a thickness of $80 - 100$ Å over the course of about three days (Indium Corporation, 2016).
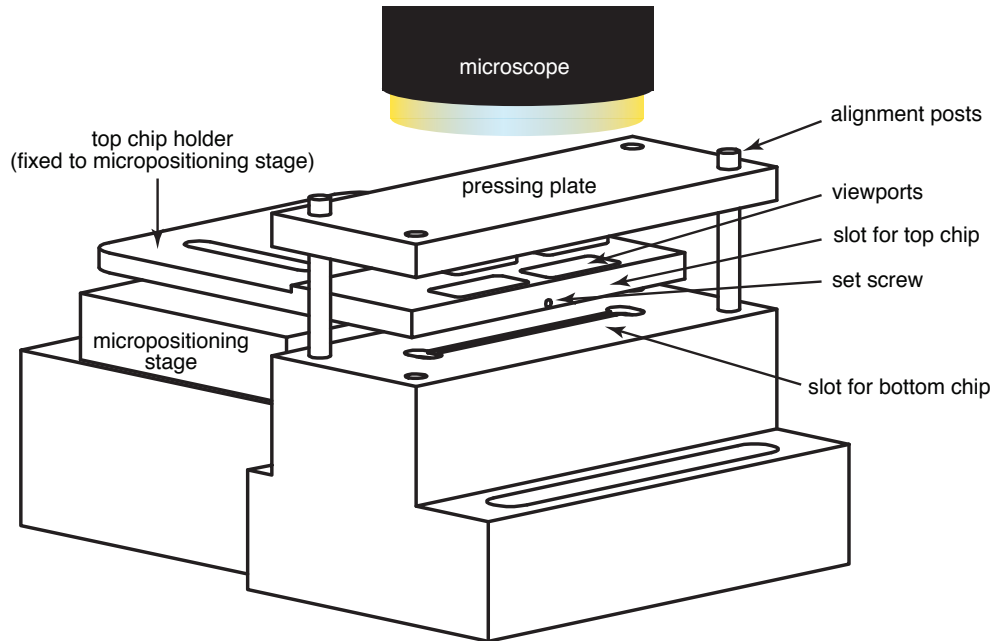
FIGURE A.3: **Alignment jig for bonded stripline devices.** Used to create devices in figure 7.6. The bottom chip sits in a slot, and the top chip is held face-down with a set screw during manual 5-axis micropositional alignment under a microscope. The top chip is slowly brought into contact with the lower chip. The jig is then removed from under the microscope, a pressing plate and weights are placed on top to apply bond forces on the order of 1 - 10 g/bump. Best-case devices were aligned to $\pm \sim 2\ \mu$m.

A.5 Josephson Junction fabrication

The transmons fabrication in this dissertation makes use of the Niemeyer-Dolan resist bridge technique (Dolan, 1977) to manufacture the required small Josephson junctions. Electron beam lithography was done in a Vistec EBPG 5000+, 100kV system. The transmons fabricated in this dissertation used a bilayer of resist consisting of a 500 nm MMA (EL13) below 70 nm PMMA (A3). The bottom layer of resist, MMA, must develop faster than the top layer of resist, PMMA, to produce an appreciable undercut for liftoff as well as producing a "bridge" of resist as shown in figure A.4. A "shadow" dose of electrons is applied at the bridge location (about 25-30 percent of the dose used for areas completely cleared) to aid in clearing the lower layer below the bridge. The silicon substrate used
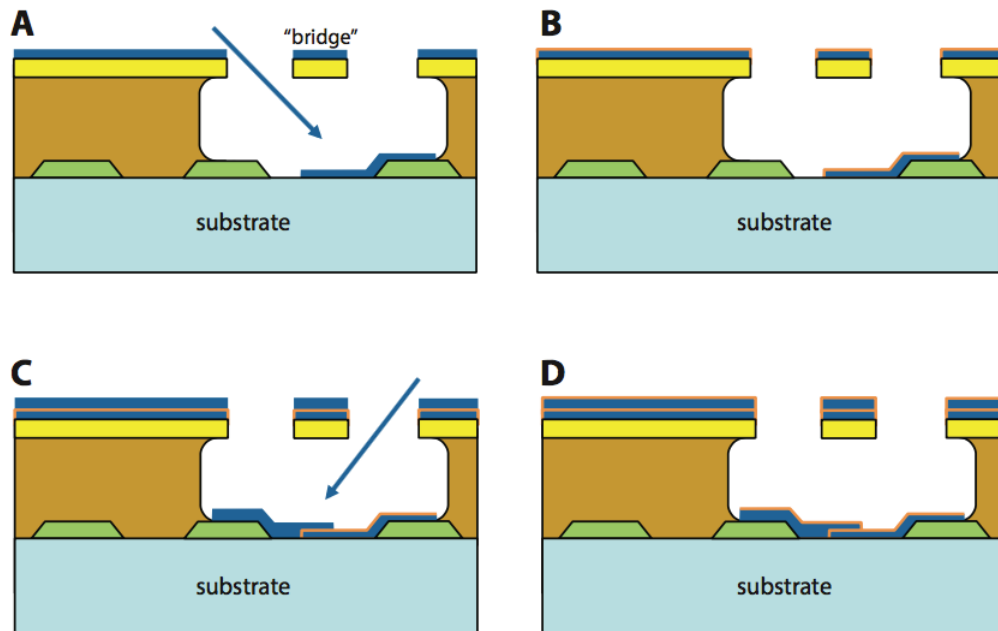
FIGURE A.4: **Josephson junction fabrication with the Dolan-bridge technique.** These cartoon cross-sections show the double-angle shaddow evaporation technique of Dolan, 1977 after the "bridge" has been written and developed in the resist bilayer. Green trapezoids are previously deposited superconducting material that may or may not be present in the design. The thick brown layer is the MMA resist while the top yellow layer is the PMMA that forms the bridge. (a) Aluminum (navy) deposition at first angle. (b) Oxidation (orange) of deposited aluminum. (c) Aluminum (navy) deposition at a second angle producing an overlap which forms the Josephson junction. (d) Final oxidation capping layer (orange) of the Josephson junction.

(Figure used with permission from Holland, 2015. See Copyright Permissions.)

for devices in this thesis is just conductive enough (even at resistivity $> \sim 10$ kΩcm) that an anticharging layer is not needed to prevent electron beam deflection during writing. (Sapphire substrates, on the other hand, do require this anticharging layer on top of the resist bilayer, usually in the form of gold or aluminum, which must then be removed before development.)

The wafer is developed using a 1:3 solution of MIBK:IPA at 25°C and cleaned in an oxygen plasma barrel asher at 300 mT for 10 seconds before immediately loading to a Plassys UMS300 for aluminum e-beam evaporation. Aluminum is deposited at angle -29°to 22.8

nm, followed by oxidation at 15 Torr for 12 minutes, followed by a second aluminum deposition at angle 29°to 68.6 nm, followed by a second oxidation at 3 Torr for 10 minutes.

The device in chapter 8 contained a single Josephson junction of dimension $500 \times 500 \ \mu\mathrm{m}$, which had a room temperature resistance that was measured to be 4.35 kΩ.

A.6 Surface roughness

The roughness of the mating surfaces forming a cavity seam may play a role in losses there, affecting g_{seam} in a way that is not yet understood. In addition, it is reasonable to expect that surface roughness of the interior cavity walls affects the dielectric loss contribution to the quality factor. Measurements of surface roughness of said mating surfaces are included in table A.6. From these data, and the images included in figure A.5, we observe that the surface roughness of the PCB's matte finish copper surface likely contributes to indium surface texture that may be unfavorable for bonding. We also note that due to indium's high ductility, the contact pressures used in this work produce significant deformation of surface texture, and the values and images presented here are those of pre-bonded surfaces. Precisely how surface roughness, ductility, contact pressure, and the presence of surface oxides affect g_{seam} is the subject of further research.

TABLE A.6: **Surface roughness of mating surfaces forming cavity seams.** Roughness parameters R_a (average roughness) and R_q (root mean square roughness) were measured with contact profilometery using a 5 mm linear trace along the surface and applying a Gaussian filter with cutoff $L_c = 800 \ \mu$m. Entries marked with (*) are indium electroplating performed by the vendor, while all others were created in-house.

Surface	Indium Thickness (μm)	R_a (μm)	R_q (μm)
Machined bulk Al alloy	0	0.47	0.65
Machined bulk copper	0	0.22	0.29
Machined bulk copper	10 (*)	0.53	0.66
Machined bulk copper	100 (*)	6.01	7.34
Silicon with 100 nm copper	0	0.01	0.01
Silicon with 100 nm copper	10	0.28	0.35
PCB	0	0.12	0.26
PCB	10	0.48	0.60

	Cu bulk	Cu on PCB	Cu on Si
Cu surface +10 µm In			
Cu surface			10 µm
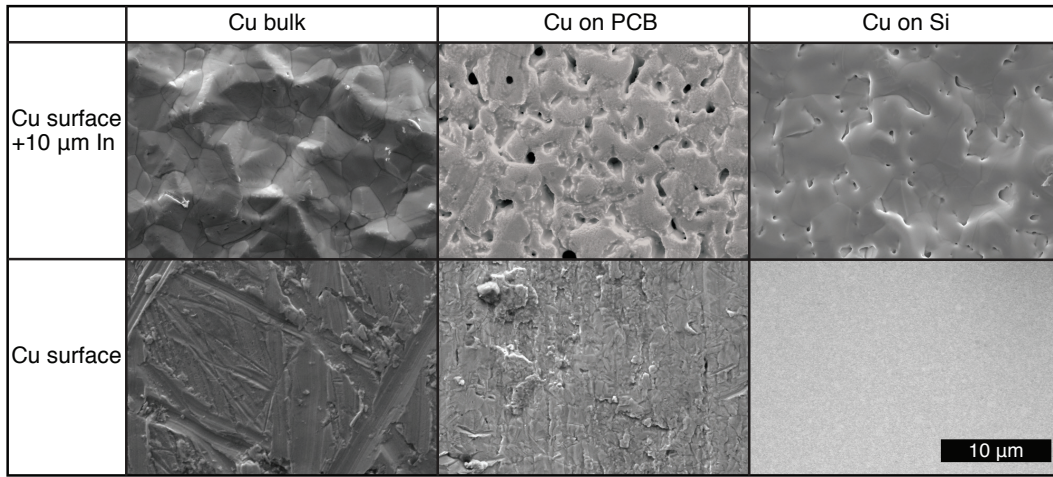
FIGURE A.5: **SEM images of electroplated indium on copper surfaces.** These images show the surface texture of copper surfaces relevant to this work with (top) and without (bottom) indium electroplated to a thickness of 10 μm. The images are of the mating surfaces before bonding. The 10 μm scale bar in the bottom right applies to all six images. Grains several microns in scale are visible in the indium on each surface, but their character differs. We show indium surfaces resulting from electroplating performed by the vendor (top left image), and those performed by our in-house process (top center and top right images).

Appendix B

Tables

B.1   Properties of select superconductors

TABLE B.1: **Some electrical and physical properties of aluminum, niobium, and indium.** Dheer, 1961 reports the penetration depth of inidum as 46 nm. The Cooper pairing interactions are found in De Gennes, 1999–Table 4.1

	Al	Nb	In
Critical temperature T_c (K)	1.18	9.3	3.41
Penetration depth $\lambda(0)$ (nm)	40-60	39	31-46
Coherence length ξ_0 (nm)	1200-1600	35-38	200-400
Gap $\Delta(0)$ ($\times 10^{-4}$ eV)	3.4	30.5	10.5
Critical Field $\mu_0 H_0$ (mT)	9.9		27.6
Debye temperature Θ_D (K)	365-428	275	108
Cooper pairing interaction $N(0)V$	0.18		0.29

B.2   3D cavity data

TABLE B.2: **Summary of measurements of cavities with H-plane constructions (cross-current seams).** See table B.3 on the next page for diagrams of the top parts and cavity parts. The seam admittance y_{seam} is calculated as described in chapter 5, and the seam conductance g_{seam} is inferred under the assumption that the measured cold $Q_i = g_{seam}/y_{seam}$.

dimensions	top part	cavity part	bond	f_0 (300 K)	f_0 (<20 mK)	Q_i (300 K)	Q_i (<20 mK)	y_{seam} (/Ωm)	g_{seam} (/Ωm)
36x18x0.3	2 - Al	Si - Al (400 nm)	clamp (1)	9.272	9.394	43	4,000	18.1	2.2×10^2
28x19x0.3	2 - Al (4N)	Si - Al (1000 nm)	clamp (1)	9.527	9.449	96	300,000	16.7	1.8×10^4
28x19x0.3	2 - Al	Si - Nb (1000 nm)	clamp (1)	9.468	9.419	40	18,000	16.7	1.1×10^3
28x19x0.3	4 - Al	5 - Al	screws	9.470	9.442	40	1,300	16.7	7.8×10^1
33x18x0.3	4 - Cu	5 - Cu	screws	9.6		107		17.7	6.0 (300 K)
28x19x5	4 - Al	6 - Al	screws	9.496	9.543	1,400	5,000	7.57	6.6×10^2
28x19x5	4 - In (10 um)	6 - In (10 um)	screws	9.501	9.537	1,600	2,960,000	7.57	3.9×10^5
28x19x0.3	4 - In (10 um)	5 - In (10 um)	screws	9.465	9.530	150	4,650,000	16.7	2.8×10^5
28x19x5	4 - In (50 um)	6 - In (50 um)	screws	9.480	9.525	710	10,000,000	7.57	1.3×10^6
28x19x0.3	2+Si - In (10 um)	Si - In (10 um)	manual press, no clamping	9.433	9.451	206	489,000	16.7	2.9×10^4
24x22x0.3	4 - In (10 um)	8 - In (10 um)	Instron , 150 C 10 kN, 100 MPa	9.247	9.308	200	752,000	16.0	4.7×10^4
24x22x0.3	4 - In (30 um)	8 - In (30 um)	Instron, 150 C 10 kN, 100 MPa	9.313	9.375	202	3,300,000	16.0	2.1×10^5
24x22x0.3	4 - In (30 um)	8 - In (30 um)	Instron, 150 C 10 kN, 100 MPa	9.207	9.269	172	83,600	16.0	5.2×10^3
24x22x0.3	4 - In (10 um)	Si - In (10 um)	Instron, 120 C 4 kN, 25 MPa	9.429	9.429	180	2,300,000	16.0	1.4×10^5
24x22x0.3	4 - In (10 um)	Si - In (10 um)	Instron, 120 C 4 kN, 25 MPa	9.306	9.418	182	252,000	16.0	1.6×10^4
24x22x0.3	4 - In (10 um)	Si - In (10 um)	nanofoil	9.319	10.157	182	5,000	16.0	3.1×10^2
24x22x0.3	Si - In (10 um)	7 - In (10 um)	In bumps	9.214	9.341	50	196,000	16.0	1.2×10^4

TABLE B.3: **Part codes corresponding to table B.2.**
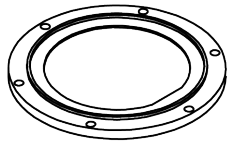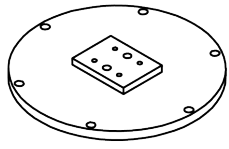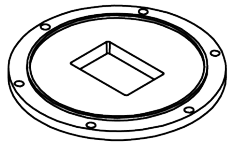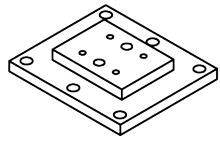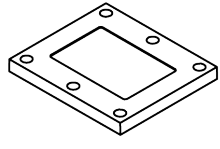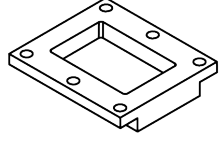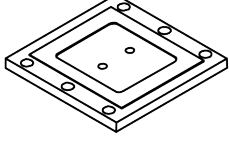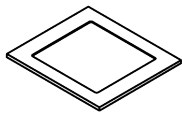
part no.	description	diagram
1	2 inch wafer holder (clamp)	
2	flat cover with 2 coupling holes	
3	5.0 mm high cavity	
4	flat cover with 2 coupling holes	
5	0.3 mm high cavity	
6	5.0 mm high cavity	
7	0.3 mm high cavity with 2 coupling holes	
8	0.3 mm high cavity	

TABLE B.4: **Cavities with E-plane cuts.** In the form of figure 5.1**(c)**.

	material	bond	f_0 (300 K)	f_0 (<20 mK)	Q_i (300 K)	Q_i (<20 mK)	notes
1	In (5 um)	screws	9.495	9.532	3510	740,000	
2	In (5 um)	hotplate reflow, screws		9.515		16,400	
3	In (100 um)	screws		9.489		77,000,000	
4	In (100 um)	hotplate reflow, screws		9.546		6,800,000	
5	In (50 um)	screws	9.400	9.438	2059	40,000,000	
6	In (100 um)	screws	9.376	9.419	1888	50,000,000	

TABLE B.5: **Bounds on seam conductance for different material interfaces from experiments of superconducting resonators contained in this thesis.** *Second line in table of cavities with H-plane cuts.

seam	$g_{\text{seam}}(\Omega\text{m}) >$
Al - Al (6061 alloy)	6.7×10^4
Al - Al (6061 alloy) with indium gasket	9.2×10^6
Al - Al (high purity)	1.8×10^4 *
In - In (electroplated on Cu)	2.4×10^{10}

Appendix C

Copyright Permissions

- Figure 3.1, figure 3.2, figure 3.5, figure 4.1, figure 5.8, figure 6.3 reproduced or adapted with permission from:
  M Reagor (2015). "Superconducting Cavities for Circuit Quantum Electrodynamics". PhD thesis. Yale University, New Haven, CT
  ©2015 by Matthew James Reagor

- Figure 3.3 is adapted with permission from:
  J. Koch et al. (2007). "Charge-insensitive qubit design derived from the Cooper pair box". *Phys. Rev. A* **76.4**, 042319
  ©2007 by the American Physical Society.

- Figure 3.4 adapted by permission from:
  D. I. Schuster et al. (2007). "Resolving photon number states in a superconducting circuit". *Nature* **445.7127**, 515–518
  ©2007 by Macmillan Publishers Ltd: Nature.

- Figure 3.8 adapted with permission from:
  M. H. Devoret, S. M. Girvin, and R. J. Schoelkopf (2007). "Circuit-QED: How strong can the coupling between a Josephson junction atom and a transmission line resonator be?" *Annalen der Physik* **16.10-11**, 767–779
  ©2007 by John Wiley & Sons, Inc.

- Figure 4.1 adapted with permission from:
  M. H. Devoret and R. J. Schoelkopf (2013). "Superconducting Circuits for Quantum Information: An Outlook". *Science* **339.6124**, 1169–1174
  ©2013 by AAAS.

- Figure 4.2 and figure 4.3 reproduced or adapted from:
  T. Brecht et al. (2016). "Multilayer microwave integrated quantum circuits for scalable quantum computing". *npj Quantum Information* **2**, 16002 EP–
  Published under a Creative Commons license (no permission necessary).

- Figure 4.3 reproduced from:
  A. R. Brown, P. Blondy, and G. M. Rebeiz (1999). "Microwave and millimeter-wave high-Q micromachined resonators". *Int. J. RF Microw. Comp. Aid. Eng.* **9**.**4**, 326–337. ISSN: 1099-047X
  ©1999 by John Wiley & Sons, Inc.

- Figure 4.4 reproduced from:
  W. R. Davis et al. (2005). "Demystifying 3D ICs: the pros and cons of going vertical". *IEEE Design Test of Computers* **22**.**6**, 498–510. ISSN: 0740-7475
  ©2005 by IEEE.

- Figure 4.5(a) reproduced from:
  T. Krems et al. (1996). "Millimeter-wave performance of chip interconnections using wire bonding and flip chip". In: 1996 IEEE MTT-S Int. Microwave Symposium Digest. 1, 247–250
  ©1996 by IEEE.

- Figure 4.5(b) and (c) reproduced from:
  K. J. Herrick, J.-G. Yook, and L. P. B. Katehi (1998). "Microtechnology and the development of three-dimensional circuits". *IEEE Trans. Microw. Theory Tech.* **46**.**11**, 1832–1844
  ©1998 by IEEE.

- Figure 8.14(e) is reproduced from:
  C. Axline et al. (2016). "An architecture for integrating planar and 3D cQED devices". *Appl. Phys. Lett.* **109**, 042601
  ©2016 by AIP publishing.

- Figure A.4 reproduced with permission from:
  E. T. Holland (2015). "Cavity State Reservoir Engineering in Circuit Quantum Electrodynamics". PhD thesis. Yale University, New Haven, CT
  ©2015 by Eric Holland.

Bibliography

Abdo, B., E. Arbel-Segev, O. Shtempluck, and E. Buks (2006). "Observation of Bifurcations and Hysteresis in Nonlinear NbN Superconducting Microwave Resonators". *IEEE Trans. on Applied Superconductivity* **16**, 1976–1987 (cited on page 151).

Al-Zoubi, A., F. Yang, and A. Kishk (2009). "A Broadband Center-Fed Circular Patch-Ring Antenna With a Monopole Like Radiation Pattern". *IEEE Trans. on Antennas and Propagation* **57**, 789–792 (cited on page 168).

Anacker, W. (1980). "Josephson Computer Technology: An IBM Research Project". *IBM J. Res. Dev.* **24**, 107–112 (cited on page 66).

Audley, M. D., W. D. Duncan, W. S. Holland, A. Walton, W. Parkes, C. Dunare, A. Gundlach, T. Stevenson, K. D. Irwin, G. C. Hilton, E. Schulte, P. A. Ade, and C. Tucker (2004). "Fabrication of the SCUBA-2 detector arrays". In: *Nucl. Instr. Meth. Phys. Res. A.* 520. LTD-10, 483–486 (cited on pages 52, 68, 133).

Awschalom, D. D., L. C. Bassett, A. S. Dzurak, E. L. Hu, and J. R. Petta (2013). "Quantum Spintronics: Engineering and Manipulating Atom-Like Spins in Semiconductors". *Science* **339**, 1174–1179 (cited on page 9).

Axline, C., M. Reagor, R. W. Heeres, P. Reinhold, C. Wang, K. Shain, W. Pfaff, Y. Chu, L. Frunzio, and R. J. Schoelkopf (2016). "An architecture for integrating planar and 3D cQED devices". *Appl. Phys. Lett.* **109**, 042601 (cited on pages 77, 144, 147, 149, 192, 223).

Barends, R., N. Vercruyssen, A. Endo, P. J. de Visser, T. Zijlstra, T. M. Klapwijk, P. Diener, S. J. C. Yates, and J. J. A. Baselmans (2010). "Minimal resonator loss for circuit quantum electrodynamics". *Appl. Phys. Lett.* **97**, 023508 (cited on pages 148, 149).

Barends, R., J. Kelly, A. Megrant, D. Sank, E. Jeffrey, Y. Chen, Y. Yin, B. Chiaro, J. Mutus, C. Neill, P. O'Malley, P. Roushan, J. Wenner, T. C. White, A. N. Cleland, and J. M. Martinis (2013). "Coherent Josephson Qubit Suitable for Scalable Quantum Integrated Circuits". *Phys. Rev. Lett.* **111**, 080502 (cited on page 89).

Barends, R., J. Kelly, A. Megrant, A. Veitia, D. Sank, E. Jeffrey, T. C. White, J. Mutus, A. G. Fowler, B. Campbell, Y. Chen, Z. Chen, B. Chiaro, A. Dunsworth, C. Neill, P. O'Malley, P. Roushan, A. Vainsencher, J. Wenner, A. N. Korotkov, A. N. Cleland, and J. M. Martinis (2014). "Superconducting quantum circuits at the surface code threshold for fault tolerance". *Nature* **508**, 500–503 (cited on pages 19, 51).

Béjanin, J. H., T. G. McConkey, J. R. Rinehart, C. T. Earnest, C. R. H. McRae, D. Shiri, J. D. Bateman, Y. Rohanizadegan, B. Penava, P. Breul, S. Royak, M. Zapatka, A. G. Fowler, and M. Mariantoni (2016). "Three-Dimensional Wiring for Extensible Quantum Computing: The Quantum Socket". *Phys. Rev. Applied* **6**, 044010 (cited on page 65).

Bennett, C. H. and G. Brassard (1984). "Quantum cryptography: Public key distribution and coin tossing". *Proc. IEEE Int. Conf. Computers, Systems and Signal Processing*, 175–179 (cited on page 14).

Bennett, C. H. and D. P. Divincenzo (2000). "Quantum information and computation". *Nature* **404**, 247–255 (cited on page 5).

Bennett, C. H., D. P. DiVincenzo, J. A. Smolin, and W. K. Wootters (1996). "Mixed-state entanglement and quantum error correction". *Phys. Rev. A* **54**, 3824–3851 (cited on page 15).

Bergeal, N., F. Schackert, M. Metcalfe, R. Vijay, V. E. Manucharyan, L. Frunzio, D. E. Prober, R. J. Schoelkopf, S. M. Girvin, and M. H. Devoret (2010). "Phase-preserving amplification near the quantum limit with a Josephson ring modulator". *Nature* **465**, 64–68 (cited on page 69).

Blais, A., J. Gambetta, A. Wallraff, D. Schuster, S. M. Girvin, M. H. Devoret, and R. J. Schoelkopf (2007). "Quantum-information processing with circuit quantum electrodynamics". *Phys. Rev. A* **75** (cited on page 19).

Blais, A., R.-S. Huang, A. Wallraff, S. M. Girvin, and R. J. Schoelkopf (2004). "Cavity quantum electrodynamics for superconducting electrical circuits: An architecture for quantum computation". *Phys. Rev. A* **69**, 062320 (cited on page 19).

Blatt, R. and D. Wineland (2008). "Entangled states of trapped atomic ions". *Nature* **453**, 1008–1015 (cited on page 9).

Blondy, P., A. R. Brown, D. Cros, and G. M. Rebeiz (1998). "Low-loss micromachined filters for millimeter-wave communication systems". *IEEE Trans. Microw. Theory Tech.* **46**, 2283–2288 (cited on pages 61, 68, 132).

Blumoff, J. Z., K. Chou, C. Shen, M. Reagor, C. Axline, R. T. Brierley, M. P. Silveri, C. Wang, B. Vlastakis, S. E. Nigg, L. Frunzio, M. H. Devoret, L. Jiang, S. M. Girvin, and R. J. Schoelkopf (2016). "Implementing and Characterizing Precise Multiqubit Measurements". *Phys. Rev. X* **6**, 031041 (cited on pages 75, 77).

Boissonneault, M., J. M. Gambetta, and A. Blais (2010). "Improved Superconducting Qubit Readout by Qubit-Induced Nonlinearities". *Phys. Rev. Lett.* **105**, 100504 (cited on page 33).

Bouchiat, V., D. Vion, P. Joyez, D. Esteve, and M. H. Devoret (1998). "Quantum coherence with a single Cooper pair". *Physica Scripta* **T76**, 165 (cited on page 25).

Bourassa, J., J. M. Gambetta, A. A. Abdumalikov, O. Astafiev, Y. Nakamura, and A. Blais (2009). "Ultrastrong coupling regime of cavity QED with phase-biased flux qubits". *Phys. Rev. A* **80**, 032109 (cited on page 43).

Braumüller, J., M. Sandberg, M. R. Vissers, A. Schneider, S. Schlör, L. Grünhaupt, H. Rotzinger, M. Marthaler, A. Lukashenko, A. Dieter, A. V. Ustinov, M. Weides, and D. P. Pappas (2016). "Concentric transmon qubit featuring fast tunability and an anisotropic magnetic dipole moment". *Appl. Phys. Lett.* **108**, 032601 (cited on page 165).

Brecht, T., Y. Chu, C. Axline, W. Pfaff, J. Z. Blumoff, K. Chou, L. Krayzman, L. Frunzio, and R. J. Schoelkopf (2017). "Micromachined Integrated Quantum Circuit Containing a Superconducting Qubit". *Phys. Rev. Applied* **7**, 044018 (cited on pages x, 164, 182).

Brecht, T., M. Reagor, Y. Chu, W. Pfaff, C. Wang, L. Frunzio, M. H. Devoret, and R. J. Schoelkopf (2015). "Demonstration of superconducting micromachined cavities". *Appl. Phys. Lett.* **107**, 192603 (cited on pages x, 55, 119, 129).

Brecht, T., W. Pfaff, C. Wang, Y. Chu, L. Frunzio, M. H. Devoret, and R. J. Schoelkopf (2016). "Multilayer microwave integrated quantum circuits for scalable quantum computing". *npj Quantum Information* **2**, 16002 EP– (cited on pages x, 54, 57, 222).

Briegel, H.-J., T. Calarco, D. Jaksch, J. I. Cirac, and P. Zoller (2000). "Quantum computing with neutral atoms". *J. Modern Optics* **47**, 415–451 (cited on page 9).

Brock, D. K. (2001). "RSFQ Technology: Circuits and Systems". *Int. J. High Speed Electron. Syst.* **11**, 307–362 (cited on page 66).

Broennimann, C., F. Glaus, J. Gobrecht, S. Heising, M. Horisberger, R. Horisberger, H. C. Kästli, J. Lehmann, T. Rohe, and S. Streuli (2006). "Development of an Indium bump bond process for silicon pixel detectors at PSI". *Nuclear Inst. and Meth. in Phys. A* **565**, 303–308 (cited on page 212).

Brown, A. R., P. Blondy, and G. M. Rebeiz (1999). "Microwave and millimeter-wave high-Q micromachined resonators". *Int. J. RF Microw. Comp. Aid. Eng.* **9**, 326–337 (cited on pages 59, 61, 62, 63, 132, 223).

Bruno, A., G. de Lange, S. Asaad, K. L. van der Enden, N. K. Langford, and L. DiCarlo (2015). "Reducing intrinsic loss in superconducting resonators by surface treatment and deep etching of silicon substrates". *Appl. Phys. Lett.* **106**, 182601 (cited on pages 60, 89).

Bruynseraede, Y., D. Gorle, D. Leroy, and P. Morignot (1971). "Surface-resistance measurements in TE011-mode cavities of superconducting indium, lead and an indium-lead alloy at low and high RF magnetic fields". *Physica* **54**, 137–159 (cited on page 160).

Bunyk, P, K Likharev, and D Zinoviev (2001). "RSFQ Technology: Physics and Devices". *Int. J. High Speed Electron. Syst.* **11**, 257–305 (cited on page 66).

Bunyk, P. I., E. M. Hoskinson, M. W. Johnson, E. Tolkacheva, F. Altomare, A. J. Berkley, R. Harris, J. P. Hilton, T. Lanting, A. J. Przybysz, and J. Whittaker (2014). "Architectural Considerations in the Design of a Superconducting Quantum Annealing Processor". *IEEE Trans. on Applied Superconductivity* **24**, 1–10 (cited on page 52).

Burin, A. L., M. S. Khalil, and K. D. Osborn (2013). "Universal Dielectric Loss in Glass from Simultaneous Bias and Microwave Fields". *Phys. Rev. Lett.* **110**, 157002 (cited on page 148).

Cabrillo, C. (1999). "Creation of entangled states of distant atoms by interference". *Phys. Rev. A* **59**, 1025–1033 (cited on page 17).

Cakmak, E., V. Dragoi, E. Pabo, T. Matthias, and T. L. Alford (2009). "Aluminum Thermo-Compression Bonding Characterization". In: Symposium DD - Microelectromechanical Systems - Materials and Devices III. 1222. MRS Proceedings (cited on page 132).

Castellanos-Beltran, M. A. and K. W. Lehnert (2007). "Widely tunable parametric amplifier based on a superconducting quantum interference device array resonator". *Appl. Phys. Lett.* **91**, 083509 (cited on page 69).

Chang, J. B., M. R. Vissers, A. D. Córcoles, M. Sandberg, J. Gao, D. W. Abraham, J. M. Chow, J. M. Gambetta, M. B. Rothwell, G. A. Keefe, M. Steffen, and D. P. Pappas (2013). "Improved superconducting qubit coherence using titanium nitride". *Appl. Phys. Lett.* **103**, 012602 (cited on page 89).

Chapman, B. J., B. A. Moores, E. I. Rosenthal, J. Kerckhoff, and K. W. Lehnert (2016). "General purpose multiplexing device for cryogenic microwave systems". *Appl. Phys. Lett.* **108**, 222602 (cited on page 69).

Chen, K.-N. and C. S. Tan (2012). "Thermocompression Cu-Cu Bonding of Blanket and Patterned Wafers". In: Handbook of Wafer Bonding. Ed. by J. J.-Q. L. P. Ramm and M.

M. V. Taklo. Weinheim, Germany: Wiley-VCH Verlag GmbH & Co. KGaA. 9, 161–180. 9783527644223 (cited on page 132).

Chen, Z., A. Megrant, J. Kelly, R. Barends, J. Bochmann, Y. Chen, B. Chiaro, A. Dunsworth, E. Jeffrey, J. Y. Mutus, P. J. J. O'Malley, C. Neill, P. Roushan, D. Sank, A. Vainsencher, J. Wenner, T. C. White, A. N. Cleland, and J. M. Martinis (2014). "Fabrication and characterization of aluminum airbridges for superconducting microwave circuits". *Appl. Phys. Lett.* **104**, 052602 (cited on pages 52, 53).

Cheng, X., C. Liu, and V. V. Silberschmidt (2012). "Thermo-mechanical characteristics of indium micro-joint under various low-temperature excursions". In: 13th Int. Conf. Electronic Packaging Technology High Density Packaging, 766–770 (cited on page 143).

Chervenak, J. A., K. D. Irwin, E. N. Grossman, J. M. Martinis, C. D. Reintsema, and M. E. Huber (1999). "Superconducting multiplexer for arrays of transition edge sensors". *Appl. Phys. Lett.* **74**, 4043–4045 (cited on page 68).

Chi, C.-Y. and G. M. Rebeiz (1996). "Conductor-loss limited stripline resonator and filters". *IEEE Trans. Microw. Theory Tech.* **44**, 626–630 (cited on pages 61, 68, 132).

Chin, C. C., D. E. Oates, G. Dresselhaus, and M. S. Dresselhaus (1992). "Nonlinear electrodynamics of superconducting NbN and Nb thin films at microwave frequencies". *Phys. Rev. B* **45**, 4788–4798 (cited on page 151).

Chu, Y., C. Axline, C. Wang, T. Brecht, Y. Y. Gao, L. Frunzio, and R. J. Schoelkopf (2016). "Suspending superconducting qubits by silicon micromachining". *Appl. Phys. Lett.* **109**, 112601 (cited on pages x, 89, 182, 189).

Cirac, J. I. and P. Zoller (1995). "Quantum Computations with Cold Trapped Ions". *Phys. Rev. Lett.* **74**, 4091–4094 (cited on page 9).

Ciuti, C. and I. Carusotto (2006). "Input-output theory of cavities in the ultrastrong coupling regime: The case of time-independent cavity parameters". *Phys. Rev. A* **74**, 033811 (cited on page 43).

Clarke, J. and F. K. Wilhelm (2008). "Superconducting quantum bits". *Nature* **453**, 1031–1042 (cited on page 9).

Cohen, L. F., A. L. Cowie, A Purnell, N. A. Lindop, S Thiess, and J. C. Gallop (2002). "Thermally induced nonlinear behaviour of HTS films at high microwave power". *Superconductor Science and Technology* **15**, 559 (cited on page 151).

Coleman, J. J., A. Rowen, S. S. Mani, W. G. Yelton, C. Arrington, R. Gillen, A. E. Hollowell, D. Okerlund, and A. Ionescu (2010). "Optimizing galvanic pulse plating parameters to improve indium bump to bump bonding". *Proc. SPIE* **7590**, 75900F–75900F–11 (cited on page 212).

Collin, R. E. (1990). Field Theory of Guided Waves. 2nd. Wiley-IEEE Press, New York. ISBN: 0198592132 (cited on page 82).

Creedon, D. L., Y. Reshitnyk, W. Farr, J. M. Martinis, T. L. Duty, and M. E. Tobar (2011). "High Q-factor sapphire whispering gallery mode microwave resonator at single photon energies and millikelvin temperatures". *Appl. Phys. Lett.* **98**, 222903 (cited on page 88).

Damaschke, B. and R. Tidecks (1989). "Inverse AC-Josephson effect in superconducting in and Pb-whiskers". *Zeitschrift für Physik B Condensed Matter* **77**, 17–23 (cited on page 138).

Davis, W. R., J. Wilson, S. Mick, J. Xu, H. Hua, C. Mineo, A. M. Sule, M. Steer, and P. D. Franzon (2005). "Demystifying 3D ICs: the pros and cons of going vertical". *IEEE Design Test of Computers* **22**, 498–510 (cited on pages 61, 63, 223).

Day, P. K., H. G. LeDuc, B. A. Mazin, A. Vayonakis, and J. Zmuidzinas (2003). "A broadband superconducting detector suitable for use in large arrays". *Nature* **425**, 817–821 (cited on page 87).

De Gennes, P. G. (1999). Superconductivity Of Metals And Alloys. Advanced Books Classics. Westview Press. ISBN: 0813345847 (cited on page 218).

Dennis, E., A. Kitaev, A. Landahl, and J. Preskill (2002). "Topological quantum memory". *J. Mathematical Physics* **43**, 4452–4505 (cited on page 16).

Deutsch, D. and R. Jozsa (1992). "Rapid Solution of Problems by Quantum Computation". *Proc. of the Royal Society of London A* **439**, 553–558 (cited on page 12).

Devoret, M. H. (1997). "Quantum Fluctuations in Electrical Circuits". In: Lecture Notes of the Les Houches Summer School. 63. 10, 351–386 (cited on pages 19, 21).

Devoret, M. H., S. M. Girvin, and R. J. Schoelkopf (2007). "Circuit-QED: How strong can the coupling between a Josephson junction atom and a transmission line resonator be?" *Annalen der Physik* **16**, 767–779 (cited on pages 39, 43, 222).

Devoret, M. H. and R. J. Schoelkopf (2013). "Superconducting Circuits for Quantum Information: An Outlook". *Science* **339**, 1169–1174 (cited on pages 9, 19, 50, 222).

Dheer, P. N. (1961). "The Surface Impedance of Normal and Superconducting Indium at 3000 Mc/s". *Proc. R. Soc. Lond. A* **260**, 333–349 (cited on pages 108, 158, 218).

Dib, N. I., W. P. Harokopus, P. B. Katehi, C. C. Ling, and G. M. Rebeiz (1991). "Study of a novel planar transmission line". In: 1991 IEEE MTT-S Int. Microwave Symposium Digest. 2, 623–626 (cited on page 60).

Dickey, J. (1959). "Self-diffusion in indium". *Acta Metallurgica* **7**, 350–353 (cited on page 132).

DisChem, Inc. (2013). *Chemistry, Relationships and Trouble Shooting of Optical Media Electroforming Baths*. Technical Report EFMP2102 (cited on page 211).

DiVincenzo, D. P., D Bacon, J Kempe, G Burkard, and K. B. Whaley (2000). "Universal quantum computation with the exchange interaction". *Nature* **408**, 339–342 (cited on page 9).

Divincenzo, D. P. (1996). "Topics in Quantum Computers". *arXiv:cond-mat/9612126* (cited on page 12).

— (2000). "The Physical Implementation of Quantum Computation". *Fortschritte der Physik* **48**, 771 (cited on pages 13, 51).

Dolan, G. J. (1977). "Offset masks for lift-off photoprocessing". *Appl. Phys. Lett.* **31**, 337–339 (cited on pages 214, 215).

Drayton, R. F. and L. P. B. Katehi (1995). "Development of Self-Packaged High-Frequency Circuits Using Micromachining Techniques". *IEEE Trans. on Microwave Theory and Techniques* **43**, 2073–2080 (cited on page 61).

Ehl, R. G. and A. J. Ihde (1954). "Faraday's electrochemical laws and the determination of equivalent weights". *J. Chemical Education* **31**, 226 (cited on page 209).

Fan, J. and C. S. Tan (2012). "Low Temperature Wafer-Level Metal Thermo-Compression Bonding Technology for 3D Integration". In: Metallurgy - Advances in Materials and Processes. Ed. by Y. Pardhi. 4. 978-953-51-0736-1 (cited on page 131).

Farrens, S. (2008). *Latest Metal Technologies for 3D Integration and MEMS Wafer Level Bonding*. Technical Report. SUSS MicroTech, Inc. (cited on page 132).

Farrington, N. E. S. and S. Iezekiel (2011). "Design of a Non-Contact Vertical Transition for a 3D MM-Wave Multi-Chip Module Based on Shielded Membrane Supported Interconnects". *Progress In Electromagnetics Research B* **32**, 405–423 (cited on page 61).

Feynman, R. P. (1982). "Simulating physics with computers". *Int. J. of Theoretical Physics* **21**, 467–488 (cited on page 12).

Fowler, A. G., M. Mariantoni, J. M. Martinis, and A. N. Cleland (2012). "Surface codes: Towards practical large-scale quantum computation". *Phys. Rev. A* **86**, 032324 (cited on pages 16, 53).

Gao, J., M. Daal, A. Vayonakis, S. Kumar, J. Zmuidzinas, B. Sadoulet, B. A. Mazin, P. K. Day, and H. G. Leduc (2008). "Experimental evidence for a surface distribution of two-level systems in superconducting lithographed microwave resonators". *Appl. Phys. Lett.* **92**, 152505 (cited on pages 147, 149).

Garro, I. L. (2003). "Micromachined microwave filters". PhD thesis. University of Birmingham, England (cited on page 61).

Geerlings, K., S. Shankar, E. Edwards, L. Frunzio, R. J. Schoelkopf, and M. H. Devoret (2012). "Improving the Quality Factor of Microwave Compact Resonators by Optimizing their Geometrical Parameters". *Appl. Phys. Lett.* **100**, 192601 (cited on pages 44, 52).

Geerlings, K. L. (2013). "Improving Coherence of Superconducting Qubits and Resonators". PhD thesis. Yale University, New Haven, CT (cited on pages 74, 94, 97, 147, 149, 180).

Girvin, S. M. (2011). "Circuit QED: Superconducting Qubits Coupled to Microwave Photons". In: Quantum Machines: Measurement and Control of Engineered Quantum Systems: Lecture Notes of the Les Houches Summer School. Vol. 96. Oxford Uniersity Press. 3 (cited on pages 19, 21).

Golosovsky, M. A., H. J. Snortland, and M. R. Beasley (1995). "Nonlinear microwave properties of superconducting Nb microstrip resonators". *Phys. Rev. B* **51**, 6462–6469 (cited on page 151).

Gottesman, D. (2010). "An Introduction to Quantum Error Correction and Fault-Tolerant Quantum Computation". In: Quantum Information Science and Its Contributions to Mathematics. Vol. 68. Amer. Math. Soc., 13–58 (cited on pages 15, 51).

Gottesman, D., A. Kitaev, and J. Preskill (2001). "Encoding a qubit in an oscillator". *Phys. Rev. A* **64**, 012310 (cited on page 16).

Greer, F., M. Dickie, R. P. Vasquez, T. J. Jones, M. E. Hoenk, and S. Nikzad (2009). "Plasma treatment methods to improve indium bump bonding via indium oxide removal". *J. Vac. Sci. & Tech. B: Microelectronics and Nanometer Structures Processing, Measurement, and Phenomena* **27**, 2132–2137 (cited on page 139).

Greiner, J. H. (1971). "Josephson Tunneling Barriers by rf Sputter Etching in an Oxygen Plasma". *J. Appl. Phys.* **42**, 5151–5155 (cited on page 130).

Grover, L. K. (1997). "Quantum Mechanics Helps in Searching for a Needle in a Haystack". *Phys. Rev. Lett.* **79**, 325–328 (cited on page 12).

Harle, L. (2003). "Microwave micromachined cavity filters". PhD thesis. University of Michigan, Ann Arbor, MI (cited on pages 59, 63).

Harris, A. I., M. Sieth, J. M. Lau, S. E. Church, L. A. Samoska, and K. Cleary (2012). "Note: Cryogenic microstripline-on-Kapton microwave interconnects". *Rev. Sci. Inst.* **83**, 086105 (cited on page 66).

Hatridge, M., S. Shankar, M. Mirrahimi, F. Schackert, K. Geerlings, T. Brecht, K. M. Sliwa, B. Abdo, L. Frunzio, S. M. Girvin, R. J. Schoelkopf, and M. H. Devoret (2013). "Quantum Back-Action of an Individual Variable-Strength Measurement". *Science* **339**, 178–181 (cited on pages 6, 15).

Henderson, R. M., K. J. Herrick, T. M. Weller, S. V. Robertson, R. T. Kihm, and L. P. B. Katehi (2000). "Three-dimensional high-frequency distribution networks. II. Packaging and integration". *IEEE Trans. on Microwave Theory and Techniques* **48**, 1643–1651 (cited on page 60).

Herr, Q. P., A. Y. Herr, O. T. Oberg, and A. G. Ioannidis (2011). "Ultra-low-power superconductor logic". *J. Appl. Phys.* **109**, 103903 (cited on page 67).

Herrick, K. H., L. P. B. Katehi, and R. T. Kihm (2001). "Interconnects for a Multi-layer Three-dimensional Silicon Architecture". *Microwave Journal*, May 2001 issue, 3204 (cited on pages 60, 61).

Herrick, K. J., T. A. Schwarz, and L. P. B. Katehi (1998). "Si-Micromachined Coplanar Waveguides for Use in High-Frequency Circuits". *IEEE Trans. Microw. Theory Tech.* **46**, 762–768 (cited on page 60).

Herrick, K. J., J.-G. Yook, and L. P. B. Katehi (1998). "Microtechnology and the development of three-dimensional circuits". *IEEE Trans. Microw. Theory Tech.* **46**, 1832–1844 (cited on pages 61, 64, 223).

Hillery, M., V. Bužek, and A. Berthiaume (1999). "Quantum secret sharing". *Phys. Rev. A* **59**, 1829–1834 (cited on page 14).

Holland, E. T. (2015). "Cavity State Reservoir Engineering in Circuit Quantum Electrodynamics". PhD thesis. Yale University, New Haven, CT (cited on pages 215, 223).

Houck, A. A., J. A. Schreier, B. R. Johnson, J. M. Chow, J. Koch, J. M. Gambetta, D. I. Schuster, L. Frunzio, M. H. Devoret, S. M. Girvin, and R. J. Schoelkopf (2008). "Controlling the Spontaneous Emission of a Superconducting Transmon Qubit". *Phys. Rev. Lett.* **101**, 080502 (cited on page 188).

Houck, A. A., J. Koch, M. H. Devoret, S. M. Girvin, and R. J. Schoelkopf (2009). "Life after charge noise: recent results with transmon qubits". *Quantum Information Processing* **8**, 105–115 (cited on page 29).

Huang, Q., G. Xu, and L. Luo (2009). "Indium Bump Fabricated with Electroplating Method". In: Int. Conf. on Electronic Packaging Technology and High Density Packaging, 650–654 (cited on page 134).

Huang, Q., G. Xu, Y. Yuan, X. Cheng, and L. Luo (2010). "Development of indium bumping technology through AZ9260 resist electroplating". *J. Micromech. Microeng.* **20**, 055035 (cited on pages 134, 195, 212).

Hughey, B. J., T. R. Gentile, D. Kleppner, and T. W. Ducas (1990). "A split high-Q superconducting cavity". *Rev. Sci. Instrum.* **61**, 1940 (cited on page 103).

Iliev, S., X. Chen, M. Pathan, and V. Tagarielli (2017). "Measurements of the mechanical response of Indium and of its size dependence in bending and indentation". *Materials Science and Engineering: A* **683**, 244–251 (cited on page 138).

Indium Corporation (2016). *Indium Cold Welding*. Application Note (cited on pages 139, 213).

Jackson, J. D. (1998). Classical Electrodynamics. 3rd. Wiley. ISBN: 047130932X (cited on pages 45, 82, 84, 166).

Jaynes, E. T. and F. W. Cummings (1963). "Comparison of quantum and semiclassical radiation theories with application to the beam maser". *Proc. of the IEEE* **51**, 89–109 (cited on page 30).

Jeffrey, E., D. Sank, J. Y. Mutus, T. C. White, J. Kelly, R. Barends, Y. Chen, Z. Chen, B. Chiaro, A. Dunsworth, A. Megrant, P. J. J. O'Malley, C. Neill, P. Roushan, A. Vainsencher, J. Wenner, A. N. Cleland, and J. M. Martinis (2014). "Fast Accurate State Measurement with Superconducting Qubits". *Phys. Rev. Lett.* **112**, 190504 (cited on page 53).

Jelezko, F. and J. Wrachtrup (2006). "Single defect centres in diamond: A review". *physica status solidi (a)* **203**, 3207–3225 (cited on page 9).

Jiang, J., S. Tsao, T. OSullivan, M. Razeghi, and G. J. Brown (2004). "Fabrication of indium bumps for hybrid infrared focal plane array applications". *Infrared physics & technology* **45**, 143–151 (cited on page 212).

Johansson, J. R., P. D. Nation, and F. Nori (2013). "QuTiP 2: A Python framework for the dynamics of open quantum systems". *Computer Physics Communications* **184**, 1234–1240 (cited on page 36).

Jordan, D. W. (2007). Nonlinear ordinary differential equations - An introduction for scientists and engineers. 4th. Oxford University Press. ISBN: 978-0-19-920824-1 (cited on page 151).

Katehi, L. P. B., J. F. Harvey, and K. J. Herrick (2001). "3-D integration of RF circuits using Si micromachining". *IEEE Microwave Magazine* **2**, 30–39 (cited on page 59).

Katehi, L. P. (1997). *High Efficiency Micromachined Antennas: Micromachined Antennas for Microwave and Mm-Wave Applications*. Office of Naval Research Final Report 033095-1-F. Ann Arbor, Michigan: Radiation Laboratory, University of Michigan (cited on pages 61, 132).

Kerckhoff, J., K. Lalumière, B. J. Chapman, A. Blais, and K. W. Lehnert (2015). "On-Chip Superconducting Microwave Circulator from Synthetic Rotation". *Phys. Rev. Applied* **4**, 034002 (cited on page 69).

Khalil, M. S., F. C. Wellstood, and K. D. Osborn (2011). "Loss Dependence on Geometry and Applied Power in Superconducting Coplanar Resonators". *IEEE Trans. on Applied Superconductivity* **21**, 879–882 (cited on pages 147, 148, 149).

Khalil, M. S., M. J. A. Stoutimore, F. C. Wellstood, and K. D. Osborn (2012). "An analysis method for asymmetric resonator transmission applied to superconducting devices". *J. Appl. Phys.* **111**, 054510 (cited on page 94).

Kimble, H. J. (2008). "The quantum internet". *Nature* **453**, 1023–1030 (cited on page 17).

Knill, E. (2005). "Quantum computing with realistically noisy devices". *Nature* **434**, 39–44 (cited on pages 15, 51).

Knill, E. and R. Laflamme (1996). "Concatenated quantum codes". *arXiv preprint quant-ph/9608012* (cited on page 16).

Knill, E., R. Laflamme, and W. H. Zurek (1998). "Resilient quantum computation". *Science* **279**, 342–345 (cited on page 16).

Koch, J., T. M. Yu, J. Gambetta, A. A. Houck, D. I. Schuster, J. Majer, A. Blais, M. H. Devoret, S. M. Girvin, and R. J. Schoelkopf (2007). "Charge-insensitive qubit design derived from the Cooper pair box". *Phys. Rev. A* **76**, 042319 (cited on pages 25, 26, 28, 222).

Krems, T., W. Haydl, H. Massler, and J. Rudiger (1996). "Millimeter-wave performance of chip interconnections using wire bonding and flip chip". In: 1996 IEEE MTT-S Int. Microwave Symposium Digest. 1, 247–250 (cited on pages 64, 223).

Kuhr, S., S. Gleyzes, C. Guerlin, J. Bernu, U. Hoff, S. Deleglise, S. Osnaghi, M. Brune, J. Raimond, S. Haroche, E. Jacques, P. Bosland, and B. Visentin (2007). "Ultrahigh finesse Fabry-Perot superconducting resonator". *Appl. Phys. Lett.* **90** (cited on page 72).

Kuper, A., H. Letaw, L. Slifkin, E. Sonder, and C. T. Tomizuka (1954). "Self-Diffusion in Copper". *Phys. Rev.* **96**, 1224–1225 (cited on page 132).

Ladd, T. D., F. Jelezko, R. Laflamme, Y. Nakamura, C. Monroe, and J. L. O'Brien (2010). "Quantum computers". *Nature* **464**, 45–53 (cited on page 51).

Lahiri, S. K. and S. Basavaiah (1978). "Lead-alloy Josephson-tunneling gates with improved stability upon thermal cycling". *J. Appl. Phys.* **49**, 2880–2884 (cited on page 130).

Lahiri, S. (1977). "A thin film resistor for Josephson tunneling circuits". *Thin Solid Films* **41**, 209–215 (cited on page 195).

Landauer, R. (1996). "The physical nature of information". *Physics letters A* **217**, 188–193 (cited on page 9).

Lau, J. H. (1996). Flip chip technologies. McGraw Hill. ISBN: 0070366098 (cited on page 65).

Lecocq, F., L. Ranzani, G. A. Peterson, K. Cicak, R. W. Simmonds, J. D. Teufel, and J. Aumentado (2017). "Nonreciprocal Microwave Signal Processing with a Field-Programmable Josephson Amplifier". *Phys. Rev. Applied* **7**, 024028 (cited on page 69).

Lee, G.-A. and H.-Y. Lee (1998). "Suppression of the CPW leakage in common millimeter-wave flip-chip structures". *IEEE Microwave and Guided Wave Letters* **8**, 366–368 (cited on pages 52, 60).

Leghtas, Z., S. Touzard, I. M. Pop, A. Kou, B. Vlastakis, A. Petrenko, K. M. Sliwa, A. Narla, S. Shankar, M. J. Hatridge, M. Reagor, L. Frunzio, R. J. Schoelkopf, M. Mirrahimi, and M. H. Devoret (2015). "Confining the state of light to a quantum manifold by engineered two-photon loss". *Science* **347**, 853–857 (cited on page 186).

Leghtas, Z., G. Kirchmair, B. Vlastakis, M. H. Devoret, R. J. Schoelkopf, and M. Mirrahimi (2013a). "Deterministic protocol for mapping a qubit to coherent state superpositions in a cavity". *Phys. Rev. A* **87**, 042315 (cited on page 16).

Leghtas, Z., G. Kirchmair, B. Vlastakis, R. J. Schoelkopf, M. H. Devoret, and M. Mirrahimi (2013b). "Hardware-Efficient Autonomous Quantum Memory Protection". *Phys. Rev. Lett.* **111**, 120501 (cited on page 16).

Lewis, R. M., M. D. Henry, and K. Schroeder (2017). "Vacuum gap micro-strip microwave resonators for 2.5D integration in quantum computing". *IEEE Trans. on Applied Superconductivity* **PP**, 99 (cited on page 60).

Li, M. J. et al. (2007). "Microshutter array system for James Webb Space Telescope". *Proc. SPIE* **6687**, 668709–668709–13 (cited on page 212).

Linder, S., H. Baltes, F. Gnaedinger, and E. Doering (1994). "Fabrication technology for wafer through-hole interconnections and three-dimensional stacks of chips and wafers". In: Proc. IEEE Micro Electro Mechanical Systems, 349–354 (cited on page 64).

Lloyd, S. (1996). "Universal Quantum Simulators". *Science* **273**, 1073–1078 (cited on page 12).

Logvinenko, S., G. Mikhina, and G. Mende (1984). "Low temperature indium resistance thermometer". *Cryogenics* **24**, 421–422 (cited on page 159).

Loo, A. F. van, A. Fedorov, K. Lalumière, B. C. Sanders, A. Blais, and A. Wallraff (2013). "Photon-Mediated Interactions Between Distant Artificial Atoms". *Science* **342**, 1494–1496 (cited on page 51).

Loss, D. and D. P. DiVincenzo (1998). "Quantum computation with quantum dots". *Phys. Rev. A* **57**, 120–126 (cited on page 9).

Macklin, C., K. O'Brien, D. Hover, M. E. Schwartz, V. Bolkhovsky, X. Zhang, W. D. Oliver, and I. Siddiqi (2015). "A near–quantum-limited Josephson traveling-wave parametric amplifier". *Science* **350**, 307–310 (cited on page 69).

Majer, J., J. M. Chow, J. M. Gambetta, J. Koch, B. R. Johnson, J. Schreier, L. Frunzio, D. I. Schuster, A. A. Houck, A. Wallraff, A. Blais, M. H. Devoret, S. M. Girvin, and R. J. Schoelkopf (2007). "Coupling superconducting qubits via a cavity bus". *Nature* **449**, 443–447 (cited on page 51).

Makin, S. M., A. H. Rowe, and A. D. Leclaire (1957). "Self-Diffusion in Gold". In: Proc. of the Physical Society B. 70. 6, 545 (cited on page 132).

Manucharyan, V. E., J. Koch, L. I. Glazman, and M. H. Devoret (2009). "Fluxonium: Single Cooper-Pair Circuit Free of Charge Offsets". *Science* **326**, 113–116 (cited on page 25).

Martinis, J. M. and A. Megrant (2014). "UCSB final report for the CSQ program: Review of decoherence and materials physics for superconducting qubits". *arXiv:1410.5793[quant-ph]* (cited on page 88).

Mattis, D. and J. Bardeen (1958). "Theory of the anomalous skin effect in normal and superconducting metals". *Phys. Rev.* **111**, 412–417 (cited on page 156).

Mazin, B. A., P. K. Day, H. G. LeDuc, A. Vayonakis, and J. Zmuidzinas (2002). "Superconducting kinetic inductance photon detectors". In: Proc. SPIE: Highly Innovative Space Telescope Concepts. 4849, 283–293 (cited on page 87).

McGarey, P., H. Mani, C. Wheeler, and C. Groppi (2014). "A 16-channel flex circuit for cryogenic microwave signal transmission". In: Proc. SPIE: Millimeter, Submillimeter, and Far-Infrared Detectors and Instrumentation for Astronomy VII. 9153, 91532F–6 (cited on page 66).

McRae, C. H., J. H. Bejanin, Z. Pagel, A. O. Abdallah, T. G. McConkey, C. T. Earnest, J. R. Rinehart, and M. Mariantoni (2017). "Thermocompression Bonding Technology

for Multilayer Superconducting Quantum Circuits". *arXiv:1705.02435[physics.app-ph]* (cited on pages 60, 132, 213).

Mermin, N. D. (2007). Quantum Computer Science: An Introduction. Cambrdige University Press. ISBN: 0521876583 (cited on pages 5, 15).

Middelmann, T., A. Walkov, G. Bartl, and R. Schödel (2015). "Thermal expansion coefficient of single-crystal silicon from 7 K to 293 K". *Phys. Rev. B* **92**, 174113 (cited on page 142).

Miller, D. L. and O. Naaman (2016). "Reciprocal Quantum Logic Comparator For Qubit Readout". Pat. US2016/0156357 A1 (cited on page 69).

Miller, T. M. and C. A. Jhabvala (2012). "Enabling large focal plane arrays through mosaic hybridization". *Proc. SPIE* **H**, 84532 (cited on page 65).

Minev, Z., K. Serniak, L. Pop, Y. Chu, T. Brecht, L. Frunzio, M. Devoret, and R. J. Schoelkopf III (2016a). "Techniques for coupling plannar qubits to non-planar resonators and related systems and methods". Pat. WO Patent App. PCT/US2016/019,801 (cited on page 164).

Minev, Z. K., I. M. Pop, and M. H. Devoret (2013). "Planar superconducting whispering gallery mode resonators". *Appl. Phys. Lett.* **103**, 142604 (cited on pages 60, 69, 76).

Minev, Z. K., K Serniak, I. M. Pop, Z Leghtas, K Sliwa, L Frunzio, R. J. Schoelkopf, and M. H. Devoret (2016b). "Planar Multilayer Circuit Quantum Electrodynamics". *Phys. Rev. Applied* **5**, 044021 (cited on pages 60, 69, 164, 169).

Mirrahimi, M., Z. Leghtas, V. V. Albert, S. Touzard, R. J. Schoelkopf, L. Jiang, and M. H. Devoret (2014). "Dynamically protected cat-qubits: a new paradigm for universal quantum computation". *New Journal of Physics* **16**, 045014 (cited on page 16).

Monroe, C. and J. Kim (2013). "Scaling the Ion Trap Quantum Processor". *Science* **339**, 1164–1169 (cited on page 9).

Monroe, C., R. Raussendorf, A. Ruthven, K. R. Brown, P. Maunz, L.-M. Duan, and J. Kim (2014). "Large-scale modular quantum-computer architecture with atomic memory and photonic interconnects". *Phys. Rev. A* **89**, 022317 (cited on page 17).

Monroe, C. R., R. J. Schoelkopf, and M. D. Lukin (2016). "Quantum Connections". *Scientific American* **314**, 50–57 (cited on page 17).

Moore, G. E. (1965). "Cramming More Components onto Integrated Circuits". *Electronics* **38** (cited on pages 48, 53).

Mutus, J., B. Foxen, E. Lucero, J. Kelly, Y. Yang, A. Yu, M. Baldwinson, Z. Chen, B. Chiaro, A. Dunsworth, C. Neil, C. Quintana, J. Wenner, and J. M. Martinis (2017). "3D Integration of superconducting qubits with bump bonds: Part 1". In: APS March Meeting 2017, H46.00006 (cited on page 213).

Nam, S. B. (1967a). "Theory of Electromagnetic Properties of Strong-Coupling and Impure Superconductors. II". *Phys. Rev.* **156**, 487–493 (cited on page 156).

— (1967b). "Theory of Electromagnetic Properties of Superconducting and Normal Systems. I". *Phys. Rev.* **156**, 470–486 (cited on page 156).

Nickerson, N. H., Y. Li, and S. C. Benjamin (2013). "Topological quantum computing with a very noisy network and local error rates approaching one percent". *Nature Comm.* **4**, 1756 EP – (cited on page 17).

Nielsen, M. A. and I. L. Chuang (2000). Quantum Computation and Quantum Information. Cambidge University Press. ISBN: 0521635039 (cited on page 5).

Nigg, S. E., H. Paik, B. Vlastakis, G. Kirchmair, S. Shankar, L. Frunzio, M. H. Devoret, R. J. Schoelkopf, and S. M. Girvin (2012). "Black-Box Superconducting Circuit Quantization". *Phys. Rev. Lett.* **108**, 240502 (cited on pages 33, 36, 175, 178).

Noroozian, O., P. K. Day, B. H. Eom, H. G. Leduc, and J. Zmuidzinas (2012). "Crosstalk Reduction for Superconducting Microwave Resonator Arrays". *IEEE Trans. Microw. Theory Tech.* **60**, 1235 (cited on page 52).

Ofek, N., A. Petronko, R. Heeres, P. Reinhold, Z. Leghtas, B. Vlastakis, Y. Liu, L. Frunzio, S. M. Girvin, L. Jiang, M. Mirrahimi, M. H. Devoret, and R. J. Schoelkopf (2016). "Extending the lifetime of a quantum bit with error correction in superconducting circuits". *Nature* **536**, 441–445 (cited on page 16).

Overcash, D., C. Watlington, M. Skove, and E. Stillwel (1971). "Temperature dependence of the critical current in tin and indium whiskers". *Physica* **55**, 317–323 (cited on page 138).

Paik, H., D. I. Schuster, L. S. Bishop, G Kirchmair, G Catelani, A. P. Sears, B. R. Johnson, M. J. Reagor, L Frunzio, L. I. Glazman, S. M. Girvin, M. H. Devoret, and R. J. Schoelkopf (2011). "Observation of high coherence in Josephson junction qubits measured in a three-dimensional circuit QED architecture". *Phys. Rev. Lett.* **107**, 240501 (cited on pages 44, 45, 75).

Papapolymerou, J., J.-C. Cheng, J. East, and L. P. B. Katehi (1997). "A micromachined high-Q X-band resonator". *IEEE Microw. Guided Wave Lett.* **7**, 168–170 (cited on pages 59, 63, 132).

Pechal, M., J.-C. Besse, M. Mondal, M. Oppliger, S. Gasparinetti, and A. Wallraff (2016). "Superconducting Switch for Fast On-Chip Routing of Quantum Microwave Fields". *Phys. Rev. Applied* **6**, 024009 (cited on page 69).

Perez-Delgado, C. A. and P. Kok (2011). "Quantum computers: Definition and implementations". *Phys. Rev. A* **83**, 012303 (cited on page 51).

Petersen, K. E. (1982). "Silicon as a mechanical material". *Proc. of the IEEE* **70**, 420–457 (cited on page 139).

Pfaff, W., C. J. Axline, L. D. Burkhart, U. Vool, P. Reinhold, L. Frunzio, L. Jiang, M. H. Devoret, and R. J. Schoelkopf. "Schrödinger's catapult: Launching multiphoton quantum states from a microwave cavity memory". *preprint arXiv:1612.05238[quant-ph]* (cited on pages 75, 77).

Pfaff, W., T. H. Taminiau, L. Robledo, H. Bernien, M. Markham, D. J. Twitchen, and R. Hanson (2012). "Demonstration of entanglement-by-measurement of solid-state qubits". *Nature Physics* **9**, 29–33 (cited on page 17).

Pobell, F. (2007). Matter and Methods at Low Temperatures. 3rd. Springer Berlin Heidelberg. ISBN: 978-3-540-46356-6 (cited on page 142).

Pozar, D. M. (2005). Microwave Engineering. 3rd. Wiley. ISBN: 0471448788 (cited on pages 75, 86, 120, 125).

Preskill, J (2015). *Quantum Computation - Lecture notes for Caltech Physics 219/Computer Science 219*. URL: http://www.theory.caltech.edu/people/preskill/ph229/#lecture (cited on page 5).

Probst, S., F. B. Song, P. A. Bushev, A. V. Ustinov, and M. Weides (2015). "Efficient and robust analysis of complex scattering data under noise in microwave resonators". *Rev. Sci. Instrum.* **86**, 024706 (cited on pages 94, 97).

Purcell, E. M., H. C. Torrey, and R. V. Pound (1946). "Resonance Absorption by Nuclear Magnetic Moments in a Solid". *Phys. Rev.* **69**, 37–38 (cited on page 188).

Rahamim, J, T Behrle, M. J. Peterer, A Patterson, P Spring, T Tsunoda, R Manenti, G Tancredi, and P. J. Leek (2017). "Double-sided coaxial circuit QED with out-of-plane wiring". *arXiv:1703.05828[quant-ph]* (cited on page 165).

Reagor, M (2015). "Superconducting Cavities for Circuit Quantum Electrodynamics". PhD thesis. Yale University, New Haven, CT (cited on pages 21, 27, 34, 50, 80, 94, 96, 115, 116, 121, 157, 222).

Reagor, M., H. Paik, G. Catelani, L. Sun, C. Axline, E. Holland, I. M. Pop, N. A. Masluk, T. Brecht, L. Frunzio, M. H. Devoret, L. Glazman, and R. J. Schoelkopf (2013). "Reaching 10 ms single photon lifetimes for superconducting aluminum cavities". *Appl. Phys. Lett.* **102**, 192604 (cited on pages x, 52, 149, 157).

Reagor, M., W. Pfaff, C. Axline, R. W. Heeres, N. Ofek, K. Sliwa, E. Holland, C. Wang, J. Blumoff, K. Chou, M. J. Hatridge, L. Frunzio, M. H. Devoret, L. Jiang, and R. J. Schoelkopf

(2016). "Quantum memory with millisecond coherence in circuit QED". *Phys. Rev. B* **94**, 014506 (cited on pages 16, 44, 75, 149).

Rebeiz, G. M. (2003). RF MEMS: Theory, Design, and Technology. Wiley. ISBN: 0471201693 (cited on page 56).

Reed, M. D. (2013). "Entanglement and Quantum Error Correction with Superconducting Circuits". PhD thesis. Yale University, New Haven, CT (cited on page 33).

Reed, M. D., L. DiCarlo, B. R. Johnson, L. Sun, D. I. Schuster, L. Frunzio, and R. J. Schoelkopf (2010). "High-Fidelity Readout in Circuit Quantum Electrodynamics Using the Jaynes-Cummings Nonlinearity". *Phys. Rev. Lett.* **105**, 173601 (cited on page 33).

Reed, M. D., L. DiCarlo, S. E. Nigg, L. Sun, L. Frunzio, S. M. Girvin, and R. J. Schoelkopf (2012). "Realization of three-qubit quantum error correction with superconducting circuits". *Nature* **482**, 382–385 (cited on page 51).

Reed, R., C. McCowan, R. Walsh, L. Delgado, and J. McColskey (1988). "Tensile strength and ductility of indium". *Materials Science and Engineering: A* **102**, 227–236 (cited on pages 137, 138).

Reid, J. R., E. D. Marsh, and R. T. Webster (2006). "Micromachined Rectangular-Coaxial Transmission Lines". *IEEE Trans. Microw. Theory Tech.* **8**, 3433–3442 (cited on page 61).

Ridenour, L. N. (1948). *Microwave Transmission Circuits*, volume 9 of MIT Radiation Laboratory Series. McGraw-Hill, New York (cited on page 103).

Rivest, R. L., A. Shamir, and L. Adleman (1978). "A Method for Obtaining Digital Signatures and Public-key Cryptosystems". *Commun. ACM* **21**, 120–126 (cited on page 12).

Roch, N., M. E. Schwartz, F. Motzoi, C. Macklin, R. Vijay, A. W. Eddins, A. N. Korotkov, K. B. Whaley, M. Sarovar, and I. Siddiqi (2014). "Observation of Measurement-Induced Entanglement and Quantum Trajectories of Remote Superconducting Qubits". *Phys. Rev. Lett.* **112**, 170501 (cited on page 51).

Rosenberg, D., D. Kim, D.-R. Yost, J. Mallek, J. Yoder, R. Das, L. Racz, D. Hover, S. Weber, A. Kerman, and W. Oliver (2017). "3D Integration for Superconducting Qubits". In: APS March Meeting 2017, H46.00001 (cited on page 213).

Sandberg, M., M. R. Vissers, J. S. Kline, M. Weides, J. Gao, D. S. Wisbey, and D. P. Pappas (2012). "Etch induced microwave losses in titanium nitride superconducting resonators". *Appl. Phys. Lett.* **100**, 262605 (cited on page 60).

Sandberg, M., M. R. Vissers, T. A. Ohki, J. Gao, J. Aumentado, M. Weides, and D. P. Pappas (2013). "Radiation-suppressed superconducting quantum bit in a planar geometry". *Appl. Phys. Lett.* **102**, 072601 (cited on page 165).

Sandberg, M., E. Knill, E. Kapit, M. R. Vissers, and D. P. Pappas (2016). "Efficient quantum state transfer in an engineered chain of quantum bits". *Quantum Information Processing* **15**, 1213–1224 (cited on page 165).

Schoelkopf, R. J. and S. M. Girvin (2008). "Wiring up quantum systems". *Nature* **451**, 664–669 (cited on pages 19, 42).

Schreier, J., A. Houck, J. Koch, D. Schuster, B. Johnson, J. Chow, J. Gambetta, J. Majer, L. Frunzio, and M. Devoret (2008). "Suppressing charge noise decoherence in superconducting charge qubits". *Phys. Rev. B* **77**, 180502(R) (cited on pages 25, 26).

Schulte, E. (2013). *Surface preparation with ONTOS7 atmospheric plasma*. Technical Report. And private communication with Eric Schulte. SET-NA (cited on page 139).

Schuster, D. I. (2007). "Circuit Quantum Electrodynamics". PhD thesis. Yale University, New Haven, CT (cited on pages 32, 41, 80).

Schuster, D. I., A. A. Houck, J. A. Schreier, A. Wallraff, J. M. Gambetta, A. Blais, L. Frunzio, J. Majer, B. Johnson, M. H. Devoret, S. M. Girvin, and R. J. Schoelkopf (2007). "Resolving photon number states in a superconducting circuit". *Nature* **445**, 515–518 (cited on pages 31, 222).

Shor, P. W. (1994). "Algorithms for Quantum Computation: Discrete Logarithms and Factoring". In: Proc. of the 35th Annual Symposium on Foundations of Computer Science.

SFCS '94. Washington, DC, USA: IEEE Computer Society, 124–134. ISBN: 0-8186-6580-7 (cited on page 12).

Shor, P. W. (1995). "Scheme for reducing decoherence in quantum computer memory". *Phys. Rev. A* **52**, R2493–R2496 (cited on page 16).

— (1996). "Fault tolerant quantum computation". *arXiv:quant-ph/9605011* (cited on page 15).

— (1997). "Polynomial-Time Algorithms for Prime Factorization and Discrete Logarithms on a Quantum Computer". *SIAM Journal on Computing* **26**, 1484–1509 (cited on page 12).

Sliwa, K. M., M. Hatridge, A. Narla, S. Shankar, L. Frunzio, R. J. Schoelkopf, and M. H. Devoret (2015). "Reconfigurable Josephson Circulator/Directional Amplifier". *Phys. Rev. X* **5**, 041020 (cited on page 69).

Sooriakumar, K., W. Chan, T. S. Savage, and C. Fugate (1995). "A comparative study of wet vs. dry isotropic etch to strengthen silicon micro-machined pressure sensor". In: Proc. 2nd. Int. Symp. Microstructures and Microfabricated Systems. Electrochemical Soc. Pennington, NJ, 259–265. ISBN: 9781566771238 [1566771234] (cited on page 139).

Steane, A. M. (1996). "Error Correcting Codes in Quantum Theory". *Phys. Rev. Lett.* **77**, 793–797 (cited on pages 15, 16).

Steffen, L., Y. Salathe, M. Oppliger, P. Kurpiers, M. Baur, C. Lang, C. Eichler, G. Puebla-Hellmann, A. Fedorov, and A. Wallraff (2013). "Deterministic quantum teleportation with feed-forward in a solid state system". *Nature* **500**, 319–322 (cited on page 51).

Sun, L., B.-H. Sun, G.-X. Zhang, D. Cao, and B. Fan (2013). "Design and Investigation of a Dual-Band Annular Ring Slot Antenna for Aircraft Applications". *Prog. in Electromag. Research C* **38**, 67–78 (cited on page 168).

Takahashi, K. (2001). "Packaging Using Microelectromechanical Technologies and Planar Components". *IEEE Trans. on Microwave Theory and Techniques* **49**, 2099–2104 (cited on page 59).

Tian, Y., C. Liu, D. Hutt, and B. Stevens (2008). "Electrodeposition of indium for bump bonding". In: *58th Electronic Components and Technology Conf. 2096–2100* (cited on page 212).

Tian, Y., C. Liu, D. Hutt, and B. Stevens (2014). "Electrodeposition of Indium Bumps for Ultrafine Pitch Interconnection". *J. Electronic Materials* **43**, 594–603 (cited on page 212).

Tinkham, M. (1996). Introduction to Superconductivity. Dover Books on Physics Series. Dover Publications. ISBN: 0486435032 (cited on page 156).

Tuckerman, D. B., M. C. Hamilton, D. J. Reilly, R. Bai, G. A. Hernandez, J. M. Hornibrook, J. A. Sellers, and C. D. Ellis (2016). "Flexible superconducting Nb transmission lines on thin film polyimide for quantum computing applications". *Superconductor Science and Technology* **29**, 084007 (cited on page 65).

Vesterinen, V., O. P. Saira, A. Bruno, and L. DiCarlo (2014). "Mitigating information leakage in a crowded spectrum of weakly anharmonic qubits". *arXiv:1405.0450v2[cond-mat.mes-hall]* (cited on page 52).

Vlastakis, B., G. Kirchmair, Z. Leghtas, S. E. Nigg, L. Frunzio, S. M. Girvin, M. Mirrahimi, M. H. Devoret, and R. J. Schoelkopf (2013). "Deterministically Encoding Quantum Information Using 100-Photon Schrodinger Cat States". *Science* **342**, 607–610 (cited on pages 16, 33, 186).

Volpert, M., L. Roulet, J. F. Boronat, I. Borel, S. Pocas, and H. Ribot (2010). "Indium deposition processes for ultra fine pitch 3D interconnections". In: 60th Electronic Components and Technology Conference (ECTC), 1739–1745 (cited on pages 134, 212).

Wang, C., C. Axline, Y. Gao, T. Brecht, Y. Chu, L. Frunzio, M. H. Devoret, and R. J. Schoelkopf (2015). "Surface participation and dielectric loss in superconducting qubits". *Appl. Phys. Lett.* **107**, 162601 (cited on pages x, 52, 89, 189).

Wang, C., Y. Y. Gao, P. Reinhold, R. W. Heeres, N. Ofek, K. Chou, C. Axline, M. Reagor, J. Blumoff, K. M. Sliwa, L. Frunzio, S. M. Girvin, L. Jiang, M. Mirrahimi, M. H. Devoret,

and R. J. Schoelkopf (2016). "A Schrödinger cat living in two boxes". *Science* **352**, 1087–1091 (cited on pages 75, 77).

Welch, W. C. and K. Najafi (2008). "Gold-indium Transient Liquid Phase (TLP) wafer bonding for MEMS vacuum packaging". In: 2008 IEEE 21st Int. Conf. on MEMS, 806–809 (cited on page 133).

Wenner, J., R. Barends, R. C. Bialczak, Y. Chen, J. Kelly, E. Lucero, M. Mariantoni, A. Megrant, P. J. J. O'Malley, D. Sank, A. Vainsencher, H. Wang, T. C. White, Y. Yin, J. Zhao, A. N. Cleland, and J. M. Martinis (2011a). "Surface loss simulations of superconducting coplanar waveguide resonators". *Appl. Phys. Lett.* **99**, 113513 (cited on pages 52, 89).

Wenner, J, M Neeley, R. C. Bialczak, M Lenander, E. Lucero, A. D. O'Connell, D Sank, H Wang, M Weides, A. N. Cleland, and J. M. Martinis (2011b). "Wirebond crosstalk and cavity modes in large chip mounts for superconducting qubits". *Superconductor Science and Technology* **24**, 065001 (cited on page 52).

Werner, T., R. Tidecks, and B. Johnston (1985). "Whiskers from the In-Pb system: Growth, handling and characteristic properties". *J. Crystal Growth* **73**, 467–481 (cited on page 138).

Wiesner, S. (1983). "Conjugate Coding". *SIGACT News* **15**, 78–88 (cited on page 14).

Wootters, W. K. and W. H. Zurek (1982). "A single quantum cannot be cloned". *Nature* **299**, 802–803 (cited on page 15).

Wu, J., J. Scholvin, and J. del Alamo (2004). "A through-wafer interconnect in silicon for RFICs". *IEEE Trans. on Electron Devices* **51**, 1765–1771 (cited on page 64).

Yoder, J., D. Kim, P. Baldo, A. Day, G. Fitch, E. Holihan, D. Hover, G. Samach, G. Samach, S. Weber, and W. Oliver (2017). "Bridging the Gap for High-Coherence, Strongly Coupled Superconducting Qubits". In: APS March Meeting 2017, H46.00003 (cited on page 182).

Zhang, P., Y. Zhang, and Z. Sun (2015). "Spontaneous Growth of Metal Whiskers on Surfaces of Solids: A Review". *J. Materials Science Technology* **31**, 675–698 (cited on page 138).

Zhang, W. and W. Ruythooren (2008). "Study of the Au/In Reaction for Transient Liquid-Phase Bonding and 3D Chip Stacking". *J. Elec. Materi.* **37**, 1095 (cited on page 195).

Zheng, M., Q. Chen, P. S. Hall, and V. F. Fusco (1998). "Broadband microstrip patch antenna on micromachined silicon substrates". *Electronics Letters* **34**, 3–4 (cited on page 168).

Zmuidzinas, J. (2012). "Superconducting Microresonators: Physics and Applications". *Ann. Rev. Cond. Matter Phys.* **3**, 169–214 (cited on pages 52, 86, 155).